

Developing Microbubble-Nanodroplet Composites for Enhanced Hydrophobic Drug Delivery

Victoria Micó Egea

The University of Leeds
School of Physics and Astronomy

March 2017

Submitted in accordance with the requirements for the degree of
Doctor of Philosophy

*The candidate confirms that the work submitted is her own and that appropriate credit has been
given where reference has been made to the work of others.*

*This copy has been supplied on the understanding that it is copyright material and that no
quotation from the thesis may be published without proper acknowledgement.*

Para mamá y papá

“Science is a quest for understanding”

Jocelyn Bell Burnell

Acknowledgements

I would like to thank my supervisor, Prof Stephen Evans for his guidance, support and advice throughout this project. This PhD has proven challenging at times and I appreciate that without his help I would probably not be writing this today. During my PhD I have had some of the best experiences of my life, and I will always be grateful to Steve for giving me this opportunity.

Thanks to Dr Sally Peyman for being the best *real* boss and one of the best friends I could have asked for. I thank Sal for showing me the real meaning of science, and for boosting my already well-developed skepticism. I am immensely grateful for her patience and understanding, particularly at the difficult times. She has been a pillar of strength on my way through this PhD and surely the reason why I sound so Yorkshire.

I would like to extend my acknowledgement to everyone involved in the Leeds Micro-bubble Consortium for useful discussions throughout the project. Thanks to Dr Louise Coletta for her invaluable help with the biological side of the project. Special thanks go to Dr Radwa Abou-Saleh for taking the time to read parts of this thesis and provide feedback, and for her support whenever needed (I owe you some cake!). Thanks to Dr James McLaughlan for assistance with the US experiments. Thanks also to Prof Richard Bushby for all the chemistry discussions. I would like to thank Dr Benjamin Johnson for his help with equipment and chemicals, and for fixing all the things I broke. And of course thanks to Miss Antonia Charalambous for staying sane with me during the last year. Preparing LONDS in company turned out to be way better.

Thanks to Super Kasia for always being so lovely and helpful and for making the effort to read some chapters and send back comments despite being in sunny Germany.

Thanks to Adam Churchman for being the most annoying person I have ever met, yet one of the best friends I have ever had. Thanks for listening whenever I needed it and for forgetting my problems soon enough. I thank him for keeping me fairly entertained during the time I have been writing my thesis and for not killing me when I was the one being annoying.

Thanks to all the MNPers for being the most awesome group of scientists. Specially, I thank Julia Gala and Fern Armistead (and Ed Sheeran) for the best dances ever, for welcoming me in their house and helping me stay sane during my writing. I am not too sure if I would have made it here without them #inspiring. Thanks also to Twiggles for teaching me Yorkshire, cricket and climbing, and to Jamos Goodchildos for never failing in making me laugh. Although they are no longer in MNP, I need to mention Dr Jenny Bain and Dr Megano for their early efforts towards understanding my accent and for some of the best anecdotes of the last few years. Thanks to Megan for showing me that the fatter the knees the better the unicorn and for convincing me that I could run. I promise I will never again put her down as my emergency contact though.

I also need to mention LUUBC (now UOLBC) for making my time in Leeds Uni even more memorable. Thanks to all the Senior Women 2015-2016 for being the funniest, most

genuine rowers I have met #sasa. Thanks to my Henley 4+ (Effy, Hatty, Nat and Britt) for rowing with me some of the best races ever, and for teaching me that every single stroke counts. Of course, if there is a rower that deserves a mention, that is my bestie Bella Schild. Despite being *an undergrad*, Bella has been one of the best friends. I thank her for being the best gym buddy and getting me into body p, and also for all her music recommendations, food advices and most importantly, for being my favourite Londoner. I am confident she will reach adulthood soon.

I would like to thank all my friends from home, Ana, Mabel, Dani and Maria, who have always been there and have never failed to entertain me when I was back home. Thanks also to Marta for being such good friend and much better than me at keeping in touch.

I am deeply grateful to Mne Raymont for his unconditional love, trust and support. Thanks Ed for being so caring and patient with all my meltdowns during my writing. The last six months would have been even harder without you. Whatever happens, please do not stop charming me. I love you.

Lastly, I want to thank my family, mum, dad, Carlos and Jorge, for all their support throughout the years I have been working towards this PhD, and for encouraging me along the way. Thanks mum and dad for being so loving, so attentive, so supportive and for simply being the best parents. I have no doubts I would not have achieved this without you and I am deeply grateful that you have always trusted me. This is for you.

Abstract

The modernisation of the pharmaceutical industry together with the sophistication of drug screening protocols have led to a dramatic increase in the number of therapeutic agents developed annually. As per 2017, there are almost 1500 FDA approved anticancer drugs. Treatments with many of those are impaired by their toxicity, pharmacokinetic profile, reduced bioavailability or poor water solubility. In an effort to improve patient experience whilst offering the most effective anticancer treatment, numerous drug delivery vehicles have been developed in recent years. These systems often encapsulate the drug to prevent its degradation and help reduce the required doses by increasing the specificity of the treatments. Drug hydrophobicity presents an added challenge for the design of drug delivery systems, as they must be capable of transporting the therapeutic agents whilst preventing their agglomeration. This project has been concerned with the design of a delivery system for hydrophobic drugs. The microbubble-nanodroplets (MB-LONDS) architecture consists of an echogenic MB decorated with LONDS, which attach to the shell of the MB via biotin-NeutrAvidin chemistry. The LONDS are able to encapsulate hydrophobic drugs in their oil core, keeping them away from the aqueous solution and thus preventing drug agglomeration and degradation. The MB acts as a vehicle for the LONDS, and its ultrasound properties can be used for both imaging and controlling the release of the LONDS.

A number of biocompatible oils were chosen and characterised in terms of their light absorption and emission properties, as well as their ability to solvate a number of hydrophobic drugs and drug mimics. Informed by the results obtained in this study squalane, triacetin and tripropionin were chosen as model oils for subsequent experiments on LOND formation. LONDS were produced in a two-step process, and generally exhibited sizes between 80 – 300 nm with good stability for at least 6 weeks when stored at 4 °C. Encapsulation of the hydrophobic drug CA4 in triacetin and tripropionin LONDS was shown to be possible, with an encapsulation efficiency of at least 76% in the case of tripropionin LONDS. To better understand the attachment of LONDS onto the MB shells, the attachment of LONDS to model membranes was investigated. This study explored three different attachment chemistries, namely the biotin-NeutrAvidin, maleimide-thiol and pyridyl-thiol. The results revealed the viability of the LONDS attachment using the different linkers, but also pointed to the existence of a high number of non-specific interactions between the LONDS and the membranes. The assembly of MB-LONDS was performed by a number of methods and with different LOND types. MB-LONDS prepared in a two-step process on-chip exhibited average sizes around 2 μm , good stability over 2 h at 37 °C and were found to be US responsive.

Publications

- **V. Mico**, A. Charalambous, S. A. Peyman, R. H. Abou-Saleh, A. F. Markham, P. L. Coletta, and S. D. Evans. Evaluation of Lipid-Stabilised Tripropionin Nanodroplets as a Delivery Route for Combretastatin A4. *International Journal of Pharmaceutics*, 526(1–2): 547-555, 2017. [1]
- A. H. Churchman, **V. Mico**, J. Gala de Pablo, S. A. Peyman, S. Freear and S. D. Evans. Combined Flow-Focus and Self-Assembly Routes for the Formation of Lipid Stabilised Oil-Shelled Microbubbles. Submitted for publication to *Microsystems & Nanoengineering*.

Conference proceedings

- **V. Mico**, S. A. Peyman, S. D. Evans. Two-step, single chip, microfluidic production of hybrid Microbubble-Nanodroplet architectures for enhanced hydrophobic drug delivery. Presented at The 21st European Symposium on Ultrasound Contrast Imaging 2016.
- **V. Mico**, A. H. Churchman, S. A. Peyman, S. D. Evans. Single step microfluidic production of microbubble architectures for hydrophobic drug delivery. Presented at Miniaturized Systems for Chemistry and Life Sciences (MicroTAS) 2014.
- **V. Mico**, S. A. Peyman, S. D. Evans. Engineering Nanodroplet-Microbubble architectures for Hydrophobic Drug Delivery. Presented at Condensed Matter in Paris 2014.

List of abbreviations

Constants

k_b	Boltz mann's constant, $1.38064 \times 10^{-23} \text{ m}^2 \text{ kg} / \text{s}^{-2} \text{ K}$
g	gravitational acceleration, 9.8 m/s^2
ρ_q	density of quartz, 2.648 g/cm^3
μ_q	shear modulus of quartz, $2.947 \times 10^{11} \text{ g/cm s}^2$
ρ_w	density of water, 1000 kg/m^3
ν_w	viscosity of water, $1 \times 10^{-3} \text{ Pa s}$

Experimental techniques

DLS	Dynamic Light Scattering
QCM-D	Quartz Crystal Microbalance with Dissipation
UV-VIS	Ultraviolet-Visible
LOC	Lab-on-a-chip
Qdots	Quantum dots
TEM	Transmission Electron Microscope
IVIS	<i>In vivo</i> Imaging System
US	Ultrasound

Chemicals

DDT	dithiothreitol
-----	----------------

PBS	Phosphate-Buffered Saline
MilliQ	18 M Ω UltraPure water
EPA	Eicosapentaenoic acid
DMSO	Dimethyl Sulfoxide
EggPC	L- α -lysophosphatidylethanolamine
DPPC	1,2-dipalmitoyl-sn-glycero-3-phosphocholine
PEG	polyethylene glycol
PEG2000-DSPE (also PEG2000)	1,2-distearoyl-sn-glycero-3-phosphoethanolamine-N-[methoxy(polyethylene glycol)-2000]
biotin-PEG2000-DSPE	1,2-distearoyl-sn-glycero-3-phosphoethanolamine-N-[biotinyl(polyethylene glycol)-2000]
POPC	1-palmitoyl-2-oleoyl-sn-glycero-3-phosphocholine
DSPC	1,2-distearoyl-sn-glycero-3-phosphocholine
PMMA	Poly(methyl methacrylate)

Miscellaneous

LONDS	Lipid-stabilised Oil Nanodroplets
MB(s)	Microbubble(s)
SBLMs	Solid-supported Bilayer Lipid Membranes
FITC	Fluorescein Isothiocyanate
TR	Texas Red
DM	Dichroic Mirror
ROI	Region of interest
λ_{ex}	Excitation Wavelength
λ_{em}	Emission Wavelength
PI	Polydispersity Index

Table of contents

Publications	viii
List of abbreviations	ix
Table of contents	xi
List of figures	xvi
1 Introduction	1
1.1 A step further: <i>theranostic</i> agents	4
1.1.1 Microbubbles as theranostic agents	5
1.2 Scope of the project and thesis layout	8
2 Theoretical background	10
2.1 MB formation and stability	10
2.1.1 Concept and formation	10
2.1.1.1 Echogenic MBs	12
2.1.2 Microfluidic formation of MBs	13
2.1.2.1 A brief introduction to microfluidics	13
2.1.2.2 The flow-focused geometry	15
2.2 Emulsions: formation and stability	16
2.2.1 Definitions	16
2.2.2 Theory of emulsification	17

2.2.3	Methods of emulsification	19
2.2.3.1	Rotor-stator homogenisers	20
2.2.3.2	High-pressure homogenisation	21
2.2.4	Mechanisms for emulsion breakdown	24
3	Experimental Techniques	27
3.1	Lipids preparation and procedures	27
3.1.1	Preparation of vesicles by tip sonication	28
3.1.2	Lipid for MB preparation	28
3.2	Qdots	28
3.2.1	Synthesis of CIS/ZnS Qdots	29
3.2.2	Determining the concentration and size of Qdots	29
3.3	Light absorption and emission studies	30
3.3.1	Fluorescence Spectroscopy	31
3.3.2	UV-VIS Spectroscopy	32
3.3.3	<i>In Vivo</i> Imaging System	32
3.4	Microscopy techniques	32
3.4.1	Epi-fluorescence microscopy	33
3.4.2	Confocal microscopy	34
3.4.3	Transmission Electron Microscopy	34
3.5	Size and concentration measurements	34
3.5.1	Dynamic Light Scattering	35
3.5.2	Single Particle tracking for size and concentration measurement	36
3.5.3	Tunable Resistive Pulse Sensing	36
3.5.4	Optical counting	37
3.6	Quartz Crystal Microbalance with Dissipation	38
3.6.1	QCM-D experimental set-up	40
3.6.2	Formation of SBLMs for QCM-D experiments	41

3.7	Formation of MBs	42
3.7.1	On-chip preparation of MBs	43
3.7.1.1	Fluidics set-up	43
3.7.1.2	Preparation of MBs	44
3.7.1.3	Preparation of MB-LONDS	45
3.7.2	Production of MBs by mechanical agitation	46
3.8	Biosafety cabinet. Functioning and protocols	46
4	Topic: characterisation of the candidate oils	48
4.1	The candidate oils	48
4.2	Light absorption and emission of candidate oils	50
4.2.1	Light absorption of candidate oils	51
4.2.2	Autofluorescence of candidate oils	52
4.3	Drug mimics in candidate oils	55
4.3.1	CIS/ZnS Qdots: solubility and fluorescence in oil	55
4.3.2	Nile Red: solubility and fluorescence in candidate oils	59
4.3.3	Calcein AM	60
4.4	Drugs in candidate oils	63
4.4.1	Combretastatin A4	63
4.4.2	Decitabine	66
4.5	Discussion	68
5	Topic: Lipid Oil Nanodroplets	71
5.1	LONDS production in a two-step homogenisation process	71
5.1.1	Sterility of LOND samples	73
5.2	Preliminary observations	74
5.3	LOND size measurements	76
5.3.1	LONDS size change throughout preparation	77

5.3.2	The effect of pressure on LONDS size	79
5.3.3	The role of the lipid shell on LONDS size	82
5.3.4	The effect of the oil on LOND size	84
5.4	Concentration measurements	86
5.4.1	The effect of pressure on LONDS concentration	87
5.4.2	The effect of oil on LOND concentration	89
5.5	Stability of LONDS	91
5.6	LONDS imaging	94
5.6.1	TEM	94
5.6.2	Epifluorescence microscopy	97
5.7	Discussion	98
6	Topic: Encapsulation in LONDS	104
6.1	Encapsulation of Qdots	104
6.2	Encapsulation of Calcein AM	107
6.3	Encapsulation of CA4	109
6.4	Discussion	115
7	Topic: Attachment of LONDS to model lipid membranes	119
7.1	A need to asses LOND binding	119
7.2	Binding affinity of biotin-Streptavidin	121
7.3	LONDS attachment to SBLMs	125
7.3.1	Three-layer systems on QCM-D	125
7.3.2	LOND-SBLMs attachment via biotin-NeutrAvidin	128
7.3.3	LOND-SBLMs attachment via PDP-thiol and Maleimide-thiol . . .	138
7.4	Discussion	149
8	Topic: MBs and MB-LONDS	155
8.1	On-chip preparation of MBs	155

8.2	Key considerations for preparing MB-LONDs	156
8.2.1	The lensing effect	157
8.3	Off-chip preparation of MB-LONDs	159
8.4	On-chip, single-step MB-LONDs preparation	161
8.5	On-chip, two-step MB-LONDs preparation	165
8.5.1	MB with mixed squalane/triacetin LONDs attachment	171
8.6	Stability of MBs and MB-LONDs	172
8.7	Ultrasound response	173
8.8	Discussion	177
9	Conclusion and future challenges	180
9.1	Current perspectives	180
9.2	Alternative applications of MB-LONDs	186
9.3	MB-LONDs: conclusions and the future	188
A	List of chemicals and instruments	191
B	Supplementary information for chapter 7	197
C	Supplementary information for chapter 8	199

List of Figures

1.1	Schematic of a lipid-stabilised oil nanodroplet (LOND)	3
1.2	Schematic of the therapeutic MB architectures	6
1.3	Schematic of the MB-LOND architecture	8
2.1	Schematic of the structure of a MB	11
2.2	Calculated resonant frequency of lipid coated MBs	13
2.3	Image of a microfluidic device used in this project	14
2.4	Microfluidic flow-focusing geometry for MB production	15
2.5	Shematic of an oil-in-water and a water-in-oil emulsion	16
2.6	Schematic of the emulsification process	19
2.7	Schematic of a rotor-stator system	21
2.8	Emulsiflex and schematic of its functioning	22
2.9	Emulsion temperature increase through the homogenising nozzle	23
2.10	Schematic of processes leading to emulsion destabilisation	25
3.1	Jablonski diagram illustrating molecular light absorption and emission	31
3.2	Schematic showing the light path in an upright epifluorescence microscope	33
3.3	Schematic showing the functioning of qNano	37
3.4	Typical bright field image of MBs used for optical counting	38
3.5	Schematic of the arrangement of viscoelastic layers on a QCM-D sensor	40
3.6	Semi-schematic showing the formation of a SBLM in QCM-D	42

3.7	Schematic showing the set-up of the microfluidic device for MB-LONDS formation	43
3.8	Design of a multiplexed microchip for microspray MB formation	44
3.9	Design of the microchip used for the two-step MB-LONDS formation	45
4.1	Molecular structure of the candidate oils, non-blends.	49
4.2	Molecular structure of the main components of olive oil	50
4.3	Light absorption of the candidate oils, recorded using a spectrophotometer .	52
4.4	Emmission spectrum of squalane	53
4.5	Radiant efficiency of squalene and squalane measured in IVIS	55
4.6	Luminescence characterisation of CIS/ZnS Qdots	56
4.7	Fluorescence of Qdots diluted in candidate oils	57
4.8	Radiant efficiency of Qdots dissolved in squalene and squalane measured in IVIS	58
4.9	Molecular structure of the fluorophore Nile Red.	59
4.10	Absorption of Nile Red in tripropionin	60
4.11	Molecular structure of calcein AM	61
4.12	Absorption of Calcein AM in triacetin	62
4.13	Absorption of Calcein AM in DMSO	63
4.14	Molecular structure of Combretastatin A4.	64
4.15	Absorption of Combretastatin A4 in triacetin	65
4.16	Absorption of Combretastatin A4 in tripropionin	65
4.17	Molecular structure of decitabine.	66
4.18	Absorption of decitabine in triacetin	67
4.19	Absorption of decitabine in DMSO	68
5.1	Schematic showing the different steps in LOND production	72
5.2	Schematic showing the functioning of a cross-filtration column	73

5.3	Two examples of agar LB Broth plates used to test the sterility of LOND samples	74
5.4	Relationship between the size of a MB and the number of LONDS and oil volume it can transport	76
5.5	Size distribution of squalane and triacetin LONDS throughout the two-step preparation process	78
5.6	DLS sizing of squalane and tripropionin LOND samples prepared under different pressures	80
5.7	Sizing of LOND samples produced under different pressures using the NanoSight instrument	81
5.8	Size distribution of squalane LONDS with different lipid coatings	83
5.9	LONDS size against oil viscosity	86
5.10	Concentration of squalane and tripropionin LONDS produced under different pressures in the Emulsiflex	88
5.11	Concentration measurement of a triacetin LOND sample as determined by qNano	89
5.12	Size change of squalane, triacetin and tripropionin LONDS over a six week period, stored at 4 °C	92
5.13	Size change of squalane and triacetin LONDS over at 37 °C over 2 h	93
5.14	TEM images of squalane LONDS	95
5.15	TEM images of triacetin LONDS	96
5.16	TEM images of tripropionin LONDS	97
5.17	Epifluorescence images of LONDS	98
6.1	Fluorescence of Qdots encapsulated in squalane LONDS	106
6.2	Fluorescence of Qdots encapsulated in squalane LONDS as measured by IVIS106	
6.3	Absorption of cross-filtered triacetin LONDS encapsulating calcein AM and of the fraction of liquid permeated during cross-filtration	109
6.4	Absorption of CA4 encapsulated in triacetin LONDS	110

6.5	Schematic showing the set-up used to study the leakage of CA4 from the triacetin LONDS	113
6.6	Leakage of CA4 encapsulated in LONDS through a dialysis membrane . . .	113
6.7	Absorption of CA4 encapsulated in tripropionin LONDS	114
7.1	Schematic showing the binding of StreptAvidin to biotin-PEG2000-DSPE in a SBLMs	121
7.2	QCM-D results for StreptAvidin binding to SBLMs with different biotin-PEG2000-DSPE concentrations	124
7.3	Schematic of the two possible scenarios for the StreptAvidin binding to QCM-D sensors	125
7.4	Example of the type of data recorded on QCM-D for a 3-layer system . . .	126
7.5	Schematic showing all LOND/SBLM combinations studied in the biotin-NeutrAvidin attachment study case	128
7.6	QCM-D results for squalane LONDS binding to SBLMs	130
7.7	Schematic showing a LONDS merging with a SBLMs	132
7.8	Summary of the interactions between squalane LONDS and SBLMs for different lipid coating combinations	134
7.9	QCM-D results for squalane LONDS binding to SBLMs	136
7.10	Summary of the interactions between triacetin LONDS and SBLMs for different lipid coating combinations	137
7.11	Schematic of maleimide and PDP reactions with DTT	138
7.12	Changes in frequency upon formation of SBLMs with different percentages of PDP-PEG2000-DSPE or Maleimide-PEG2000-DSPE	140
7.13	Schematic showing all LOND/SBLM combinations for the study of the PDP-thiol linking chemistry	141
7.14	Schematic showing all LOND/SBLM combinations for the study of the maleimide-thiol linking chemistry	142
7.15	QCM-D results for squalane LONDS binding to PDP-containing SBLMs . .	144
7.16	QCM-D results for squalane LONDS binding to maleimide-containing SBLMs	146

7.17	Summary of PDP/maleimide LOND/SBLM interaction experiments	148
8.1	Microspray formation of MBs	156
8.2	Images of fluorescent MBs and MBs showing fluorescence due to the lensing effect	157
8.3	Schematic of a flow cell used to wash and image MB-LOND samples	158
8.4	MB-LONDS formed off-chip	160
8.5	Illustration showing the formation of MB-LONDS on a single step on-chip .	162
8.6	MB-LONDS prepared in a single-step on-chip	164
8.7	Fluorescence imaging of the gradual mixing taking place throughout the mixing serpentine	167
8.8	MB-LONDS formed in a two-step process on-chip	168
8.9	Epifluorescence images of squalane and triacetin MB-LONDS imaged in a flow cell	169
8.10	Confocal images of MB-LONDS formed in a two-step process on-chip	170
8.11	Confocal image of a MB coated with a 50/50 mixture of squalane and triacetin LONDS	171
8.12	Lifetime of MBs and MB-LONDS at 37 °C	173
8.13	Attenuation of different MB and MB-LOND populations as a function of the ultrasound excitation frequency (2 – 14 MHz)	175
8.14	Schematic and data collected for the acoustic response of MBs and MB-LONDS injected in a phantom model vessel.	176
9.1	Preliminary assessment on the delivery of CA4 to SVR cells using tripropionin LONDS	183
9.2	Cross-section of a catheter with an US responsive coating	187
9.3	MB-LONDS could be used to deliver gas and nutrients to plants.	188
B.1	Additional control experiments for biotin-NeutrAvidin attachment experiments	197
B.2	Additional control experiments for maleimide/PDP attachment experiments	198

Chapter 1

Introduction

Cancer causes the death of more than 8 million people every year worldwide, and has a high incidence in modern society, affecting 1 in 5 people during their lives. In the last 20 years or so the improvement of anticancer chemotherapies has dramatically increased survival rates of cancer patients. [2] Recent research in the area has been prolific, with major advances reported periodically. Treatment efficiency and patient experience have been paramount to the latest developments. Among the challenges faced by the pharmaceutical community is the fact that many current anticancer drugs present a high number of non-ideal characteristics. For example, anticancer agents often exhibit high levels of toxicity, rapid metabolism and low adsorption, which impair cancer treatments. [3] To overcome these limitations, a multitude of drug delivery systems for the directed administration of therapeutic agents have been proposed. [4, 5] These systems rely on the idea of facilitating the transport of drugs *in vivo*, for example encapsulated in a nanocarrier, thus preventing undesired side effects for the patient, improving the specificity of the treatments and enhancing drug efficacy. Many of these drug delivery systems have proven useful for the delivery of water-soluble drugs, showing promising results both *in vitro* and *in vivo*.

Drug loaded liposomes are an excellent example of the drug delivery systems. [6–9] Liposomes consist of a spherical, self-assembling lipid bilayer enclosing an aqueous volume that serves as a drug compartment. Liposomes are generally formed with naturally occurring phospholipids, which enhances their biocompatibility and biodegradability. The modification of the liposome shell to include polyethylene glycol (PEG) constituted an important advancement towards effective treatments with liposomal formulations. [10] Many studies have shown that PEG chains grafted onto the surface of the liposomes,

usually attached covalently attached onto a DSPE lipid, have the ability to *hide* the liposomes from the immune system, which contributes to extending their blood-circulation time thus improving therapeutic treatments. [11–15] These PEG-containing liposomes are so called *stealth* liposomes. Since they were first formulated for the encapsulation of the anticancer drug doxorubicin, stealth liposomes have been assessed for the encapsulation of a vast majority of existent anticancer drugs. [3] A number of these liposomal formulations have shown promise in Phase III trials for the treatment of breast cancer, [16–18] ovarian cancer, [19, 20] and myeloma [21].

Notably, there is a high percentage of new pharmaceuticals that show poor water solubility or are hydrophobic. Some authors have estimated that these could account for up to 60% of the newly developed drugs. [22] *In vivo* treatments with these agents present numerous problems, such as reduced bioavailability due to agglomeration, [23] decreased efficacy and even toxicity. [24, 25] The lipophilicity of therapeutic compounds, or its ability to dissolve in a solvent other than water, is often expressed in terms of the logarithm of its partition coefficient between n-octanol and water. This is known as the $\log P$ value of the drug and it is defined as $\log P = \log (c_{octanol}/c_{water})$. [26, 27] It is generally accepted that lipophilic drugs have $\log P$ values from -0.4 to $+5.6$. [28] Several routes have been proposed for the delivery of hydrophobic drugs. One approach is to structurally modify the therapeutic compound to improve its water solubility. [29] These *prodrugs* typically undergo a chemical change *in vivo* yielding the active form of the drug. [30] However, prodrug synthesis is often complex and time consuming, and can lead to toxic breakdown products. [31, 32] Another possibility is to solubilise the hydrophobic compound in a solvent other than water. Paclitaxel, for example, is one of the most effective anticancer drugs ever synthesised, and widely used nowadays against a range of cancer types including lung and ovarian. [33] Its poor water solubility ($\sim 6 \mu\text{g}/\text{ml}$) was partially overcome by formulating it in a polyoxyethylated castor oil/ethanol mixture for injection, known by its trademark Taxol. However polyoxyethylated castor oil is not an inert carrier, and it is known to cause a number of adverse side effects in patients such as anaphylaxis and other severe hypersensitivity reactions. [34]

Alternatively, several encapsulation methods have been explored for the delivery of hydrophobic drugs. For example polymer-based micelles and microspheres have been shown to successfully incorporate hydrophobic drugs. [35–39] Among the existing methods, nanoemulsions are a cheap and versatile option for improving the delivery of poor

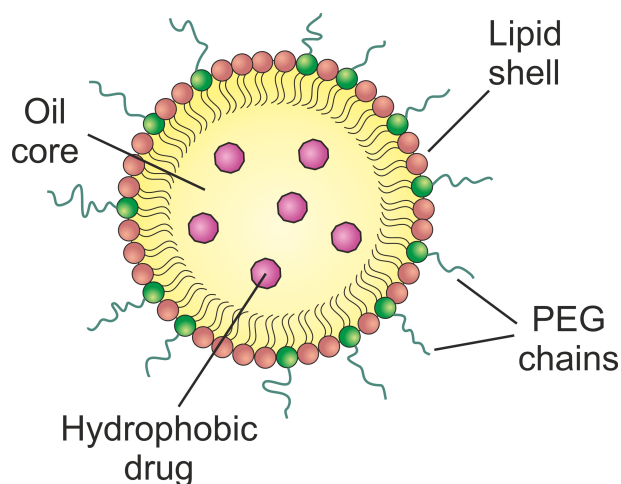


Figure 1.1: Schematic showing the structure of a Lipid-stabilised Oil NanoDroplet (LOND). Hydrophobic drugs are contained in the oil core of droplet, which is stabilised by a lipid monolayer and dispersed in water. PEG chains embedded onto the shell of the nanodroplets enhance their circulation time *in vivo*.

water soluble compounds. [40] Nanoemulsions consist of nanometer-sized oil droplets dispersed in water, which are stabilised with the presence of a surfactant in the oil-water interface. [41] One of the advantages of these systems is that the ingredients used for their formulation can be chosen to be biocompatible. For instance, phospholipids are of particular relevance for therapeutic nanoemulsions and have been extensively used as surfactants in such preparations. [42–46] In lipid-stabilised oil nanodroplets (LONDS) hydrophobic drugs can be encapsulated in their oil core, which prevents the drug from agglomerating in aqueous solutions. The structure of a LOND is shown schematically in figure 1.1. As for liposomes, one of the main mechanisms to improve the blood circulation time of lipid-stabilised nanoemulsions is the inclusion of a pegylated lipid in the shell composition. Nazzal and co-workers found a 7-fold increase in the mean residence time for tocotrienol nanoemulsions with grafted PEGs onto their surfaces. [47] Similarly, the study conducted by Ganta et al. showed that a pegylated nanoemulsion had a 1.3-fold longer half-life compared to a non-PEG-modified nanoemulsion. [48] Furthermore, the presence of PEG chains have been observed to influence the biodistribution of the nanoemulsions, and also to reduce accumulation in the liver. [49] The length of the PEG chains on the shell of the nanodroplets has also been reported to affect their fate *in vivo*. Particularly, Hak et al. noted greater cellular targeting and uptake for nanoemulsions with lower PEG contents (5mol% – 10mol%). [50] This was attributed to the brush configuration of the PEG chains on the surface at higher molar concentrations.

To date, nanoemulsions have shown promise for the encapsulation and delivery of a

number of anticancer agents. Ganta et al. reported increased efficiency of Paclitaxel against ovarian cancer cells delivered in a flaxseed oil nanoemulsion. [51] They observed that half the amount of drug was needed to inhibit cellular growth when Paclitaxel was administered in the nanoemulsion, compared to treatments with free Paclitaxel. This suggested improved bioavailability of the compound as a result of its encapsulation. Similarly, Jing et al. studied the delivery *in vivo* of Paclitaxel in a nanoemulsion consisted of a mixture of coconut oil-derived medium chain triglycerides and soybean oil-derived long chain triglycerides (known as MCT/LCT injectable lipid emulsion) stabilised with PEG400. [52] They reported reduced off-site toxicity and more potent antitumour efficacy in mice for their formulation, compared to conventional preparations. Another example is the delivery of the drug Dacarbazine encapsulated in soybean oil nanodroplets, found to have an increased efficacy when administered *in vivo*. [53]

1.1 A step further: *theranostic* agents

It is possible to extend the application of drug delivery systems to diagnostic purposes. In this way, they could be used for sequential assessment of the state of the disease and treatment, for example to determine the volume of a tumour prior to the treatment. The term *theranostics* refers to systems designed to combine diagnostic and therapeutic capabilities into a single agent. Theranostic agents hold great potential towards personalised medicine, which assesses the individual needs of patients to adequate treatments to each particular case. [54] There are numerous examples of theranostic agents developed in the last few years. In those, different imaging probes such as MRI contrast and fluorescence agents have been combined with various therapeutic agents. [55,56] For example, Wang and co-workers developed a theranostic agent for monitoring the stability of polymer-DNA complexes in cells by taking advantage of a Qdot-FRET¹. [57] This architecture combined plasmid DNA conjugated to QDots, and cyanine conjugated to chitosan, all assembled together via the biotin-StreptAvidin chemistry. Proximity of the cyanine and the Qdots resulted in FRET-mediated emission, whereas degradation of the complex derived in emission from only the Qdots. Ke et al. designed a poly(lactic acid) polymeric particle shelled with gold nanoshells. [58] These composites could be used for enhanced ultrasound (US) imaging, whilst the gold nanoshells provided them with the ability to be used for light-

¹fluorescence resonance energy transfer (FRET)

induced thermotherapy. More recently, Chen et al. [59] developed polymeric microcapsules composed of several tannic acid and poly(N-cinyl-pyrrolidone) layers assembled together through hydrogen bonding. The capsules were shown to have excellent US contrast properties controlled by varying the number of layers in the capsule shell. These US properties were used to deliver the drug doxorubicin to breast cancer cells *in vitro*.

1.1.1 Microbubbles as theranostic agents

Microbubbles are among the agents that can be developed for theranostic applications. Gas-filled lipid-stabilised microbubbles (MBs) have been extensively used as US contrast agents over the last 20 years. [60–62] Perfluorocarbon gases are typically used as the core of the MBs due to their low water solubility, which delays MB dissolution. [63] In addition, it is a requirement for clinical MBs to have sizes under 8 μm to avoid embolisms. The excellent ultrasonic capabilities exhibited by MBs arise from the acoustic impedance mismatch between the MB gas core and its surroundings, and also from the high compressible nature of the encapsulated gas. When exposed to an US pulse, the MB core expands and contracts with the applied pressure. This results in strong scattering of US, which enhances the signal received and therefore the contrast in clinical imaging. [64]

US has the notable ability to sensitise cell membranes and enhance the cytotoxic effect of drugs, when used in combination. Remarkably, US can cause pores to open in cell membranes which improves the transport of therapeutic compounds across them. [65] This phenomenon is called *sonoporation*. Several studies demonstrated in the late 90s the enhancement of cellular sonoporation in presence of MBs. [66,67] Studies carried out since then have provided insights of the mechanism underlying this phenomenon. [68–70] Cavitating MBs create flow streams that cause high levels of mechanical stress in nearby membranes. This can result in the formation of small pores in the cell membranes. [71,72] The dynamics of MB cavitation strongly depend on the intensity of the applied US, and thus the sonoporative effects. An overview of the process under the different conditions has been recently published. [73] Sonoporation holds a great potential to enhance drug delivery, and this characteristic is an asset in the use of therapeutic MBs over other theranostic agents.

Two different types of therapeutic MBs may be differentiated: those in which the

MBs and the therapeutic agent are co-administered, and those in which a drug payload is physically associated to the structure of the MBs. Both methods have been recently compared elsewhere. [79] This literature review focuses in delivery methods that involve structures combining MB and drug payloads, and these will be discussed below. One of the main advantages of MBs over other theranostic agents is their versatility as a result of their lipid coating. The properties of the shell can be easily tuned by simply modifying its lipid composition. This for example allows for varying the charge of the MBs, incorporating a positively or negatively charged lipid, or to incorporate ligands for functionalisation, such as biotin. This versatility has allowed for different ways of incorporating drug payloads onto MBs. [80] Figure 1.2 shows an schematic of the different approaches reported to date. One of the first routes was proposed by Yellowhair and co-workers in the late 90s. [75] They successfully incorporated a prodrug of dexamethasone into the structure of the MB, presumably embed in its lipid membrane. The same group reported the construction of a MB with an inner oil layer, in which Paclitaxel was successfully incorporated. [77] A

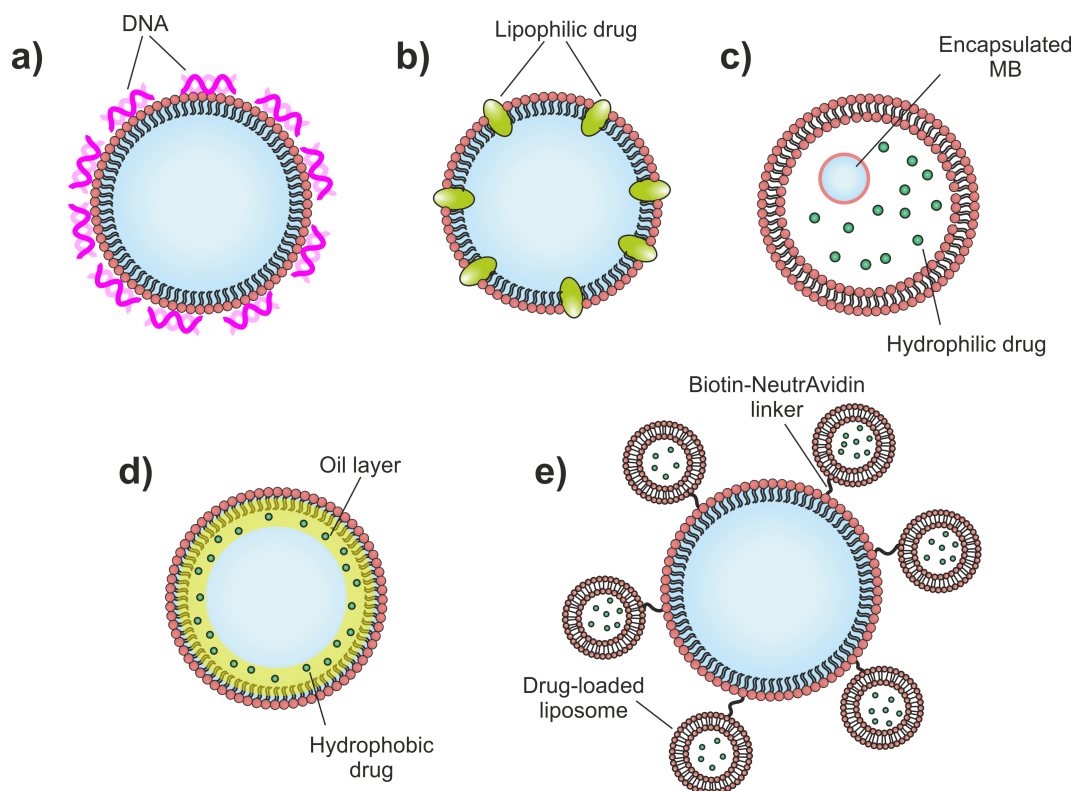


Figure 1.2: Schematic showing the structure different therapeutic MBs. a) Attachment of DNA to the MB shell for gene therapy [74] b) Lipophilic drug embedded in the MB shell. [75] c) Ibsen et al. proposed the encapsulation of a MB within a large vesicle. [76] d) Thickened shell with the addition of an oil layer. [77] e) MB-liposome complex proposed by Kheirilomoom et al. [78] Liposomes attach to the MB lipid shell via the biotin-Avidin (NeutrAvidin, StreptAvidin) interaction.

few years later Lentacker et al. prepared MBs with a plasmid DNA adhered to their shell via electrostatic interaction. [74] The charge in the MB shell not only allowed for the incorporation of the plasmid DNA, but also protected the cargo from degradation by nucleases. Another example is the work carried out by Ibsen et al., that focused in the development of a liposomal architecture that encapsulated a MB. These architectures were found to be US responsive, and showed success in encapsulating doxorubicin. [76]

The MB-liposome complex (figure 1.2e) has undoubtedly been the focus of a great deal of attention in recent years. This architecture consists of a MB decorated with liposomes, bound to the MB shell using the affinity of the biotin-Avidin (or NeutrAvidin/StreptAvidin). Compared to the other therapeutic MBs architectures, the liposomes allow for encapsulation of larger amounts of drugs in their inner volume. Furthermore the encapsulation of the drug is not subjected to the charge or lipophilic characteristics of the drugs, thus widening the usability of these complexes. Since the architecture was first reported by Ferrara and co-workers, [78] many researches have worked towards the application of the complexes. Lentacker et al. used MB-liposome complexes to deliver doxorubicin to melanoma cells *in vitro*. [81] They reported a dramatic enhancement of the treatment when the cells were exposed to the MB-liposome complexes and US, which was attributed to the release of the liposomes as a result of the US application and the sonoporation of the cell membrane, which contributed to liposome uptake. The use of the MB-liposome complexes has not been limited to the delivery of chemotherapeutic drugs. Sanders and co-workers took advantage of the architecture for gene delivery. [82]. They conjugated liposomes containing plasmid DNA to MBs, and tested the transfection efficiency to melanoma cells. The study concluded that gene transfer using liposomes containing plasmid DNA could be greatly enhanced by attaching them to MBs and exposing the complexes to US. Alternative chemistries for the binding of liposomes to MBs have been proposed. This is because the injection of exogenous proteins is known to cause an immune response in the organism, which limit the clinical application of MB-liposome complexes. [83] For instance, Lozano et. al explored DNA hybridization to tether liposomes onto the the MB shell. [84] In another study, Geers et al. used the thiol chemistry to bind liposomes containing doxorubicin and MBs. [85]

1.2 Scope of the project and thesis layout

The aim of this project was to develop a novel architecture for enhancing the delivery of therapeutic hydrophobic drugs. The MB-LONDS composite consists of an echogenic MB that acts as a vehicle for LONDS, attached to the MB shell, which are able to encapsulate poorly water soluble therapeutic agents. This architecture is shown conceptually in figure 1.3. The US properties of the MB would provide spatial and temporal control over the release of the LONDS, improving the specificity of the treatments. This architecture aimed to be used as a theranostic agent, allowing for simultaneous US imaging and drug delivery. There was an interest in performing the assembly of the architectures on-chip to have a grater control over the size distribution of the architectures and over MB surface functionalisation. Furthermore microfluidics could allow for automation of the fabrication, which would be desirable for the architectures to find a clinical application.

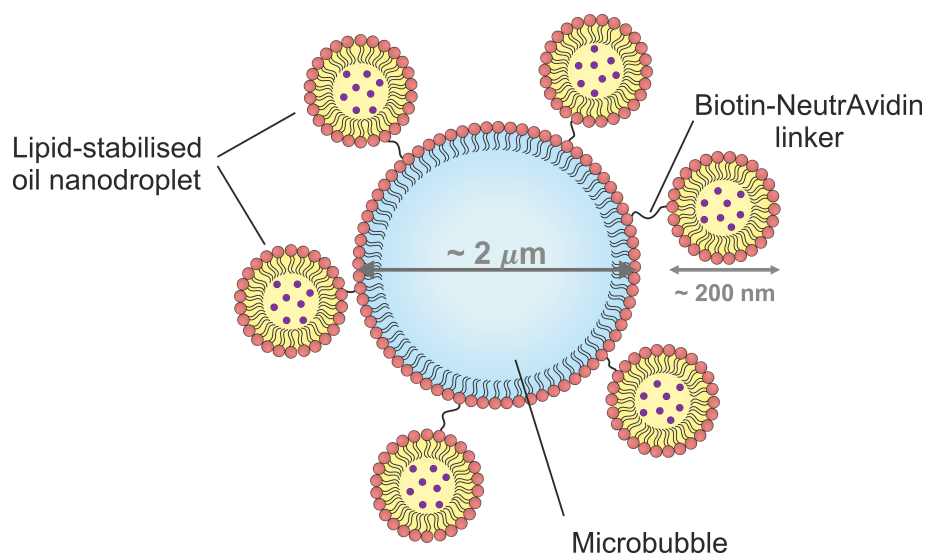


Figure 1.3: Schematic showing the structure of a the MB-LONDS architecture. LONDS with sizes around 200 nm are attached to the shell of the MBs ($\sim 2 \mu\text{m}$) via the biotin-NeutrAvidin link chemistry². This composite is a theranostic agent in which the US properties of the MBs can be used for imaging purposes and also to spatially control the release of the LONDS. Building this architecture was the main goal of this project.

This project consisted of several steps that aimed to provide the basis towards building the MB-LONDS architectures. These steps were: i) identification and characterisation of a number of biocompatible oils for LOND formation; ii) formation of LONDS; iii) encapsulation of drug mimics and hydrophobic drugs in LONDS; iv) attachment of LONDS to model membranes; and finally v) assembly of MB-LONDS. Thus, based on these steps,

²other linkers, such as maleimide-thiol and PDP-thiol, are also explored in this thesis

this thesis is structured as follows:

- **Chapter 2** describes the theoretical background underlying the production of MBs and LONDs. LONDs were understood as single nanodroplets within an oil-in-water nanoemulsions stabilised with a surfactant i.e. phospholipids.
- **Chapter 3** presents the experimental techniques and methods used throughout this project; it includes descriptions of the devices operation and also the protocols followed for measurements.
- **Chapter 4** describes the choice of the candidate oils for LOND formation and their characterisation, in terms of their optical absorption and emission, and also their ability to dissolve hydrophobic drug mimics and the hydrophobic drug CA4.
- **Chapter 5** provides the results of studies on LOND production with the different biocompatible oils. The formation of LONDs is a two-step process that includes homogenisation of the samples under high pressure. LOND formation was studied in the context of the production pressure, the encapsulated oil and the lipid used for stabilisation. The chapter also contains the findings on the stability of the LONDs under different conditions.
- **Chapter 6** presents the results from a series of experiments aimed at assessing the encapsulation of hydrophobic drug mimics and the hydrophobic drug CA4 in LONDs.
- **Chapter 7** presents the results from a study on the attachment of LONDs to model membranes via three different linking chemistries: biotin-NeutrAvidin, maleimide-thiol and PDP-thiol.
- **Chapter 8** is concerned with the assembly of the MB-LOND architectures. The results on the formation of the composites with different methods are presented.
- **Chapter 9** summarises the main findings presented in this thesis and provides an outlook to future studies in this field.

Chapter 2

Theoretical background

This chapter contains the theory details on formation and stability of microbubbles (MBs) and lipid-stabilised oil nanodroplets (LONDs) as the components of nanoemulsions.

2.1 MB formation and stability

This section is concerned with the formation and stability of lipid-stabilised MBs. Microfluidic formation of MBs is emphasised, and a short introduction to the microfluidics relevant to this process is included.

2.1.1 Concept and formation

Microbubbles (MBs) are small gas pockets with sizes in the micrometer range, typically between 0.5–100 μm , that are dispersed in liquid (figure 2.1). Due to the air-liquid surface tension, MBs are thermodynamically unstable and require of the presence of a surfactant to be stable. The surface tension causes the MB to be spherical, as the pressure p_i inside the bubble is greater than the pressure p_0 outside it. [86] The relationship between these pressures is given by the Young-Laplace equation

$$p_i - p_0 = \frac{2\gamma}{R} \quad (2.1)$$

where γ is the surface tension and R is the radius of the MB.

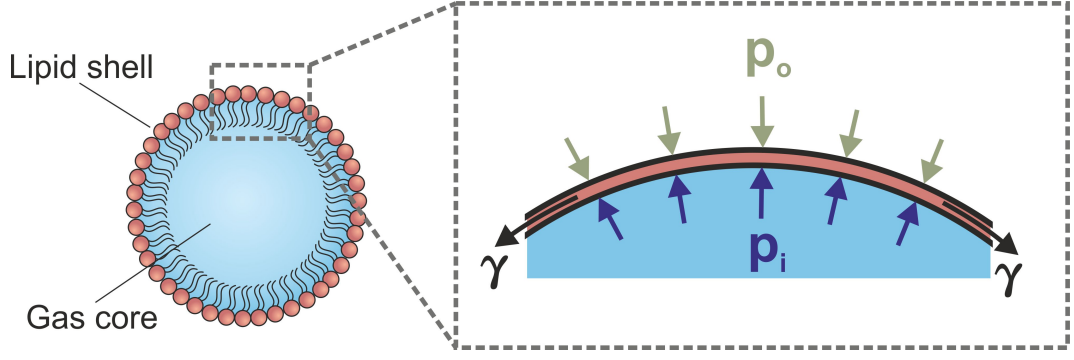


Figure 2.1: Schematic of the structure of a MB. The radius of curvature and surface tension create a pressure difference between the inside and the outside of the MB, which is a driving force for the gas to escape the MB volume.

Equation 2.1 shows that the gas inside the MB finds a driving force to diffuse from the inside to the outside of the MB. Smaller MBs will experience larger interfacial pressure and thus they would dissolve more rapidly. For example, the pressure difference between the inside and the outside for a MB with a radius $R = 2 \mu\text{m}$ is $\Delta p = 72 \text{ kPa}$ in absence of a surfactant ($\gamma \sim 72 \text{ mN/m}$), whereas in presence of a surfactant this pressure would be reduced to $\Delta p = 45 \text{ kPa}$ ($\gamma \sim 45 \text{ mN/m}$). [87–90] Thus the presence of a surfactant reduces the surface tension and therefore the Laplace pressure and the driving force for dissolution, enhancing gas retention in the MB. The rate at which gas dissolves in the surrounding media, when it is not coated with a lipid shell, does depend on temperature and pressure, as well as its diffusivity in the liquid. This diffusivity rate is given by [91]

$$\frac{dR}{dt} = \frac{D(c_i - c_s)R_g T}{M_w \left(p_0 + \frac{4\gamma}{3R_0}\right)} \left(\frac{1}{R_0} + \frac{1}{\sqrt{\pi D t}}\right) \quad (2.2)$$

where D is the diffusivity constant of the interface at temperature T and pressure p_0 , c_i is the initial dissolved gas concentration in the solution, c_s is the gas concentration at the MB surface, R_g is the gas constant, M_w is the molecular mass of the gas, R_0 is the initial radius of the MB, γ is the surface tension and t is the time. [90] There are two direct consequences of this equation. First, that the presence of a surfactant layer affects the gas dissolution rate, as the interfacial tension decreases resulting in a reduction of the diffusivity constant. [92] [93] Second, that an increase of the molecular mass of the gas encapsulated in the MBs will translate into enhanced stability. [89,94]

2.1.1.1 Echogenic MBs

MBs are highly echogenic due to the compressible nature of their gas core together with their ability to scatter acoustic waves. [90] The dynamics of the core compression are governed by the Rayleigh-Plesset equation [95]

$$\frac{d^2 R}{dt^2} \frac{dR}{dt} R + \frac{3}{2} \left(\frac{d^2 R}{dt^2} \right)^2 + \frac{4\nu}{R} \frac{dR}{dt} + \frac{2\gamma}{\rho R} = \frac{p_i - p_o}{\rho} \quad (2.3)$$

with ρ the density of the liquid, R the radius of the MB, ν is the viscosity of the surrounding medium, γ is the interfacial tension and p_i and p_o the pressures inside and outside of the MB respectively. [96] If the effects of both the stiffness and the viscous damping of the shell are considered, the resonant frequency ω_r of a MB undergoing small-amplitude oscillation is given by [97]

$$\omega_r^2 = \frac{1}{\rho R_0^2} \left[3\chi \left(P_0 + \frac{2\gamma}{R_0} + \frac{E_{shell}}{R_0} \right) - \frac{2\gamma}{R_0} - \frac{6E_{shell}}{R_0} \right] - \frac{2}{\rho^2 R_0^4} \left[2\mu + \frac{6\mu_{shell}\epsilon}{R_0} \right]^2 \quad (2.4)$$

where R_0 is the equilibrium radius of the MB, χ is the polytropic gas index (1.07), P_0 is the hydrostatic pressure (101×10^3 Pa) and μ is the viscosity of the surrounding liquid (0.001 Pa·s). E_{shell} is the elasticity modulus of the lipid shell and $\mu_{shell}\epsilon$ is the viscosity of the MB shell multiplied by the thickness of the shell. [97,98] Morgan et al. found that the elasticity parameter E_{shell} had a smaller effect on the resonant frequency of a MB than the viscosity parameter μ_{shell} , thus allowing E_{shell} to be set to 0 without effect. [97] The resonant frequency of MBs coated with lipids changes with the radius of the MB. This dependence is shown in figure 2.2 . For example, for a MB with a radius $R_0 = 1 \mu\text{m}$, $\omega_r = 23$ MHz, whereas $\omega_r = 3$ MHz for a $R_0 = 6 \mu\text{m}$ MB.

Typically, MBs are made to resonate using an acoustic source operating in the MHz regime. If the excitation frequency is equal to the natural resonant frequency of the MB it will be excited *on resonance* and provide optimum scattering. [90]

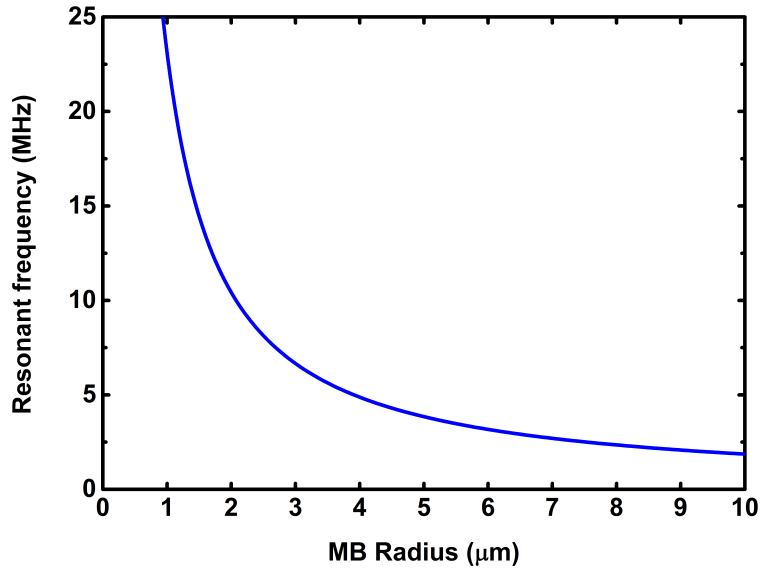


Figure 2.2: Calculated resonant frequency of lipid coated MBs. The parameters used to produce this plot are $\gamma = 0.051$ N/m, $E_{shell} = 0$ N/m and $\mu_{shell}\epsilon = 2 \times 10^{-10}$ m, taken from reference [97].

2.1.2 Microfluidic formation of MBs

In this project, MBs and MB-LONDS were formed in microfluidic devices. However, MB production has been shown possible with a number of different techniques that have been reviewed elsewhere. [99, 100] Within this report, ‘microfluidic production’ of MBs and MB-LONDS will be referred to simply as ‘*on-chip*’. This section gives an overview of microfluidics from the point of view of the production of MBs. Reynolds number and its importance are introduced, and the concept of chip-integrated micromixers and their use in the production of MB-LONDS are discussed.

2.1.2.1 A brief introduction to microfluidics

A *lab-on-a-chip* (LOC) is a miniaturized device in which small liquid volumes can be precisely manipulated. [101] LOC devices typically consist of small channels etched on glass or a polymer. These channels have sub-millimeter dimensions, in which fluid dynamic phenomena such as laminar flow become more important (figure 2.3). [102] The low volumes utilised in microfluidic devices leads to a decrease of the amount of reagents used, and therefore a reduction in the production cost. Similarly, the small area over which process take place in a microfluidic device enables automation and speeds up production times.

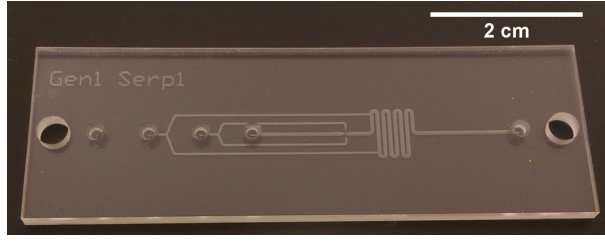


Figure 2.3: LOC devices consist of micrometer-sized channels etched on a glass or polymer, where chemical reactions or other processes take place. The image shows a microfluidic device used in this project to prepare MBs.

Microfluidics have been demonstrated to be a powerful tool for the production of a range of micrometer and nanometer-sized particles. [103–108] The production of nanoparticles using LOC devices is rapid, reproducible and well controlled, which is particularly desirable if the product is to find clinical applications. [109]

The channels in LOC devices are typically of the order of tens of micrometers. In these small structures laminar flow dominates, and therefore the movement of the fluid is highly predictable. [102, 110, 111] The nature of the flow in the channels of a LOC device can be predicted using the Reynolds number, defined as the ratio between inertial to viscous forces:

$$R_e = \frac{\rho v D}{\eta} \quad (2.5)$$

where ρ is the density of the fluid, v is the fluid velocity, D is the hydrodynamic diameter of the channel and η is the viscosity of the fluid. D is calculated using:

$$D = \frac{4 \cdot A}{P} \quad (2.6)$$

with A the area of the channel and P its perimeter. Turbulent flow occurs at large Reynolds numbers ($R_e \gg 1$), whereas small Reynolds numbers result in linear flows ($R_e \ll 1$). The Reynolds number is much less than 1 in most microfluidic devices, such that the viscous effects are dominant.

Low Reynolds numbers make the rapid mixing of two or more liquids in microfluidic devices difficult, as turbulent mixing does not commonly occur under laminar flow. [110] There are numerous examples in the literature of mixing schemes integrated in microfluidic devices, and designed to enhance the mixing efficiency. [112–117] These *micromixer* components are broadly known as *passive mixers*, and in them mixing occurs by a combination of diffusion and advection. [118] One specific design that easily allows for passive mixing is a curved channel periodically repeated. [119, 120] In curved channels, fluid near the center

of the channel passes a higher velocity than the fluid surrounding the walls. This velocity mismatch gives rise to a secondary re-circulating flow of the liquid from the periphery of the channel. [121, 122] These *serpentines* typically operate at low Reynolds numbers between $0.5 \leq Re \leq 100$, [118] and promote mixing up to 97% in some cases. [119]

2.1.2.2 The flow-focused geometry

Microfluidically produced MBs are formed in two different types of LOC device, namely T-junctions [92, 123] and flow-focused geometries. [124–126]. This section centers its attention in the latter, as it was the geometry used for MB production within this project.

In flow-focused geometries a continuous gas stream and two side liquid phases containing a surfactant (commonly lipid) are brought together near a small orifice called a *nozzle*. The gas flow feeds the gas meniscus that eventually forms a *micro-jet* through the nozzle. Inertia and surface tension split the gas stream in small gas volumes that are stabilised by the surfactant. [127–131] The addition of a step with a depth of $25 \mu\text{m}$ in the outlet, beyond the nozzle, results in a pressure drop that creates an *atomisation* process. [132] This MB production regime, known as *micro-spray*, decreases MB size and enhances their concentration significantly, up to clinically relevant concentrations $10^8 - 10^9$ MBs/ml. [133]

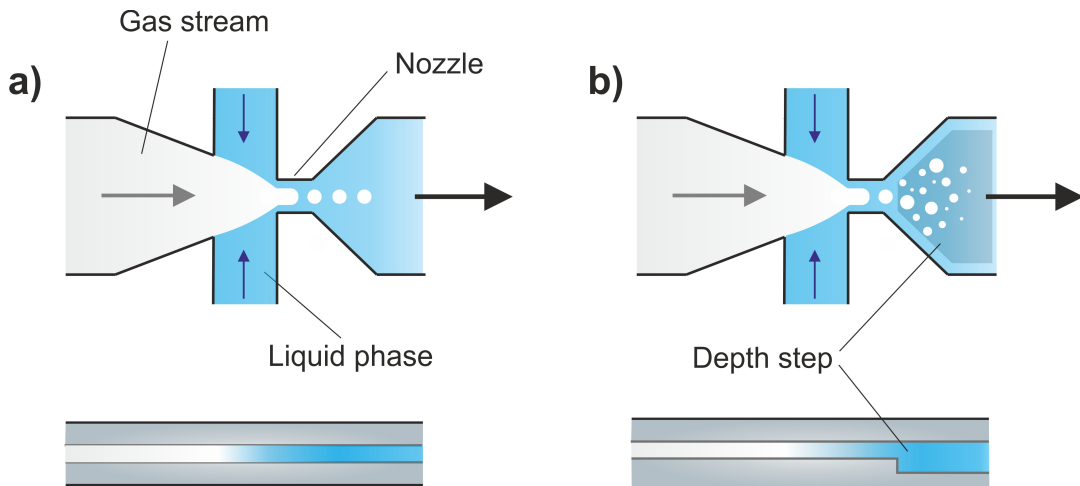


Figure 2.4: a) Schematic showing a flow-focused geometry, typically used for microfluidic formation of MBs. The arrows indicate the direction of the flow inside the device. A continuous gas phase is *pinched* by two side liquid phases at a small orifice called *nozzle*. This gas split results in the formation of the MBs. The cross section of a typical device is shown below the illustration. b) The addition of a $25 \mu\text{m}$ depth step beyond the nozzle reportedly increases the number of MBs produced in flow-focusing devices. [133] The cross section of this device is shown below the schematic.

2.2 Emulsions: formation and stability

This section is concerned with the technical aspects of emulsions. The section first revises the concept of emulsion and the concepts of nanoemulsion and microemulsion. It then contains mathematical details of the thermodynamics conditions required for nanoemulsions to form and stabilise. The different techniques for emulsion formation are discussed, focusing in the ultra-high pressure homogenisation.

2.2.1 Definitions

Dickinson [134] defined emulsions as a “heterogeneous system of two or more immiscible liquid phases, with one of the phases dispersed in the other as droplets of macroscopic or colloidal size”. Although not exclusively, the term emulsion often refers to oil-in-water mixtures, in which oil droplets, with sizes in the range of a few nanometers to a few micrometers, are dispersed in the water phase. The existence of emulsions is subjected to the stability of the droplets of the disperse phase against coalescence. *Emulsifiers* are, by definition, molecules driven to the interface between the two phases, lowering the surface tension and thus facilitating stabilisation of the droplets. [134–136] *Surfactants* are a widely used type of emulsifier due to the ability of these molecules to arrange on the oil-water interface so that its hydrophilic group is in contact with the water phase, whilst keeping its hydrophobic tails in the typically non-polar oil.

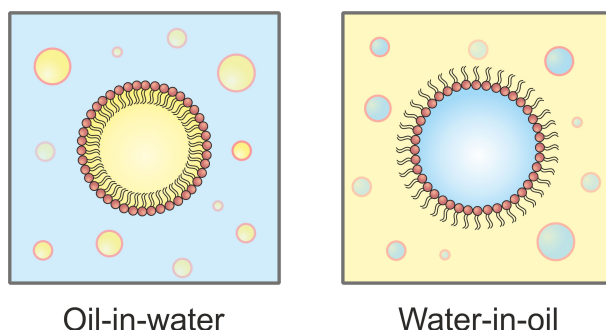


Figure 2.5: Emulsions are dispersions of one liquid into another liquid in which it is immiscible. A surfactant stabilises the interface between the liquids and makes the system thermodynamically stable. Oil-in-water and water-in-oil emulsions are the most common types of emulsions. In this project, the individual oil droplets dispersed in water are called LONDS.

Over the last 20 years or so there has been considerable confusion between the terms *microemulsions* and *nanoemulsions*. [137] The term *nanoemulsion* was only coined in 1996, [138] whereas emulsions with characteristics typical of those included in the “nanoemulsion” category were well-established before then, and were referred to as microemulsions, miniemulsions or ultrafine emulsions. [139–141] There has been controversy about the size limit that should be used to distinguish between “micro” and “nano” emulsions. Different authors have defined a variety of limits such as 500 nm, [142] 200 nm, [143] or 100 nm [144] to classify emulsions as “nano”. The size of the droplets of an emulsion are indeed a factor determining the properties of the mixture. For example, the reduction of the droplet size translates into reduced sedimentation (or *creaming*) [137] of the emulsion, which can increase the stability of the system. Also the appearance of the emulsions changes as the size of the droplets changes. Nanoemulsions formed of smaller droplets (< 200 nm) often appear clear or transparent, as the size of the droplets is smaller than visible wavelengths, [141] whilst larger droplet sizes lead to milky appearance of the emulsion.

In this report, “nanoemulsion” will be used to refer to emulsions with droplets in the nanometer range, typically between 90 – 300 nm. These droplets will be referred to as *nanodroplets*, or *LONDS* (Lipid-stabilised Oil Nano-Droplets). All emulsion prepared in this report fall within this category.

2.2.2 Theory of emulsification

The state of the phases α and β of an emulsion can be described in terms of their temperature T , volume V and number of moles of each species present in the system n . At constant pressure P , the Gibbs energy of each phase is given by [145, 146]

$$\begin{aligned} dG_\alpha &= -S_\alpha dT_\alpha - V_\alpha dP_\alpha + \sum \mu_{i,\alpha} dn_{i,\alpha} \\ dG_\beta &= -S_\beta dT_\beta - V_\beta dP_\beta + \sum \mu_{i,\beta} dn_{i,\beta} \end{aligned} \tag{2.7}$$

with S the entropy of the system, and μ_i the chemical potential of each component of the system. In systems including two different phases, an interfacial term must be considered. In many cases in which the the relative interfacial region is small compared to the bulk phases, this contribution is often ignored. However, in cases such as colloidal dispersions,

the term is an an important factor determining the behaviour of the system. [146]. In a similar fashion to the α and β phases, the Gibbs energy for the interfacial phase, defined as a plane, can be expressed as

$$dG_\sigma = -S_\sigma dT_\sigma + \gamma dA_\sigma + \sum \mu_{i,\sigma} dn_{i,\sigma} \quad (2.8)$$

Here γ is the interfacial tension. The planar definition of the interface allows for neglecting the term $-V_\sigma dP_\sigma$, and instead, the term γdA_σ accounts for the area change in the system.

In bulk thermodynamics, and during the emulsification process, large oil volumes are broken down into smaller oil droplets (figure 2.6). The Gibbs energy G in state I is given by the bulk Gibbs energy of the oil and the water, and also the free energy on the interface between the liquids

$$G^I = G_{\text{water}}^I + G_{\text{oil}}^I + G_{\text{interface}}^I \quad (2.9)$$

with

$$G_{\text{interface}}^I = \gamma A^I \quad (2.10)$$

Upon emulsification, the Gibbs energy of the system is corrected by the entropic term, TS , where T is the temperature and S is the entropy of the system, as the creation of a large number of droplets increases the configurational entropy: [136,147]

$$G^{II} = G_{\text{water}}^{II} + G_{\text{oil}}^{II} + G_{\text{interface}}^{II} - TS^{II} \quad (2.11)$$

with

$$G_{\text{interface}}^{II} = \gamma A^{II} \quad (2.12)$$

Thus the change in the Gibbs energy ΔG of the system transitioning from I to II is

$$\Delta G = \gamma \Delta A - TS^{II} \quad (2.13)$$

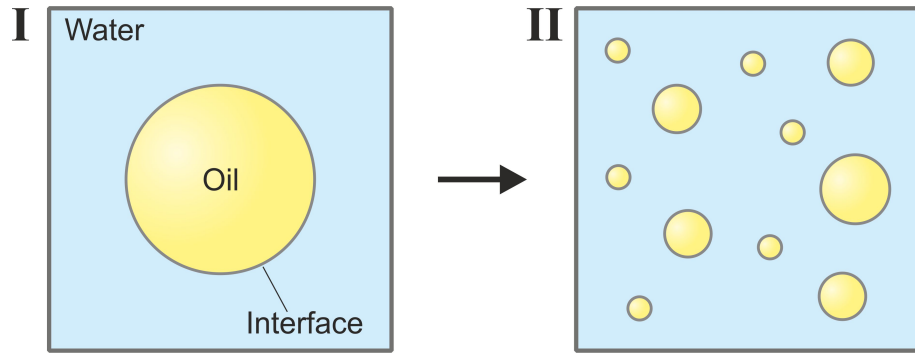


Figure 2.6: Schematic showing the emulsification of an oil-in-water mixture. The transition of the system from I to II is a non-spontaneous process that depends on the energy on the water-oil interface.

The interfacial term is in general larger than entropic one, $\gamma\Delta A \gg TS^{\text{II}}$, meaning

$$\Delta G \approx \gamma\Delta A \quad (2.14)$$

Equation 2.14 shows that $\Delta G > 0$. This implies that emulsification is a non-spontaneous process and thermodynamically unstable. [136, 146, 147]

The addition of a surfactant to the system plays two important roles in emulsion formation. First, the interfacial tension is reduced, thus the energy required to transition the system from I to II is lowered. Second, an energy barrier is created from state II to I, as the surfactant prevents droplet coalescence, therefore making the system stable in state II. [134, 147] Equation 2.14 shows the energy required for a system to transition between states I and II, and it is clear from this equation the crucial role played by the surfactant. For example, in the formation of an oil-in-water emulsion (volume fraction $\phi = 0.01$) with droplets of radius $r = 100$ nm and in absence of a surfactant ($\gamma = 0.05$ N/m), the change in the Gibbs energy is $\Delta G \approx 10^5$ J/m³. However, in presence of a surfactant, the interfacial tension would be lower $\gamma = 0.005$ N/m, and therefore the value of the free energy would also be lower $\Delta G \approx 10^4$ J/m³. [134, 137, 148] In addition to lowering γ and preventing the droplets from coalescence, the surfactant also allows for the existence of interfacial tension gradients, which are crucial for droplet deformation and subsequent breakage. [136]

2.2.3 Methods of emulsification

As discussed above, emulsion formation relies on progressive breakage of oil volumes into smaller oil pockets. This process is non-spontaneous, and requires external energy to

occur. This energy must be greater than the value of the Gibbs energy of the system. The first step for a droplet to deform is to be under external stress. The amount of energy required to disrupt a droplet of radius r has to exceed the Laplace pressure in the droplet (equation 2.1)

$$P_L = \frac{2\gamma}{r}$$

For a droplet of radius $r = 100$ nm and interfacial tension $\gamma = 0.005$ N/m, the Laplace pressure is $P_L = 10^5$ Pa. Disruption of such droplets would occur when external stress is applied, which could be due to a velocity or pressure gradient. [134,135,141]

The shear stress necessary to form droplets with radius r can be predicted using Taylor estimate of ruptured droplet into another immiscible liquid

$$\sigma = \frac{\gamma}{\eta r} \tag{2.15}$$

where η and σ are the viscosity and the shear rate of the continuous medium. [149] For a droplet of radius $r = 100$ nm, with interfacial tension $\gamma = 0.005$ N/m created in water ($\eta = 10^{-2}$ Pa·s), the shear stress necessary for this droplet to form would be $\sigma = 5 \times 10^6$ s⁻¹. Shear rates of this order of magnitude are in general not accessible for most common mixing devices, including high-speed blenders. [141] High pressure and ultrasonic homogenisers are two well established techniques for producing emulsions with droplet radius $r < 500$ nm. [150–152]

High pressure homogenisation was the method used to produce nanoemulsions. It was used in combination with a rotor-stator system, which did not suffice by itself to produce optimal nanoemulsions. The following sections revise these two specific methods for emulsion formation.

2.2.3.1 Rotor-stator homogenisers

Rotor-stator homogenisers consist of a fixed slotted stator which houses a mobile rotor (figure 2.7). The rotor creates a region of lower pressure to which the crude emulsion moves, giving rise to a circulating current and roughly dispersing the oil into the water phase. The proximity between the rotor and the fixed stator, together with the high acceleration of the fluid due to the rotor gyration, creates high shear forces that reduce

droplet size. [153] The pressure difference Δp created by the rotor can be estimated as [154]

$$\Delta p \approx \frac{\rho \Omega^2 d^2}{2} \quad (2.16)$$

where ρ is the fluid density, d is the distance from the axial line of the rotor, with d_{max} the distance to the inner wall of the stator, and Ω is the angular speed of the rotor. This equation shows that the pressure difference increases as the fluid is closer to the wall. Considering water as the fluid ($\rho = 1000 \text{ kg/m}^3$) in a rotor-stator system with $d_{max} = 1 \text{ cm}$ and $\Omega = 1000 \text{ s}^{-1}$, the pressure difference results $\Delta p = 50 \text{ kPa}$. This pressure difference is about 3 orders of magnitude lower than the pressure applied in the high pressure homogenisers, and therefore homogenisation in rotor-stator devices is reportedly less efficient than that achieved with other high pressure devices. [155–157] The separation between the rotor and the stator is typically of the order of millimeters, and the rotor speed can range between $2000 - 13000 \text{ min}^{-1}$. [158,159] By varying the speed of the rotor or the thickness of the rotor-stator gap the intensity of the shear can be altered. [154]

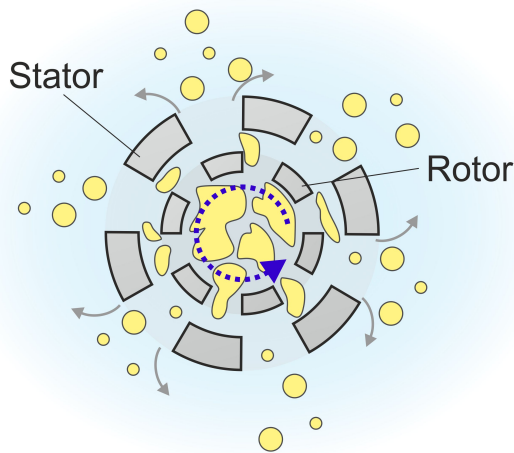


Figure 2.7: Schematic showing the cross-section of a rotor-stator homogeniser. A fixed slotted cylinder (stator) houses a rotor connected to a motor. Pressure differences created by the gyration of the rotor creates circulation of the fluid and also emulsification. The crude emulsion is subjected to high shear stress close to the walls of the stator, which result in droplet disruption.

2.2.3.2 High-pressure homogenisation

High pressure homogenisers (or ultra-high pressure homogenisers) are one of the most efficient and widely used techniques for the production of emulsions. High pressure homogenisers consist of a pump and a homogenising nozzle (figure 2.8a). The pump is used

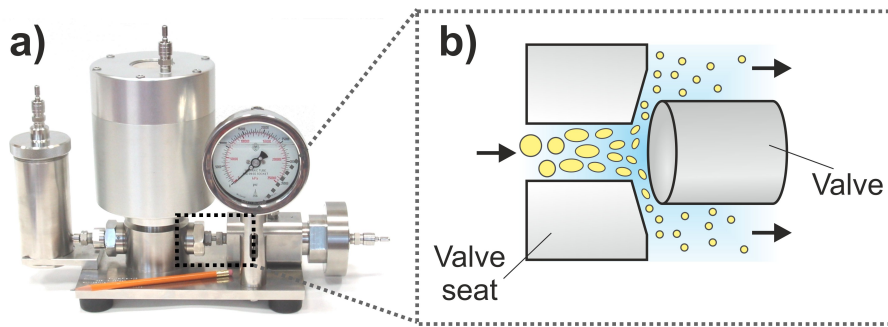


Figure 2.8: a) Image of a modern, commercially available high pressure homogeniser. Specifically, this is an Avestin Emulsiflex C-5, which was the device used to prepare LONDS in this study. b) Schematic showing the structure of the homogenising nozzle. The crude emulsion is forced through the small gap between the valve and the valve seat, which results in dispersion of the oil in the water phase

to move the liquid towards the homogenising nozzle, in where it is forced under pressure through a small orifice between a valve and the valve seat (figure 2.8b). [134,160–163]

For a short time (10^{-3} s), the liquid experiences mechanical stress under laminar flow at the valve entrance and the valve orifice, and also turbulence and cavitation at the valve outlet. [155,157,163] Modern homogenisers can exert pressures up to 300 MPa, and are able to achieve emulsions with droplet in the nanometer range. The efficiency of the homogenisation also depends on the design of the homogenising valve to a high extent, including its geometry and dimensions. [163] Due to the shear forces and conversion of mechanical work into heat, the temperature of the sample increases linearly with the homogenisation pressure. [164,165] It is therefore not uncommon to assemble a cooling heat exchanger or similar device to the outlet, in order to control the temperature of the liquid, as excess heat has the potential of affecting droplet formation. In addition, overheating of the sample could be particularly concerning for preparations including temperature sensitive components, such as hydrophobic drugs to be encapsulated. The temperature rise ΔT of the liquid during high pressure emulsification can be estimated to be [166]

$$\Delta T = \frac{P}{C \cdot \rho} \quad (2.17)$$

where P is the applied pressure, C is the specific heat of the liquid and ρ its density. Figure 2.9 shows the temperature change at the exit of the homogenising nozzle for different production pressures, for the specific cases of squalane-in-water and triacetin-in-water emulsions ($\phi = 0.1$). The temperature changes expected for the production pressures used within this project (35 – 175 MPa) were $\sim 10 - 45$ °C. Hence the outlet was kept at 4 °C to avoid overheating of the emulsions.

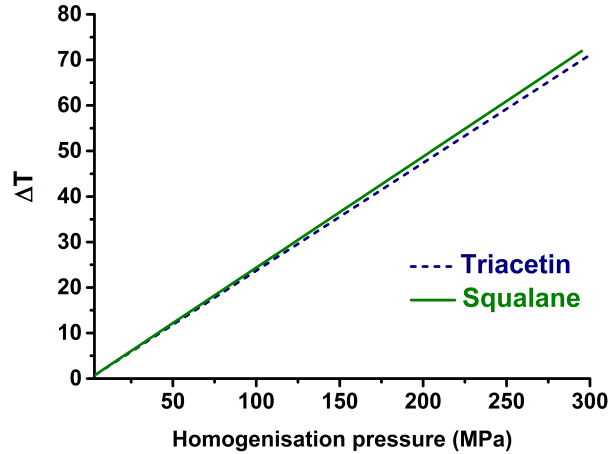


Figure 2.9: Calculated temperature increase through the homogenising nozzle with the homogenisation pressure for squalane-in-water and triacetin-in-water emulsions.

Several authors have studied the dependence of the emulsion droplet size with the production pressure. [135, 157] The energy density is used to compare the mechanical energy input per unit volume in the area where droplet disruption occurs. In high pressure devices, the energy density is simply [167]

$$E_d = \Delta P \quad (2.18)$$

with ΔP the pressure difference at the homogenising nozzle. E_d has a direct effect on the size of the droplets after homogenisation. In general, the increase in the homogenising pressure results in reduced droplet size. [165, 168–170] For high pressure homogenisers this relationship can be written as [134, 157]

$$d = C \cdot E_d^b \quad (2.19)$$

The constant C depends on the efficiency of the droplet disruption, and b depends on the flow conditions under which the oil volume is dispersed into the continuous phase. For high-pressure homogenisers, b is between -0.6 (turbulent-inertial flow regime) and -0.75 (turbulent-viscous flow regime)¹. [155] The reduction in droplet size is limited by the amount of surfactant available in the continuous phase, as there must be enough to fully coat newly created droplets. Emulsification of the system at this stage has been reported not to have an effect in the size distribution of the droplets, and occasionally lead to increased droplet size due to *overprocessing*. [147] As for droplet size, the number

¹The flow regime depends on the dimensions of the homogeniser. [147]

of droplets in an emulsion is limited by the amount of surfactant. There are however limited studies concerned with this. At constant E_d , droplet size has been observed to increase for increasing oil volume, [169] which could be attributed to insufficient surfactant to completely cover the new droplets. [159]

Together with the homogenisation pressure, the oil volume and the presence of enough surfactant, there are other factors that affect the size of the droplets. The viscosity of the continuous phase and the oil, and the interfacial tension between the oil and the water both play a role in the final droplet size. For the turbulent conditions that occur at the homogenising valve in high-pressure homogenisers, the maximum size droplet that persists during homogeniation is [135, 147, 171, 172]

$$d = \frac{\gamma}{(E_d \cdot \eta_c)^{\frac{1}{2}}} \quad (2.20)$$

with η_c the viscosity of the continuous phase. This expression holds if droplet disruption occurs mostly under a turbulent-viscous regime. For water as the continuous phase, the regime under which droplets are formed in high-pressure homogenisers is turbulent-inertial. [171] In case turbulent-inertial regimes dominate the droplet breakage, the maximum diameter that survives is

$$d = \left(\frac{\gamma^3}{E_d \cdot \rho} \right)^{\frac{1}{5}} \quad (2.21)$$

This tendency has been qualitatively explained from the point of view of the turbulence created at the nozzle. Droplet deformation time is increased for larger oil viscosity and, at constant energy input, only disruptions that last for longer than droplet deformation time can cause effective droplet disruption. [134]

2.2.4 Mechanisms for emulsion breakdown

There are several mechanisms associated to the breakdown of emulsions, each of which arises from specific characteristics of the emulsion. These processes are shown schematically in figure 2.10. Emulsions destabilising processes may occur simultaneously or consecutively, and the analysis of the forces involved are not simple. [136]

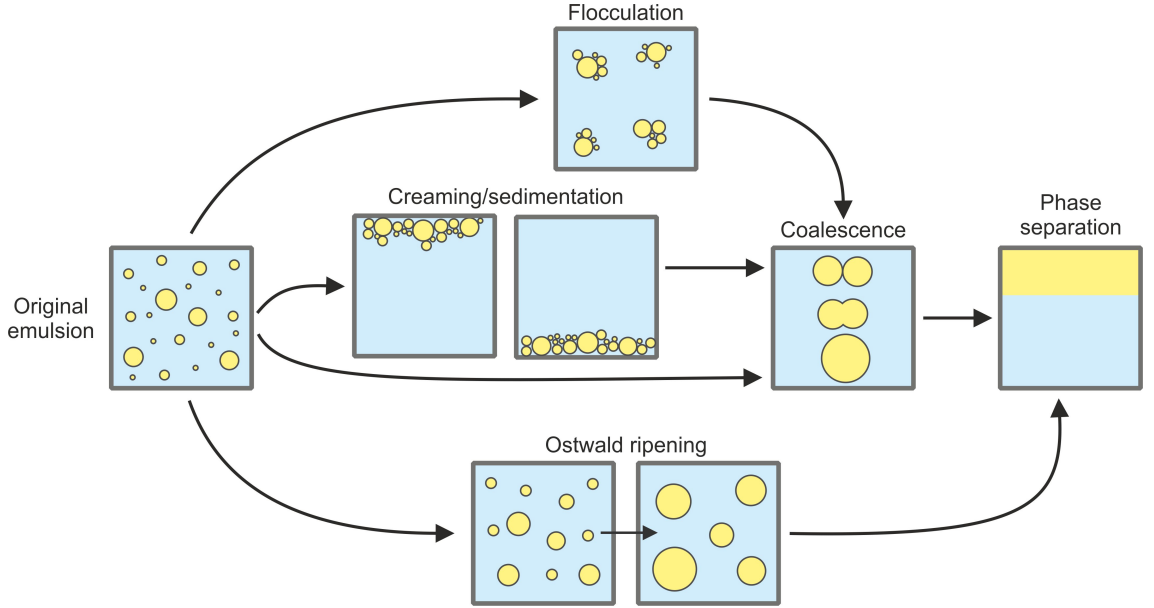


Figure 2.10: Emulsion destabilisation can occur through different pathways. These breakdown processes can take place simultaneously or consecutively, and can lead to complete separation of the oil and the water phase.

The size and density of the droplet affects directly the rate of sedimentation (or creaming) of emulsions. These two processes arise from the density mismatch between the disperse and the continuous phase. For sufficiently small droplets, Brownian motion dominates over gravitational force, thus conferring nanoemulsions ($r < 50$ nm) with enhanced stability against these two processes. [173] Nanoemulsions such as the ones prepared within this project ($\sim 100 - 300$ nm) are susceptible of both sedimentation (or creaming) and Brownian motion. The concentration of droplets at a distance h from the top of the emulsion ($\phi(h)$) is given by [147]

$$\phi(h) = \phi_0 \cdot e^{\frac{-4\pi r^3 \Delta\rho g h}{3kT}} \quad (2.22)$$

where ϕ_0 is the concentration of the droplets at the top of the emulsion, $\Delta\rho$ is the density difference between the medium and the disperse phase, g is the gravity, h is the position from the top of the emulsion, T is the absolute temperature and k is Boltzmann's constant. A reduction in the density difference between the droplets and the medium can lead to diminishing the sedimentation (or creaming) of nanoemulsions. These processes lead to concentration of the emulsions in specific regions. It is not surprising then that additional breakdown processes follow sedimentation and creaming of the nanoemulsions, as they are favoured by the proximity between the droplets.

Ostwald ripening and coalescence are considered the two main mechanisms for nanoemulsion breakdown. [147,173] Coalescence is the process by which smaller droplets merge into larger oil volumes. The susceptibility of two nanodroplets stabilised with a surfactant to coalesce has been attributed to the dynamics of the stabilising molecules at the interface. [174] Ostwald ripening is the process by which larger oil droplets grow in size in detriment of smaller droplets, which are reduced in size. This phenomenon arises from the partial solubility of the disperse phase in the continuous phase, and the increase in solubility of the material inside the droplet as the size of the former decreases. [175] Ostwald ripening can be assessed as [147,176]

$$r^3 = \frac{8 S_b \gamma V_m D}{9 \rho R T} t \quad (2.23)$$

where S_b is the solubility of the disperse phase in the continuous phase, γ is the interfacial tension, V_m and D are the molar volume and the diffusion coefficient of the disperse phase, respectively, ρ is the density of the disperse phase and R is the gas constant. In cases in which the solubility of the disperse phase in the continuous phase is very small, Ostwald ripening is negligible.

Chapter 3

Experimental Techniques

This chapter provides an overview of the experimental techniques used in this project. These include imaging, sizing and counting techniques, QCM-D, UV-VIS spectroscopy and fluorescence spectroscopy. The chapter also contains details of the methods followed to prepare SBLMs, MBs and Qdots, used within the project. A list of all the chemicals used and their suppliers, as well as the equipment and manufacturers, can be found in appendix A.

3.1 Lipids preparation and procedures

Upon arrival, lipids were dissolved in 1 : 1 chloroform:methanol for aliquoting, in order to equally fraction the lipid mass. Chloroform:methanol was removed by placing the sample under nitrogen for at least 30 min, until a lipid film was formed around the walls of the vial. The samples were stored dried at $-80\text{ }^{\circ}\text{C}$ until required. To prepare the specific lipid combinations, the lipids were newly resuspended in chloroform:methanol. Following the mixing of the different lipid species, chloroform:methanol was removed under nitrogen for 30 min. The lipid mixtures were always prepared according to their mole percentage; lipid percentages in all the preparations that are mentioned within this report correspond mol% unless otherwise stated. The lipids were then resuspended in PBS for further preparation via vortexing, unless stated otherwise.

3.1.1 Preparation of vesicles by tip sonication

Vesicles for bilayer formation were prepared by tip sonicating 1 mg/ml lipid mixtures in PBS for 30 min at 4 °C. For clarity, details on the lipid composition of the different vesicle preparations are provided in the correspondent sections. After sonication, unwanted titanium particles from the sonication tip were removed by centrifuging the solution at 14500 rpm for 1 min. After the titanium precipitated to the bottom of the vial, the supernatant was carefully transferred to a new container. PBS was added to the vesicle solution when dilution of the sample was required.

3.1.2 Lipid for MB preparation

The lipid shell of the MBs generally consisted of 95% DPPC and 5% biotin-PEG2000-DSPE or PEG2000-DSPE. [177] 0.1% Atto 488 or Atto 590 DOPE was added to the lipid mix for fluorescence imaging when required. Dried lipid mixtures were resuspended in bubble solution (1% glycerol 4 mg/ml NaCl) [133] or PBS to make a 1 mg/ml lipid solution. The vial was then sonicated in a heated sonication bath (~ 60 °C) for at least 1 h or until the solution appeared cloudy and homogeneous. The solution was allowed to cool down to room temperature and then vortexed to ensure homogeneity of the sample. When required, 10 μ l of C_6F_{14} was added to the lipid solution, which has the effect of increasing MB lifetime. [178]

3.2 Qdots

Hydrophobic Qdots were used in preliminary studies as a hydrophobic drug mimic. This section describes the experimental method followed to synthesise CIS/ZnS Qdots, and describes the procedure used to determine the concentration of the QDots in the synthesised sample.

3.2.1 Synthesis of CIS/ZnS Qdots

CIS/ZnS Qdots were prepared as described in the literature, introducing a few minor modifications to obtain Qdots with larger sizes. [179] This was expected to translate into longer emission wavelengths, nearer the infrared, which is desirable for biomedical applications.

Indium acetate (0.584 g), copper iodide (0.380 g) and 1-dodecanethiol (10 ml) were mixed in a three-necked flask, kept under a flow of nitrogen reflux with the use of a bubbler connected to a condenser column. The dodecanethiol provided the hydrophobic coating required for these Qdots, as they must be able to disperse in oils. The mixture was then heated to 100 °C while stirring. The temperature was kept at 100 °C for 10 min, until a transparent solution was formed. The flask was heated up to 210 °C. As the temperature was raised, the color of the mixture changed from yellow to dark orange, indicating nucleation and growth of the nanocrystals (starting at about 180 °C). The heat was turned off after 15 min. The colour of the solution was dark red. The stability of the Qdots was improved by adding an inorganic zinc (ZnS) shell. Zinc diethyldithiocarbamate (Zn DEC) (8 mol) was diluted in 1-octadecene ODE (10 ml). Then this solution was progressively added to the Qdots synthesis while stirring. The temperature of the reaction was then set to 100 °C and refluxed for 1 h. The incubation was followed by the washing procedure. Centrifugation of the nanocrystal solution (10 min, 5000 rpm) led to their precipitation so the solvent could be removed without losing Qdots. A fresh isopropanol-acetone-chloroform (1 : 10 : 1) was added and the pellet resuspended by brief sonication. The whole process was repeated two times, followed by another two washes using only acetone to resuspend the Qdots. The sample was finally resuspended in hexane and stored in the fridge.

3.2.2 Determining the concentration and size of Qdots

The Qdot concentration can be calculated from the molar extinction coefficient if their size is known. The size of the Qdots was first determined based on the position of the maximum of the spectral emission peak using an empirically derived expression [180,181]:

$$d = 68.952 - 0.2136\lambda + 1.717 \times 10^{-4}\lambda^2 \quad (3.1)$$

where d is the size of the Qdots and λ is the maximum emission wavelength. The molar extinction coefficient, ϵ , of CuInS₂ has been shown to be given by

$$\epsilon(3.1eV) = 2123d^{3.8} \quad (3.2)$$

Once the molar extinction coefficient had been determined the concentration, C , was calculated using the Beer-Lambert law [182]:

$$A = \epsilon CL \quad (3.3)$$

where L is the path length of the radiation beam used.

3.3 Light absorption and emission studies

Molecular light absorption and emission are the result of discrete electronic energy levels, whose separation is defined by Planck's equation

$$\Delta E = h\nu \quad (3.4)$$

where h is Planck's constant and ν is the frequency of the absorbed light. Equation 3.4 implies that photons with specific energy ΔE need to be absorbed by the molecule, in order for the electrons to overcome the energy gaps between the energy levels. In other words, the *quantization* of the electronic levels in a molecule results in the absorption of light of specific wavelengths. A molecule that becomes *excited* after the absorption of light is likely to lose its excess energy by the emission of radiation (figure 3.1). [183] Electrons promoted to higher electronic energy states relax to the lowest energy level in around 10^{-8} s, resulting in the release of a photon. This effect is known as *fluorescence*. Certain molecules can undergo an *intersystem crossing*, which translates into much longer relaxation times of the order 10 s⁻¹. This phenomenon is called *phosphorescence*. [184]

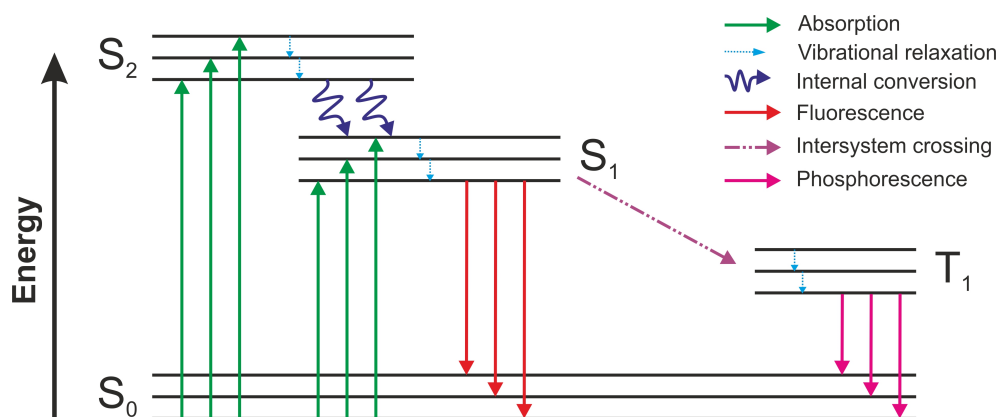


Figure 3.1: Molecular light absorption and emission processes, illustrated schematically. Due to the quantization of the molecular energy levels, only specific light wavelengths are absorbed or emitted by electrons moving between different levels. Absorbed light can promote electrons to higher energy levels, that relax to the lowest energy levels following different paths. [184]

Fluorescence and light absorption in the UV-VIS have been widely used in this project to investigate the autofluorescence properties of candidate oils, and also to determine the concentration of compounds in solution via the Beer-Lambert law (equation 3.3). This section describes the techniques used to study fluorescence and light absorption of compounds and samples.

3.3.1 Fluorescence Spectroscopy

Fluorescence spectroscopy was used to measure the fluorescence emission of different samples. The fluorescence spectrometer used within this project was equipped with a xenon lamp to produce the excitation light, which can range 250 – 790 nm. In this spectrometer, monochromators are used to select both the excitation and emission wavelengths. These monochromators contain holographic gratings in order to reduce stray light. The fluorescence was detected with photomultiplier tubes. Quartz cuvettes with 1 cm light path length were used in all of the experiments. In all cases, emission spectra were recorded for a range of excitation wavelengths, from 250 – 550 nm, and in steps of 25 nm, unless stated otherwise.

3.3.2 UV-VIS Spectroscopy

Light absorption of compounds is typically measured using a UV-VIS spectrometer. This instrument measures the radiant power of light after it has passed through a liquid sample. By computing the ratio of radiant power through the solution of interest and a reference, it provides the transmittance and absorption of the compound. The light from the source is modulated through a monochromator, which only allows one narrow band of wavelengths to pass through the sample. Quartz cuvettes with a 1 cm path length were used for all of the measurements. Spectra were recorded between 200 – 700 nm, performing a minimum of three measurements per same sample and averaging the results.

3.3.3 *In Vivo* Imaging System

In Vivo Imaging System (IVIS) is a highly sensitive imaging system which allows for non-invasive bioluminescence studies *in vivo*. IVIS finds multiple application in the clinical research; for example, it is broadly used for localising fluorescent compounds delivered *in vivo* using drug delivery system under development. [185, 186] IVIS is equipped with 10 excitation filters with a 30 nm bandwidth, which enable the modulation of the excitation light in between 430 – 730 nm. When imaging in epi-illuminating mode, the specimen is irradiated with a defined λ_{em} , that excites the fluorophore within the specimen. Emission light modulated through the emission filter is detected with a CCD camera placed over the specimen. There are 18 emission filters which record emitted light ranging 490 – 850 nm. IVIS measures the radiant efficiency, defined as the ratio between the power of the emission and excitation light:

$$\text{Radiant Efficiency} = \frac{\text{Emitted light}}{\text{Excitation light}} \left[\frac{\text{photons / s / cm}^2 / \text{str}}{\mu\text{W} / \text{cm}^2} \right] \quad (3.5)$$

3.4 Microscopy techniques

This section describes the microscopy techniques used to image LONs and MB-LONs within this project.

3.4.1 Epi-fluorescence microscopy

In an epi-fluorescence microscope, a fluorescent specimen is illuminated with a nearly monochromatic light, which results in fluorescence emission on a narrow spectral band (figure 3.2). Epi-fluorescence microscopes are generally equipped with a high intensity mercury-vapour lamp as a light source. An excitation filter (ExF) is placed in the light path to select the wavelength for illuminating the sample. A dichroic mirror (DM) is used to direct the light to the sample, and to allow the fluorescence emitted light to reach an emission filter (EmF) and ultimately a detector.

Two epi-fluorescence microscopes were used for taking fluorescence images. One was mounted under the fluidic set-up for MB production, and was used to confirm the formation of MBs and their fluorescence when applicable. This microscope is referred to as Nikon Eclipse Ti-U in this report. The second one (referred to as Nikon E600) was equipped with a more sensitive camera, and therefore was used to image MB-LONDS composites contained in a home-made flow cell. Both microscopes were equipped with a FITC (ExF 465 - 495 nm, DM 505 nm, EmF 515 - 555 nm) and a Texas Red (ExF 540 - 580 nm, DM 595 nm, EmF 600 - 660 nm) filter.

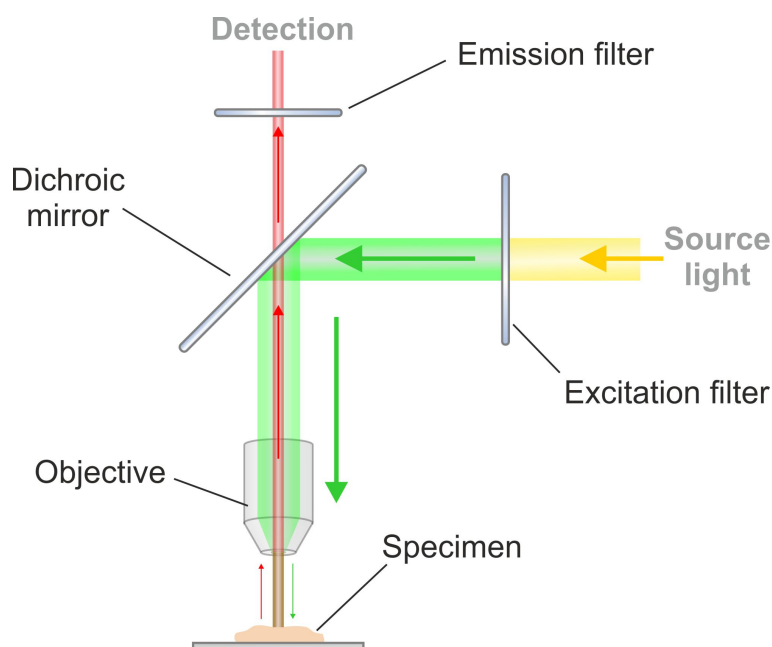


Figure 3.2: Schematic showing the light path in an upright epifluorescence microscope. An excitation filter is used to select the wavelength with which the fluorescent specimen is illuminated. A dichroic mirror placed on the light path helps directing the beam. The emitted fluorescence wavelength is further refined using an emission filter before the detector, usually a CCD camera.

3.4.2 Confocal microscopy

A confocal microscope is a fluorescence microscope with an pinhole added on the light path, which excludes light emitted in regions of the specimen other than the focal point. The rejection of light from out-of-focus regions results in a small depth of detection, reducing the recorded fluorescence background and also allowing *3D* mapping of the samples. A set of mirrors is used to direct the focused light beam across the sample, usually from a laser source (laser scanning confocal microscope). The confocal microscope used in this project was equipped with 488 nm, 552 nm and 638 nm lasers, which allowed for visualisation of Atto 488 DOPE, Atto 590 DOPE and Nile Red. The system was also equipped with 2×, 10× objectives, and also 60×, 100× oil immersion objectives.

Confocal microscopy was used to image MB-LONDS composites using polyethylene terephthalate spacers with a thickness of 50 μm were to construct a chamber delimited by the coverslip and a microscope slide. The chamber was sealed using wax, which prevented the sample from drying off, and also avoided direct contact between the sample and the microscope objectives.

3.4.3 Transmission Electron Microscopy

Transmission electron microscopy (TEM) uses a beam of electrons focused on a thin sample to produce an image with a resolution of up to 10^{-10} m. The contrast of the imaging depends on the density of the specimen compared to its surroundings. Thus heavy metal stains such as uranyl acetate are regularly used in TEM imaging for increasing the contrast of biological samples, as uranyl ions interact with proteins and lipids, increasing the electron density and therefore the contrast of the images. TEM was used to image LONDS. Sample preparation is detailed in section 5.6.1 (page 94).

3.5 Size and concentration measurements

This section describes all the techniques used to size and determine the concentration of LONDS, MBs and MB-LONDS composites.

3.5.1 Dynamic Light Scattering

DLS is a technique for measuring size distribution of particles in solution. The particles are irradiated with a monochromatic beam (specifically, a He-Ne laser 633 nm was used in this project), which is scattered in all directions by the particles undergoing Brownian motion. Over time, the displacement of the particles produces fluctuations of the intensity of the scattered light. The dynamic properties of the solute depends on its size, as described by the Stokes-Einstein equation

$$D = \frac{k_b T}{6\pi\eta r} \quad (3.6)$$

where D is the translational diffusion coefficient of the particle, k_b is Boltzmann's constant, T is the temperature, η is the dynamic viscosity of the solution and r is the radius of the particle, assumed to be spherical. The analysis of the intensity fluctuations over time can be analysed using an autocorrelation function. [187] For a monodisperse sample, cumulants-based analysis uses a single exponential decay,

$$C = e^{-2Dq^2\tau} \quad (3.7)$$

where τ is the decay rate of the function, D is the diffusion coefficient of the particles in the solution and q is the scattering vector $q = \frac{4\pi n}{\lambda} \sin \frac{\theta}{2}$, with n the refractive index of the media, λ the wavelength of the laser used for illuminating the sample (633 nm), and θ the scattering angle. Within this project, the scattered light was always recorded at the backscatter angle, and therefore $\theta = 173^\circ$. The fitting of autocorrelation function is only valid for solutions particles homogeneous in size. [188] This analysis also estimates the width of the size distribution, the polydispersity index (PI), which in the specific setup used within this project ranges 0 – 1.

A ZetaSizer was used to determine the size of LONDS within the project. Plastic disposable cuvettes were used to analyse the samples. Generally, 10 μl of the LONDS sample was diluted in 990 μl in PBS. Three measurements were performed on each sample, each of which provided the average of a number of readings, optimised by the Zetasizer according to sample characteristics such as polydispersity and concentration (typically between 11 and 17 runs per measurement). These three measurements were used to

produce an average result for size distribution. Mode and average sizes of LONDS were determined from this average result.

3.5.2 Single Particle tracking for size and concentration measurement

In a similar fashion to DLS (section 3.5.1), NanoSight relies on light scattering from particles in solution and their Brownian motion (equation 3.6). [189] A 532 nm laser is shone into a chamber containing particles in solution, at a 45° angle. Light scattered from each particle is visualised with a 20× objective, and a camera mounted onto it is used to record videos of the solution (typically 30 s videos). Single particle tracks are analysed on the recorded videos, providing individual diffusion coefficients and therefore sizes individually calculated for each particle (equation 3.6).

A NanoSight instrument was used for determining the concentration of LOND samples, and also to obtain an alternative size measurement of the LONDS. LONDS 1 : 10⁶ dilutions were generally used, unless otherwise stated. PBS was always filtered through a 200 nm pore size membrane. NTA software was used to record the data. Three videos of 30 s each were recorded per experiment; the volume of the sample inside the observation chamber was exchanged between different video recordings, so that a different set of particles was analysed each time. NTA provides a value for the mode size of the particles finding the maximum intensity in the distribution, and average size integrating the area under the distribution curve.

3.5.3 Tunable Resistive Pulse Sensing

qNano is based on the tunable resistive pulse sensing technique, and provides a measurement of particles suspended in a solution containing electrolytes. qNano consists of a conical nanopore etched in a flexible polyurethane membrane, placed between two fluid chambers that contain an electrode each. A nanoparticle suspension is conventionally placed in the top chamber, and the particles are driven through the nanopore using a combination of pressure and voltage (electrophoretic mobility and electro-osmosis). Particles passing through the nanopore cause temporary blockages of the current between the top of the bottom chamber, known as *blockade* events. The functioning of a qNano is schemat-

ically shown in figure 3.3. The blockade signal is measured and analysed by the software, comparing it to the blockade signal from a sample of known diameter. The number of blocking events gives a measure of the concentration of the particles in the solution, whereas the magnitude of the event provides information about the size of that specific particle. [190]

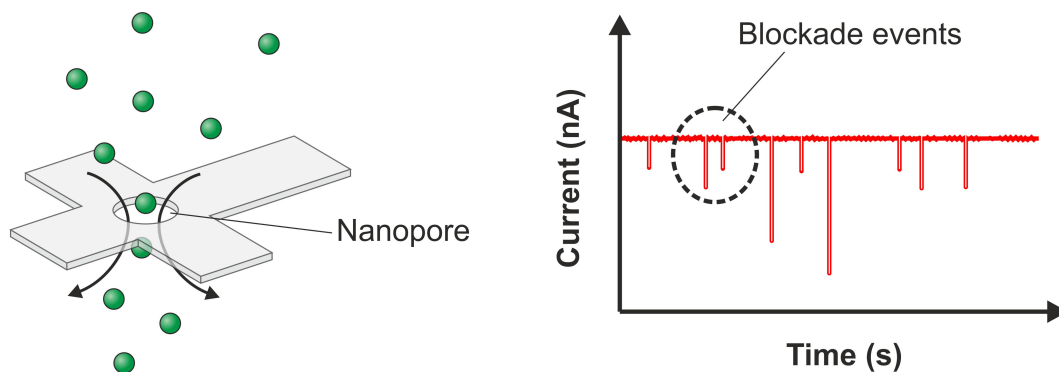


Figure 3.3: Schematic showing the functioning of qNano. Nanoparticles passing through a nanopore cause temporary decrease of the current between two electrodes, one at each side of the nanopore. The magnitude of these *blockade* events provides information regarding the size of the particles, whereas the number of events recorded relates to the concentration of the particles in the solution.

qNano was used to determine the size and concentration of LONDS. In all qNano measurements shown within this report, the concentration of LONDS was measured using a 200 nm nanopore. A 1 : 1000 dilution of carboxylated polystyrene calibration particles were used as reference. In general, 1 : 1000 dilutions (in PBS) of the LOND samples were used for concentration measurements.

3.5.4 Optical counting

The size and concentration of MBs and MB-LONDS were measured optically. Microscope images were analysed to account for the number of MBs present in a known volume, and the size of the MBs were measured whenever their diameters fell within the optical limit of the microscope. Bright field images were taken using the Nikon Eclipse Ti-U. Polyethylene terephthalate spacers with a thickness of 50 μm were used to construct a chamber delimited by the coverslip and the microscope slide. The specific separation between the two provided a known volume for the imaging chamber. The spacers also prevented the coverslip from coming into close contact with the slide, and therefore prevented

the MBs from being squeezed. This could distort the shape of the MBs and potentially compromise the measurement of the radius. After a gentle shake of the vial, around $30\ \mu\text{l}$ of MB (or MB-LONDS) solution was carefully pipetted near the boundary of the coverslip, capillary action helping the liquid into the chamber. Figure 3.4 shows an example of a MB sample imaged in bright field. MBs appear as dark rings on a clearer background, with a characteristic white spot in their center. Sets of 10 or 15 pictures were taken, from different regions of the specimen, to increase the statistical significance of the measurement. The images were analysed using imageJ, implementing a in-house made macro that automatically counts and sizes the MBs. MBs with sizes below the optical resolution of the microscope ($\sim 0.75\ \mu\text{m}$) are not counted optically, therefore limiting this technique. [191]

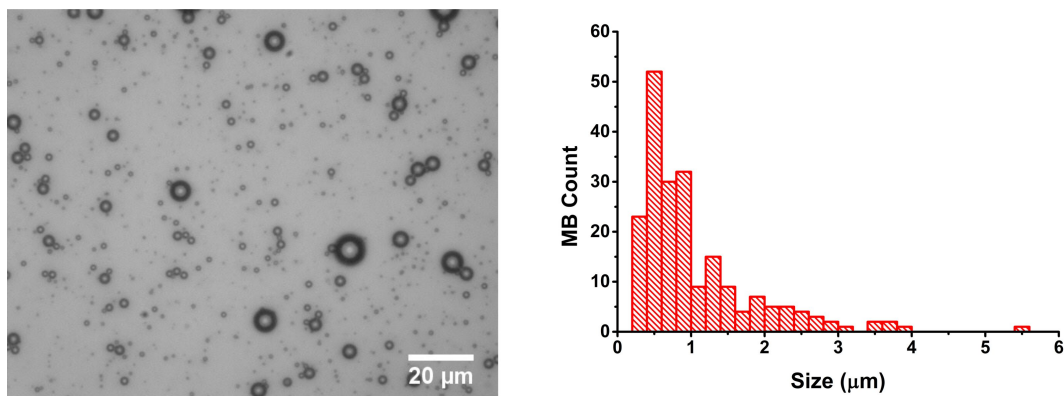


Figure 3.4: MBs imaged in bright field, using a $40\times$ objective with $1.5\times$ internal magnification. A macro is implemented in imageJ to count and determine the size of the circular areas of the MBs on the picture. The histogram shows the size distribution of the MB in this specific bright field image.

3.6 Quartz Crystal Microbalance with Dissipation

Quartz Crystal Microbalance with Dissipation (QCM-D) was used to study the binding affinity of StreptAvidin and biotin, and also the attachment of LONDS to model membranes via the biotin-NeutrAvidin binding chemistry. Alternative linking chemistries (PDP/Maleimide-thiol) for the attachment of LONDS to model membranes were also explored using QCM-D. For both studies, solid-supported bilayer lipid membranes (SBLMs) were chosen as a model surface for the attachment of StreptAvidin and to mimic the NeutrAvidin-functionalised MB surface to study LOND attachment. QCM-D takes ad-

vantage of the piezoelectric properties of the quartz and uses it as a mass adhesion sensor, which is able to resolve down to 0.5 ng/cm². When a rigid film is adsorbed onto an oscillating quartz crystal, the change in the oscillation frequency of the sensor is proportional to the change in mass, as described by the Sauerbrey equation, [192]

$$\Delta f = -\frac{2nf_o^2}{A\sqrt{\rho_q\mu_q}}\Delta m \quad (3.8)$$

where f_o is the resonant frequency of the crystal, A is the area of the crystal, n is the overtone at which Δf is being studied and ρ_q and μ_q are the density and shear modulus of quartz, respectively. The Sauerbrey equation assumes that the mass adhered to the crystal is homogeneously distributed over the crystal, that it does not have any energy dissipation and that its internal friction is negligible. [193] However, organic layers adsorbed on the quartz sensor are generally highly viscoelastic and have large energy dissipation during oscillation. In this case, Δf is no longer directly proportional to Δm , but it depends on the mechanical properties of the film, including shear modulus and viscosity. [194] Based on the Kelvin-Voigt viscoelastic model, Δf and ΔD of two thin viscoelastic layers covering the surface of a quartz crystal oscillating in a Newtonian liquid can be calculated as [193–199] (figure 3.5)

$$\Delta f \approx -\frac{1}{2\pi\rho_q h_q} \left(\frac{\eta_3}{\delta_3} + \sum_{i=1,2} \left(h_i \rho_i \omega - 2h_i \left(\frac{\eta_3}{\delta_3} \right)^2 \frac{\eta_i \omega^2}{\mu_i^2 + \omega^2 \eta_i^2} \right) \right) \quad (3.9)$$

$$\Delta D \approx \frac{1}{2\pi f \rho_q h_q} \left(\frac{\eta_3}{\delta_3} + \sum_{i=1,2} \left(2h_i \left(\frac{\eta_3}{\delta_3} \right)^2 \frac{\mu_i \omega}{\mu_i^2 + \omega \eta_i^2} \right) \right) \quad (3.10)$$

where ρ_q and h_q are the density and thickness of the quartz crystal, respectively, η_3 is the viscosity of the bulk liquid, δ_3 is the penetration depth of the shear wave in the liquid, ω is the angular frequency of the oscillation, and the properties of the viscoelastic layers are represented by four parameters: density (ρ_i), viscosity (η_i), shear modulus (μ_i) and thickness (h_i).

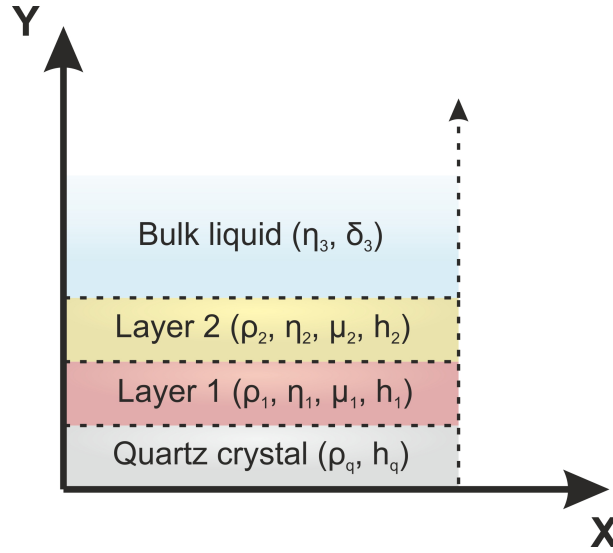


Figure 3.5: Schematic of the arrangement of viscoelastic layers on a QCM-D sensor. The system oscillates in bulk liquid with an angular frequency ω .

For fitting the data obtained in the QCMD experiments, the parameters δ_3 and η_3 were typically fixed to $\delta_3 = 1000 \text{ kg/m}^3$ and $\eta_3 = 0.001 \text{ Pa}\cdot\text{s}$. For the layers, the thickness h_i was normally varied between $10^{-10} - 10^{-7} \text{ m}$, the shear modulus μ_i between $10^4 - 10^{12} \text{ Pa}$ and the viscosity η_i between $0.001 - 0.01 \text{ kg}\cdot\text{ms}$. The density of the layers was adjusted depending on the the specific binder. For LONDS, the density was that of the encapsulated oil, 850 kg/m^3 in the case of squalane, and 1150 kg/m^3 for triacetin LONDS.

3.6.1 QCM-D experimental set-up

QCM-D sensors are made of a quartz thin layer placed between two electrodes. Upon the application of an electrical field, the quartz crystal oscillates at its resonant frequency, which vary depending on the adsorbed layers onto it. QCM-D crystals are commercially available with a range of different coatings, such as gold and copper, for experiments with different binders. Silica-coated quartz crystals were used in all QCM-D experiments in this report.

Prior to the experiments, the QCM-D sensors were always thoroughly cleaned, in this order, by 5 min sonication in 1% Decon90, MilliQ and 70% isopropanol. After this, any liquid remaining on the sensors was dried under a N_2 stream. The crystals were then cleaned in a UV/Ozone oven for 20 min. Once cleaned, the sensors were placed inside the flow chambers in the QCM-D instrument, and the chambers tightly locked to ensure

correct crystal hold. A buffer was then flown in the chambers, using a high precision multichannel dispenser. The specific resonances for each sensor were found, including a number of harmonics (typically 3th to the 11th). All solutions flowed in the sensors chambers were always degassed beforehand to prevent the formation of air pockets on the surface. Degassing was performed immersing the bottles containing the solutions in an ultrasonication bath while connected to a vacuum pump for at least 15 min. The measurement in QCM-D was started flowing a buffer into the flow chambers at 0.1 ml/min and until the baseline for f and D was stable (i.e. no drifting). The buffer used for obtaining this stable baseline was typically the one in the first sample is prepared (i.e. PBS). Once the signals reached a steady value, the measurement was re-started, which effectively calibrated the values for the frequency and dissipation to 0. This means that the frequency and dissipation signals observed after calibration reflect the changes due to the adhesion of mass, Δf and ΔD . All QCM-D results shown in this thesis were obtained following an identical procedure, and thus any changes in frequency and dissipation in the different systems are comparable. This calibration step was followed by sequentially flowing the sample solutions into the modules at 0.1 ml/min.

3.6.2 Formation of SBLMs for QCM-D experiments

Solid-supported bilayer lipid membranes (SBLMs) were used to study the binding of StreptAvidin and LONs in QCM-D. The formation of a SBLMs in QCM-D is shown schematically in figure 3.6. Vesicles flowed into the system accumulate on the QCM-D sensors and eventually fuse to form a SBLM (figure 3.6, region 1). [200–202] SBLM formation is typically followed by washes with different buffers, to ensure complete removal of excess material before performing any further experiments. First, a rinse with the same buffer (typically PBS) in which the vesicles were contained is performed (figure 3.6, region 2). No changes in frequency or dissipation are detected, as the number of ions coupled to the detector is constant throughout this washing step. Second, a washing step with MilliQ is performed (figure 3.6, region 3). The reduction in the number of ions in the SBLMs environment translates into a reduction in the frequency (as less mass is coupled to the sensor). Similarly, a reduction in the dissipation is observed, given that the friction of the SBLMs with its surroundings is reduced. The washing cycle is finished with the original buffer (figure 3.6, region 4), during which the original frequency and dissipation values are

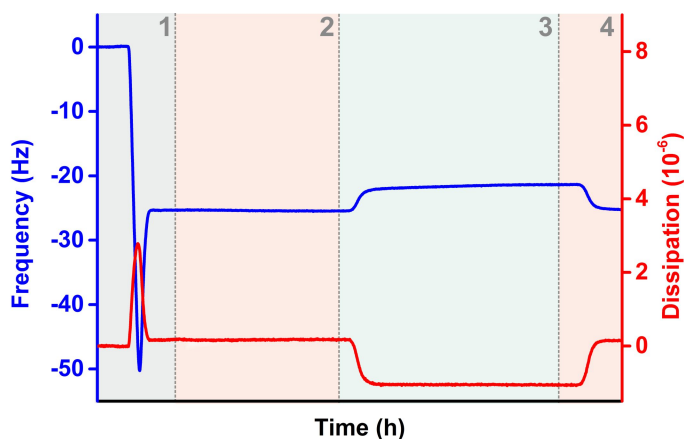


Figure 3.6: Semi-schematic showing the formation of a SBLM in QCM-D. Vesicles flowed into the chambers are accumulated on a silica-coated quartz crystals and eventually break to form a SBLM (1). The system undergoes a series of rinses, starting with the same buffer that contained the vesicles (2) and followed by MilliQ (3) to ensure complete removal of excess material. The washing cycle is always finished with buffer (4).

recovered.

In these experiments, SBLMs were always formed by vesicle adsorption and rupture on the surface of the QCM-D sensors. Vesicles were prepared as described in section 3.1.1 (page 28). POPC was used as main lipid in all SBLMs formed, to which different percentages of molecules of interest (such as biotin-PEG2000-DSPE or PEG2000-DSPE) were added. The vesicle solution was adjusted to a final concentration of 0.2 mg/ml. Prior to SBLM formation, the QCM-D sensors were prepared as described in section 3.6.1. Once they were set up, the vesicle solution was flowed into the chambers at a flow rate of 0.1 ml/min. PBS and MilliQ washes followed SBLMs formation. The flowing time varied between experiments, but was never less than 20 min. As mentioned above, this rinsing cycle was always finished with a PBS rinse before the addition of StreptAvidin or LONDS.

3.7 Formation of MBs

In this project, MBs were formed both using microfluidics and by mechanical agitation, and MB-LONDS were always formed on-chip. This section describes the two methods used for preparing MBs, the experimental procedure for preparing MB-LONDS. All microfluidically prepared MBs were formed in the micro-spray regime. Two different geometries were used, one for the production of MBs only, and one for the production of MB-LONDS composites. These geometries are described below, and the experimental set-up for using

them is provided. All chip designs shown in this section were designed by Dr. Sally A. Peyman.

3.7.1 On-chip preparation of MBs

This section describes the production of MBs and MB-LONDS microfluidically.

3.7.1.1 Fluidics set-up

The microchips were fabricated by Epigem in poly(methyl methacrylate) (PMMA) and SU-8 via photolithography. Home-built PMMA manifolds, which contained PTFE tubes for liquid and gas lines were brought into firm contact with the microchips using a lever clamping arm. The manifold also contained a PTFE tube connected to the outlet, for sample collection. Manifolds were designed to specifically fit the inlets and the outlet of each of the microchips. Fluid flow to the microchip was delivered via a pressure P-Pump and the gas was regulated by a digital gas flow controller. A second fluid flow (for the addition of LONDS) was controlled using a syringe pump. Both the pressure P-pump and the syringe pumps, as well as the gas flow were controlled via a PC. This set-up was mounted onto an inverted Nikon Eclipse Ti-U used to monitor the functioning of the fluidics as well as MB formation (see 3.4.1).

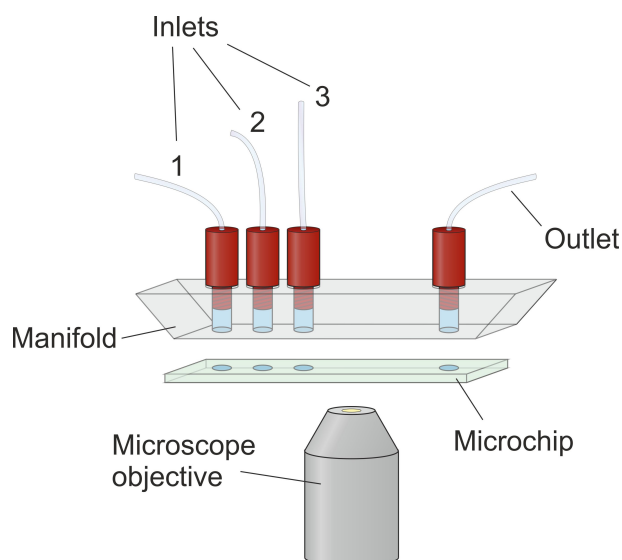


Figure 3.7: Schematic showing the set-up of the microfluidic device for MB-LONDS formation. Liquid and gas inlets were fitted onto an in-house made manifold, which was later brought into firm contact with the microchip using a lever clamping arm. The set-up allowed for live, *in situ*, microscopic visualisation. Inlets 1, 2 and 3 were used to bring in LONDS solution, the gas phase and the lipid solution, respectively.

3.7.1.2 Preparation of MBs

For MB formation a chip with 4 independent MB formation devices (referred to as $4\times$ multiplexed chip, or simply multiplexed) allowed for rapid preparation of MBs (figure 3.8) [133]. This chip had two inlet channels, one for the gas phase and one for the lipid solution for MB stabilisation. Both the gas and the liquid inlet channels branched into four separate channels to feed the four flow-focusing modules. The width of the liquid inlets was $50\ \mu\text{m}$ and the gas inlet $30\ \mu\text{m}$. The chips had a depth of $25\ \mu\text{m}$, with an additional layer of $25\ \mu\text{m}$ beyond the nozzle for a 3D expansion in the MB formation area to facilitate MB formation in the micro-spray regime.

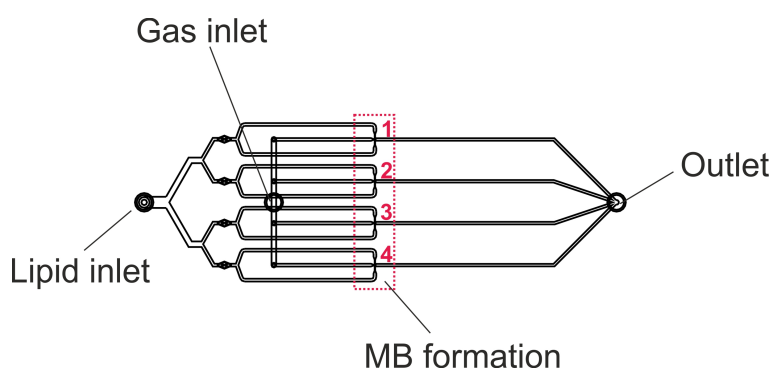


Figure 3.8: Multiplexed microchip design for MB formation. The chip contains four identical flow-focusing modules, numbered 1 – 4. MBs are formed in the micro-spray regime. Chip design is credited to Dr. Sally A. Peyman, and it is detailed in reference [133].

Lipid solution was prepared as described in section 3.1.2. Once the lipid solution had cooled down, it was introduced into the device using a pressure pump (section 3.7.1.1) at $80\ \mu\text{l}/\text{min}$. This corresponds to $20\ \mu\text{l}$ per flow-focusing module. The Reynolds number (equation 2.5, page 14) for the lipid inlets at this flow rate was calculated to be $R_e \approx 9 \times 10^{-3}$, which is considerably less than one and thus the flow here was expected to be laminar. C_4F_{10} or C_3F_8 gas were pumped in the chip at 103 or 140 kPa, depending on if a spray-like profile appeared at the nozzle. The Reynolds number beyond the nozzle could only be estimated using the velocity of the liquid, as there velocity of the gas in the channels, at the given pressure, was unknown. Hence the calculated value, $R_e \approx 6 \times 10^{-3}$ would be grater if the contribution of the gas velocity was considered. In fact, the flow in this region was observed to be turbulent, which indicates that gas plays an important role in determining the flow regime beyond the nozzle.

3.7.1.3 Preparation of MB-LONDs

For MB-LONDs formation, the microchip design included a flow-focused region for MB formation in the micro-spray regime, followed by a serpentine mixing geometry to allow for attachment of LONDs to MBs (figure 3.9)¹. The width of the channels for the liquid phases the gas were 300 μm . At the nozzle region, the width of the liquid inlets was 50 μm and the gas inlet was 30 μm . The depth of the channels was 25 μm , with an additional layer of 25 μm in the outlet. LONDs were added to incorporate to the MB solution after the nozzle region. These channels narrowed down from 300 μm to 100 μm to avoid back pressure created by the long, narrow channels, and the LONDs solution moving backwards in the channel. The depth of the serpentine was 50 μm , and the width was 270 μm . The total length of the region for MB and LONDs mixing and attachment was 56.6 mm.

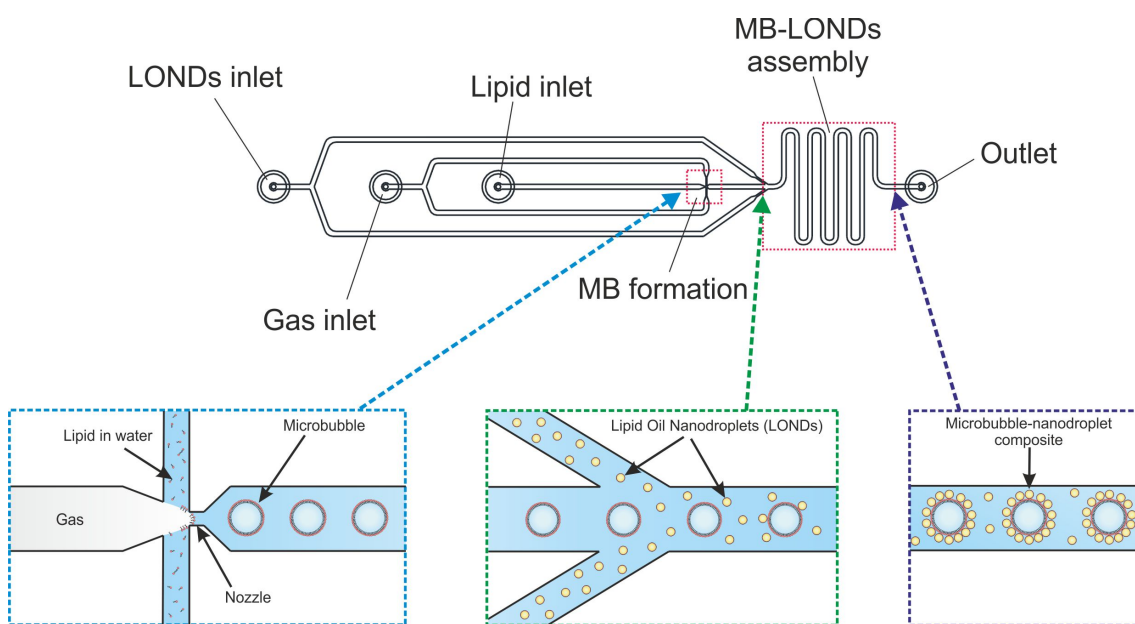


Figure 3.9: Microchip design for MB-LONDs formation. MBs are formed first, in the micro-spray regime, and LONDs are added further down stream. LONDs and MBs are mixed together through the mixing serpentine, where the LONDs bind to the MB surface via the biotin-NeutrAvidin chemistry.

For MB-LONDs formation, the lipids were first prepared as described in section 3.1.2. The lipid mixture was introduced into the microfluidic device through the aqueous phase inlet and perfluorobutane C_4F_{10} was flowed through the central inlet. Liquid flow rate was 20 $\mu\text{l}/\text{min}$ and the gas pressure was 103 psi. Similarly to the calculation done previously

¹design credited to Dr. Sally Peyman.

for the multiplexed microspray chip, the Reynolds number in the liquid inlets was found to be $R_e \approx 9 \times 10^{-3}$. The estimate for the Reynolds number in the serpentine area resulted $R_e \approx 0.02$, which would be enlarged if considering the contribution of the gas velocity. Prior to MB-LONDS preparation, LONDS were incubated with $3 \mu\text{M}$ of NeutrAvidin with gentle agitation to allow mixing. LONDS were incorporated mixed with the MB solution at a concentration of 10^{11} LONDS/ml at $20 \mu\text{l}/\text{min}$ flow rate. Preceding imaging, the sample was washed from unattached LONDS, unless otherwise stated. This was done with 1 ml PBS in a vial, allowing the MB-LONDS to rise, due to their intrinsic buoyancy, through the liquid volume up to the top. This top layer was collected and the process was repeated again through a fresh PBS volume to ensure removal of most of the excess material. Alternatively, MB-LONDS were cleaned in a flow cell in which PBS flowed at $0.13 \text{ ml}/\text{min}$ for about 2 h. This was done for MB-LONDS imaging, and both epi-fluorescence and confocal fluorescence microscopy were used.

3.7.2 Production of MBs by mechanical agitation

Mechanical agitation is a method for MB production in which energetic shaking of a surfactant-containing solution with a head-space gas results in gas encapsulation by the surfactant. For preparation of mechanically agitated MBs, lipids were prepared as described in section 3.1.2. After bath sonication, the lipid solution was gassed with C_3F_8 or C_4F_{10} for around 10 min, which displaces the other gas molecules dissolved in the liquid and remaining in the head-space volume. The lipid solution and the head-space gas were mechanically agitated for 30 s using a mechanical agitator. The MB solution was normally diluted 1 : 10 before imaging.

3.8 Biosafety cabinet. Functioning and protocols

Preparation of LONDS for *in vivo* or *in vitro* experiments required the samples to be sterile. This work was performed inside a Class II A1 Biosafety Cabinet. The cabinet (also referred to as *biohood*) is an enclosed space that allows samples susceptible of contamination to be handled safely. In this case, the cabinet prevented sterile samples from being infected with bacteria, which is crucial for the preparation of samples towards *in*

vitro cell work or *in vivo* testing, and also impedes air from the inside to leave the cabinet and reach the operator. This type of cabinet has an internal, vertical and laminar filtered air stream, which continuously exchanges the air volume inside the cabinet, flushing away any pathogens in the cabinet's air volume. There is also an *inflow* air stream, which flows at 0.40 m/s into a grille placed near the operator, by the entry of the cabinet, and reaching the sterile environment inside the cabinet. Biosafety cabinets commonly have a sliding transparent glass window that allows the operator to see inside and serves as a door to prevent contaminants from getting in the biohood when not in use.

When switched on, the cabinet has a warm up period of 220 s. During this time, the air circulation is started and reaches its optimal values, and also the air volume inside the cabinet starts to be refreshed. Once the warming up process is completed, the cabinet is suitable for working with samples that require biosafety. At this point, all surfaces inside the cabinet were sprayed and wiped with TriGene disinfectant and then with 70% ethanol. Laboratory utensils and consumables required for sample handling inside the cabinet were sprayed with 70% ethanol before introducing them inside the biohood. This included the packaging of sealed consumables, such as syringes and serological pipettes, and the operator's gloves before any experimental procedures. Avoiding contact of sterile consumables with other inner surfaces in the biohood is important to avoid bacterial infections. For the same reason, consumables that got in contact with sensible samples were never reused.

Once the biosafety work was completed, all objects were removed from the cabinet. All the surfaces inside biohood were cleaned with TriGene and 70% ethanol and the glass window was slid down to stop the air flow. An UV light built-in the cabinet was switched on for exhaustive cleaning of the inner surfaces and to prevent the formation of bacteria colonies.

Chapter 4

Topic: characterisation of the candidate oils

This chapter contains the characterisation of the candidate oil, including their photochemical properties (light absorption and autofluorescence), and their ability to solvate drug mimics and the hydrophobic drugs Combretastatin A4 (CA4) and decitabine.

4.1 The candidate oils

The first steps in this project focused on the selection and study of a number of candidate oils for LOND formation. Given the interest in using oils to form nanoemulsions for drug delivery, biocompatibility was among the desired characteristics of the oils. Table 4.1 contains a list of the oils preliminary chosen, together with their density, viscosity and water solubility. The molecular structure of the candidate oils are shown in figures 4.1 and 4.2. From the molecular point of view, oils containing a single type of molecule were prioritised over blends in early stages of the project, as for medical applications having full knowledge of the components of a delivery system is of major importance. For example, this is the case of olive oil, which contents of oleic, linoleic and palmitic acids in olive oil strongly depends on method of production, as well as the olive variety. [203–205], and therefore oils with unlike origin could exhibit significantly different properties. Inherent therapeutic properties of the candidate oils was also deemed, such is the case of squalene, which has been reported to be tumour-inhibiting [206, 207] and eicosapentaenoic acid (EPA), which evidence shows to have chemopreventative efficacy against colorectal cancer. [208, 209]

Table 4.1: Some physical properties of the candidate oils*

Oil	Solubility in H ₂ O (g/l)	Viscosity at 20 °C ($\times 10^{-3}$ Pa s)	Density (kg/m ³)
Squalane	-	12	805
Squalene	0.124×10^{-3}	11	858
Olive oil	-	85	918
Triacetin	61	23	1160
Tripropionin	0.003	10	1082
Isoamyl acetate	2	7	876
EPA	0.284×10^{-3}	35	923

* For reference, H₂O has approximately a density 1000 kg/m³ and a viscosity 1×10^{-3} Pa s at 20 °C.

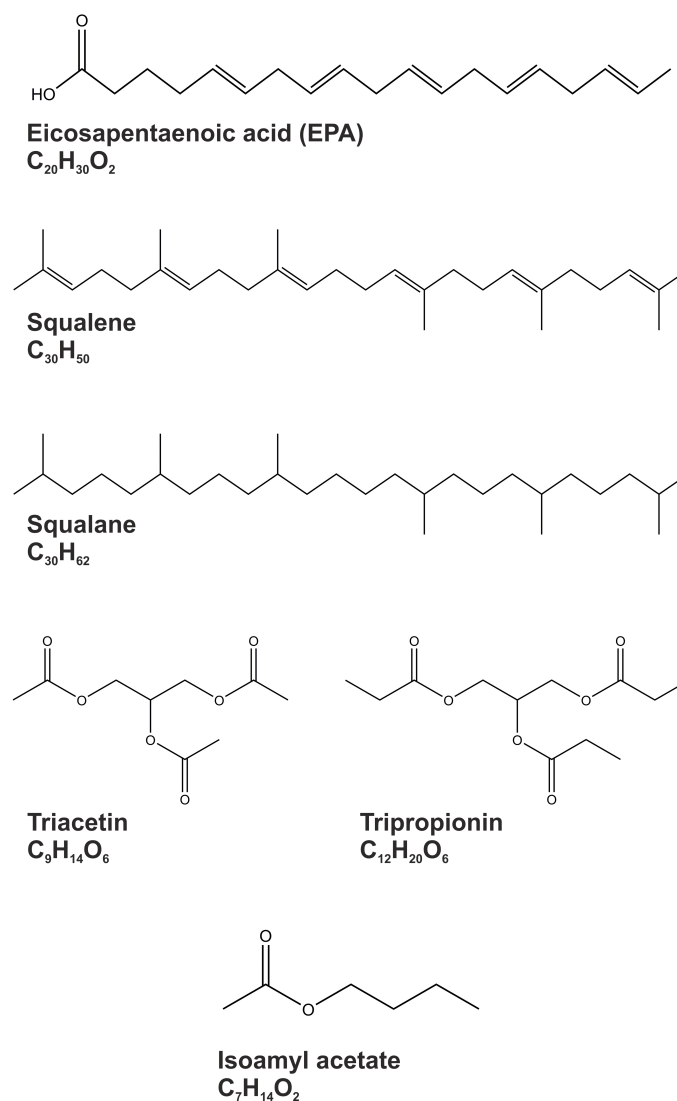


Figure 4.1: Molecular structure of the candidate oils, non-blends.

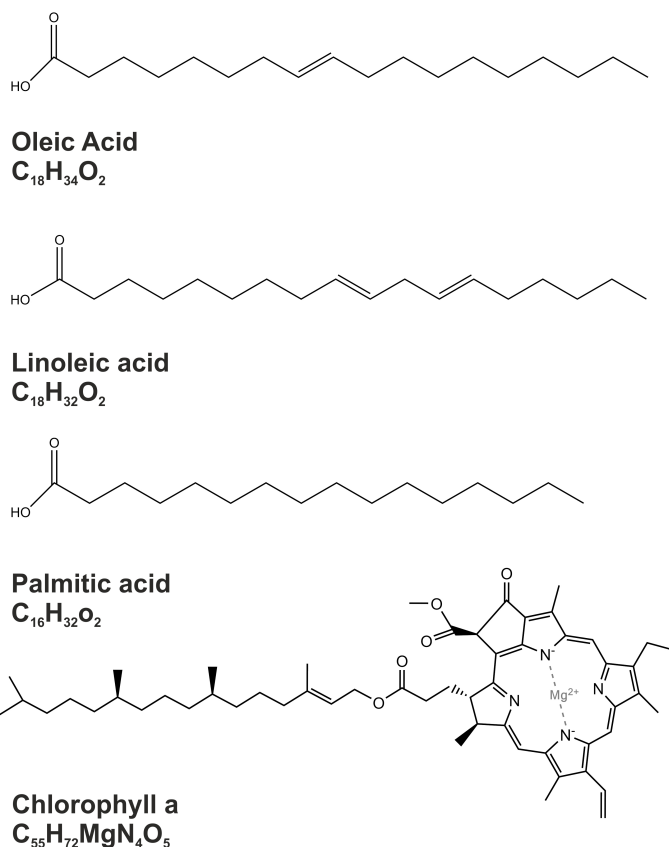


Figure 4.2: Molecular structure of the main components of olive oil, oleic, linoleic and palmitic acid. The structure of chlorophyll a is also shown, as this molecule largely contributes to the autofluorescence of olive oil.

4.2 Light absorption and emission of candidate oils

The use of oil as a solvent for hydrophobic drugs to facilitate their delivery *in vivo* required information about the physical properties of the oil itself, as well as the solubility of target compounds in the oil. This study focused first in understanding the light absorption and autofluorescence of the candidate oils (see candidate oils on table 4.1). The understanding of the fluorescence properties of the candidate oils was important as fluorescence probes, such as Qdots or fluorescently tagged phospholipids, were intended to be used as drug mimics or detection tools in LONDS, and the different fluorescence signals had to be unambiguously identified. It was also necessary to ensure that no interference between the different fluorescent signals occurred. Knowledge about the absorptive properties of the candidate oils was of special relevance for this project, as light absorption was used to

quantify the amount of drug encapsulated in this LONDS, and therefore ensuring the oils did not significantly absorb light on the same region as the model therapeutic compounds was a must.

4.2.1 Light absorption of candidate oils

The absorption of light by candidate oils was studied by recording their absorption spectrum in the UV/VIS range (section 3.3.2, page 32), 900 – 200 nm in a spectrophotometer. Figure 4.3 shows the absorption spectra of the candidate oils. Due to the sensitivity of the apparatus, only intensities up to 1 a.u. could be recorded. The UV, visible and infrared regions of the electromagnetic spectrum are shown in shadowed colours on this figure. Due to the lack of references to the UV-VIS light absorption of the candidate oils unrefined olive oil purchased from a local supermarket was analysed and used as a control sample, as its absorption in this range has been broadly studied. [210] It is important to note that any other olive oil, purchase anywhere else would have likely shown a slightly different absorption profile. For the purpose of this particular study, this was considered acceptable. This oil was found to absorb light between 400 – 500 nm, which is characteristic of the olive oils containing chlorophyll a molecules, carotenoids, and other pigments. [203,204,211] Interestingly olive oil purchased from Sigma-Aldrich did not show this characteristic spectrum. This is likely due to the removal of highly absorbent molecules during the refinement process. The rest of the candidate oils showed absorption in the UV range, probably arising from the presence of oxidative products in the samples, known to absorb strongly in the UV. [212–215] The wavelengths absorbed by the candidate oils (not taking unrefined olive oil into consideration) fall far from the range of wavelengths on which the excitation wavelength of many common fluorophores is found. For example, the excitation wavelength for Atto 488 DOPE is $\lambda_{ex} = 488$ nm, which is the shortest excitation wavelength out of those of the fluorophores used within this project. This suggests that the light absorption of the oils would not interfere with any fluorophores contained in the oil or used in combination with other phospholipids to stabilise the oil in LONDS.

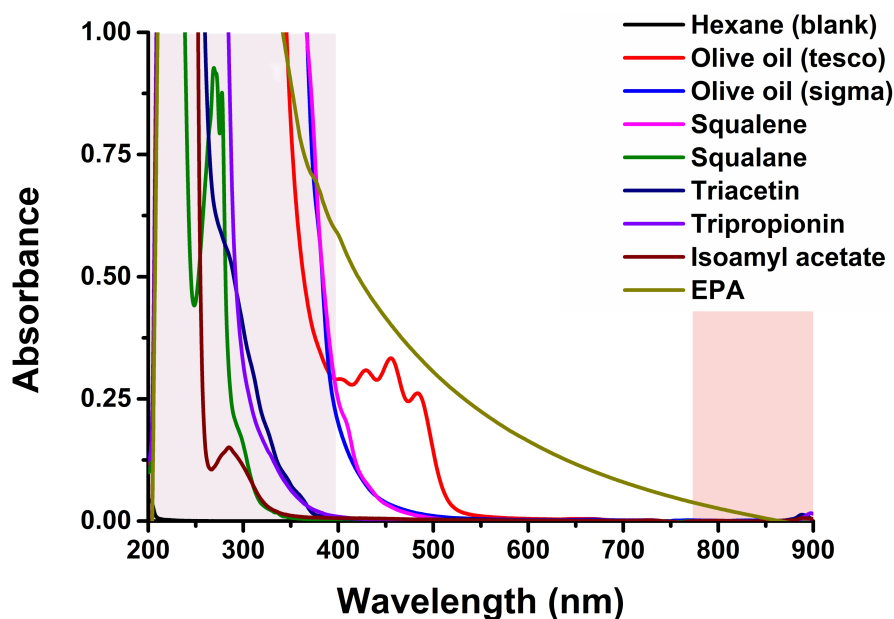


Figure 4.3: Light absorption of the candidate oils, recorded using a spectrophotometer. The regions of the electromagnetic spectrum are shown in shadowed colours: light violet for UV (200 – 400 nm), white for the visible spectrum (400 – 790 nm) and red for the wavelengths in the near infrared (790 – 900 nm).

4.2.2 Autofluorescence of candidate oils

The intrinsic fluorescence properties of the candidate oils were studied recording their emission spectrum. The oils were excited with a specific excitation wavelength (λ_{ex}), ranging 250 – 550 nm, and the maximum of the emission peak was identified as the emission wavelength (λ_{em}). In the case of EPA, the range of excitation wavelengths was 350 – 650 nm. An intensity attenuator was used when recording the emission spectra of squalane, squalene and olive oil, in order to avoid saturating the detector. As an example of the recorded data, the emission spectrum of squalane is shown in figure 4.4, for five different λ_{ex} and their correspondent emission profiles. In this specific case, λ_{em} was observed to shift for each λ_{ex} , with values around the maximum $\lambda_{em} = 384$ nm.

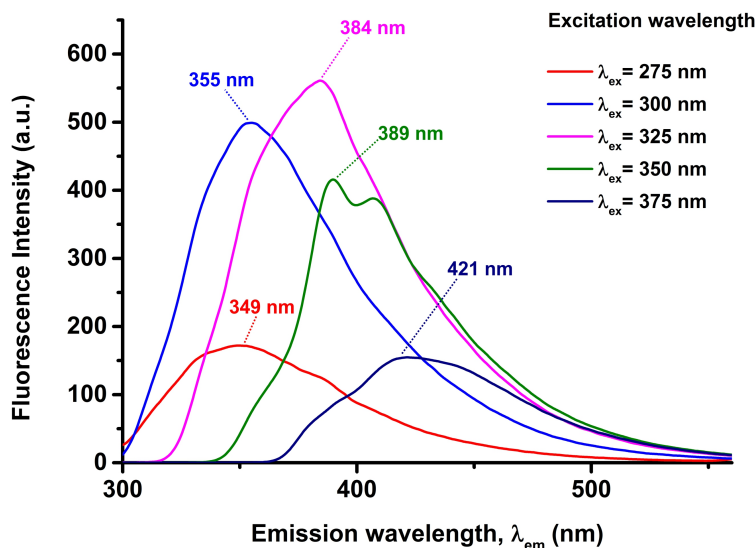


Figure 4.4: Emission spectrum of squalane, recorded using an intensity attenuator. The sample was radiated with different excitation wavelengths, λ_{ex} , and the fluorescence signal was recorded in each case. The maximum emission intensity for each excitation wavelength, λ_{em} , are showed on the graph.

Table 4.2 summarises the fluorescence emission maxima λ_{em} for several excitation wavelengths, λ_{ex} , for each of the candidate oils. In each case, the maximum λ_{em} is shown in bold font for clarity. Two other λ_{ex} , spaced +25 nm and -25 nm from the λ_{ex} that produced the highest intensity peak are also shown. It is important to note that the intensity attenuator was used to record the emission spectra of olive oil, squalane and squalene. Although no quantitative data can be extracted from this, it shows that the emission intensity at λ_{ex} was stronger for these three oils, compared to triacetin, tripropionin, isoamyl acetate and EPA. Furthermore, the autofluorescence of the candidate oils arose with λ_{ex} in the UV range, which is in agreement with the absorption spectra of the oils shown in figure 4.3. This suggests that oxidative products and impurities give rise to these fluorescent properties.

IVIS was used to measure the radiant efficiency of squalane and squalene. The experiment was performed to study the autofluorescence of these two candidate oils with an alternative technique, and also to determine whether oil autofluorescence could be produced and detected in this system. IVIS was expected to be used in the study of fluorophore encapsulation in LONDS, and therefore the characterisation of potential fluorescence signal produced by the oils alone was important. The lowest excitation wavelength producible at IVIS was $\lambda_{ex} = 430$ nm, which falls far the wavelength window observed to give rise to the autofluorescence of squalane and squalene ($\lambda_{ex} = 325$ nm for squalane, $\lambda_{ex} = 350$ nm

Table 4.2: Autofluorescence of the candidate oils. Higher intensity peaks for each oil are shown below. The maximum intensity peak and the corresponding excitation and emission wavelengths are in bold font.

Oil	Excitation wavelength	Emission wavelength	Intensity (a.u.)
	λ_{ex} (nm)	λ_{em} (nm)	
Olive oil*	325	406	47
	350	423	81
	375	446	58
Squalane*	300	355	499
	325	384	560
	350	390	416
Squalene*	325	451	40
	350	463	100
	375	461	61
Triacetin	325	422	693
	350	430	775
	375	435	387
Isoamyl acetate	275	350	967
	300	353	780
EPA	525	587	600
	550	600	653
	575	610	635
Tripropionin	325	375	8.1
	350	428	6.4

* An intensity attenuator was used to record the spectra of olive oil, squalane and squalene.

for squalene, table 4.2). Hence no fluorescence signal was expected. For imaging, squalane and squalene were placed in a $6\times$ well plate. Figure 4.5 shows an optical image of the well plate containing the oils, on which the radiant efficiency is superimposed (coloured scale) to a gray image. Circular ROI profiles were used to delimit the wells that contained the two oils under study. The radiant efficiency of the ROIs relate to the epi-fluorescence signal detected by the system. As expected, no fluorescence signal was detected upon excitation of the squalane and squalene with $\lambda_{ex} = 430$ nm. Informed by these results, further IVIS experiments performed with these oils could neglect fluorescence contribution from the oils.

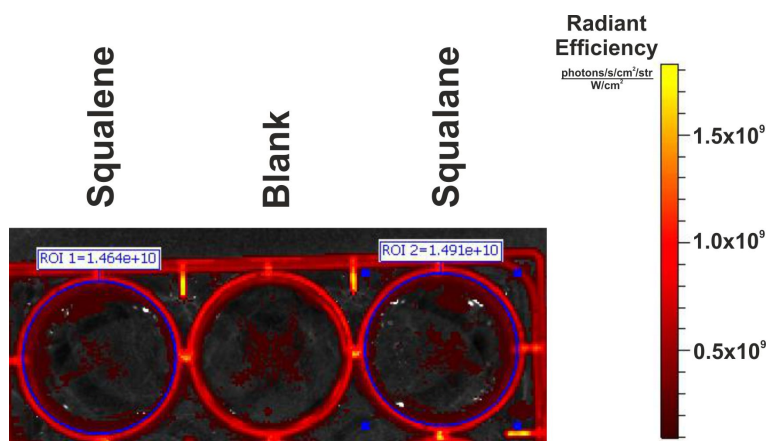


Figure 4.5: Radiant efficiency of squalene and squalane measured using IVIS. The sample was excited with $\lambda_{ex} = 430$ nm. The image shows a superimposition of the radiant efficiency, in a coloured scale, to the optical image, in gray scale.

4.3 Drug mimics in candidate oils

Drug mimics were used for preliminary oil solubility and detection tests, to avoid excessive spending of the therapeutic compounds, as the cost of those is normally higher than that of the mimics. Three different hydrophobic drug mimics were chosen: CIS/ZnS Qdots (section 3.2, page 28), the fluorophore Nile Red and Calcein AM. This section describes the study of the solubility of the hydrophobic drug mimics in the candidate oils.

4.3.1 CIS/ZnS Qdots: solubility and fluorescence in oil

CIS/ZnS Qdots were synthesised as described above (section 3.2, page 28). The Qdots were made hydrophobic by coating them with a layer of dodecanethiol, as they were to be used encapsulated in the LONDS and serve as mimics of the hydrophobic drugs. The incubation times for Qdots preparation were increased in order to obtain larger Qdots with emission spectra shifted towards the near infrared, which find a wide range of applications in biomedical imaging. [216–219] The characterisation of the light absorption and emission spectra of the Qdots was essential for them to be used as model drugs in fluorescence experiments. Figures 4.6a and 4.6b show the emission spectra and absorption spectra of the Qdots dissolved in hexane, respectively. The emission spectrum revealed a maximum emission at 790 nm, which is a longer wavelength than what has been previously reported for CIS/ZnS Qdots. [179, 180, 220] The longer emission wavelength was a result of the

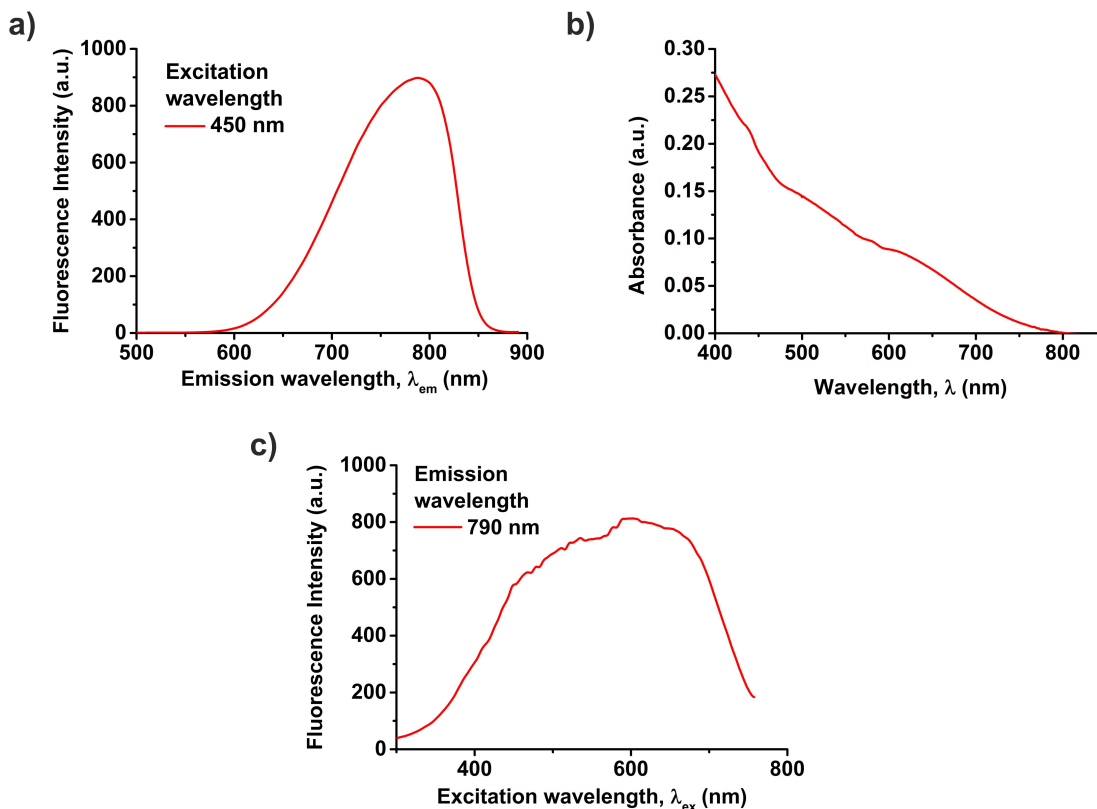


Figure 4.6: Luminescence characterisation of CIS/ZnS Qdots. a) Emission spectrum; the sample was excited with $\lambda_{ex} = 450$ nm, producing a maximum intensity at $\lambda_{em} = 790$ nm. b) Light absorption of the CIS/ZnS Qdots in the UV/VIS range. c) Excitation spectrum; the sample was excited in a range of wavelengths (300 – 750 nm) and the fluorescence intensity of $\lambda_{em} = 790$ nm recorded within this range. From the maximum intensity on this graph, the optimal λ_{ex} for this Qdots samples was found to be $\lambda_{ex} = 589$ nm.

longer incubation times of the precursor solution (section 3.2, page 28), compared to the literature. Figure 4.6c shows the Qdots excitation spectrum for $\lambda_{em} = 790$ nm. This spectrum revealed a broad excitation band, with a peak at $\lambda_{ex} = 589$ nm.

After Qdots synthesis, Qdots concentration and size were determined theoretically as described earlier (section 3.2.2), and were found to be $d = 7.37$ nm and $C = 1.70$ μ M. The concentration results are in agreement with the literature. [180] The estimated size of these Qdots is larger than that typically reported for QDots prepared within this method. This suggests that the longer incubation time used in the preparation of this batch of Qdots had the effect of increasing the size of the Qdots, which was desired. [179]

The Qdots were initially suspended in hexane. Attempts to dissolve them in squalane, squalene, triacetin and isoamyl acetate were performed. This was done by adding the Qdots in hexane to the oils, and by removing the hexane placing the solution under a stream of N_2 for at least 30 min. The solutions were visually inspected to confirm the dispersion of the Qdots in the liquid, which was guided by the absence of large agglomerates

within the solution. Qdot solution blended with the candidate oils upon gentle shaking in all cases except for triacetin. In this case, the Qdots agglomerated around the walls of the vial, on the surface of the oil. Resuspension of the Qdots via vortexing the bath sonicating the solution was unsuccessful. This effect was likely due to the relative high polarity of triacetin, and the non-polar nature of the dodecanethiol coating of the Qdots. The reduction in the number of dipole-dipole interactions in triacetin, by the addition of the hydrophobic Qdots is energetically unfavorable, resulting in exclusion of the hydrophobic Qdots from the triacetin volume. [221] The fluorescence properties of the Qdots diluted in squalane, squalene and isoamyl acetate were studied. All three solutions were excited with a $\lambda_{ex} = 589$ nm, which corresponds to the λ_{ex} for these Qdots. Figure 4.7 shows the emission spectra of Qdots in the three oils tested, as well as the emission spectra of the Qdots dissolved in hexane, for reference. Qdots diluted in squalane and isoamyl acetate did not show significant changes in their fluorescent properties. Interestingly, the fluorescence signal of Qdots was absent when these were dissolved in squalene. This quenching of the Qdots fluorescence signal could be due to energy transfer or electron transfer between the Qdots and the oil. Squalene contains a number of double bonds that are not present in the squalane molecule, which could facilitate energy transference between the Qdots and the squalene molecules. The concentration of Qdots dispersed in squalane and squalene for this study are equivalent, and therefore this suggests that the loss of fluorescence signal in the case of squalene was due to quenching.

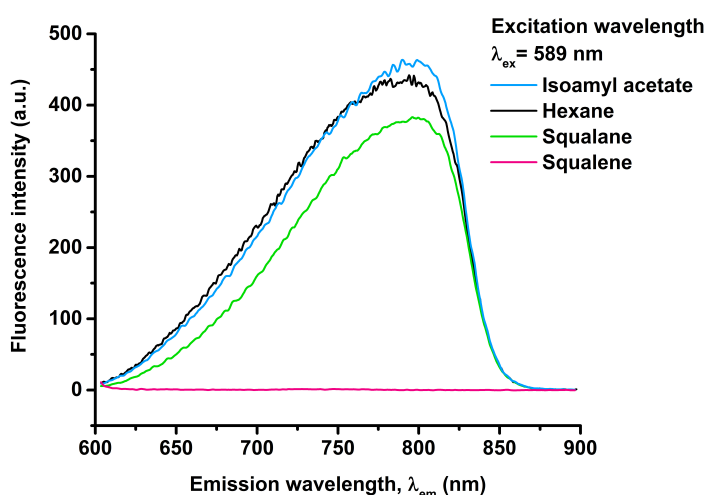


Figure 4.7: Fluorescence signal of Qdots diluted in candidate oils. The samples were excited with $\lambda_{ex} = 589$ nm in all the cases. The fluorescence signal of Qdots diluted in hexane is shown for comparison.

IVIS was used to measure the radiant efficiency of Qdots dissolved in squalane and squalene. Qdots were added to the oils in hexane, and the solvent removed by placing the solution under a N_2 stream for at least 30 min. The radiant efficiency of two different concentrations of Qdots in the oils were used, 170 nM and 850 nM. Figure 4.8 shows the radiant efficiency of the sample excited with $\lambda = 640$ nm ($\lambda_{em} = 800$ nm), superimposed to an optical image of the same area, both taken in IVIS. The ROI profiles delimit the wells that contained each sample, and provide a measure of the radiant efficiency of the area. Qdots dissolved in squalane exhibited fluorescence that increased with concentration. Qdots did not show any fluorescence when dissolved in squalene, supporting the observation made in figure 4.7. This figure suggests that the quenching of the Qdots fluorescence, when dissolved in squalene, is not an effect of the concentration of the Qdots, as no changes in fluorescence were observed for the two different concentrations of Qdots used.

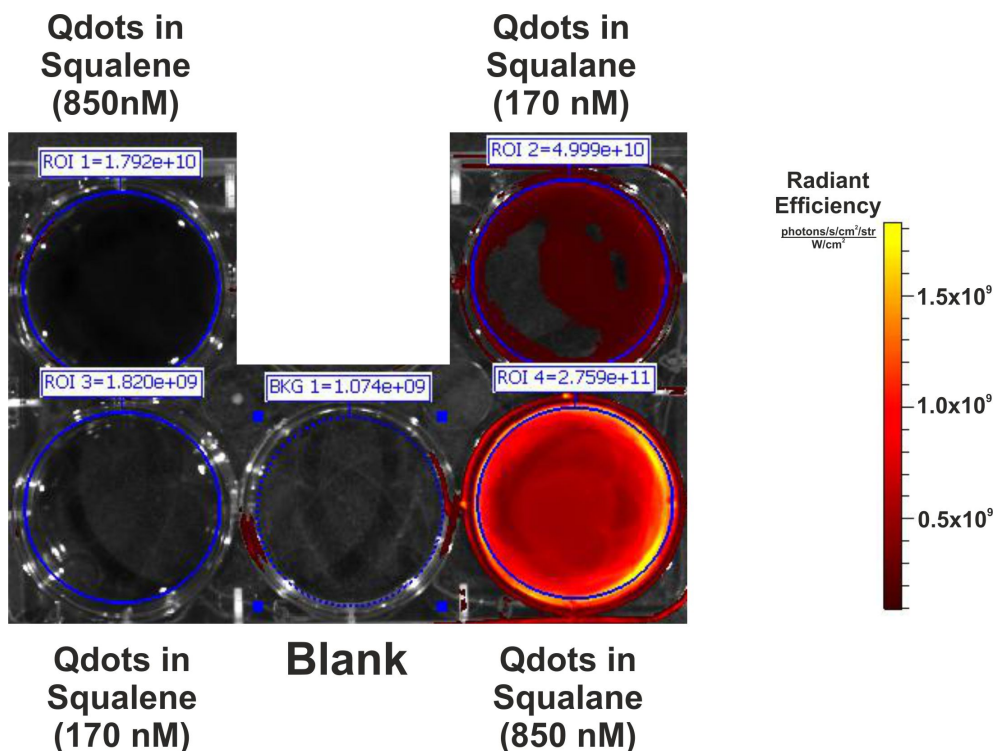


Figure 4.8: Radiant efficiency of Qdots dissolved in squalene and squalane measured using IVIS. The sample was excited with $\lambda_{ex} = 640$ nm. The image shows a superimposition of the radiant efficiency, in a coloured scale, to the optical image, in gray scale.

4.3.2 Nile Red: solubility and fluorescence in candidate oils

Nile Red is a lipophilic dye broadly used in cell biology. The molecular structure of Nile Red is shown in figure 4.9. Nile Red has an amphiphilic character, which makes it a useful tool for dyeing lipid rich environments, such as lipid membranes and droplets. [222, 223] Nile Red has also been used as a fluorescent tag in drug delivery systems. [52, 224] When incorporated in a hydrophobic environment, Nile Red exhibits a strong fluorescence signal that has been found to vary according to the polarity of the solvent. [225] In contrast, when Nile Red is contained in water its fluorescence disappears. This feature turns Nile Red into an interesting hydrophobic drug mimic to be encapsulated in LONDS; the strong fluorescence of Nile Red dispersed in oil could be used to fluorescently track the LONDS, and also the *switch-off* of the fluorescent signal in water could be used as an indicator of the LONDS content release into an aqueous environment.

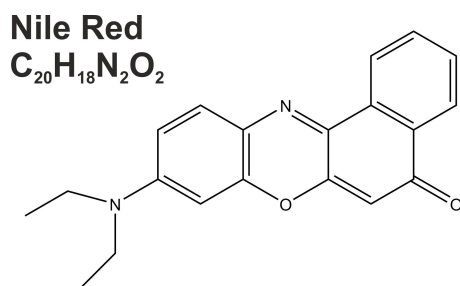


Figure 4.9: Molecular structure of the fluorophore Nile Red.

The solubility of Nile Red in the candidate oils was tested visually to determine which candidate oils were able to dissolve Nile Red whilst maintaining its fluorescence signal. Approximately 5 μg of Nile Red were added to each candidate oil and the samples were vortexed to assist the dispersion of the Nile Red. Nile Red was successfully incorporated into squalane, squalene, triacetin and tripropionin LOND samples. The fluorescence of Nile Red encapsulated in oils was only used as a method for LONDS tracking, thus quantitative studies of the Nile Red signal in all of the different candidate oils were not performed. To serve as an example, the absorptive properties of Nile Red in candidate oils was studied in tripropionin. The absorption spectrum of different concentrations of Nile Red in tripropionin were recorded, and are shown in figure 4.10a. As expected, the light absorption increased with the concentration of Nile Red in the oils, and it was possible to fit the absorbance intensity of $\lambda = 530$ nm to a linear regression, according to Beer's

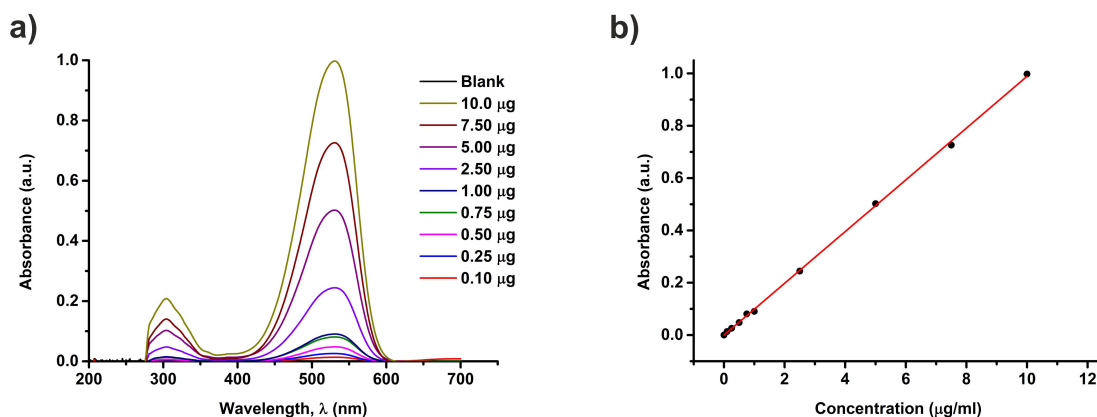


Figure 4.10: a) Absorption of Nile Red dissolved in tripropionin (in $\mu\text{g}/\text{ml}$). The maximum absorption is $\lambda = 530$ nm. b) Calibration curve for Nile Red dissolved in tripropionin. Each point corresponds to the maximum absorption of each Nile Red concentration at $\lambda = 530$ nm, fitted to a linear regression $y = (0.0989 \pm 0.0005)x$. From the fitting, the molar extinction coefficient of Nile Red in tripropionin was found to be $\epsilon = 3150$ m^2/mol .

Lambert law (equation 3.3). The molar extinction coefficient of Nile Red in tripropionin was also determined from the fitting, resulting $\epsilon = 3150$ m^2/mol .

4.3.3 Calcein AM

Calcein AM is a dye used in cell biology as a marker to differentiate viable from dead cells. The calcein AM molecules have the ability to cross cell membranes and become fluorescent when hydrolysed by cellular esterases in the cytoplasm of a live cell (figure 4.11). [226,227] The hydrophobicity of the acetomethoxy (AM) group makes Calcein AM difficult to dissolve in water, and therefore it is commonly dissolved in DMSO to perform cell assays. Calcein AM was chosen as a drug mimic due to its hydrophobicity, and also due to its fluorescence properties, which are only activated inside cells. Calcein AM encapsulated in the oil core of LONs could be used to study the release of the LONs contents, as the compound would only be fluorescent upon dispersion in the cytoplasm of a cell. Understanding the mechanism by which calcein AM is released from the LONs could help determine the pathways by which hydrophobic drugs would leave the LONs once they are inside the cell or its surroundings.

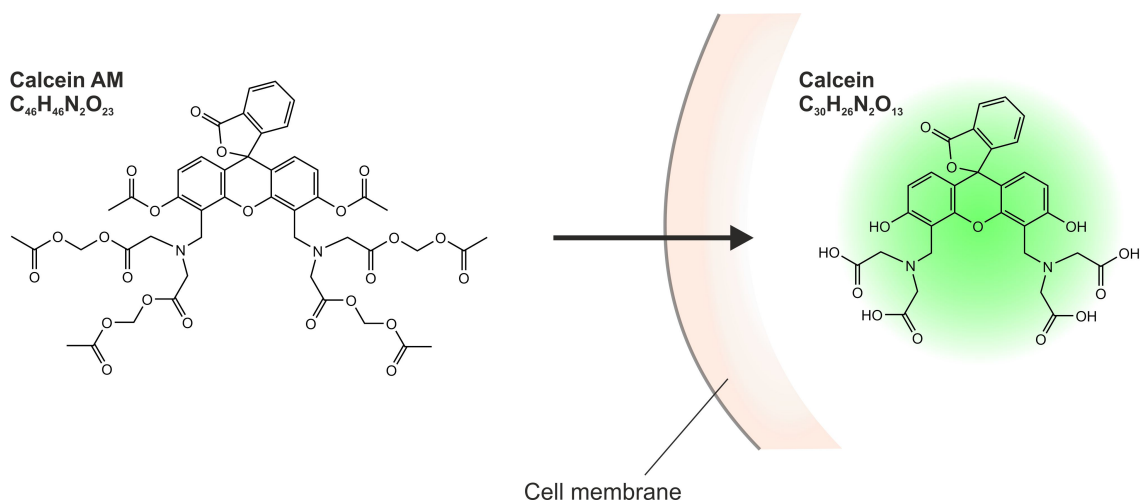


Figure 4.11: Calcein AM is a non-fluorescent molecule capable of crossing cell membranes. Once in the cytoplasm, cellular esterases hydrolyse calcein AM, resulting in fluorescent calcein. Once hydrolysed, calcein has emission/excitation at $\lambda_{ex} = 495$ nm and $\lambda_{em} = 516$ nm.

Investigating the solubility of calcein AM in all of the candidate oils was difficult due to the way the compound is supplied by the manufacturer. Calcein AM is provided as a dried, thin film in a small plastic vial that requires the addition of a suitable solvent. Calcein AM shows poor water solubility but is a relatively highly polar molecule, thus triacetin was chosen as the candidate oil to test the solubility of calcein AM. Figure 4.12a shows the absorption spectra for different concentrations of calcein AM in triacetin. Unlike other spectra shown previously (such as Nile Red in tripropionin, figure 4.10), calcein AM showed an absorption profile with two local maxima in the region $\lambda = 280 - 290$ nm. Due to the fact that absorption magnitude of the two was almost identical, $\lambda = 284$ nm was arbitrarily chosen as the maximum, and used to produce the calibration curve (figure 4.12), which fitted, as expected, to a linear regression. The molar extinction coefficient of calcein AM in triacetin was also determined from the fitting of the graph to the Beer-Lambert law (equation 3.3, with $L = 1$ cm), resulting $\epsilon = 340$ m²/mol.

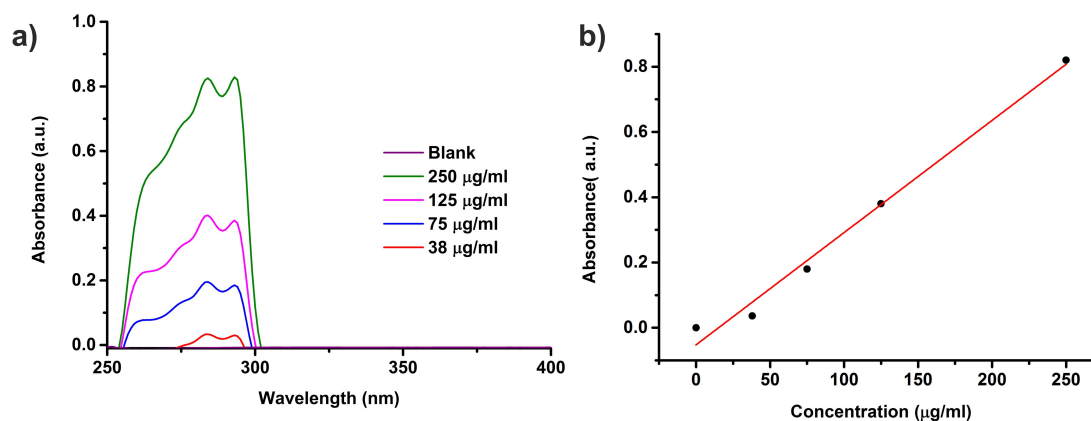


Figure 4.12: Calcein AM in triacetin. a) Absorption of calcein AM in triacetin, at different concentrations. b) Calibration curve for calcein AM dissolved in triacetin. Each point corresponds to the maximum absorption of each calcein AM concentration at $\lambda = 284$ nm, fitted to a linear regression $y = (3.4 \pm 0.2) \times 10^{-3}x$. From the fitting, the molar extinction coefficient of calcein AM in triacetin was determined to be $\epsilon = 340$ m²/mol.

The fluorescence profile shown in figure 4.12 suggests that calcein AM was dissolved by the triacetin. However it is important to note that the concentrations used to produce the absorption spectra, and subsequent calibration curve are calculated assuming that all the compound (1 mg) dissolved in 1 ml of triacetin. To compare to with the solubility of calcein AM in a different solvent, a series of dilutions of calcein AM in DMSO were prepared. Figure 4.13 shows the absorption spectra and calibration curve produced fitting the maximum absorption of the different calcein AM concentrations. Both figures 4.12a and 4.13a show absorption spectra with two local maxima. As for calcein AM in triacetin, the absorption at $\lambda = 285$ nm was used to produce the calibration curve, and this was used to estimate the molar extinction coefficient $\epsilon = 380$ m²/mol. Within experimental error, this value for ϵ is in agreement with that obtained for calcein AM in triacetin (see figure 4.12).

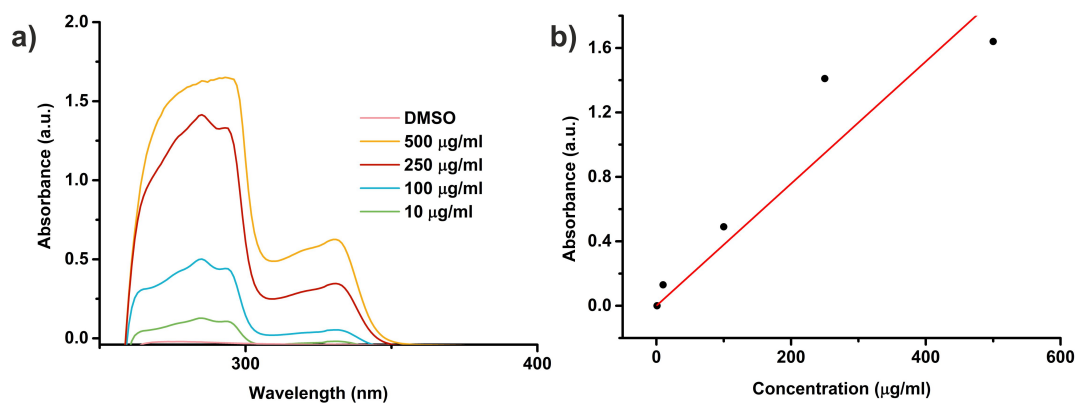


Figure 4.13: Calcein AM in DMSO. a) Absorption of calcein AM dissolved in DMSO, at different concentrations. b) Calibration curve for calcein AM in DMSO. Each point corresponds to the maximum absorption of each CA4 concentration at $\lambda = 285$ nm, fitted to a linear regression $y = (3.8 \pm 0.5) \times 10^{-3}x$. The molar extinction coefficient for this solution was found to be $\epsilon = 380$ m²/mol.

4.4 Drugs in candidate oils

Combretastatin A4 (CA4) and decitabine were the chosen hydrophobic drugs to test the encapsulation in LONDS. This section describes the study of the solubility and fluorescence properties of these drugs in the candidate oils.

4.4.1 Combretastatin A4

Combretastatin A4 (CA4) is a vascular disrupting agent, which selectively cause rapid shut down of established tumour vasculature. [228,229] The molecular structure of CA4 is shown in figure 4.14. CA4 exhibits low water solubility, which limits its bioavailability and makes *in vivo* anticancer treatments difficult. Strategies such as the development of water-soluble prodrug have been proposed. [230–232] CA4 has also been incorporated into carriers to improve *in vivo* delivery. [108,233]

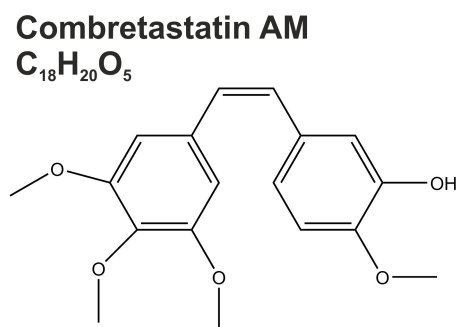


Figure 4.14: Molecular structure of Combretastatin A4.

The solubility of CA4 in the candidate oils was studied by adding 25 mg of CA4 to each oil and vortexing the solutions to assist the dispersion of the CA4. Upon visual inspection, CA4 crystals were seen at the bottom of the vials in all the oil the candidate oil, suggesting poor solubility of the drug. Thus the samples were bath sonicated for about 2 min and then vortexed again in an attempt to maximise the dissolution of the drug. At this stage, CA4 crystals had disappeared in the triacetin and tripropionin samples, whereas the drug remained insoluble in squalane and olive oil. The polarity of CA4 is the reason for the solubility differences in the different oils. The CA4 molecule contains polar regions within its structure, and therefore the number of dipole-dipole interactions created by the addition of triacetin is energetically favourable. However, squalane is a largely non-polar molecule (figure 4.1), and therefore no dipole-dipole interactions are formed when CA4 is contained in the oil. This is likely to make the dispersion of the drug in the oil energetically unfavourable. [221]

Following solubility tests of CA4 in the candidate oils only two, triacetin and tripropionin, emerged as viable oils for the formation of LONDS encapsulating CA4. For this reason, the absorption of CA4 in candidate oils was limited to triacetin and tripropionin. Figure 4.15 shows the absorption spectra of CA4 in triacetin, and a calibration curve produced fitting the absorption at $\lambda = 309$ nm against the concentration to a linear regression. Figure 4.16a shows the absorption spectrum of CA4 in tripropionin at different concentrations, and the calibration curve derived from it (figure 4.16b). A change in the absorption trend was found from 25 $\mu\text{g}/\text{ml}$ of CA4 in tripropionin, and therefore only data points below this concentration were used to produce the calibration curve in this case. This implies that only concentrations of CA4 in tripropionin in this concentration range could be accurately determined in further experiments aiming to use light absorption to measure drug concentration. Both figure 4.16a and b show an absorption profile capped at

around $\lambda = 250$ nm. This is probably due to an instrumental limitation, as the absorption of CA4 falls close to the detection limit of the instrument (around $\lambda = 250$ nm). The molar extinction coefficient for CA4 dissolved in triacetin and tripropionin were estimated from the fitting to the Beer-Lambert law, resulting $\epsilon = 907$ m²/mol and $\epsilon = 1190$ m²/mol.

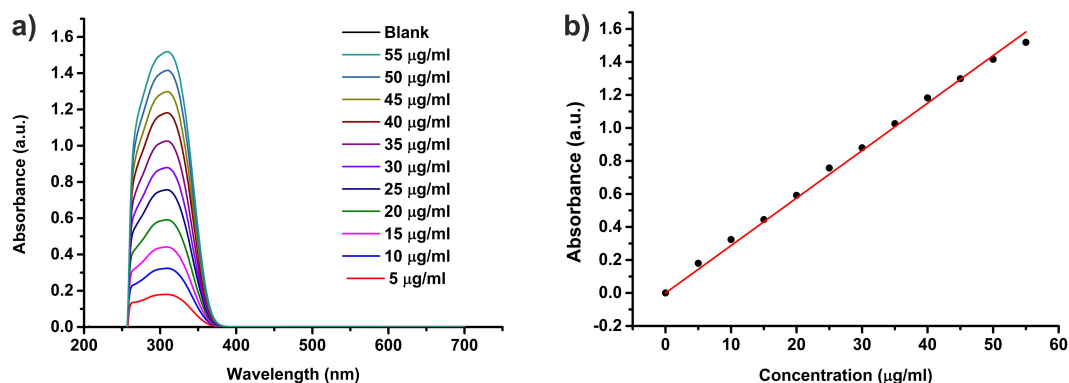


Figure 4.15: Combretastatin A4 (CA4) in triacetin. a) Absorption of CA4 dissolved in triacetin at different concentrations. b) Calibration curve for CA4 in triacetin. Each point corresponds to the maximum absorption of each CA4 concentration at $\lambda = 309$ nm, fitted to a linear regression $y = (0.0287 \pm 0.0003)x$. The molar extinction coefficient for this solution was determined from the fitting $\epsilon = 907$ m²/mol.

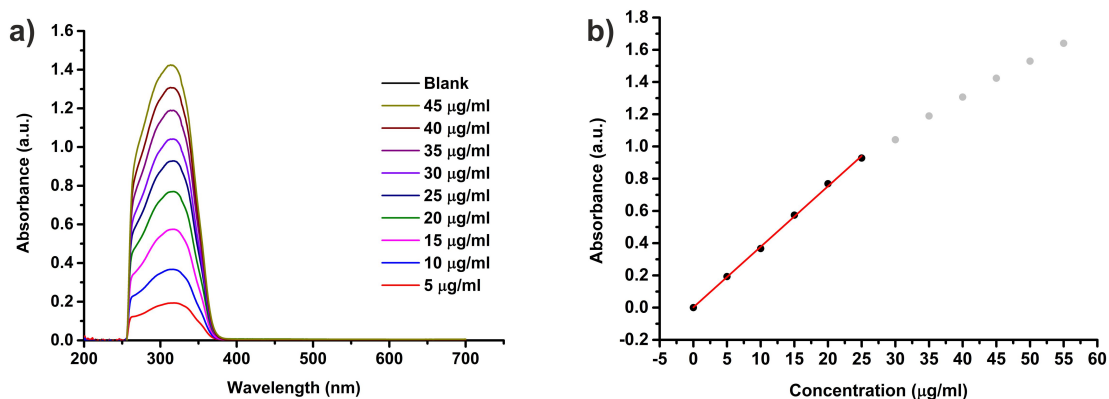


Figure 4.16: Combretastatin A4 (CA4) in tripropionin. a) Absorption of CA4 dissolved in tripropionin at different concentrations. b) Calibration curve for CA4 in tripropionin. Each point corresponds to the maximum absorption of each CA4 concentration at $\lambda = 312$ nm, fitted to a linear regression $y = (0.0377 \pm 0.0003)x$. Only the experimental points between 0 – 25 µg/ml were used for the fitting (shown in black, with the linear fitting superimposed.). The molar extinction coefficient for this solution was determined from the fitting $\epsilon = 1190$ m²/mol.

4.4.2 Decitabine

Decitabine is a drug that reactivates the expression of genes silenced by DNA hypermethylation, a process known to contribute to the transformation of cells into cancer cells. [234,235] The molecular structure of decitabine is shown in figure 4.17. Decitabine is soluble in water, but its stability is highly dependent on pH and temperature. [236] Patient treatment with decitabine requires of frequent, periodic administration, as the compound degrades quickly. [237] A few studies have investigated the effect in animals of low dose treatments with decitabine delivered using drug delivery systems such as liposomes and polymeric nanoparticles. [238, 239]

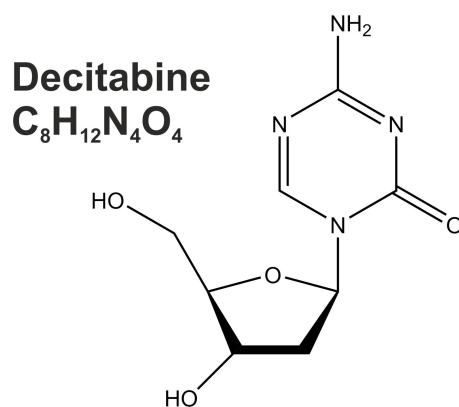


Figure 4.17: Molecular structure of decitabine.

In this study, decitabine was considered as a drug to be encapsulated in LONDs due to its reduced stability when dissolved in water. It was hoped that, by dissolving the decitabine in an oil and encapsulation in a LOND, it might be possible to enhance the stability of the compound compared to when dissolved in water. Drug dispersion in an oil and subsequent encapsulation in LONDs could prevent its degradation by reducing the condition changes to which unencapsulated decitabine is exposed to during a treatment. Due to its high polarity and water solubility, triacetin was chosen as candidate oil to test the solubility of decitabine. The concentration of the decitabine in triacetin was 5 mg/ml. The solution was vortexed and bath sonicated for short time periods to increase the dispersion of decitabine, after which all the macroscopic drug agglomerates disappeared. However, the solution remained cloudy, suggesting low solubility of the compound in triacetin. As described in previous sections, absorption spectra of different concentrations of decitabine in the oil were recorded using a spectrophotometer (section 3.3.2, page 32). The solution

was kept in ice to prevent the degradation of the drug in triacetin, if this occurs. Figure 4.18a shows the absorption spectra of different concentrations of decitabine dissolved in triacetin. All the absorption spectra showed a maximum absorption at $\lambda = 267$ nm, and also a large amount of background absorption or light scattering by the solution. This points at drug agglomerates in the solution, which scatter a large fraction of the light passing through the cuvette. Light scattering results in a reduction of the radiant power recorded by the detector, which then translates into a broad-band absorption reading, far from the absorption wavelength of the drug. From the data shown in figure 4.18a, a calibration curve was produced, plotting the maximum absorption at $\lambda = 267$ nm against the concentration of the decitabine in the solution. This plot was fitted to a linear regression (figure 4.18b). The value for the molar extinction coefficient in this case was found to be $\epsilon = 52440$ m²/mol, suggesting strong light scattering.

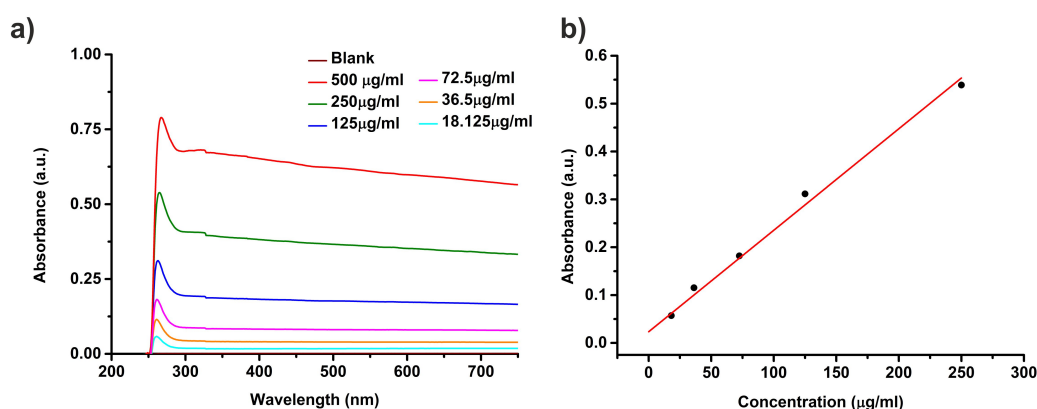


Figure 4.18: Decitabine in triacetin. a) Absorption of decitabine dissolved in triacetin at different concentrations. b) Calibration curve for decitabine in triacetin. Each point corresponds to the maximum absorption of each CA4 concentration at $\lambda = 267$ nm, fitted to a linear regression $y = (2.3 \pm 0.1)x$. The molar extinction coefficient was found to be $\epsilon = 52440$ m²/mol.

DMSO was used to obtain an absorption spectra to compare to the absorption spectra of decitabine in triacetin. Figure 4.19 shows the absorption of different concentrations of decitabine in DMSO, and the calibration curve produced by plotting the maximum absorption against the concentration. The maximum absorption in the spectra shown in figure 4.19 shifted towards smaller wavelengths as the concentration of decitabine was reduced. The peak for the absorption spectrum of 1000 $\mu\text{g}/\text{ml}$ decitabine was found at $\lambda = 278$ nm, whereas the maximum absorption of decitabine at 18 $\mu\text{g}/\text{ml}$ was found at $\lambda = 264$ nm. This is likely to be an artifact created by the detection limit of the instrument, which is at around $\lambda = 250$ nm, or a slight change of the refractive index of

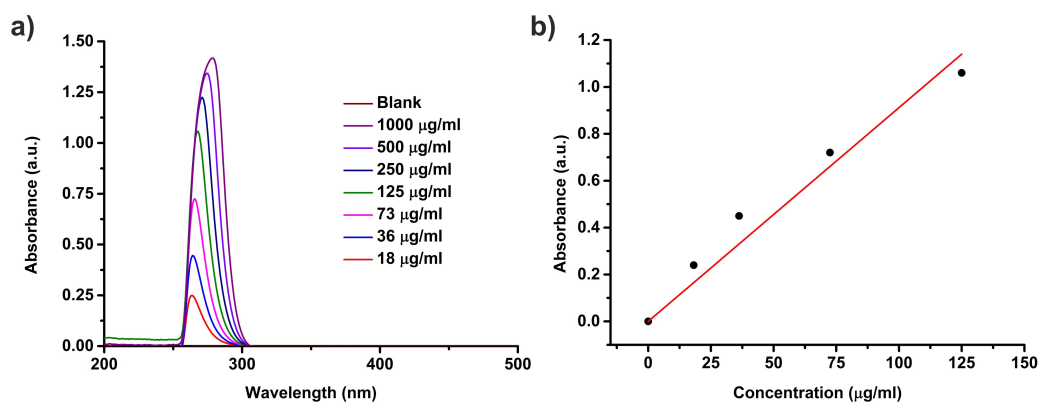


Figure 4.19: Decitabine DMSO. a) Absorption of decitabine dissolved in DMSO at different concentrations. b) Calibration curve for decitabine in DMSO. Each point corresponds to the maximum absorption of each CA4 concentration at, fitted to a linear regression $y = (9.1 \pm 0.6)x$. The molar extinction coefficient of decitabine dissolved in DMSO was found to be $\epsilon = 207500 \text{ m}^2/\text{mol}$.

the solution due to the high concentration of the CA4. [240]

The data shown in this section suggests that decitabine does not dissolve in triacetin as desired; the presence of large drug agglomerates could explain the light scattering detected in the absorption spectrum of the drug in triacetin (figure 4.18a), thus pointing at poor solubility of decitabine in triacetin. Furthermore, decitabine is reportedly water soluble, [234] which could lead to problems when trying to encapsulate it in LONDS dispersed in an aqueous solution (such as PBS). These reasons led to dismissal of decitabine as a model drug for LOND encapsulation, and no further experiments were performed with this compound.

4.5 Discussion

One of the objectives of this project was to use LONDS as capsules for hydrophobic drugs. The drugs would be contained in the oil core of the LONDS, keeping the hydrophobic molecules dispersed and retaining their functionality. Unambiguous identification of light emission and absorption from added fluorophores and of the candidate oils was crucial, as the determination of the concentration of a drug encapsulated within the LONDS rely on the absorptive properties of the encapsulated substances. Furthermore, the fluorescence tracking of LONDS is subjected to the fluorescent properties of incorporated fluorophores.

In an effort to characterise the luminescent properties of the candidate oils, their light

absorption and emission spectra were studied (section 4.2). The candidate oils were found to absorb light in the UV range, probably due to the presence of oxidative products and impurities. Similarly, the candidate oils showed autofluorescence when excited with $\lambda_{ex} < 400$ nm, except for EPA, that showed a maximum emission intensity when excited with $\lambda_{ex} = 550$ nm. The fluorescently labelled phospholipids used within this project, Atto 590 DOPE ($\lambda_{ex} = 593$ nm, $\lambda_{em} = 622$ nm) and Atto 488 DOPE ($\lambda_{ex} = 500$ nm, $\lambda_{em} = 520$ nm), exhibited excitation and emission wavelengths far from those of the oils. Besides this, the fluorescent signal from these fluorophores was expected to be significantly stronger than the autofluorescence of the oils.

Qdots and the fluorescent dye Nile Red were chosen as drug mimics. Qdots were prepared increasing the incubation time in an attempt to shift their emission wavelengths towards the near infrared, and coated with dodecanethiol to enhance their hydrophobicity. The emission, absorption and excitation spectra of the Qdots were obtained using an UV-VIS. The data was used to estimate the size and concentration of the Qdots, as previously described. [180] Qdots were found to have a diameter $d = 7.37$ nm and a concentration $C = 1.70$ μ M. The size estimate for these Qdots is larger than what is typically reported for CIS/ZNs Qdots prepared following this protocol ($\sim 3 - 4$ nm), which suggests that the increased incubation times during the synthesis had the desired effect on the size of the Qdots. Qdots were found to dissolve in squalane, squalene and IPA, but impossible to dissolve in triacetin, probably due to the non-polarity of the dodecanethiol coating and the strong polarity of the triacetin molecules. Qdots absorption and emission fall far from the absorption and emission wavelengths of the candidate oils. The signals from the Qdots should be unambiguously differentiable from the oil signal (section 4.2).

Combretastatin A4 (CA4) and decitabine were chosen as hydrophobic drugs for encapsulation in LONDS. CA4 is a lipophilic drug that exhibits poor water solubility, and it is commonly administered dissolved in DMSO. [241] CA4 was found to dissolve in triacetin and tripropionin, and calibration curves for different concentrations of the drug in the two oils were obtained. These were to assist determining the concentration of CA4 in LONDS. Decitabine is a water soluble epigenetic drug which is soluble in water, which reduced stability when in solution. It was hoped that the encapsulation of the compound in a LOND hydrophobic core would contribute to enhancing its stability. Triacetin was used to solubilise the compound. The light absorption data for this mixture showed strong background scattering, suggesting the presence of agglomerates in the solution. This poin-

ted at poor dispersion of decitabine in triacetin, which eventually led to discarding this drug as a candidate for LOND encapsulation.

The study of the solubility of the drug mimics and hydrophobic drugs in the candidate oils showed challenging. Although *a priori* the *hydrophobicity* of compounds was assumed to permit easy solubilisation in an oil-like solvent, the dispersion of the compounds in the candidate oils was found to depend strongly on the polarity of both the compound and the oil. Polar oils, such is the case of triacetin and tripropionin, were more efficient at dissolving polar compounds (such as Calcein AM and CA4). The non-polar oil squalane was found to be a good solvent for non-polar dodecanethiol-coated Qdots, but the dispersion of the hydrophobic drugs in this oil was impossible. The ability of triacetin first, and then tripropionin, to dissolve the model hydrophobic drugs directed the work done in this project.

Chapter 5

Topic: Lipid Oil Nanodroplets

This chapter presents the results relating to the production and characterisation of lipid oil nanodroplets (LONDs). The chapter discusses LOND production in a two-step process that includes ultra-high pressure homogenisation of oil-in-water mixtures. LONDs were prepared using different candidate oils, lipid coatings and production pressures. The LONDs were characterised in terms of their size, concentration and stability over time.

5.1 LONDs production in a two-step homogenisation process

This section describes the formation of LONDs, in a two-step homogenisation of oil-in-water mixtures containing lipid. This process is shown schematically in figure 5.1.

The LOND preparation procedure was initiated by preparing the lipids, which act as stabiliser of the oil nanodroplets. All lipid mixtures were prepared as described earlier (section 3.1, page 27). Fluorescent lipid was added to the lipid mix when fluorescence tracking of the LOND shell was required. After removal of the methanol:chloroform, the lipids were re-suspended in 0.7 ml of oil by vortexing and bath-sonication, achieving lipid resuspension in around 10 min. For samples encapsulating drugs or drug mimics, the compound was solubilised in the oil to the desired concentration before adding it to the lipids. Once the lipid was fully resuspended in the oil, PBS was added to the oil-lipid mixture, to make a 4 ml final volume.

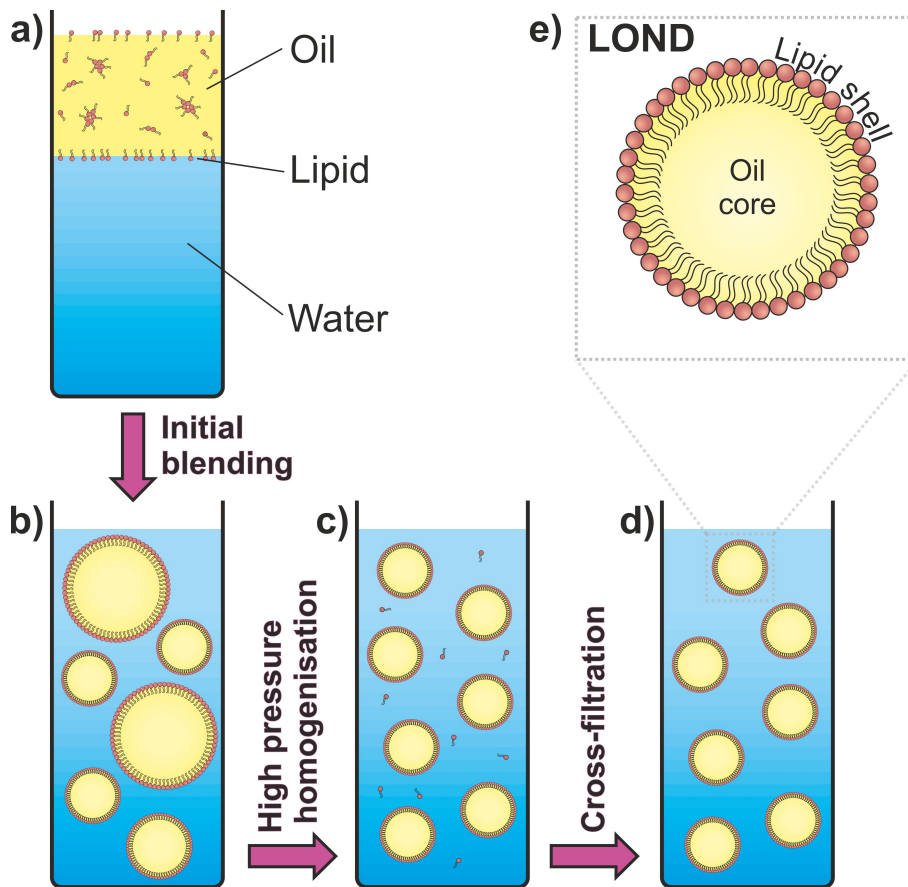


Figure 5.1: LOND production is a two-step homogenisation process started with blending of oil-in-water and lipid mixtures using a Polytron (a to b), followed by a high pressure homogenisation process in an Emulsiflex (b to c). Cross-filtration was used to remove excess lipid in the solution after preparation (c to d). e) LONDS are oil droplets stabilised with a lipid shell, dispersed in water.

The homogenisation process was started with an initial blending step using a Polytron (figure 5.1a to b). Rotor-stator systems (section 2.2.3.1, page 20) have been reported to be less efficient than high pressure homogenisation in oil-in-water droplet disruption, [155] and therefore this step in LOND preparation was only used to roughly mix the oil-water emulsion (see section 2.2.3.1, page 20). This step also aided dissolution of bigger lipid agglomerates. Polytron blending of the sample was carried out at 12500 rpm for 10 min, at 40 °C under atmospheric pressure. Then 6 ml of PBS were added to the solution to make 10 ml final volume.

The second step in the LOND formation process consisted of a fine homogenisation of the oil-in-water mixture using an Emulsiflex (section 2.2.3.2, page 21). This process reduces the size of the LONDS in the solution and improves size homogeneity (figure 5.1b to c). The outlet of the Emulsiflex was kept at 4 °C to avoid emulsion overheating. The sample was emulsified for 20 min, during which the sample volume passed multiple times

through the homogenising nozzle.

LONDS preparation was finished with a washing step to remove excess lipid (also fluorescent dye and/or drug when applicable) from the solution (figure 5.1c to d). The washing was done by cross-filtration, a technique in which the sample moves tangentially to the filter (figure 5.2). Particles smaller than the pore size of the filter permeate out of the moving liquid whereas bigger particles are retained and continue circulating. The cross-filtration set-up used in these experiments uses columns in which the liquid moves vertically from bottom to top. Hollow fibers surround the inside of the tube, and act as a barrier for the bigger particles (> 60 kDa). The LOND solution was flowed at 40 ml/min through the column for at least 2 h.

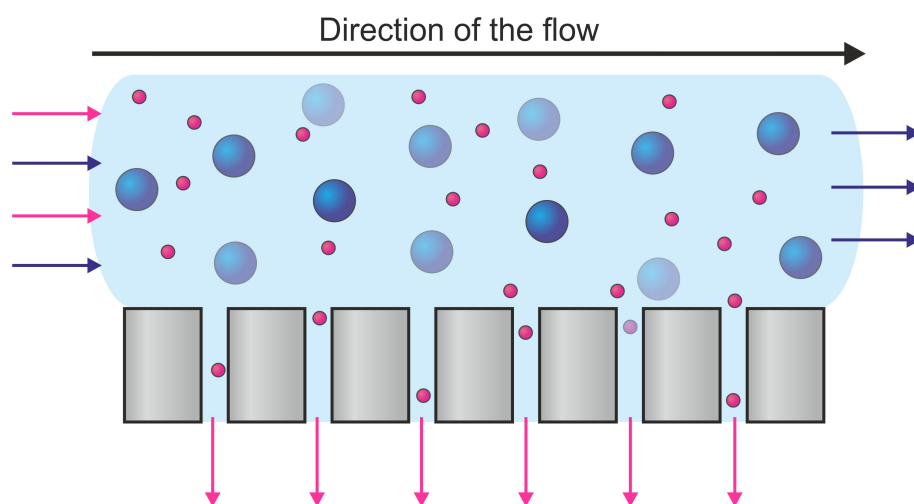


Figure 5.2: Schematic showing the functioning of a cross-filtration column. The solution moves tangentially to the filter, which acts as a barrier for larger particles such as LONDS, shown in blue, whilst the smaller ones, shown in pink, can permeate (i.e. excess lipid, unencapsulated drug).

5.1.1 Sterility of LOND samples

Sterility is a requirement for LOND samples to be used in experiments with cells *in vitro* or for *in vivo* testing. In these cases some of the preparation steps were performed in a Class II Biosafety Cabinet, including the preparation of the lipid mixtures, addition of oil and addition of PBS (section 3.8, page 46). As an alternative to the cross-filtration step, dialysis was used in some cases in which sterility was crucial, as the set-up for this filtration technique can be fully carried on inside the Biosafety Cabinet. For sample dialysis, dialysis tubes with 8 kDa cut-off were used. The tubes were filled with 4 ml of

the LOND solution, firmly closed and turned up-side-down inside a beaker containing 1 l of PBS. A magnetic stirrer was used to agitate the solution and hence maximise the liquid exchange between the dialysis tube and the surroundings. LOND samples were dialysed at 4 °C overnight. After dialysis an extra filtration step through a 200 nm syringe filter was used to remove any bacteria in the solution. [46]

Absence of bacteria was regularly tested by incubating 10 μ l of LONDS in 5 ml of DMEM with 5% fetal bovine serum (FBS) and enriched with L-Glutamine 200 mM at 37 °C for 48 h. Turbidity of the DMEM after the incubation time indicated bacterial growth. Alternatively, the sterility of LOND samples was tested by plating 10 μ l of LOND sample on an agar plate containing LB Broth, and incubated at 37 °C for 48 h. The presence of bacteria in the LOND samples translated into growth of bacterial colonies on the plate. Figure 5.3 shows an example of agar plates incubated with LONDS. Bacterial colonies appeared as dark yellow circles, visible by eye. In contrast, sterile LOND samples did not grow any bacterial colonies during incubation time.

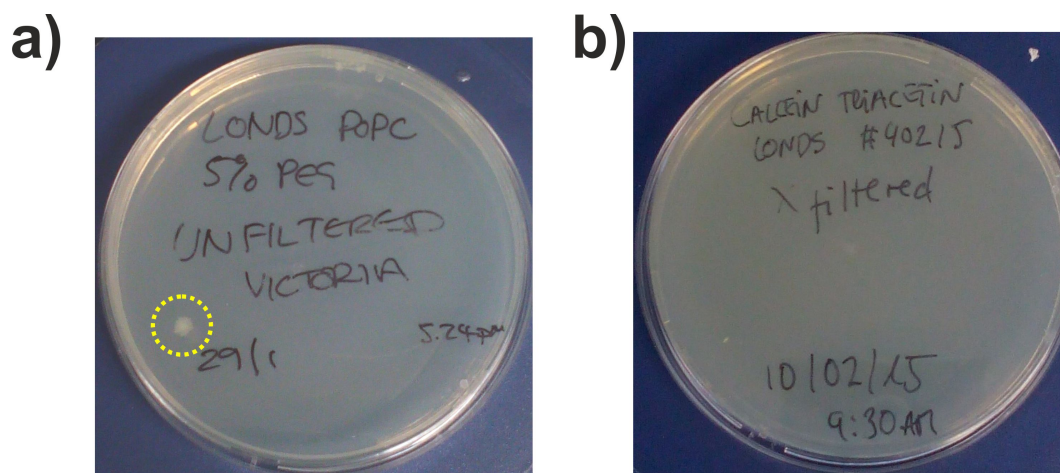


Figure 5.3: Two examples of agar LB Broth plates used to test the sterility of LOND samples. After LOND plating, the samples were incubated at 37 °C for 48 h. a) Shows an infected LOND sample. A bacterial colony, marked with a dotted yellow line, was observed after the incubation time. b) Sterile LOND sample, in which no bacterial colonies grew, under the same conditions.

5.2 Preliminary observations

The formation of LONDS was attempted with with all of the candidate oils (figure 4.1, page 49). Following early results, a number of decisions were made regarding the choice

of oils:

- EPA and isoamyl acetate were found to form LONDS that destabilised quickly after preparation. Oil accumulated on the walls of the tube that contained the sample, which was suspected to be due to droplet coalescence. These two candidate oils were discarded, and no further experiments were performed with them.
- Squalane, squalene, olive oil, triacetin and tripropionin were found to form stable LONDS when following the two-step homogenisation process described above. Except for triacetin oil, these oils were found to form nanoemulsions with bright white appearance, which is characteristic of emulsions in which the relative size polydispersity of the oil droplets scatters a wide range of wavelengths. [242] Due to the similarities between squalane and squalene, squalane was chosen over squalene due to its better stability and resistance to auto-oxidation. [243] Therefore squalene LONDS were only used in preliminary experiments. Triacetin LONDS showed in general larger polydispersity and lower concentration than the other LOND samples, differences that were attributed to high solubility of triacetin in water. Importantly, triacetin was found to not to form stable LONDS when only POPC was used to stabilise the oil. In fact, triacetin (together with other short-chain triglycerides) has been previously reported to form unstable when a combination of PC lipid and polysorbate 80 was used as stabiliser. [244] Hence, all triacetin LONDS prepared within this report included 5% PEG2000-DSPE or 5% biotin-PEG2000-DSPE in their shells.

It is important to note that the oil choice for LONDS formation was strongly affected by the solubility of the model hydrophobic drugs in the oils. CA4 showed very poor solubility in squalane, and therefore encapsulation of the drug in this type of LONDS was unsuitable. Hence, triacetin was used to form all the LONDS encapsulating CA4. Towards the end of the project, tripropionin was also introduced as carrier oil. LONDS formed with tripropionin showed excellent size and concentration characteristics, that together with the ability to dissolve CA4, made this oil a promising candidate for the delivery of CA4. The lipid shell for encapsulating tripropionin was modified, with respect to the lipid shell regularly used to encapsulate other candidate oils. The reason for this was a rapid LOND destabilisation (spanning hours) observed when POPC only was used to form tripropionin LONDS. Hence, POPC was substituted by DSPC, which has higher gel to liquid phase transition temperature compared to POPC (55 °C versus -2 °C).

This implies that DSPC is at its gel phase at room temperature, thus its diffusion in the LOND shell is slower, which translates into a more rigid coating that could reduce oil leakage. Also 20% cholesterol was added to the lipid shell composition, as it is known to reduce permeability and increase the stability of lipid nanocarriers. [245] Unfortunately, only a small number of experiments have been performed with tripropionin due to its late inclusion as a candidate oil and time restrictions of the project.

Within this project, squalane and triacetin LONDS were used as model LOND samples. Some results concerning tripropionin LONDS will also be shown in this chapter, as well as a smaller dataset for squalene LONDS.

5.3 LOND size measurements

Size is a critical characteristic of the LONDS if they are to find a clinical application. LONDS with larger diameters may be able to transport larger drug amounts, but they may be, for example, more difficult to deliver *in vivo*. [246] The aim of this research was to combine LONDS with MBs into a novel MB-LOND architecture. The number of LONDS that a MB would be capable of transporting directly relates to the size of both the MB and the LONDS. This can be estimated from geometrical factors (i.e the surface area of the MB, and the cross-section of the LONDS), resulting $N = 4 \left(\frac{d}{a}\right)^2$, with N the number of LONDS per MB, d the diameter of the MB and a the diameter of the LONDS. Figure 5.4a

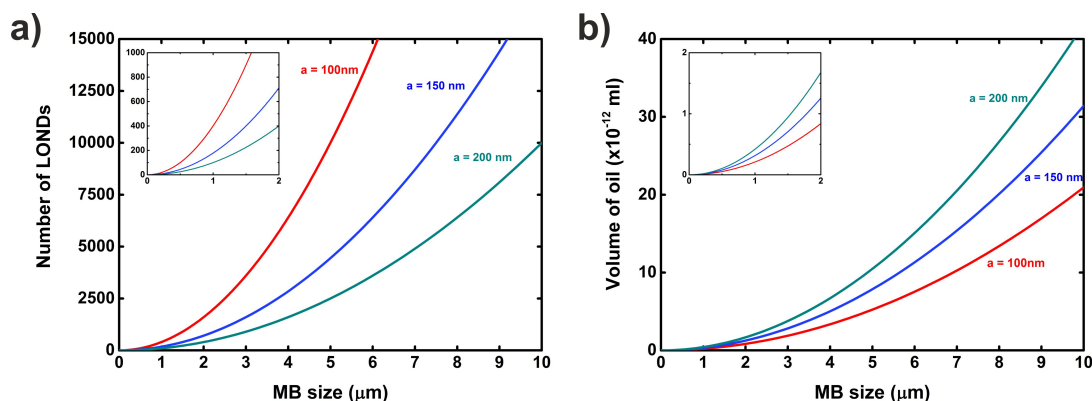


Figure 5.4: a) The number of LONDS that a single MB can transport depends on the dimensions of both the MB and the LONDS. From geometrical considerations, and assuming that LONDS cover 100% of the MB surface, this relationship is given by $N = 4 \left(\frac{d}{a}\right)^2$. b) The volume of the oil that the MB is able to transport is given by the number of LONDS attached to its shell, as $V = \frac{2}{3}\pi d^2 a$.

shows the number of LONDS that can be transported by a MB according to its diameter, for three different LOND sizes. This estimation assumes that all LONDS have the same size, and that they cover 100% of the MB surface area. The volume of oil that a MB can transport is defined by the number of LONDS attached to its shell, and can be expressed as $V = \frac{2}{3}\pi d^2 a$. Figure 5.4b shows the dependence of the oil volume that a MB can carry as a function of its size, for three different LOND diameters.

This section presents three short studies that aimed to better understand the role of different variables in LONDS size, namely: homogenisation pressure, lipid shell composition and oil core. LOND sizes were measured using three different techniques (section 3.5, page 34): DLS using a ZetaSizer, tunable resistive pulse sensing using a qNano, and single particle tracking using a NanoSight instrument. These techniques have different advantages and disadvantages. For example, DLS has an easy, user friendly, interface and provides quick measurements. However, DLS results are not reliable for samples with high size polydispersity. In these cases, NanoSight or qNano would provide a much accurate sizing result¹.

5.3.1 LONDS size change throughout preparation

LOND samples were sized at each step of production, to understand size refinement throughout the homogenisation process (i.e. blending and subsequent ultra-high pressure homogenisation). Figure 5.5 shows the DLS size distribution of squalane and triacetin LONDS coated with POPC and 5% biotin-PEG2000-DSPE, shown as the variation of intensity scattered from the sample. The initial blending using a polytron resulted in a sample with high size polydispersity (figure 5.5a and d). This figure indicates that, although the initial blending assists dissolving macroscopic lipid agglomerates, it does not produce droplets with uniform size and in the nanometer range. It is important to note that the high polydispersity index of the sample at this stage (PI \sim 0.9 for squalane LONDS, PI \sim 0.6 for triacetin LONDS) made cumulant-based evaluation of the DLS data impossible. This meant that no quantitative data could be obtained from this graph, and it was only used for qualitative analysis.

In the case of squalane LONDS, subsequent ultra-high pressure (175 MPa) homogenisation using an Emulsiflex (figure 5.5b) led to a LOND sample with improved size

¹NanoSight and qNano also provide a measurement of the concentration of the LONDS in the solution.

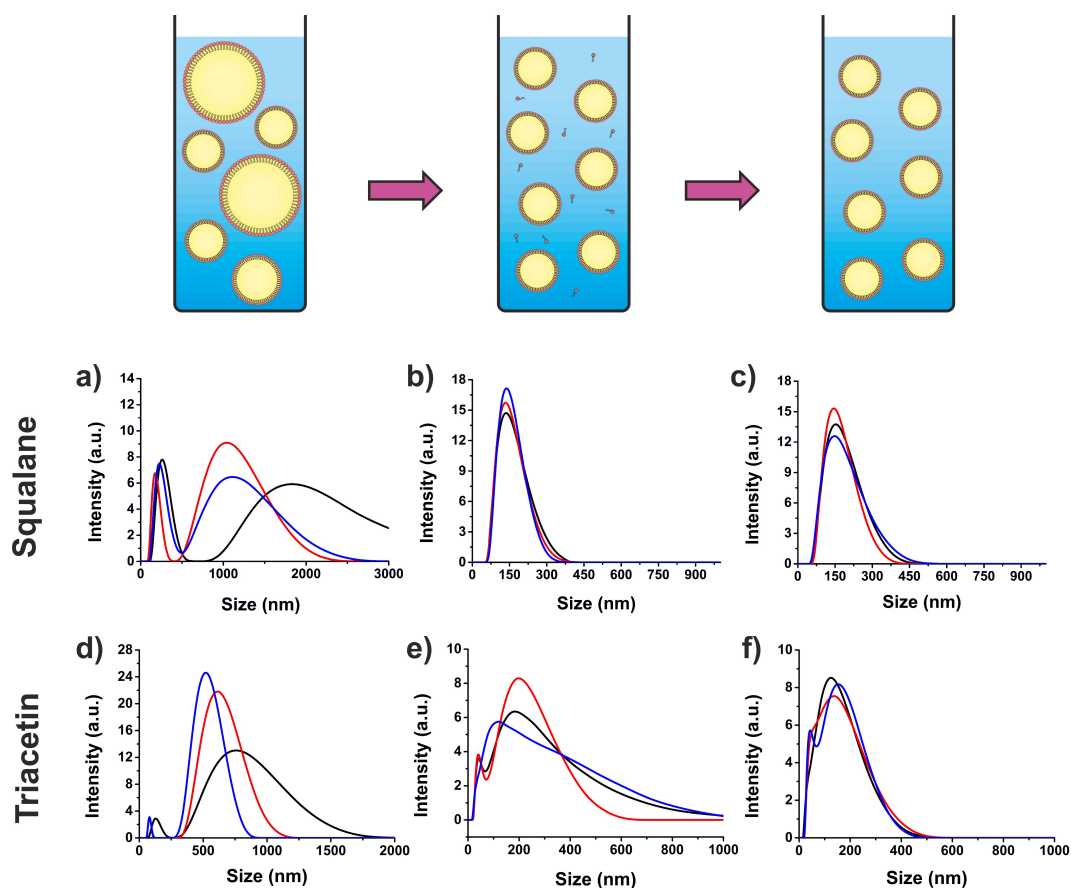


Figure 5.5: Size distribution of squalane and triacetin LONDS throughout the two-step preparation process. The lipid shell of these LONDS was POPC and 5% biotin-PEG2000-DSPE. The insets show schematically the production stage to which the size distributions correspond. Size distribution of the squalane LONDS a) after initial blending, b) after ultra-high pressure homogenisation, and c) after cross-filtration. Size distribution of the triacetin LONDS d) after initial blending, e) after ultra-high pressure homogenisation, and f) after cross-filtration.

monodispersity. This figure shows three size measurements of the same sample; all three show the same size distribution with average size at (142 ± 9) nm, demonstrating repeatability of the measurements. The mode size increased slightly after filtration, to (165 ± 4) nm (figure 5.5c). This apparent size change of about 9% could be due to the removal of small lipid aggregates from the mixture. This size change was accompanied by a spread in the size distribution, which could indicate that cross-filtration gave rise to mild sample coalescence. It was noted from the results shown in figure 5.5 that high-pressure homogenisation was necessary to obtain a fine nanoemulsion, with oil droplets ranging 100 – 300 nm.

For triacetin LONDS, high pressure homogenisation refined the mode size of the droplets to < 200 nm (figure 5.5e). The mode size of this LOND sample was (166 ± 40) nm. It is important to note that, unlike squalane LONDS, the three measurement runs on this sample were significantly different, pointing towards a large size polydispersity

of the LONDS. Cross-filtration reduced the size distribution of the sample, with mode at (116 ± 15) nm (figure 5.5f), which was a reduction of about 30%. The average size of this LOND sample was also significantly reduced compared to the unfiltered sample, around 43%, from 306 nm to 173 nm. However, it should be noted that the polydispersity of the sample was reduced through cross-filtration, which is supported by the improved coincidence of the three measurement runs performed on this sample. The substantial difference in the LONDS size distribution difference could be due the dissolution of larger oil droplets during cross-filtration, due to the high solubility of triacetin in water. Given that the experimental conditions under which these triacetin LONDS were identical to those under which the squalane LOND sample were prepared, these results suggest that the oil plays an important role in the characteristics of the LONDS. This effect has been studied in more detail and the results will be presented later on in this chapter.

5.3.2 The effect of pressure on LONDS size

The pressure applied during the homogenisation process is the most important variable affecting the size of the LONDS. [134] If the LONDS are to be combined with MBs to build more complex architectures, they would ideally have diameters ~ 200 nm or lower. To study size changes of LONDS produced at different pressures, two LOND samples were studied: a squalane LOND sample stabilised with POPC, and a tripropionin LOND sample with a POPC + 20% cholesterol + 5% biotin-PEG2000-DSPE shell. Small sample aliquots were taken after 10 min homogenisation at pressures between 35, 70, 105, 140 and 175 MPa. Size variation between the LONDS in a given sample could be significant at low production pressures, thus the samples were sized using both NanoSight and DLS to compare both techniques; whereas DLS is based on the scattering of light from the whole sample, NanoSight relies on individual particle tracking and therefore it is more sensitive to size polydispersity. [187, 247]

Figure 5.6a shows the average size of squalane and tripropionin LOND samples prepared under different pressures, as determined by DLS. As expected, the average LOND size decreased as the production pressure was increased. This is consistent with observations for different oils (and surfactants). [165, 166, 168, 248] The experimental points for squalane LONDS were fitted to $y = C \cdot x^b$ (equation 2.19), whereas the data for tripropionin LONDS was fitted to a linear regression. For squalane LONDS, the values of the

parameters C and b were determined from the fitting, resulting in $C = (8 \pm 2) \times 10^3$ nm/MPa, and $b = -0.70 \pm 0.06$. This is in agreement with previous observations, which reported values of b between 0.6 and 0.75 for production regimes dominated by inertial or shear forces, respectively. [135,155] This suggests that LOND production in the Emulsiflex holds likeness to other high pressure homogenising processes for nanoemulsion manufacturing. The average size of the squalane LONDS produced at 175 MPa was (215 ± 34) nm, and (92 ± 11) nm in the case of tripropionin LONDS. Figure 5.6b shows the PI values for the samples prepared under different pressures. The graph was fitted as a guide to the eye. For squalane LONDS, there is a significant drop of the PI between the sample prepared under 35 MPa and 70 MPa of about 40%. This shows that LONDS prepared under 35 MPa have broad size distribution, which is quickly refined when the production pressure is increased. The PI values reached a plateau for production pressures > 35 MPa, suggesting that there was not a significant improvement of the size distribution between 70 – 175 MPa. The average size of LONDS prepared at 175 MPa, together with the relatively low $PI = 0.15$ of the sample at this stage, support the use of LONDS produced under these conditions. Thus, and as mentioned above, after optimisation, LONDS produced within this project were prepared at 175 MPa. The PI for tripropionin LONDS was reduced by 18% throughout the studied pressure range. This change suggests moderate improvement of the monodispersity of the sample through the process, and points at high size monodispersity of the sample even when produced under the lower pressures (35, 70 MPa)

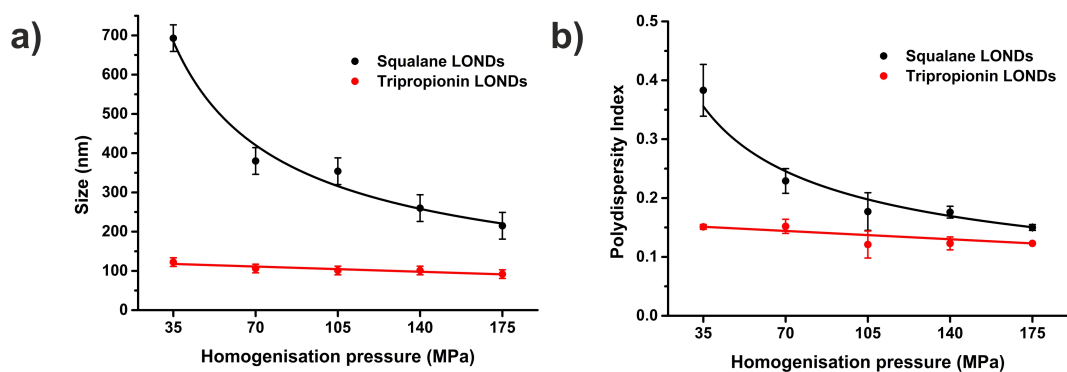


Figure 5.6: DLS sizing of LOND samples prepared under different pressures. Squalane LONDS were stabilised with POPC, and tripropionin LONDS were stabilised with POPC + 20% cholesterol + 5% biotin-PEG2000-DSPE. a) Average size of LOND samples at different production pressures. The data points for squalane LONDS were fitted to $y = C \cdot x^b$, and to a linear regression for tripropionin LONDS. b) Change in the PI with increasing production pressure. Fitting intends to be a guide to the eye.

Figure 5.7 shows the size data obtained with the NanoSight instrument. As for DLS, the size of the LONDS was observed to decrease upon increasing the production pressure. In a similar fashion as with the DLS results, the data points for squalane LONDS were fitted to equation 2.19, with $C = (7 \pm 2) \times 10^3$ nm/MPa and $b = -0.71 \pm 0.05$, as determined from the fitting. The value for b is in agreement with the literature, [155] and it is also in agreement with the value for b from the fitting of the DLS data points, within experimental error. The average squalane LOND size produced at 35 MPa was (550 ± 40) nm, which is much higher than LONDS produced under any other conditions and supports the observations made with DLS (figure 5.6). The large average sizes recorded for squalane LONDS prepared under 35 MPa suggests that this specific pressure does not suffice to create LONDS with the desired diameter (~ 200 nm). Besides this, and considering the PI value provided from DLS for this same sample, this lower production pressure does not provide LOND samples with monodisperse sizes. Similarly to what was observed for DLS sizing, the size of the LONDS reached a plateau at production pressures > 35 MPa. In the case of tripropionin LONDS, the experimental points were fitted to a linear regression. Increasing pressures between 30 – 140 MPa produced only a modest decrease of the LOND size ($\sim 3\%$).

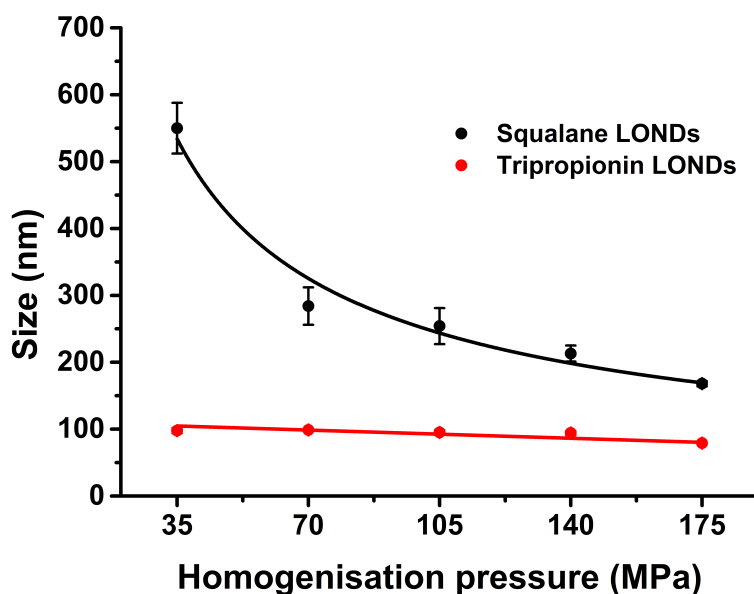


Figure 5.7: Sizing of squalane and tripropionin LOND samples produced under different pressures, using the NanoSight instrument. The data points for squalane LONDS were fitted to $y = C \cdot x^b$ (equation 2.19), and a to linear regression for tripropionin LONDS.

The size changes observed in figures 5.6 and 5.7 suggest that tripropionin LONDS reached an optimum state even at lower production pressures, and that further sample

processing did not have a significant effect on its size distribution. This points at higher deformability of the tripropionin LONDS, as smaller LOND sizes can be achieved with relatively low pressures, which could be attributed to the lower viscosity of the tripropionin compared to squalane. Furthermore the differences in the lipid shell (i.e. the presence of the cholesterol and the pegylated lipid in the case of tripropionin LONDS) could contribute to a more rapid stabilisation in the case of tripropionin, thus preventing re-coalescence of the oil at the homogenising nozzle.

5.3.3 The role of the lipid shell on LONDS size

The presence of a surfactant in the solution is crucial for the formation of a stable emulsion and its properties have a strong influence in this process, as they determine the interfacial tension of the droplets. [41, 249–251] LONDS were aimed at forming a new vehicle for hydrophobic drug delivery, via their attachment to the shell of MBs. Hence the lipid shell of the LONDS was expected to include, for example, phospholipids to allow for specific binding between the LONDS and the MBs, such as biotinylated ones, or pegylated lipids, to enhance LOND biocompatibility and potentially their stability. [10] To anticipate the likely variation of LOND shell lipid composition, and to study possible effects of the lipid shell on the size of LOND samples, four squalane LOND samples with different lipid shells were prepared. The lipid shells were: 1) POPC, 2) POPC + 5% biotin-DOPE, 3) POPC + 5% PEG2000-DSPE, and 4) POPC + 5% biotin-PEG2000-DSPE. The ultra-high pressure homogenisation step was performed at 175 MPa for all of the samples. The samples were sized with DLS, and the results are shown in figure 5.8. Each size distribution is the result of three size measurements performed on the same sample. The standard deviation of is shaded.

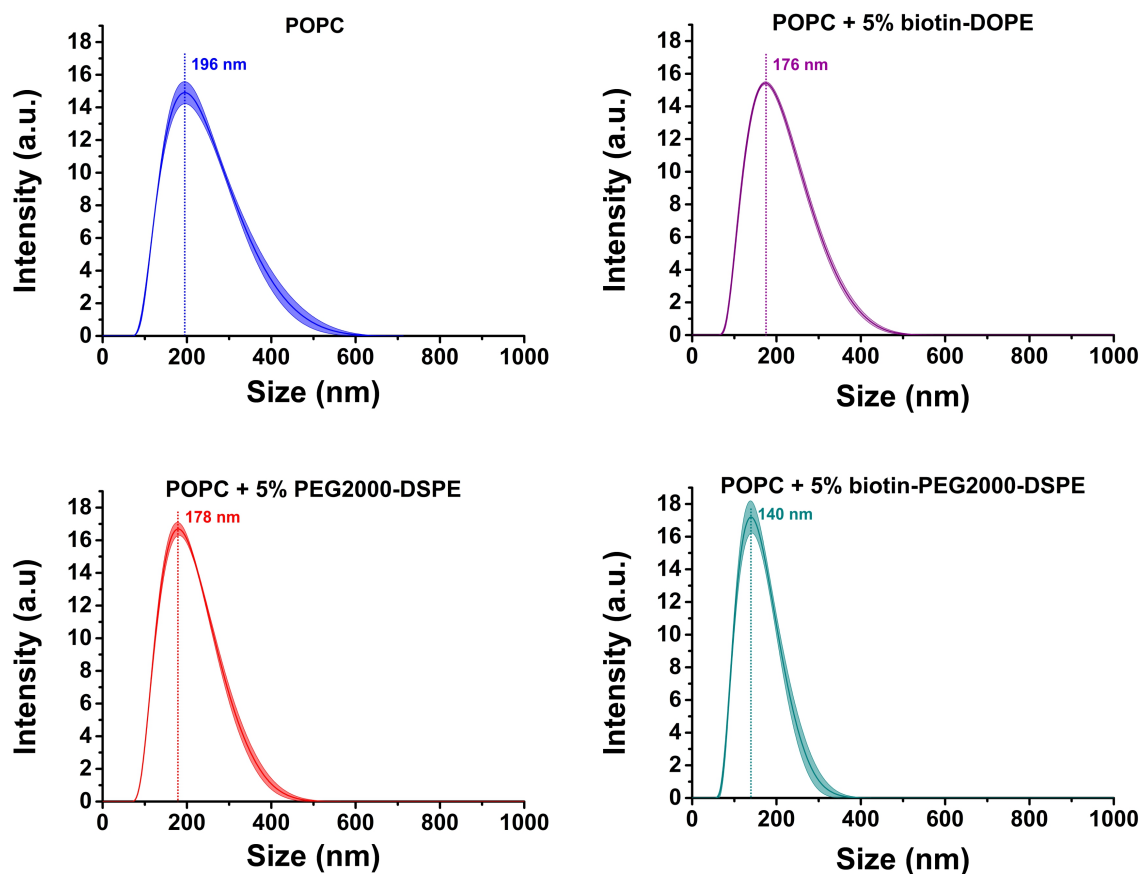


Figure 5.8: Size distribution of squalane LONDS with different lipid coatings. The figures show the average size distribution of three runs, and its standard deviation (shaded).

The size distribution of the different LOND samples were analysed and the results are summarised in table 5.1. POPC-coated LONDS were found to have the largest size, whereas LONDS coated with POPC + 5% biotin-PEG2000-DSPE had the smallest size. When comparing other squalane LOND samples prepared within the project, POPC LONDS were, on average, 25% bigger than LONDS coated with POPC + 5% biotin-PEG2000-DSPE or POPC + 5% PEG2000-DSPE ($n_{\text{POPC}} = 11$, $n_{\text{BPEG}} = 4$, $n_{\text{biotinPEG}} = 12$). In average, the size difference between PEG2000-DSPE and biotin-PEG2000-DSPE containing LONDS was about 4.5%, indicating that PEG biotinylation does not have a significant effect in the LONDS size. This also suggests that the differences with respect to POPC coated LONDS were likely due to the presence of the PEG chains. A reduction in the size of nanodroplets upon the addition, and subsequent increase of the concentration of PEG2000-DSPE in the lipid shell has been reported before, and attributed to the increase of the curvature of the lipid membrane due to the close packing of the PEG chains. [50, 252] PEG chains have been widely used in drug delivery systems due to their ability to shield the surface of the nanocarriers. PEG attached to

the phospholipids headgroups (i.e. PEG2000-DSPE, biotin-PEG2000-DSPE) undergoes steric repulsion from the nanocarrier surface, and contributes to its stability, as observed for other lipid-coated capsules such as liposomes. [253,254] The size difference observed between PEG-containing LONDS and the other species (table 5.1) could also be due to the decrease in the number of aggregated particles in presence of the PEG chains, which would reduce the average particle size. [255–257]

Table 5.1: Sizes of squalane LONDS prepared at 175 MPa, with different lipid coatings. All the samples were sized using DLS. The standard deviation (SD) of the size distributions shown in figure 5.8 are also included. The average mode size of samples prepared under the same conditions within the project is also included, with $n_{\text{POPC}} = 11$, $n_{\text{BPEG}} = 4$, $n_{\text{biotinPEG}} = 12$, and the uncertainties correspond to the standard error of the

Lipid shell	Average size (nm)	Mode size (nm)	SD (nm)	Project average mode size (nm)
POPC	247 ± 5	196 ± 4	79	194 ± 9
POPC + 5% biotin-DOPE	214 ± 2	176 ± 1	66	-
POPC + 5% PEG2000-DSPE	212 ± 3	178 ± 1	62	140 ± 10
POPC + 5% biotin-PEG2000-DSPE	164 ± 4	140 ± 1	45	145 ± 6

5.3.4 The effect of the oil on LOND size

The characteristics of the oil, such as viscosity and density, have previously been reported to have an effect on the size of the nanodroplets in nanoemulsions. [172,258–262] Generally, oils used as model systems in the literature to study the size changes due to the viscosity or density of the oil fall far below the biocompatibility required in clinical applications. All the oils used within this project have high levels of biocompatibility. There was an interest in replicating previous studies, which focused in the characterisation of emulsions of non clinical grade oils. To study the potential size variability of LONDS prepared with different candidate oils, triacetin, tripropionin and squalane were used to prepare LONDS. The resulting sample was sized using two different techniques (three in the case of triacetin LONDS). All the samples were stabilised with a phospholipid shell that included 5% biotin-PEG2000-DSPE, in order to avoid size differences associated to the presence/absence of the PEG chains (section 5.3.3). Similarly, all LOND samples were prepared under 175 MPa in the Emulsiflex. Table 5.2 summarises the findings for this experiment. Tripropionin LONDS were found to have the smallest diameter, and both size measurements, with DLS and using the NanoSight instrument, are in agreement. Squalane

Table 5.2: Average size of LOND samples, as measured using three different techniques. Each result is the average of at least 2 size measurements, of two different LOND samples. The uncertainties correspond to the standard error of the mean. Lipid shells are: A) POPC + 5% biotin-PEG2000-DSPE, B) DSPC + 5% biotin-PEG2000-DSPE + 20% Cholesterol

Oil	Lipid shell	LOND average size (nm)		
		DLS	NanoSight	qNano
Triacetin	A	202 ± 38	127 ± 12	280 ± 9
Tripropionin	B	105 ± 11	102 ± 9	-
Squalane	A	165 ± 11	133 ± 10	-

LONDS DLS and NanoSight instrument size measurements show a discrepancy of about 6%, if considering the uncertainties of each measurement. This difference could be purely due to production variation between the samples sized with each technique ($n_{DLS} = 4$, $n_{NanoSight} = 5$). The limitations of DLS when sizing polydisperse samples could also introduce some error to the measurement. There are notable differences between the sizes of triacetin LONDS obtained with the different techniques. Within error, the data obtained by DLS and qNano are in agreement. However the results provided by the NanoSight instrument considerably deviate from the other two. It is possible that smaller triacetin LONDS were not detected in qNano which would therefore provide a larger average size for these LOND samples. Similarly, their light scattering signal could be hidden by that scattered by larger LONDS in the solution, thus increasing the average size.

Highly viscous oils have been reported to form droplets considerably larger than those formed with oils with lower viscosity oils. [258, 263] When comparing the results shown in table 5.2 with the literature, similar size dependence with the viscosity of the oils is observed for squalane and tripropionin LONDS. Figure 5.9 shows a plot of the size of tripropionin, squalane and triacetin LONDS as a function of the oil viscosity. The data points were fitted to a linear regression. [263] The viscosity of squalane at 20 °C is $\eta = 12$ mPa·s, whereas the viscosity of tripropionin is $\eta = 10$ mPa·s at this temperature (table 4.1, on page 49). [264] Correspondingly, squalane LONDS show a larger average size than tripropionin LONDS, both formed under the same conditions. Triacetin has the highest viscosity out of the three candidate oils used in this particular study, with viscosity 23 mPa. For the case of triacetin LONDS, the size increase with increased viscosity of the oil

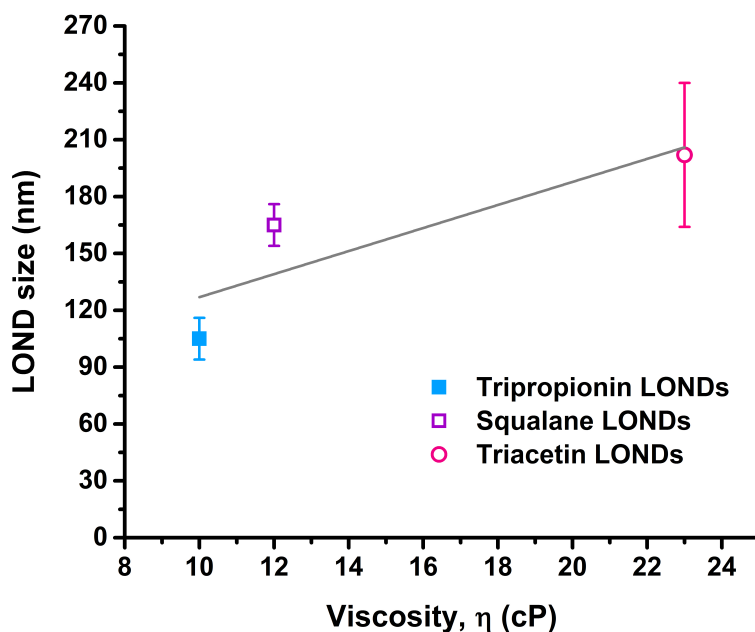


Figure 5.9: Size of the LONDS as function of the viscosity of the oil, for tripropionin, squalane and triacetin LONDS. The data points were fitted to a linear regression.

is only true if considering the sizing results obtained by DLS and qNano.

5.4 Concentration measurements

In the literature, nanoemulsions are often treated as a bulk material, and there have been not many references concerned with the determination of the number of nanoparticles forming the nanoemulsion. In general, the oil volume fraction ϕ is considered to determine the number of droplets present in a nanoemulsion. This is true in general, unless the solubility of the oil in water is not negligible. Although there are a few references to the indirect study of the concentration, [265, 266] there have not been systematic studies on the factors affecting the concentration of nanodroplets aimed at drug delivery. In this project, the number of LONDS that attach to the MB surface defines the amount of drug that it is possible to transport in the MB-LONDS. Therefore knowing the number of oil nanodroplets present in the nanoemulsions was important.

This section presents the study of the dependence of LOND concentration and two different factors: 1) the production pressure in the Emulsiflex and 2) the encapsulated oil. The concentration of LONDS was measured using two different instruments, the qNano and the NanoSight (section 3.5, page 34). qNano was available throughout the project, and

it was used to perform measurements at the beginning of the project, whereas NanoSight was used for later experiments.

LOND concentration was estimated by considering the LONDS to be perfect spheres with diameter² $d = 200$ nm and volume given by $V = \frac{4}{3}\pi \left(\frac{d}{2}\right)^3$. Assuming that all the oil present in the crude emulsion (0.7 ml, $\phi = 0.07$) is encapsulated by the lipid, the concentration of LONDS would theoretically be $\sim 2 \times 10^{13}$ ml⁻¹. This estimate was used as a guide when performing experimental measurements on the LOND samples.

5.4.1 The effect of pressure on LONDS concentration

Emulsion production relies on breakage of the oil phase into small oil droplets that stabilise with the lipid present in the solution (section 2.2, page 16). Higher shear forces at the homogenising nozzle in the Emulsiflex lead to more efficient dispersion of the oil phase, leading to increased concentrations. In order to study the dependence of the LOND concentration and the production pressure during ultra-high pressure homogenisation, concentration measurements of LONDS prepared under 35, 70, 105, 140 and 175 MPa were performed. Squalane and tripropionin LONDS were chosen as model LONDS for this experiment, and were stabilised with POPC and POPC+ 20% + 5% biotin-PEG2000-DSPE, respectively. In each case, the crude emulsions were processed for 10 min at each pressure, starting from the lowest one, and small sample volumes were collected before increasing the pressure. A NanoSight instrument was used to determine the concentration of the LOND samples, that were diluted 1 : 100000 to perform the measurements.

²early sizing results on different squalane LOND samples provided results between 190 – 220 nm, thus $d = 200$ nm was considered for this estimate.

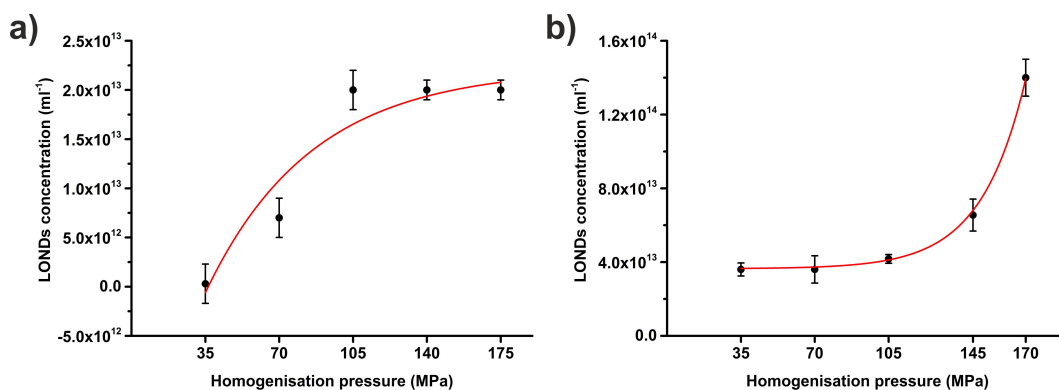


Figure 5.10: Concentration of a) squalane and b) tripropionin LOND samples produced under different pressures in the Emulsiflex. The concentration measurements were performed using a NanoSight instrument and the data points were fitted as a guide to the eye.

Figure 5.10 shows the concentration of LOND samples produced under different pressures in the Emulsiflex. The data was fitted as a guide to the eye. As expected, the number of LONDS in the solution, for both squalane and tripropionin LONDS, was observed to increase with increasing pressures. The concentration of squalane LONDS reached a steady value at $(2.2 \pm 0.4) \times 10^{13} \text{ ml}^{-1}$. This could be explained from the point of view of the surfactant available in the solution, as more droplets are created throughout the homogenising process. Ultra-high pressure emulsification relies on droplet breakage and immediate stabilisation by the surfactant, and lack of surfactant in the solution would lead to re-coalescence of the droplets after their disruption in the homogenising nozzle. [147, 166] It is also interesting to note that the value of the concentration at the plateau is, within experimental error, the same as that obtained theoretically through size considerations ($\sim 2 \times 10^{13} \text{ ml}^{-1}$). This suggests that all the squalane was successfully dispersed and encapsulated with the lipid. In the case of tripropionin, LOND concentration was observed to increase slowly for increasing production pressures between 35 – 145 MPa. Sample processing under 175 MPa resulted in a significant increase of LOND concentration $\sim 53\%$, to a final value $(1.4 \pm 0.1) \times 10^{14} \text{ ml}^{-1}$. This is in agreement with the theoretical value of LOND concentration based on the LONDS dimensions³, $1.3 \times 10^{14} \text{ ml}^{-1}$. The differences observed in the dependence of LOND concentration with the production pressure between squalane and tripropionin LONDS could be attributed to the different viscosity of the oils. In a similar fashion to affecting the size, the enhancement of the droplet deformability at the homogenising nozzle due to lower viscosity oils results in more efficient dispersion of the oil in the water phase.

³for $d \sim 120 \text{ nm}$, and $\phi = 0.07$

5.4.2 The effect of oil on LOND concentration

The physical characteristics of the oils, such as their viscosity and density, are known to affect the properties of the nanodroplets in a nanoemulsion. [267,268] To study the effect of the oil in the concentration of LONDS, samples of triacetin, tripropionin, squalane, squalene were studied using qNano and/or NanoSight. The pressure applied at production was 175 MPa. Figure 5.11 shows an example of concentration data obtained using qNano, for triacetin LONDS coated with POPC + 5% biotin-PEG2000-DSPE. LONDS crossing the nanopore create a blockade event whose magnitude provides a measurement of its size, whereas the number of LONDS that obstruct the pore provide a measurement of the concentration of the sample. In this particular case, there were 1.9×10^9 LONDS/ml⁻¹, with an average size of (295 ± 7) nm. The size of the pore used to perform measurements on each sample defines the accuracy of the technique. Hence, particles too small to create a significant blockade event might not be detected. An example of this can be seen in figure 5.11, which does not show any particles smaller than 200 nm. Although some LONDS below 200 nm may exist in the sample, they were too small to be detected with this pore size, therefore reducing the total particle count and affecting the concentration measurement.

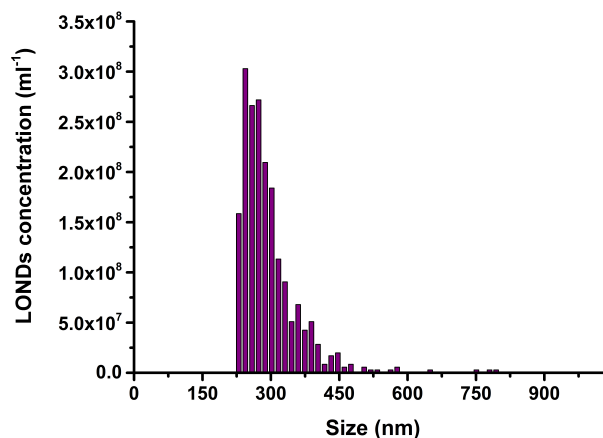


Figure 5.11: Concentration measurement of a triacetin LOND sample as determined by qNano. The concentration of the sample was 1.9×10^9 ml⁻¹. The instrument cut-off (for particles < 200 nm in this case) is defined by the size of the nanopore used for the measurements.

Table 5.3 summarises concentration data for different types of LONDS. The uncertainty in the concentration of squalane, triacetin and tripropionin LONDS corresponds to the standard error of the mean, from averaging the values obtained for different samples ($n > 3$ in all cases). Differences between the concentrations measurements performed with

qNano and NanoSight were observed, and can be, to a certain extent, explained by the limitations of the sizing techniques. [187,247] For triacetin LONDS, both the concentration measurements are within experimental error. However, in the case of squalane LONDS, the two concentration measurements differ by one order of magnitude. The standard error associated to the measurement in qNano is very high, about 70% ($n = 4$), which shows that the concentration differences between all the samples studied were large. It is possible that the LOND samples measured in qNano were of lower quality than the samples measured in NanoSight, prepared later on in the project.

Tripropionin LONDS exhibit the highest concentration (10^{14} ml^{-1}), whereas triacetin LOND samples appear to have the lowest one (10^{10} ml^{-1}). Differences in the oil water solubility (table 4.1, page 49) could explain the differences observed in the concentration of LONDS samples formed with different oils. For example, the higher solubility of triacetin could make a fraction of the triacetin solubilise in water, before being encapsulated by the lipid. Similarly, higher solubility could translate into lower retention of the oil in the LONDS. Squalane and squalene show concentrations in the same order of magnitude, when measured using NanoSight. This is not surprising, provided that the squalane and squalene molecules are very similar, non-polar and close physical characteristics, and therefore nanoemulsions prepared with either of these oils could be expected to have similar properties.

Table 5.3: Concentration of LONDS formed with different oils, as measured by the qNano and/or NanoSight instruments. All the uncertainties correspond to the standard error except for the concentration of squalane, which is the uncertainty associated to the measurement of the concentration in a single experiment.

Oil	Concentration (LONDS/ml)	
	qNano	NanoSight
Squalane	$(6.4 \pm 4.5) \times 10^{12}$	$(7.1 \pm 2.4) \times 10^{13}$
Squalene	-	$(2.6 \pm 0.4) \times 10^{13}$
Triacetin	$(3.2 \pm 1.2) \times 10^{10}$	$(3.3 \pm 1.4) \times 10^{10}$
Tripropionin	-	$(4.5 \pm 1.3) \times 10^{14}$

5.5 Stability of LONDS

Drug delivery systems often rely on encapsulation of a therapeutic agent, thus protecting the drug until its administration. It is clear that good stability over time is desirable for such systems, if they are to retain the drug until it is deposited in the place of interest. This project aimed to combine LONDS and MBs into a novel architecture for the delivery of drugs. The techniques used to prepare the MBs (microfluidics) and the LONDS (high pressure homogenisation) are impossible to combine in a single device, and therefore the preparation of LONDS must precede the formation of MBs. The need for ensuring that LONDS remain stable over this time window is evident. Besides this, LONDS would ideally retain similar physical characteristics (i.e. size and concentration) over a long enough period of time, so that different LOND batches could be used for different experiments. To study the stability of LONDS over time, the size distribution of LOND samples was monitored using DLS. Sample agglomeration or degradation was expected to translate into a size distribution change, such as a broadening of the original size distribution or appearance of new peaks. Two different studies of the stability of LONDS were performed: i) an investigation to determine the stability of LONDS upon storage conditions (4 °C) during six weeks, and ii) a study on the stability of LONDS under physiological conditions (37 °C) and during a clinically relevant time (2 h). The later experiment intended to be a better approach to those conditions a LOND would be exposed to when used *in vivo*. However it is important to note that these conditions are impossible to completely replicate *in vitro*, and therefore any results should be interpreted tentatively.

Figure 5.12 shows the mode size variation of squalane, triacetin and tripropionin LONDS over six weeks, stored at 4 °C. Both the squalane and the triacetin LOND samples were produced under identical conditions, and POPC + 5% biotin-PEG2000-DSPE was used for stabilisation of the oil. Tripropionin LONDS were stabilised with POPC + 20% cholesterol + 5% biotin-PEG2000-DSPE. Each experimental point was produced averaging three DLS runs, and the data points were fitted to a linear regression with slope 0. The graphs show a size variation of around 16% in the case of squalane LONDS, of 13% for triacetin LONDS and 15% for tripropionin LONDS. There was a relatively small variation of the LONDS diameter within this time, which suggested good stability against agglomeration and coalescence.

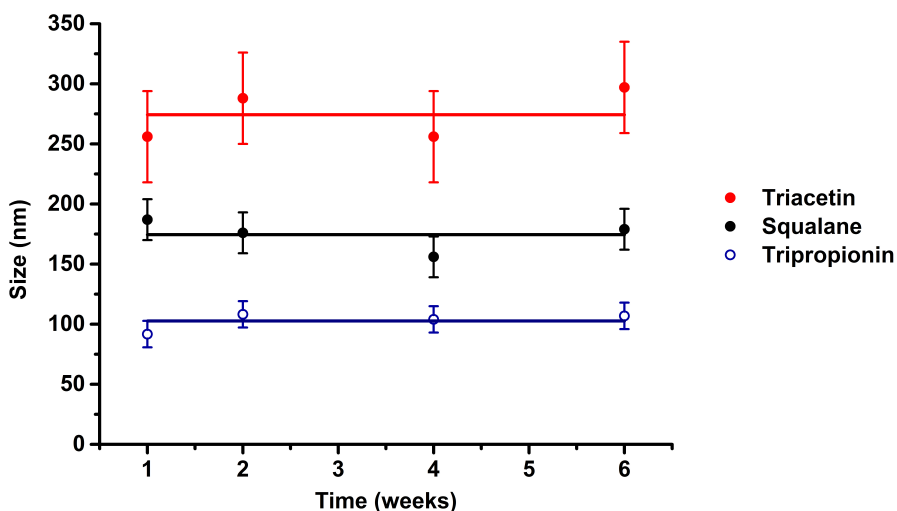


Figure 5.12: Size change of squalane, triacetin and tripropionin LONDS over a six week period, stored at 4 °C, measured with DLS. Experimental points were produced averaging three size measurements on the same sample.

The stability of LONDS stored at 4 °C was also studied by determining the concentration of LOND samples within time. Agglomeration of LONDS in solution would likely lead to not only an increase in the average size of the sample, but could also reduce the number of LONDS. Furthermore, solubilisation of the oil in the aqueous phase would lead to a reduction in LOND concentration. The concentration of two LOND samples, at two different times after production was determined using the NanoSight instrument. The first sample was squalane LONDS, stabilised with POPC + 5% biotin-PEG2000-DSPE and was sized after production and 10 weeks later; the second sample was tripropionin LONDS, stabilised with DSPC + 20% Cholesterol + 5% biotin-PEG2000-DSPE, and was sized after production and 4 weeks later. Table 5.4 summarises the results obtained for these two samples. Although the concentration of both samples remained in the same order of magnitude, the number of LONDS in solution diminished about 27% in the case of squalane LONDS, and about 71% in the case of tripropionin LONDS. It is important to note that the technique by which the samples were studied, single particle tracking, is sensitive to local variations of the LOND concentration. This means that, although the samples for analysis were prepared with extra care to ensure the greatest homogeneity, small concentration variations within the sample could translate into an apparent reduction of the number of LONDS in the solution. From the stability results shown in figure 5.12, it can be argued that the changes in concentration were not large enough to have an effect in the average size distribution of the sample, as this remained constant during the studying time.

Table 5.4: Concentration of LOND samples as measured by the NanoSight instrument. For both samples, t_0 corresponds to the measurements performed shortly after LOND preparation. For squalane LONDS, $t_1 = 10$ weeks, whereas for triacetin LONDS $t_1 = 4$ weeks.

Oil	Lipid shell	Concentration at t_0 (ml^{-1})	Concentration at t_1 (ml^{-1})
Squalane	POPC + 5% biotin-PEG2000-DSPE	$(4.8 \pm 0.5) \times 10^{13}$	$(3.5 \pm 0.3) \times 10^{13}$
Tripropionin	DSPC + 20% Cholesterol + 5% biotin-PEG2000-DSPE	$(7.3 \pm 0.7) \times 10^{14}$	$(2.1 \pm 0.5) \times 10^{14}$

Figure 5.13 shows the size variation of triacetin, squalane and tripropionin LONDS at 37 °C and over 2 h. As above, both LOND samples were produced under identical conditions, and the lipid shell was POPC + 5% biotin-PEG2000-DSPE. Tripropionin LONDS were stabilised with DSPC + 20% cholesterol + 5% biotin-PEG2000-DSPE. In this case, the LOND samples were kept constantly at 37 °C for 2 h and measurements of their size distribution were taken every 15 min. A 2 h period was considered comparable to the time scales over which LONDS must remain intact during an *in vivo* experiment. Within experimental error, the size of the LONDS did not change, suggesting that LONDS remained stable during this period, and also that the LONDS did not undergo agglomeration.

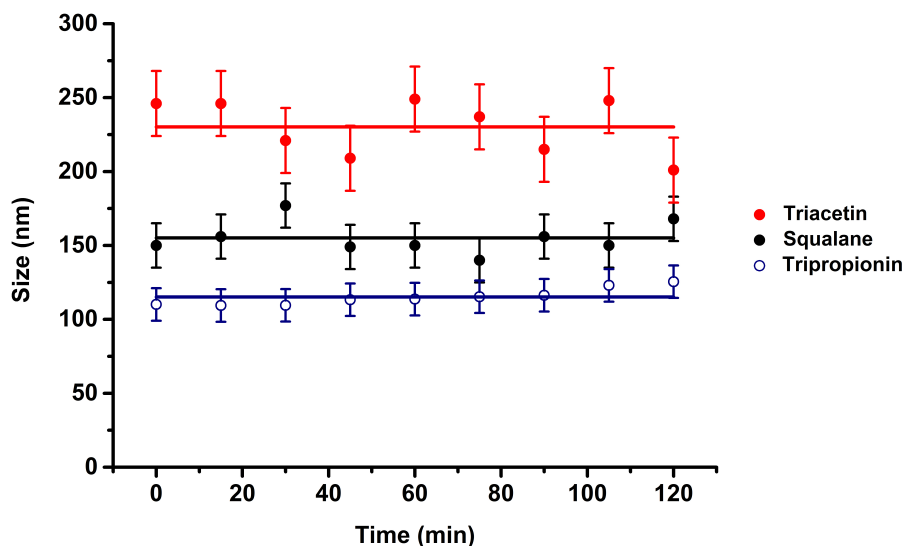


Figure 5.13: Size change of squalane, triacetin and tripropionin LONDS over at 37 °C over 2 h, as determined with DLS. Experimental points were produced averaging three size measurements on the same sample.

5.6 LONDS imaging

This section contains the experimental results relating to the imaging of LONDS. In this project, imaging of LONDS was performed with epifluorescence microscopy and TEM. TEM imaging was used to confirm the existence of the LONDS, whereas epifluorescence microscopy was used to confirm the detection of LONDS incorporating a fluorescent probe in their structure.

5.6.1 TEM

LONDS formed from different candidate oils were imaged using TEM. Specifically, squalane LONDS (empty and encapsulating Qdots), triacetin LONDS (empty and encapsulating CA4) and tripropionin LONDS (empty, two different oil shells) were imaged. Samples for TEM imaging were prepared by depositing 15 μl of the LOND samples (10^{11} LONDS/ml, in PBS) on a carbon coated grid. The solution was left on the grid for 30 s, and the excess liquid dried out using blotting paper. The sample was subsequently stained by dropping 15 μl of uranyl acetate (1%) on the grid and incubating for 15 s, after which the excess liquid was removed with blotting paper. TEM images were analysed using imageJ.

Figure 5.14 shows TEM images of squalane LONDS, that appeared as characteristic globular structures ranging 100–300 nm. Empty squalane LONDS (figure 5.14a and b) and squalane LONDS encapsulating hydrophobic Qdots (figure 5.14d and e) were imaged. Both samples were stabilised with POPC + 5% biotin-PEG2000-DSPE and prepared following the two-step process, with 175 MPa applied in the Emulsiflex. The two LOND samples did not show significant differences under TEM. Size histograms for the two samples are shown in figure 5.14c and f. A normal distribution fitted to each histogram was used to determine average size and standard deviation of the samples. Empty LONDS were found to have an average size (111 ± 6) nm (LONDS measured $n = 187$, standard deviation of the sample $\sigma = 85$ nm). Squalane LONDS encapsulating Qdots had an average size (112 ± 4) nm ($n = 98$, $\sigma = 39$ nm). These results suggest that the encapsulation of Qdots had no effect in the size of squalane LONDS. It is important to note that the resolution of the specific TEM microscope used to take the images shown in figure 5.14 was not enough to

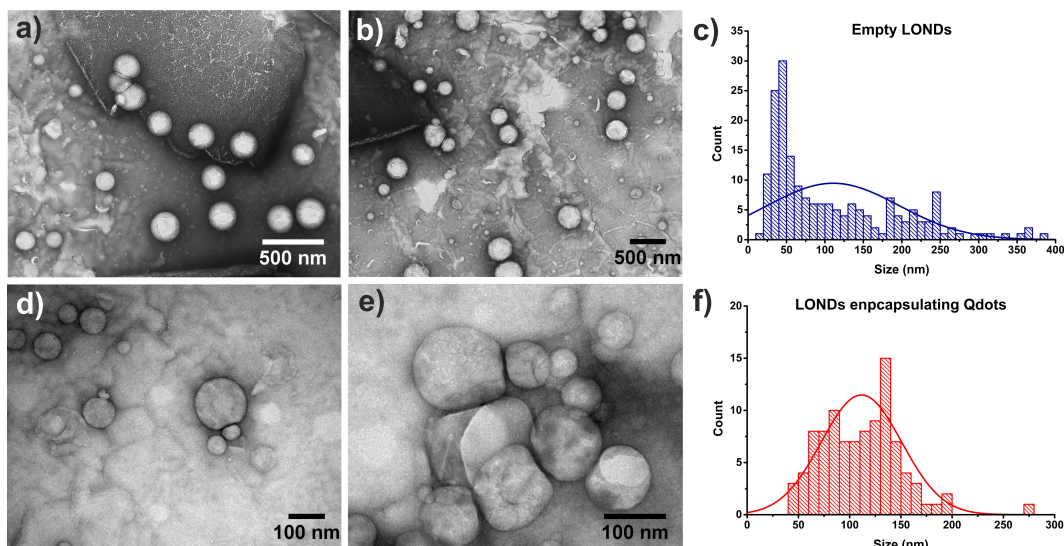


Figure 5.14: TEM images of squalane LONDS. The lipid shell was made of POPC. a) and b) show a population of squalane LONDS. c) Size histogram for the same squalane LONDS sample, with average size (111 ± 6) nm, $n = 187$, $\sigma = 85$ nm d) and e) show a population of squalane LONDS encapsulating Qdots. f) Size histogram for the same squalane LONDS sample with Qdots, average size (112 ± 4) nm with $n = 98$, $\sigma = 39$ nm.

resolve individual Qdots (with sizes around ~ 7 nm).

Triacetin LONDS were imaged on TEM. Two samples were examined: an empty triacetin LOND sample and triacetin LONDS encapsulating CA4. The concentration of the drug in the oil, prior to LONDS formation, was 25 mg/ml. Both samples were stabilised with POPC + 5% biotin-PEG2000-DSPE, and prepared under 175 MPa in the Emulsiflex. Empty triacetin LONDS (figure 5.15a) were found to have an average size of (140 ± 4) nm (LONDS measured $n = 91$, standard deviation of the sample $\sigma = 40$ nm), as determined from the fitting of the the size histogram (figure 5.15b). The average size of triacetin LONDS encapsulating CA4 (figure 5.15c) was found to be (166 ± 5) nm ($n = 55$, $\sigma = 39$ nm) from the size histogram shown in figure 5.15d.

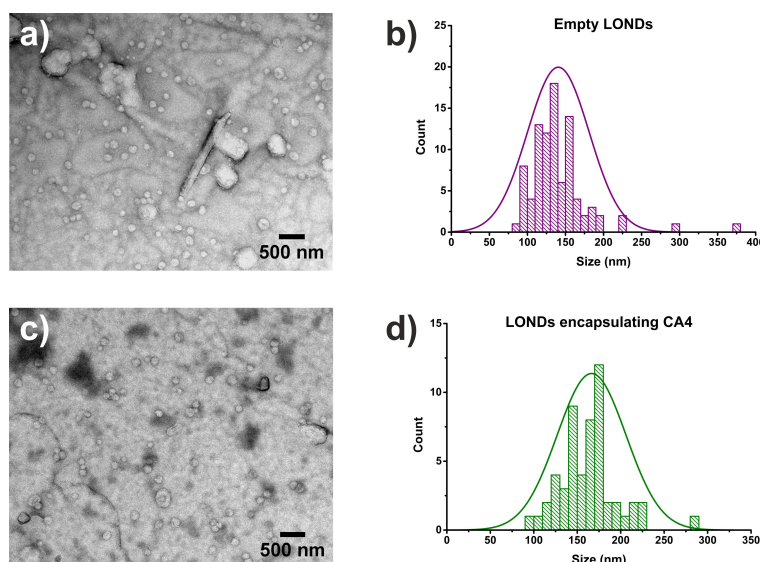


Figure 5.15: TEM images of triacetin LONDS. POPC and 5% biotin-PEG2000-DSPE were used to stabilise the oil. a) Empty triacetin LONDS and b) size histogram (average size of (140 ± 4) nm, $n = 91$, $\sigma = 40$ nm). c) Triacetin LONDS encapsulating CA4 and d) size histogram (average size (166 ± 5) nm, $n = 55$, $\sigma = 39$ nm).

Tripropionin LONDS were also examined under TEM. Two samples stabilised with different lipid coatings were imaged. Figure 5.16a shows tripropionin LONDS stabilised with POPC only. It was difficult to observe any intact LONDS in this sample, in contrast to squalane and triacetin LOND samples, in which distinctive globular structures could be seen. In order to improve the stability of tripropionin LONDS, the lipid shell was modified, as discussed above (section 5.2). The mixture DSPC + 20% Cholesterol + 5% biotin-PEG2000-DSPE was used to produce tripropionin LONDS, and figure 5.16b and c show the TEM images of this new sample. LONDS appeared to have lost their structure under the vacuum conditions in TEM, exhibiting a layered appearance. This could be due to the increased rigidity of the lipid shell by the addition of DSPC and cholesterol. [269,270] This type of LONDS was found to have an average size (89 ± 3) nm ($n = 71$, $\sigma = 23$ nm), as determined from the fitting to the size histogram (figure 5.16d). It is interesting to note that this sample shows the smallest standard deviation, compared to the other LOND samples studied using TEM, which suggests enhanced monodispersity. Provided that the preparation method for this LOND sample was identical to those described previously (figures 5.14, 5.15), this improved size monodispersity could be related to the increased rigidity of the lipid shell. However, further experiments would be required to confirm this hypothesis.

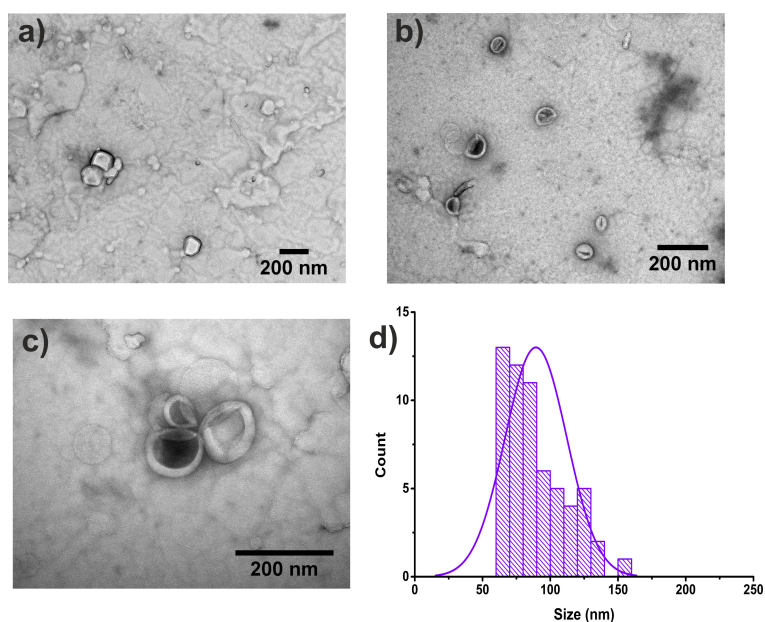


Figure 5.16: TEM images of tripropionin LONDS. a) Tripropionin LONDS stabilised with POPC only. b and c) Tripropionin LONDS stabilised with DSPC + 20% Cholesterol + 5% biotin-PEG2000-DSPE. d) Size histogram used to determine the average size of the tripropionin LOND sample shown in c and d (average size (89 ± 3) nm, $n = 71$, $\sigma = 23$ nm)

5.6.2 Epifluorescence microscopy

To test the fluorescence tracking of LONDS, LONDS were imaged using the epifluorescence microscope. As discussed above, the fluorescently tagged lipids Atto 488 and Atto 590 DOPE were added to the lipid shell composition when fluorescence tracking of the LONDS was necessary. Alternatively, the encapsulation of Nile Red in LONDS also allowed for fluorescent tracking. The resolution limit of a conventional epifluorescence microscope is around 250 nm, which implies that LONDS would appear simply as fluorescent dots under the fluorescence microscope, and no structure could be resolved using this technique.

Figure 5.17 shows an example of two epifluorescence images of LONDS. For these experiments, LOND samples were diluted 1 : 1000 in PBS, meaning a final concentration of LONDS in solution of the order of 10^9 LONDS/ml. Squalane LONDS stabilised with POPC, 5% biotin-PEG2000-DSPE and 0.1% Atto 590 were imaged using a $40\times$ objective (figure 5.17a). Figure 5.17b shows squalane LONDS encapsulating Nile Red, and stabilised with POPC and 1% biotin-DOPE, imaged using a $100\times$ objective. Triacetin LONDS encapsulating Nile Red and stabilised with POPC and 5% biotin-PEG2000-DSPE with were imaged using a $40\times$ objective. LOND samples appeared polydisperse, and a few big

fluorescence agglomerates with sizes⁴ $> 1 \mu\text{m}$. Individual fluorescence dots were possible to resolve in both magnifications (40 \times and 100 \times), and also when the fluorescence signal came from a fluorescently tagged phospholipid added to the LOND lipid shell (Atto 590 DOPE) and when the fluorophore was encapsulated in the oil (Nile Red).

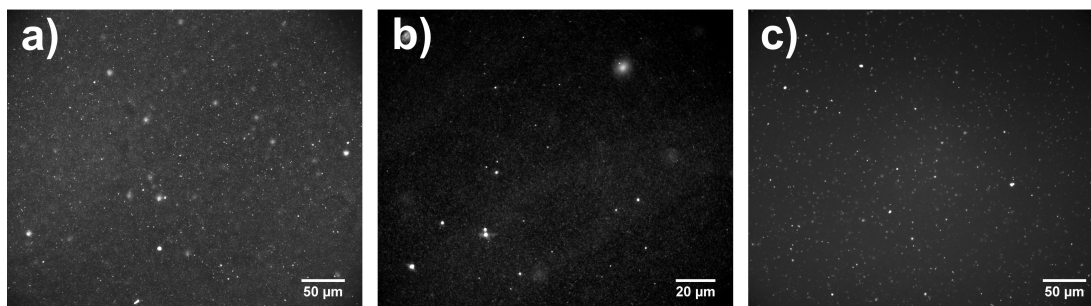


Figure 5.17: Epifluorescence images of LONDS. a) Squalane LONDS with 0.1% Atto 590 in the shell. Imaged under the 40 \times objective. b) Squalane LONDS encapsulating Nile Red. 100 \times objective. c) Triacetin LONDS encapsulating Nile Red. Taken using the 40 \times objective.

5.7 Discussion

Over the past decade or more, nanoemulsion formation and stability has been an important endeavour, as they find application in a wide range of fields, from food [144,271] to materials science [272,273]. [274] Remarkably, nanoemulsions have also been used in the pharmaceutical industry to deliver, or enhance the delivery of hydrophobic drugs. [40] This project aimed to combine lipid-stabilised, oil-filled nanodroplets (LONDS) and MBs in a more complex architecture that would retain the potential of the nanoemulsions to deliver hydrophobic drugs, but that would also incorporate the ultrasound properties of the MBs. It becomes apparent that a precise characterisation of the LONDS is vastly important if they are to be combined with MBs and find a medical application.

In this project, LONDS were formed from a oil-in-water and lipid mixture, in a two-step homogenisation process that included a first blending step that roughly mixes the components and dissolves larger lipid agglomerates, followed by a ultra-high pressure homogenisation step in an Emulsiflex (section 5.1). The size of the LONDS was refined at each step, as shown in section 5.3.1. Also, the size of the LONDS formed following this method are in agreement with other nanoemulsions prepared in this way. [165,260,274,275]

⁴Probably a number of LONDS clustered together.

The formation of LONDS was attempted with all the candidate oils, and early results lead to the discarding of EPA and isoamyl acetate. The solubility of the model hydrophobic drug CA4 added further restrictions to the oils used for LONDS preparation, it only dissolved in triacetin. Although CA4 only dissolved in triacetin, and showed poor solubility in squalane, both squalane and triacetin were used as model oils to form LONDS throughout this project. Overall, triacetin LONDS showed larger sizes and lower concentration than any other candidate oil, and also higher polydispersity index, which made sizing using DLS difficult. This was attributed to the high water solubility of triacetin, which could induce oil leaking from the LONDS and its dissolution in the aqueous phase.

Tripropionin was introduced as a candidate oil later in the project, thus only preliminary results with this oil have been presented. Tripropionin showed great potential forming LONDS, producing monodisperse samples with high concentrations ($\sim 10^{14}$ ml⁻¹), and also the ability to dissolve the model drug CA4. These LONDS show great potential for the delivery of CA4, and therefore future, detailed studies of their stability over time and drug retention will be crucial for understanding drug delivery using this platform. Tripropionin LONDS were first stabilised using only POPC in the lipid shell, which lead to rapid LONDS destabilisation, as reflected in the samples as the appearance of white precipitate (thought to be lipid) and also an increase of the sample polydispersity (as measured with the NanoSight instrument). Modification of the shell to incorporate cholesterol and biotin-PEG2000-DSPE, as well as substituting POPC with DSPC, with a higher transition temperature, dramatically increased the stability of this type of LONDS. This specific shell composition has been previously used in nanoemulsions for drug delivery. [45, 50] Indeed, preliminary results demonstrated this LONDS to be stable for at least four weeks (table 5.4), compared to the few hours that POPC-stabilised tripropionin LONDS remained stable. It has been hypothesised that the increase in the rigidity of the shell could have a positive effect in the retention of the oil by the lipid shell, contributing to LOND stability. [276] It is possible that the use of this lipid shell in encapsulating triacetin could improve the size distribution of these LONDS, and contribute to the reduction of the polydispersity index of the samples, which caused a number of problems during this project.

In an effort to better understand the factors affecting the size and concentration of LONDS, an extensive study was performed. Applied pressure in the Emulsiflex was found to be an important variable in LOND production. [165, 260] Squalane LONDS were used

to study this dependence. The average size of LOND samples was found to decrease with increasing pressures, which is in correspondence with increased shear forces at the homogenising nozzle as the energy input (pressure) is incremented (section 5.3.2). Similarly, increasing pressures lead to higher concentration of LONDS in the solution, pointing at more efficient oil breakage under higher pressures (section 5.4.1). Interestingly, both the size of the LONDS and the concentration were found to quickly reach a plateau for production pressures > 35 MPa, suggesting that the physical characteristics of the system (such as surface tension of the phospholipid, and oil viscosity) do not allow for further splitting of the oil droplets. The oil encapsulated in the LONDS was also found to have an effect in LOND size and concentration (section 5.4.2). As mentioned above, tripropionin was found to form highly concentrated LOND samples ($\sim 10^{14}$ ml $^{-1}$), whereas the concentration of triacetin LOND samples were, in average, four orders of magnitude lower ($\sim 10^{10}$ ml $^{-1}$). The concentration of LOND samples encapsulating squalane or squalene was also found to be high, about 10^{13} ml $^{-1}$. The water solubility of triacetin has been suggested as a reason behind the reduced concentration of LONDS formed with this oil. Permeation of triacetin from the LONDS to the aqueous phase could lead to the dissolution of a number of LONDS. The lipid shell of these shrunken LONDS would potentially rearrange to form micelles, or stay in the solution as smaller lipid agglomerates such as dimers. The disappearance of some LONDS could also have the effect of modifying the average size distribution and concentration of triacetin LOND samples, and could also contribute to increase the PI of the samples. This effect could be hypothesised to be gradual over time, and until an equilibrium between the amount of triacetin diluted in the water phase and contained in the LONDS is reached. More experiments would be however necessary to test this hypothesis. Squalane LONDS were used as model LONDS to study the effect of the lipid coating in the LONDS size (section 5.3.3). Four different LOND samples, prepared under the same conditions and with different lipid shells, were sized to study size variations with the different coatings. POPC-stabilised LONDS were found to have the the largest average size, and considering other samples prepared and sized within the project, these LONDS are, in average, 25% bigger than LONDS coated with POPC + 5% biotin-PEG2000-DSPE or POPC + 5% PEG2000-DSPE. This size difference has been explained from the point of view of the increased LOND stability in presence of the PEG chains, which have been well characterised as steric barriers for nanoparticles used in drug delivery. In fact, this size reduction has been reported before, and attributed to the curvature change in the

lipid shell in presence of the PEG chains. [50, 252] Besides, and in absence of the PEG chains, LONDS may have an increased tendency to agglomerate, which could contribute to enlarging the average size of the samples. The benefits of the presence of PEG chains in LONDS potentially go beyond the evident improvement of LONDS stability *in vitro*. Indeed, the development of effective stealth liposomes is largely due to the incorporation of PEG in their shell compositions. [10] The presence of the PEG chains substantially enhances their residence time *in vivo*, and also allows for further targeting efficiency and activity. [277–280] It is expected that LONDS would be benefited similarly by the presence of PEG chains in their composition when administered *in vivo*. However a detailed study would be necessary to test this hypothesis.

Imaging of LONDS using TEM and epifluorescence microscopy confirmed the existence of LONDS. Epifluorescence microscopy showed that fluorescence tracking of LONDS with Atto 590 DOPE into their lipid shells, as well as LONDS encapsulating Nile Red, was possible. Although the optical resolution does not allow for observation of the LONDS structure, this investigation showed that individual LONDS could be detected individually. TEM images provided valuable sizing data, for squalane, triacetin and tripropionin LONDS. A summary of the sizing obtained for the three types of LONDS, with three different sizing techniques (namely DLS, the NanoSight instrument and direct measurement on TEM images) is presented in table 5.5. It is important to note that DLS provides a measurement of the hydrodynamic radius of the LONDS, by analysing the light scattered from the bulk sample, whereas the NanoSight instrument is capable of determining the sizes of the individual particle, and similarly, TEM sizing is a direct measurement of the LOND size. Therefore, DLS provides slightly larger average size results for all three types of LONDS. In addition, TEM images are likely to correspond to the relics of the LONDS, [281] as they could partially lose their shape once the sample is deposited onto the grid and dried out. This could have an effect in the measured size of the LONDS. Despite the limitations of the experimental techniques, the sizing for squalane and tripropionin LONDS is mostly in agreement across the different techniques used. There was a small discrepancy between the sizes of triacetin LONDS measured by DLS and the NanoSight instrument, as discussed earlier, and there was also a discrepancy with the average size that resulted from the analysis of the TEM images. This difference was not noticeable for either squalane or tripropionin LONDS. This could be due to the higher volatility of triacetin under the vacuum conditions in TEM, as evaporation of triacetin could translate

into reduction of LONDS size.

Table 5.5: Average sizes of squalane, triacetin and tripropionin LONDS. The lipid shell of squalane and triacetin LONDS was POPC + 5% biotin-PEG2000, whereas DSPC + 20% cholesterol + 5% biotin-PEG2000-DSPE was used to stabilise tripropionin LONDS. The LONDS sized with three different techniques

Oil	Size (nm)		
	DLS	NanoSight	TEM
Squalane	165 ± 11	133 ± 10	112 ± 7
Triacetin	202 ± 38	127 ± 12	153 ± 6
Tripropionin	105 ± 11	102 ± 9	89 ± 3

The stability of triacetin and squalane LONDS, prepared under identical conditions and stabilised using POPC + 5% biotin-PEG2000-DSPE was studied by sizing the samples over time, with DLS. Two different experiments were performed 1) upon sample storing at 4 °C, the stability was studied over six weeks; 2) upon sample incubation at 37 °C, their stability over 2 h was studied. Both experiments showed no size changes of the LONDS within time, suggesting excellent stability and reinforcing their robustness as capsules for hydrophobic drugs to find clinical applications. Notably, the stability results for LONDS over six weeks are found in agreement with some previous reports on similar systems, in which nanoemulsions were reported stable for two, [258,261,282,283] and four [144] weeks. There are also a few references to nanoemulsions stable for more than two months. [46,47,51,275,284]. Furthermore, and to complete the investigation on the stability of LONDS, the concentration of two different LOND samples was monitored over time. As discussed above, nanoemulsions have been classically treated as bulk material, and there are only a few scattered references to the number of particles per unit volume in the nanoemulsions. [265] In this project, the NanoSight and qNano instruments allowed for the study of the concentration of LONDS in the samples, which was a crucial parameter in the experiments carried on in this project. For this case study, squalane and tripropionin LONDS were used, both prepared under identical conditions and both including 5% biotin-PEG2000-DSPE in the lipid shell⁵. In both cases, the concentration remained in the same order of magnitude, and although some differences were observed, they were attributed to small differences within the sample. An extended study of the variation of the concentration over time would be required to complete this investigation. As discussed earlier, this would be especially relevant for tripropionin LONDS, which showed promising initial results.

⁵tripropionin LONDS were stabilised with DSPC + 20% cholesterol + 5% biotin-PEG2000-DSPE, following results obtained previously.

The results shown in this chapter demonstrate that the choice of oil and lipid shell have an effect on the final LOND product, which could be relevant for LONDS finding clinical applications and also in the assembly of the complex MB-LONDS architecture. Importantly, the results point at PEG chains as a key factor affecting LOND size and stability. These results are relevant for subsequent LOND samples encapsulating model hydrophobic drugs and for *in vitro* cell studies, which were always, following these results, prepared including 5% biotin-PEG2000-DSPE in their lipid shell. Similarly, the production conditions have a crucial role in the size and concentration of the samples, and informed by these results, 175 MPa was selected as the pressure for optimal LONDS production.

Chapter 6

Topic: Encapsulation in LONDS

This chapter contains the results on the encapsulation of drugs and drug mimics in LONDS. Three hydrophobic drug mimic candidates were studied in this project, namely Nile Red, hydrophobic Qdots and calcein AM. The encapsulation of the Qdots and calcein is described in this chapter, and the results concerning encapsulation efficiency and retention of the mimics are included. The drug CA4 was encapsulated in triacetin LONDS and tripropionin LONDS. This process is described and the data regarding the encapsulation and leakage of the drug from the LONDS is also presented.

6.1 Encapsulation of Qdots

Qdots were chosen as hydrophobic drug mimics due to their excellent fluorescent properties. Qdots synthesis is a relatively versatile process, in that it allows for the modification of the Qdots with different surface chemistry. For these experiments, in-house prepared Qdots were coated with a hydrophobic dodecanethiol shell (section 3.2 on page 28). These Qdots were found impossible to disperse in triacetin, largely due to the polarity of the oil, and therefore only squalane was used to prepare LONDS encapsulating Qdots (section 4.3.1, on page 55). LONDS were prepared following the protocol described in section 5.1 (page 71), with a minor modification; prior to the addition of the oil to the dried lipid, 2.4 μM Qdots diluted in hexane were added to 0.7 μl of squalane, and the solution was placed under nitrogen for at least 30 min to remove any traces of hexane. The number of Qdots was adjusted so that the each of the resulting LONDS would encapsulate ~ 100 Qdots. To reduce the complexity of the system, and also to reduce the cost of these preliminary

experiments, POPC only was used to stabilise the LONDS. Cross-filtration followed the preparation process to remove unencapsulated material.

Squalane LONDS encapsulating Qdots were sized using DLS, and were found to have an average size (206 ± 3) nm. The average size of *empty* squalane LONDS, as shown in the previous chapter, was (194 ± 9) nm (table 5.1, on page 84), which is in agreement with the DLS measurement for this specific sample. This suggests that the encapsulation of Qdots did not affect the LONDS size. To study the efficiency of the Qdots encapsulation, a fluorescence assay was conducted in the fluorometer (section 3.3.1, page 31). A cross-filtered and an unfiltered fractions of this squalane LOND samples were excited with $\lambda_{ex} = 589$ nm and their emission spectra recorded. This excitation wavelength was chosen following the fluorescence studies performed on this Qdots sample after synthesis (figure 4.6, on page 56). Differences in the fluorescence intensity between these two samples would evidence loss of fluorescent material (i.e. Qdots) during the filtration process, which would indicate poor incorporation or retention in the LONDS volume. Figure 6.1a shows the emission spectra of the unfiltered and filtered samples. The fluorescence difference between the two spectra are of about 7%, which suggests that the Qdots were encapsulated in the LONDS, and that the filtration process did not promote their leakage. Provided the strong hydrophobicity of the dodecanethiol coating on these Qdots, it is not surprising that most of them remained in the LONDS core. Individual Qdots, or small agglomerates, coated with phospholipids could be removed during cross-filtration, giving rise to the small difference observed in the fluorescence. The variation of the fluorescence intensity as a function of the concentration of this LOND sample, cross-filtered, was also studied. Figure 6.1b shows the dependence between fluorescence signal from the encapsulated Qdots and the concentration of the LONDS. The intensity was found to increase exponentially up to 2.5×10^{12} ml⁻¹, as $y = Ae^{x/t} + y_0$. From this point, the intensity decreased as linearly for increasing concentrations. This is likely due to light scattering by the LONDS. As will be described later in this chapter, the addition of a solvent to the LONDS solution, in order to release the LONDS contents reduced large light scattering by intact LONDS, and improved the recording of fluorescence and absorption spectra.

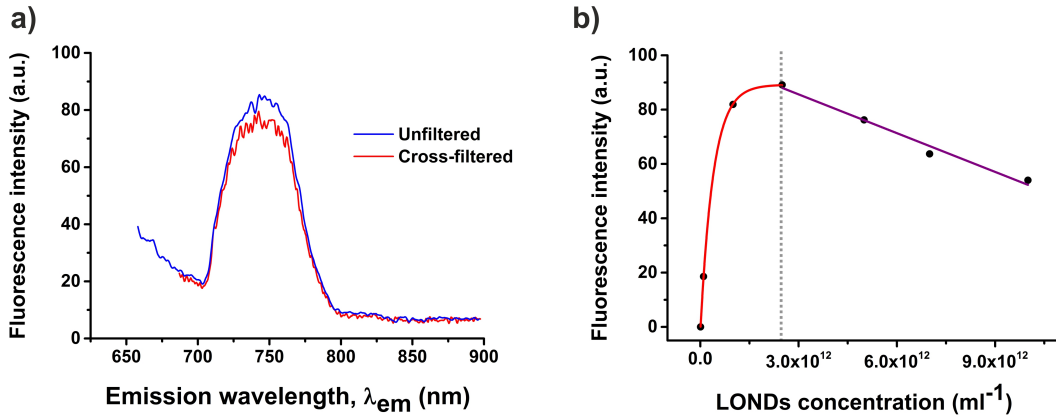


Figure 6.1: a) Emission spectrum of Qdots encapsulated in squalane LONDS. An unfiltered and a cross-filtered fraction of the same LOND samples were excited with $\lambda_{ex} = 589$ nm. The difference between the two signals is of about 7%. b) Variation of the fluorescence signal of LONDS encapsulated in LONDS as a function of the LOND concentration. This LOND sample was filtered prior to the experiment. The intensity was found to grow exponentially up to 2.5×10^{12} LONDS/ml (in red), when the intensity reduced linearly (in purple). A dotted line indicates this tendency change.

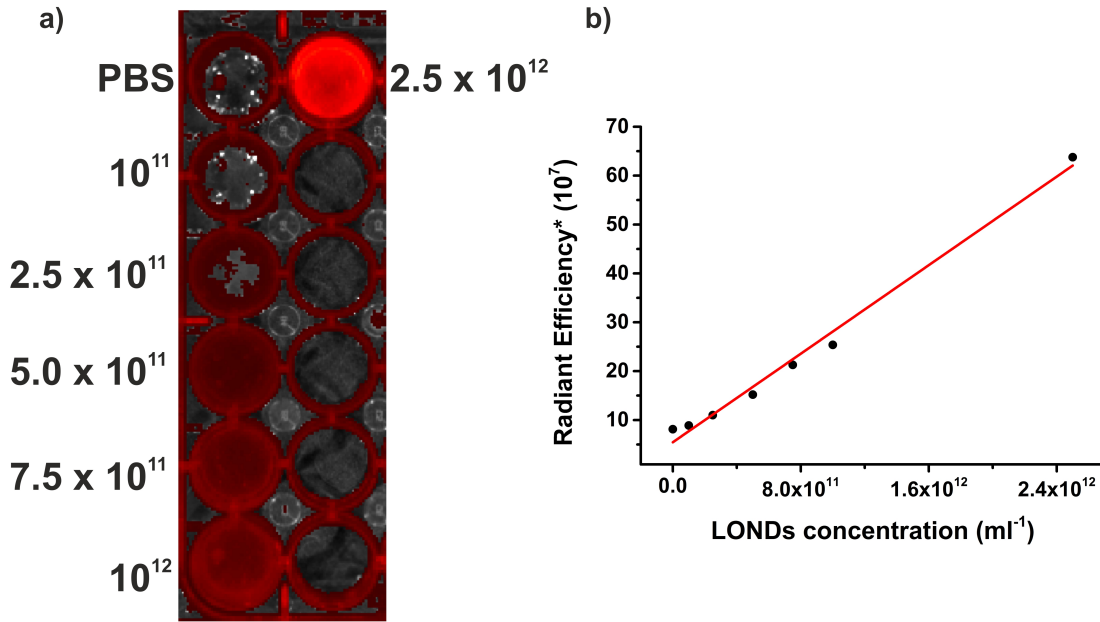


Figure 6.2: a) Dilutions of LONDS encapsulating Qdots were placed in a well-plate for IVIS imaging, with concentrations ranging $10^{10} - 10^{13}$ ml^{-1} . The fluorescence signal recorded by IVIS was superimposed to the optical image of the same region. b) The radiant efficiency (*with units $\frac{\text{photons/s/cm}^2/\text{str}}{\mu\text{W/cm}^2}$) against the LONDS concentration was fitted to a linear regression.

IVIS was used to study the dependence of the Qdots concentration in LONDS on the fluorescence signal. Dilutions of LONDS in PBS were placed in a 24-well plate for imaging. Sequences of excitation/emission wavelength pairs were tested, in order to maximise the

fluorescence signal recorded; the sample was excited with a $\lambda_{ex} = 535$ nm light, and the emission filter was set to record $\lambda_{em} = 820$ nm. Figure 6.2a shows an image of a section of the well plate containing sequential dilutions of LONDS. In this image, the epi-fluorescence signal is superimposed to the bright field picture. The concentration of the LONDS (expressed as the number of particles per ml, ml^{-1}) in each well is indicated next to the image. This image demonstrates that home-made Qdots were detectable using the IVIS system, and also that Qdots encapsulated in LONDS could be detected. Circular ROIs that matched the shape of each well were used to determine the radiant efficiency of each sample, which were then plotted against the concentration of the LONDS and fitted to a linear regression, as shown in figure 6.2b. As expected, an increase in the number of LONDS in the solution, and therefore of the number of Qdots in the well, translated into an increase of the fluorescence signal detected by IVIS. This suggests successful encapsulation of Qdots in the LONDS, and also good retention upon sample cross-filtration.

6.2 Encapsulation of Calcein AM

Calcein AM is a molecule that remains non-fluorescent until cleaved by sterases once in the cytoplasm of a live cell. This property made calcein AM a candidate to study the release of the LONDS contents (section 4.3.3, on page 60).

For LONDS preparation, calcein AM was dissolved in triacetin at 1.4 mg/ml prior to the addition of the oil to the dried lipid (section 5.1, page 71). Triacetin LONDS encapsulating calcein AM were sized using qNano. Blockages arose using a 200 nm pore for sizing the LONDS in the sample, which could be due to the polydispersity of the sample, or calcein AM agglomerates not encapsulated in the LONDS. Therefore, a 800 nm pore was used for the sizing, which could give rise to a miscounting of the smaller LONDS present in the solution, as their blockade signal would be lost against the background. Indeed, the average size for the sample was found to be 320 nm, which is larger than any other triacetin LONDS preparation. To test the encapsulation and retention of calcein AM in the LONDS, the absorption of the cross-filtered LONDS sample (at a concentration of about 10^{10} LONDS/ml), and the fraction of the permeate collected for the first 15 min of cross-filtration, were measured in a spectrophotometer (section 3.3.2 on page 32). The goal of the experiment was to determine whether calcein AM was retained in the LONDS

upon cross-filtration, or if it was removed during the filtration process. Figure 6.3 shows the absorption of the cross-filtered LOND sample, as well as the absorption of the liquid permeated during the first 15 min of cross-filtration. The absorption of calcein AM in triacetin is shown for comparison, with a characteristic double peak absorption around 284 nm (figure 4.12, page 62). The absorption of the permeate suggests that a fraction of calcein AM was washed from the sample, as it partially retained the the maximum absorbance at 280 nm. Using the linear regression from the calibration curve of calcein AM in triacetin, $y = (3.4 \pm 0.2) \times 10^{-3}x$, the concentration of calcein AM in the permeate was calculated, resulting in $88 \pm 5 \mu\text{g/ml}$. This indicates that there were $\sim 880 \mu\text{g}$ of calcein AM in the volume collected during the first 15 min of the cross-filtration, a 60% of the total amount used for the preparation of this LOND sample. The absorbance of the cross-filtered triacetin LOND sample did not show the characteristic peak observed for calcein AM in triacetin. This could be due to two reasons: 1) light scattering from the LONDS could prevent encapsulated calcein AM molecules from absorbing light¹; 2) calcein AM could be not encapsulated or retained in the LONDS and quickly washed out during cross-filtration of the sample. Calcein AM is a highly lipophilic dye, able to rapidly cross cellular membranes. [285] Hence it is possible that the lipophilicity of the compound facilitates its release from the LONDS core into the aqueous solution. Several studies have investigated the release of the fluorescent analogous of calcein AM (calcein) from liposomes. These studies found that the compound was able to permeate through the liposomal bilayer without disrupting it; furthermore around 8% of calcein encapsulated in POPC liposomes permeated to the surroundings within 15 h. [286, 287] The evidence in the literature suggests that a similar process could take place for calcein AM encapsulated in LONDS. This could result in an unwanted dependence of the concentration of calcein AM with the time since preparation, which is not desirable unless the LOND samples were to be used immediately after production.

¹As it will be discussed in the next section, when determining the concentration of CA4 in LOND samples, the use of a solvent to such as DMSO to break the LONDS and release their contents helped reducing light scattering.

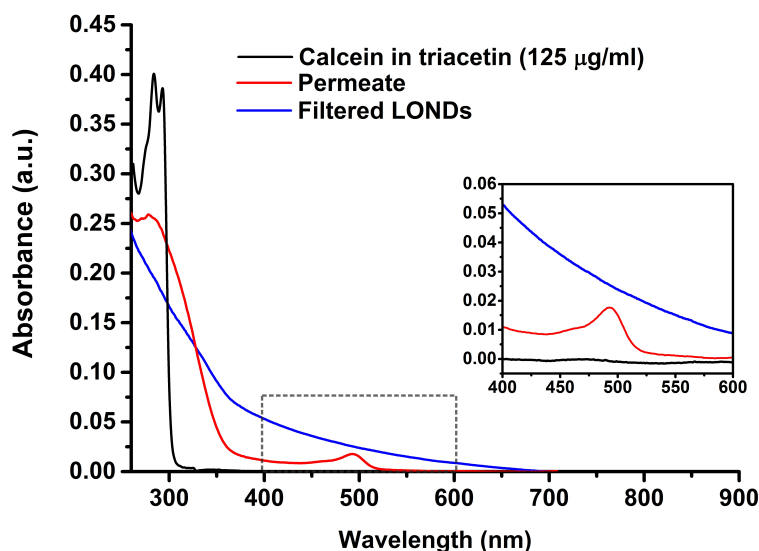


Figure 6.3: Absorption of cross-filtered triacetin LONDS encapsulating calcein AM and of the fraction of liquid permeated during cross-filtration. The absorption of calcein AM diluted in triacetin is shown as comparison. The inset shows a zoom in of the region 400 – 600 nm.

6.3 Encapsulation of CA4

The hydrophobic drug CA4 was found to be soluble in triacetin and tripropionin (section 4.4.1 on page 63). Following these results, CA4-containing LOND samples utilising triacetin and tripropionin were prepared.

As for LOND preparations encapsulating hydrophobic drug mimics, CA4 was first dissolved in the oil and then added to the dried lipid. The concentration of CA4 encapsulated in the LONDS was determined by studying the absorption spectra of the drug. To do this 10 μl of LOND solution was dispersed in 990 μl of DMSO. DMSO is known to modulate the permeability of lipid membranes and also to be able to dissolve lipid, thus it was used to release the LONDS contents. [288–290] The addition of DMSO reduced light scattering seeing previously during the recording of absorption spectra of intact LONDS, improving the quality of the recorded data. The maximum absorption wavelength was expected to be around $\lambda = 309$ nm. Upon determination of the position of the maximum absorption peak, the calibration curves produced for the drug in triacetin and tripropionin (section 4.4.1, page 63) were used to determine the concentration of the drug in the LOND samples. Dialysed (section 5.1.1, page 73) and unfiltered samples were compared, in order to determine whether CA4 was retained in the LONDS or leaked to the solution.

Figure 6.4a shows the absorption recorded for triacetin LONDS containing CA4, diluted in DMSO. These LONDS were stabilised with POPC + 5% biotin-PEG2000-DSPE + 0.1% Atto 590 DOPE, and the concentration of CA4 in the precursor oil was 25 mg/ml. This sample is referred to as *sample 1*. Figure 6.4b shows the absorption of CA4 in a triacetin LOND sample prepared with 50 mg/ml of CA4 in the precursor oil. This was done in order to increase the concentration of the drug in the final LOND sample. This sample will be referred to as *sample 2*. The light absorption of dialysed and unfiltered fraction of the LOND samples 1 and 2 were recorded. A white precipitate was observed in the bottom of the vials upon leaving the samples upright for a few hours, for both samples. To determine whether the precipitate contained CA4, absorption measurements of the supernatant, for both the dialysed and non-filtered samples, were taken. The maximum absorption was at $\lambda = 309 \text{ nm}$, which is in agreement with the absorption maximum previously found for CA4 in triacetin (figure 4.15). Both figure 6.4a and b show a reduction in the absorption between the unfiltered and the dialysed sample, and more significantly, between the whole sample and the supernatant fraction.

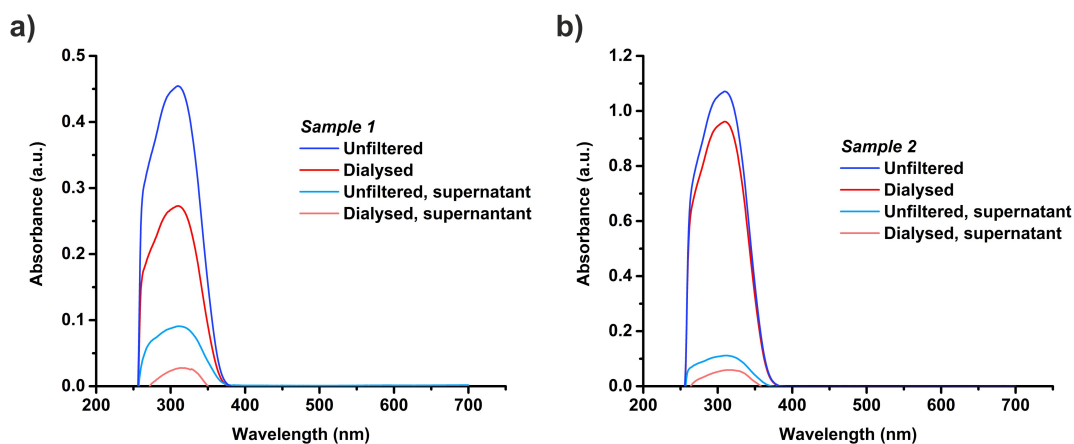


Figure 6.4: Absorption of CA4 encapsulated in triacetin LONDS. The absorption corresponds to $10 \mu\text{l}$ of LOND sample diluted in $990 \mu\text{l}$ of DMSO. Dialysed and unfiltered samples, as well as the supernatant and the mixed samples were studied in each case. a) *Sample 1* triacetin LONDS prepared with $25 \mu\text{g/ml}$ of CA4 in the precursor oil. b) *Sample 2* triacetin LONDS prepared with $50 \mu\text{g/ml}$ of CA4 in the precursor oil.

Table 6.1 contains the analysis of the results presented in figure 6.4. The table shows the maximum absorption values for each peak and the concentration of CA4 in each case, calculated using the linear regression $y = 0.0287x$. Comparing the concentration of CA4 in the precursor oil used to prepare sample 1 and 2 with the concentration of the drug in the unfiltered samples, the encapsulation of CA4 appeared to be $> 90\%$ in both cases.

Table 6.1: Light absorption and corresponding concentration of CA4 in triacetin LONDS. The concentration of the drug was calculated from the absorption of the drug in each case, and using the calibration curve obtained for different concentrations of CA4 in triacetin, $y = 0.0287x$ (see figure 4.15 on page 65).

	Unfiltered LONDS	Unfiltered LONDS, supernatant	Dialysed LONDS	Dialysed LONDS supernatant
Sample 1				
Absorption	0.454	0.091	0.273	0.028
CA4 ($\mu\text{g}/\text{ml}$)	1580	315	948	97
Sample 2				
Absorption	1.071	0.114	0.961	0.059
CA4 ($\mu\text{g}/\text{ml}$)	3720	387	3340	205

In sample 1, a reduction of around 40% in the concentration of CA4 was observed for between the unfiltered and the dialysed fractions. However, the concentration of CA4 dropped only about 10% in sample 2. This could be due to sample precipitation towards the filtration membrane in the dialysis device, preventing the liquid volume in the sample 2 from being exchanged with the surrounding solution, which would translate into more CA4 retained in the sample. The results for sample 1 point at CA4 transfer from the dialysis device to the surrounding solution. This could be due to two reasons. First, the relatively high solubility of triacetin in water (table 4.1, page 49) could lead to leakage of the triacetin contents of the LONDS, which could then trigger the leakage of CA4 from the LONDS into the triacetin in the surrounding solution. Second, CA4 is a polar molecule that contains large non-polar regions (figure 4.14, page 64), whereas triacetin is a largely polar oil (figure 4.1, page 49). In fact, the dissolution of CA4 in triacetin required multiple vortexing and bath sonication steps, which indicates that the inclusion of triacetin in between the CA4 molecules is not a spontaneous process. It is possible that CA4 molecules or small CA4 agglomerates get coated with excess lipid, as it could be energetically favourable for the phospholipid tails to be in close contact with the non-polar regions of CA4. This hypothetical process could enhance the leakage of the CA4 from the LONDS to the surrounding solution.

There were significant differences in drug concentration between the mixed sample and the supernatant. For sample 1, the reduction of CA4 concentration between the supernatant (top solution, after the white precipitate was formed) and the mixed sample are of 80% and 89% for the unfiltered and dialysed samples, respectively. In the case of

sample 2, the reductions between the supernatant and the whole sample were 89% and 93%, for the unfiltered and dialysed samples, respectively. These results raise the following points:

1. Most of the drug (80 – 93% depending on the case) was contained in the precipitate. This could be due to the presence of large drug agglomerates, which could be lipid coated and would sink to the bottom of the vial.
2. A reduction of the CA4 concentration between the mixed sample and its supernatant, upon precipitation, were observed in all the four cases studied. This suggests that dialysis did not suffice to remove all non-encapsulated drug, and also points at the existence of large drug agglomerates that were not able to cross the dialysis membrane.
3. The concentration of CA4 in the supernatant of sample 1 and sample 2, after dialysis, are 97 $\mu\text{g}/\text{ml}$ and 205 $\mu\text{g}/\text{ml}$, respectively. This suggests that the increase in the amount of CA4 in the precursor oil had an effect on the final, real concentration of CA4 in LONDS; doubling the amount of CA4, from 25 $\mu\text{g}/\text{ml}$ to 50 $\mu\text{g}/\text{ml}$, resulted in approximately double concentration of CA4 in the LONDS solution.

To further test the hypothesis of CA4 being poorly retained in the LONDS an experiment to study its leakage from LONDS was performed. A dialysis tube containing 1 ml of unfiltered sample 1 (concentration of the drug was 1440 $\mu\text{g}/\text{ml}$) was placed in a beaker containing 24 ml of clean PBS, and stirred using a magnetic stirrer (figure 6.5). The experiment was conducted at room temperature. Sample volumes were taken from the PBS volume in the beaker at different times; leakage of the CA4 from the dialysis tube would reflect as an increase in the concentration of CA4 in the volume outside the dialysis tube. The volume of liquid removed from the beaker was replaced with PBS to keep the total volume constant and avoid an artificial increase of the drug concentration. The absorption spectra of all the liquid fractions were obtained, in order to determine the amount of leaked CA4 from the sample to the surrounding solution. Figure 6.6 shows the increase in the CA4 concentration in the surrounding solution within time, determined using the calibration curve obtained for CA4 in triacetin ($y = 0.0287x$). The data was normalised to the initial amount of CA4 in the sample (1440 $\mu\text{g}/\text{ml}$), and the data points were then fitted to $y = 100 \times (1 - e^{k \cdot x})$, where k is the release rate constant. [291] The value

for k was determined from the fitting, resulting $k = (4.6 \pm 1.3) \text{ h}^{-1}$. Only a small increase in the concentration of CA4 was detected after 100 min, suggesting that the diffusion had reached an equilibrium. In fact, the concentration of CA4 at $t = 250 \text{ min}$ was $C = 57.2 \text{ } \mu\text{g/ml}$, which corresponds to $1425 \text{ } \mu\text{g/ml}$ of CA4 in the 25 ml total volume. This implies that all of the CA4 initially in the dialysis tube almost completely diffused out ($\sim 99\%$).

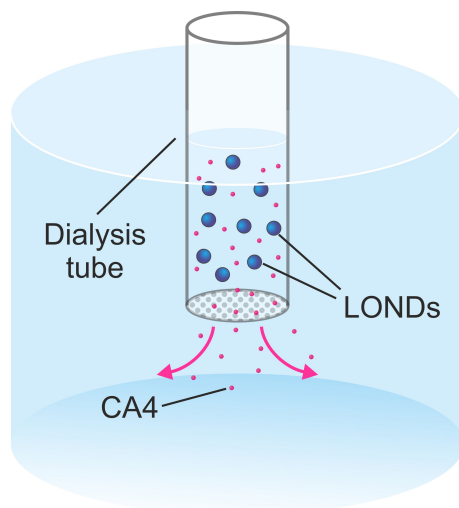


Figure 6.5: Schematic showing the set-up used to study the leakage of CA4 from the triacetin LONDS. A magnetic stirrer was used to increase the buffer exchange between the solution and the volume inside the dialysis tube.

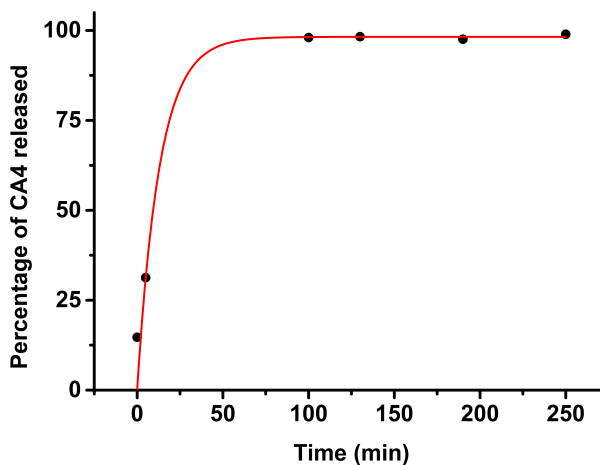


Figure 6.6: Diffusion of CA4 through the membrane in a dialysis tube results in an increase of the drug concentration in the surrounding solution. The concentration of CA4 was determined from the absorption of the samples, and using the calibration curve $y = 0.0287x$. The data points were fitted to $y = 100 \times (1 - e^{-k \cdot x})$. [291]

Following the results on CA4 encapsulation in triacetin LONDS, an alternative oil and lipid shell combination for the formation of CA4-containing LONDS was tested. A sample of tripropionin LONDS encapsulating CA4 was prepared. The lipid shell of these LONDS

was DSPC + 20% cholesterol + 5% biotin-PEG2000-DSPE + 0.1% Atto 590 DOPE. Dialysed and unfiltered tripropionin LONDS, from the same LONDS batch, were analysed to determine the concentration of CA4. The results are shown in figure 6.7. The maximum absorption peak was found at $\lambda = 312$ nm, which is in agreement with previous results (figure 4.16, page 65). The concentration of CA4 was calculated using the calibration curve obtained for CA4 in tripropionin, $y = 0.0377x$, and the results are shown in table 6.2.

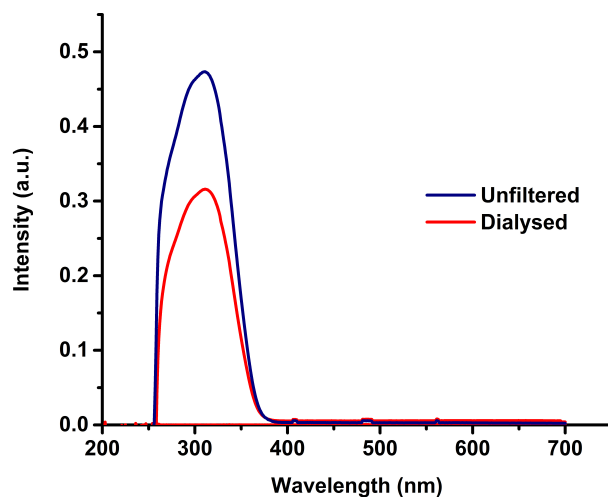


Figure 6.7: Absorption of CA4 encapsulated in tripropionin LONDS. The absorption shown in this figure corresponds to $10 \mu\text{l}$ of LOND sample diluted in $990 \mu\text{l}$ of DMSO. The absorption of dialysed and unfiltered LONDS were studied.

Table 6.2: Absorption and concentration of CA4 in tripropionin LONDS. The concentration of the drug was calculated from the absorption of the drug, and using the calibration curve obtained for different concentrations of CA4 in tripropionin, $y = 0.0377x$ (see figure 4.16, page 65).

	Unfiltered LONDS	Dialysed LONDS
Absorption	0.473	0.316
CA4 ($\mu\text{g}/\text{ml}$)	1254	838

Comparing the amount of the drug in the precursor oil (25 mg/ml) and that detected in the unfiltered sample suggests that the efficiency of the encapsulation was of about 72%. The reduction of the CA4 concentration upon dialysis of the sample was of about 33%, suggesting that the retention of CA4 in tripropionin LONDS was better than in triacetin LONDS. This could be due to the reduced water solubility of tripropionin compared to that of the triacetin. All the absorption spectra measurements were performed at room

temperature. The transition temperature of DSPC, which was the main lipid component of these LONDS shell, is 55 °C, and in contrast, the transition temperature of POPC is -2 °C. This implies that the lipid shell of this LOND sample was more rigid than that of the studied triacetin LONDS. [292] Several studies have investigated the dependence of compound retention in liposomes with the fluidity of their lipid bilayers. [287, 293] In general, these references report that higher fluidity of the lipid shell translates into poorer retention of the compounds in the liposomes. It is likely that the same is true for compounds encapsulated in the LONDS.

6.4 Discussion

This project aimed to use lipid-stabilised oil nanodroplets (LONDS) as capsules for hydrophobic drugs. In-house made Qdots, Nile Red and calcein AM were selected as hydrophobic drug mimics, to be used as substitutes of more expensive therapeutic compounds when performing preliminary studies of LONDS encapsulation efficiency and permeability.

Nile Red was found to dissolve easily in all the candidate oils, and LONDS prepared with oil containing Nile Red looked alike to *empty* LONDS, in terms of size and concentration. Fluorescence tracking of LONDS encapsulating Nile Red was tested with epifluorescence microscopy, showing that individual dots could be detected (section 5.6.2, on page 5.6.2). No systematic studies to test possible leakage of Nile Red from the LONDS have been performed. However, the fluorescence of Nile Red is known to highly quench when in water, [222, 294] which would itself be a mechanism for detecting permeation of Nile Red into the solution if occurred.

Hydrophobic Qdots were found to solubilise in squalane and thus encapsulated in squalane LONDS. The encapsulation efficiency of the Qdots in LONDS was studied by comparing the absorption spectrum of an unfiltered fraction of the sample and the cross-filtered one. The spectra showed a light absorption difference of about 7% between the unwashed LONDS sample and the cross-filtered fraction, which suggested an encapsulation efficiency of about 93%. The loss of fluorescence material could be due to individual Qdots, or small Qdot agglomerates, coated with lipid, and with masses below 60 kDa, that may have been able to filter out. The fluorescence signal from Qdots encapsulated in these LONDS was also tested using a fluorometer. This experiment found increasing

fluorescence intensities with increasing LONDS concentration up to 2.5×10^{12} LONDS/ml, after which point the intensity was found to decrease linearly with further increases in LOND concentration. This was attributed to light scattering by LONDS as their number in solution increased, which would translate into an artificial reduction of the photons reaching the photodetector. IVIS was also used to test the fluorescence of Qdots encapsulated in LONDS. In this case, different dilutions of cross-filtered LONDS were placed in a 24-well plate for imaging. After performing an optimisation of the excitation/emission wavelengths, the sample was excited with $\lambda_{ex} = 535$ nm, and the emission recorded at $\lambda_{em} = 820$ nm. These wavelengths are slightly different to those determined with the fluorometer, respectively $\lambda_{ex} = 589$ nm and $\lambda_{em} = 790$ nm (figure 4.6, on page 56), and are thought to relate to the sensitivity of the IVIS detectors. As expected, the radiant efficiency was found to increase linearly with the LONDS concentration. In contrast to the fluorescence study using the fluorometer, no maximum (followed by a decrease) in the fluorescence signal was observed in the case of IVIS. This is likely due to the fact that in IVIS the illumination source and the detector are placed on the same side of the sample, whereas in the fluorometer the emitted light has to travel through the sample, being attenuated by LONDS scattering.

Problems during production were found for LOND samples encapsulating Qdots. Specifically, the Qdots agglomerated at the homogenising nozzle, causing blockages that prevented the Emulsiflex from correct functioning. Attempts to reduce the agglomeration of Qdots before the ultra-high pressure homogenisation stage included extended sample blending in the polytron (> 30 min) and an added bath sonication of the crude emulsion. However these did not significantly reduce the blockages in the Emulsiflex. Because of these issues no further experiments were performed with this type of LONDS. Alternative LONDS production methods, such as sonication, could help overcome this problem and allow for preparation of Qdots encapsulated in LONDS. [43]

Calcein AM is molecule whose fluorescence is only triggered upon cleavage by cellular sterases. The polarity of the calcein AM made it impossible to dissolve in the candidate oils other than in triacetin, and therefore this oil was use to produce LONDS encapsulating calcein AM. The study to determine its encapsulation efficiency involved the measurement of the light absorbed by the cross-filtered LONDS sample, as well as that of the permeate fraction produced during the first 15 min of the cross-filtration process. The results from this experiment suggest that a large fraction of the calcein AM in the LONDS sample

washed from the solution upon cross-filtration. This pointed at either low efficiency of the incorporation of the calcein AM into the LONDS, or poor retention post production. Although several studies have investigated the permeability of calcein through the liposomal bilayer, [286, 287, 295] there are no references in the literature to essays performed with calcein AM encapsulated in oil droplets. Instead calcein AM is used for cell staining, and typically added to the cell environment in DMSO. [108, 296–298] As a result of these observations, calcein AM was discarded as hydrophobic drug mimic and no further experiments were performed with this compound.

Two drugs were chosen in this project: decitabine and the hydrophobic drug combretastatin A4 (CA4). Decitabine is a water soluble compound that quickly degrades when dissolved in aqueous solution (section 4.4.2, page 66). It was hoped that encapsulation of decitabine in LONDS could help enhancing its delivery *in vitro* by keeping the compound away from water, thus preventing its degradation. CA4 was chosen due to its hydrophobic profile, which impairs the delivery of the drug *in vivo*, yet its high efficacy when tested *in vitro* (section 4.4.1, page 63). Initially, both compounds were tested for solubility in the candidate oils. Decitabine was found difficult to disperse it in the candidate oils, as discussed on page 66, in chapter 4, which eventually lead to discarding decitabine as a candidate drug. CA4 was found to dissolve in triacetin and tripropionin, and two samples of triacetin LONDS encapsulating CA4 were prepared. For each sample, the concentration of CA4 in the precursor oil was 25 mg/ml and 50 mg/ml. Following sample preparation a white precipitate was observed in both samples, which was hypothesised to contain a large amount of non-encapsulated drug. To test this hypothesis, and study the encapsulation efficiency of CA4 in the LONDS, the absorption of CA4 in dialysed and unfiltered fractions of the samples, as well as of the whole sample and the supernatant obtained after sample precipitation were obtained. The results shown in figure 6.4 and table 6.1 point at a large percentage of the CA4 (80 – 93%) contained in the precipitate, suggesting poor drug encapsulation in the LONDS, and/or poor retention. A fraction the the drug was also lost during dialysis; specifically 40% for sample 1 and 10% for sample 2. To test the encapsulation/retention of CA4 LONDS, a study was conducted to determine the leakage of CA4 from a LONDS sample placed in a dialysis tube. Gradual CA4 diffusion from the inside of the tube would increase the concentration of the drug in the buffer solution. This hypothesis was tested obtaining the absorption spectra of small liquid fractions collected at different times, and using the calibration curve for CA4 in triacetin to calculate the

concentration of the drug in the solution. The results found in this experiment showed that all the drug initially contained in the dialysis tube (1140 $\mu\text{g}/\text{ml}$) was free to diffuse through the dialysis membrane and to the surrounding solution. All the drug permeated in about 1 h.

The results obtained for triacetin LONDS encapsulating CA4 suggested that these LONDS were not suitable for the delivery of CA4. As discussed previously, the high solubility of triacetin in water could give rise to problems such as leakage of the LONDS contents after production, and even complete solubilisation of the oil in the water phase prior to LONDS formation. Tripropionin was tested as a candidate oil, due to its similarities with triacetin for dissolving drugs and its reduced water solubility. Solubility tests for CA4 in tripropionin were promising (section 4.4.1, page 63) and a tripropionin LOND sample containing CA4 was prepared. For LOND formation with this oil, an alternative lipid shell was used, composed of DSPC + 20% cholesterol + 5% biotin-PEG2000-DSPE + 0.1% Atto 590 DOPE. This lipid shell has been used for nanoemulsion stabilisation before. [45,50] Encapsulation efficiency of CA4 in tripropionin LONDS was found to be of around 70%, and the reduction in the concentration of CA4 in the sample during dialysis was of about 33%, which constitutes a significant improvement with respect to CA4 in triacetin LONDS. Both the physical characteristics on tripropionin and the more rigid lipid shell could play a role in enhanced retention of the CA4. These results are promising, and more experiments to study drug retention and leakage in detail will be needed.

Chapter 7

Topic: Attachment of LONDS to model lipid membranes

This chapter describes the study of the attachment of LONDS to supported lipid membranes as a model for the MB surface. QCM-D was used to determine the binding of StreptAvidin/NeutrAvidin to a range of solid supported bilayer membranes (SBLMs) and to study the specific and not specific binding of LONDS to SBLMs. A number of different SBLMs/LONDS combinations and linking chemistries were explored. Specifically, the biotin-NeutrAvidin, the maleimide-thiol and the pyridyl disulphide-thiol linking chemistries were examined. Whereas biotin-NeutrAvidin has been widely used in biotechnological applications due to its high affinity, injection of exogenous proteins *in vivo* gives rise to immune responses that could impair the use of drug delivery systems built with this chemistry. Thus there was an interest in probing alternative linking chemistries for the attachment of LONDS to model membranes, towards the attachment onto MBs to form MB-LONDS.

7.1 A need to assess LOND binding

The aim of this study was to produce a novel complex architecture combining MBs and LONDS for hydrophobic drug delivery. In these composites, the MBs act as a vehicle for the LONDS, which contain the drug in their oil core. The attachment of LONDS to the MB surface is key in the assembly of the architectures. Correct functioning of the attachment mechanism must be confirmed to ensure the optimal formation of MB-LONDS. However, directly monitoring the attachment of LONDS to MBs is a complex problem. The sizes

of the MBs (typically $< 8 \mu\text{m}$) and the LONDS ($\sim 100 - 250 \text{ nm}$) challenges the use of microscopy for studying the assembly of the architectures. Although fluorescently tagged LONDS were shown to be traceable with fluorescence microscopy (figure 5.17 on page 98), quantification of the binding to a MB surface would be limited by their sub-resolution size and by rotations of the MB. In addition, MBs have relatively short lifetimes, preventing extended observation of LONDS attachment to the MB shells.

To reduce the complexity of the MB-LONDS system the MB shell was replicated with a SBLM. SBLMs are robust, easy to prepare systems that find a vast number of applications for the study of lipid membranes *in vitro*. [196, 299–302] The addition of biotinylated lipid in to the SBLMs allows for the binding of LONDS via the biotin-NeutrAvidin link chemistry, closely resembling the process occurring on the MB surface. The biotin-NeutrAvidin chemistry was chosen for LOND attachment in analogy to previous studies which have reported the successful assembly of MB-liposome complexes using this interaction . [78, 133] Alternative linking chemistries such as the pyridyl disulphide (PDP)-thiol and the maleimide-thiol were also explored by incorporating a lipid modified with the anchoring molecule of interest into the SBLM. QCM-D was chosen to monitor the LONDS binding experiments as it allows for precise observation of small mass changes occurring on the QCM-D sensors (section 3.6, on page 38), and it is therefore not restricted by the dimensions of the LONDS.

The attachment experiments were initiated by evaluating the binding of StreptAvidin to SBLMs containing different percentages of biotin-PEG2000-DSPE. Once the attachment of the protein was confirmed, a set of experiments aimed to monitor the attachment of LONDS to the SBLMs were carried out. Three different assembly chemistry were studied:

1. Biotin-StreptAvidin(or NeutrAvidin)¹, incorporating 5% biotin-PEG2000-DSPE into the SBLM/LONDS. Control experiments included SBLMs containing 5% PEG2000-DSPE (non biotinylated), and also absence of PEG chains (POPC only SBLMs). These experiments were performed with both triacetin and squalane LONDS.
2. PDP-thiol chemistry, incorporating 5% PDP-PEG2000-DSPE to the SBLM/LONDS. Control experiments included SBLMs with 5% PEG2000-DSPE (no PDP). These experiments were performed with squalane LONDS.

¹no differences between the binding of StreptAvidin or NeutrAvidin to biotin have been reported.

- Maleimide-thiol chemistry, adding 5% maleimide-PEG2000-DSPE to the SBLM/LONDS. Control experiments included SBLMs with 5% PEG2000-DSPE (no maleimide). The experiments were performed using squalane LONDS.

7.2 Binding affinity of biotin-Streptavidin

As a preliminary study, the binding of StreptAvidin to biotin incorporated into SBLMs was studied using QCM-D (figure 7.1). The binding of the StreptAvidin to the biotin-PEG2000-DSPE translates into a frequency change in QCM-D, as the mass on the sensor changes. For a simple molecular interaction, the StreptAvidin-biotin binding can be described with the Hill-Langmuir equation [303]

$$f = f_{max} \frac{[StreptAvidin]}{[Streptavidin] + K_d} \quad (7.1)$$

where $[StreptAvidin]$ is the concentration of the protein in the solution, and K_d is dissociation constant at half-maximal occupation of the binding sites. [304]

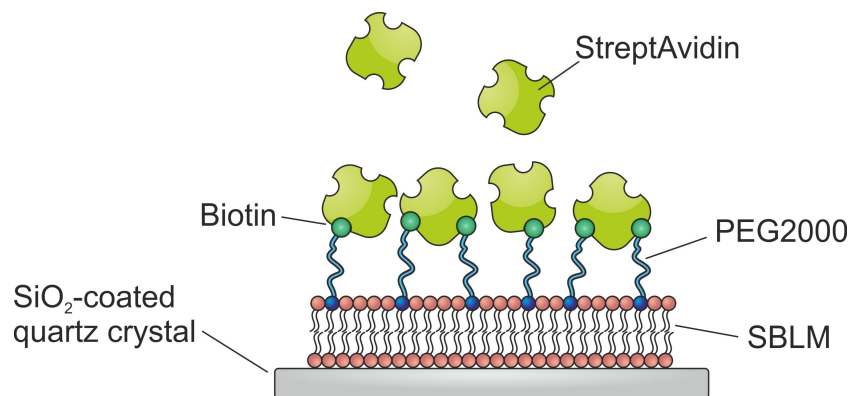


Figure 7.1: Schematic showing the binding of StreptAvidin to biotin-PEG2000-DSPE in a SBLMs. The kinetics of this binding were studied in QCMD. SBLMs containing different percentages of biotin-PEG2000-DSPE were formed on SiO₂-coated QCM-D sensors and then coated with StreptAvidin.

For these experiments, SBLMs were formed on SiO₂-coated QCM-D sensors as described in section 3.6.2 (41). Three different cases were studied, and in each of them the SBLM was prepared including a different concentration of biotin-PEG2000-DSPE. The composition of the three different SBLMs was: 1% biotin-PEG2000-DSPE + 99% POPC, 5% biotin-PEG2000-DSPE + 95% POPC and 10% biotin-PEG2000-DSPE + 90% POPC

SBLM. Two control SBLMs were used in these experiments, namely, a 5% PEG2000-DSPE + 95% POPC SBLM, and a 100% POPC. These control experiments were performed to rule out non-specific interactions between the StreptAvidin and the SBLMs, when no of biotin was added to the SBLMs. Following SBLMs formation and subsequent PBS and MilliQ rinses, three different protein concentrations were consecutively added to each SBLM. The concentration of StreptAvidin was adjusted to be $4\times$, $8\times$ and $16\times$ the number of available biotin-PEG2000-DSPE in each SBLMs. This meant that the concentration was higher for experiments with SBLMs containing higher biotin-PEG2000-DSPE, as the ratio of StreptAvidin to biotin was kept constant (table 7.1). In each experiment protein solution was flowed into the flow chamber at 0.1 ml/min until the frequency reached a plateau, which indicated full coverage of SBLMs with StreptAvidin.

Table 7.1: Concentrations of StreptAvidin used for each SBLM.

SBLM composition	biotin-StreptAvidin ratio	[StreptAvidin] (nM)
1% biotin-PEG2000-DSPE + 99% POPC	4x	11
	8x	23
	16x	45
5% biotin-PEG2000-DSPE + 95% POPC	4x	56
	8x	113
	16x	225
5% biotin-PEG2000-DSPE + 95% POPC	4x	56
	8x	113
	16x	225
10% biotin-PEG2000-DSPE + 90% POPC	4x	113
	8x	225
	16x	451
(Control) 100% POPC	4x	56
	8x	113
	16x	225
(Control) 5% PEG2000-DSPE + 95% POPC	4x	56
	8x	113
	16x	225

Figure 7.2 contains the QCM-D data obtained for all the cases studied. Frequency and dissipation changes are shown for each experiment, and the time at which each protein concentration was flowed in the chamber is indicated on each graph. SBLMs formed successfully in figure 7.2a-d. The QCM-D response on the formation of the SBLMs is characterised by an initial drop in the frequency, accompanied by an increase in the dis-

sipation signal. Vesicle rupture on the surface results in removal of material adhered to the sensor, which translates into an abrupt reversal in the frequency and dissipation signals (section 3.6.2, on page 41). For case e in figure 7.2, which used vesicles containing 10% biotin-PEG2000-DSPE, the pattern observed for the change in frequency and dissipation does not fit with the description associated to SBLM formation. In this case it is possible that vesicles simply adhered on to the surface of the QCM-D sensor, protected by the PEG chains, which should adopt the brush configuration at this specific molar percentage. [305, 306]

The control experiments (figure 7.2a,b) showed no changes in frequency and dissipation upon addition of the StreptAvidin solution, suggesting that non-specific binding of the protein did not occur, thus confirming the specificity of the binding of StreptAvidin to the biotin-PEG2000-DSPE. Binding of StreptAvidin was observed in all cases involving biotinylated SBLMs (figure 7.2c,d,e). For the SBLMs containing 1% and 5% biotin-PEG2000-DSPE,² full surface coverage with StreptAvidin took place within ~ 10 min of injection. For the 10% biotin-PEG2000-DSPE case, full coverage of the SBLM occurred within 20 min of the injection. Provided that the ratio of biotin/StreptAvidin was kept constant throughout the experiment, full coverage was expected to take place in similar time frames. For the reasons explained above, vesicles containing 10% biotin-PEG2000-DSPE are thought to remain intact on the SiO₂ surface. It is therefore possible that the slower kinetics of the StreptAvidin in this case, as compared to the 1% and 5% cases, could be due to its difficulty in accessing the binding sites. This possibility is illustrated in figure 7.3.

The frequency changes recorded upon the addition of the StreptAvidin were plotted against the concentration of the protein solution for cases c, d and e in figure 7.2. The dissociation constant K_d could be determined from the fitting of the plots to equation 7.1. For SBLMs containing 1%, 5% and 10% biotin-PEG2000-DSPE, the value of K_d was found to be $K_d = (8.3 \pm 0.2) \times 10^{-10}$ M, $K_d = (7.1 \pm 1.4) \times 10^{-10}$ M and $K_d = (2.6 \pm 1.0) \times 10^{-10}$ M, respectively. These values fall short from the accepted value $K_d \approx 10^{-14}$ M, at $pH = 7$ and 25 °C. [307] These differences could be due to the level of detection of the instrument, which could limit the accuracy of the measurement. Another reason behind this discrepancy could be the existence of inhomogeneities in the SBLMs (as for example

²there are around 4.3×10^{12} and 8.5×10^{11} biotin binding sites in the 1% and 5% biotin-PEG2000-DSPE SBLMs, respectively

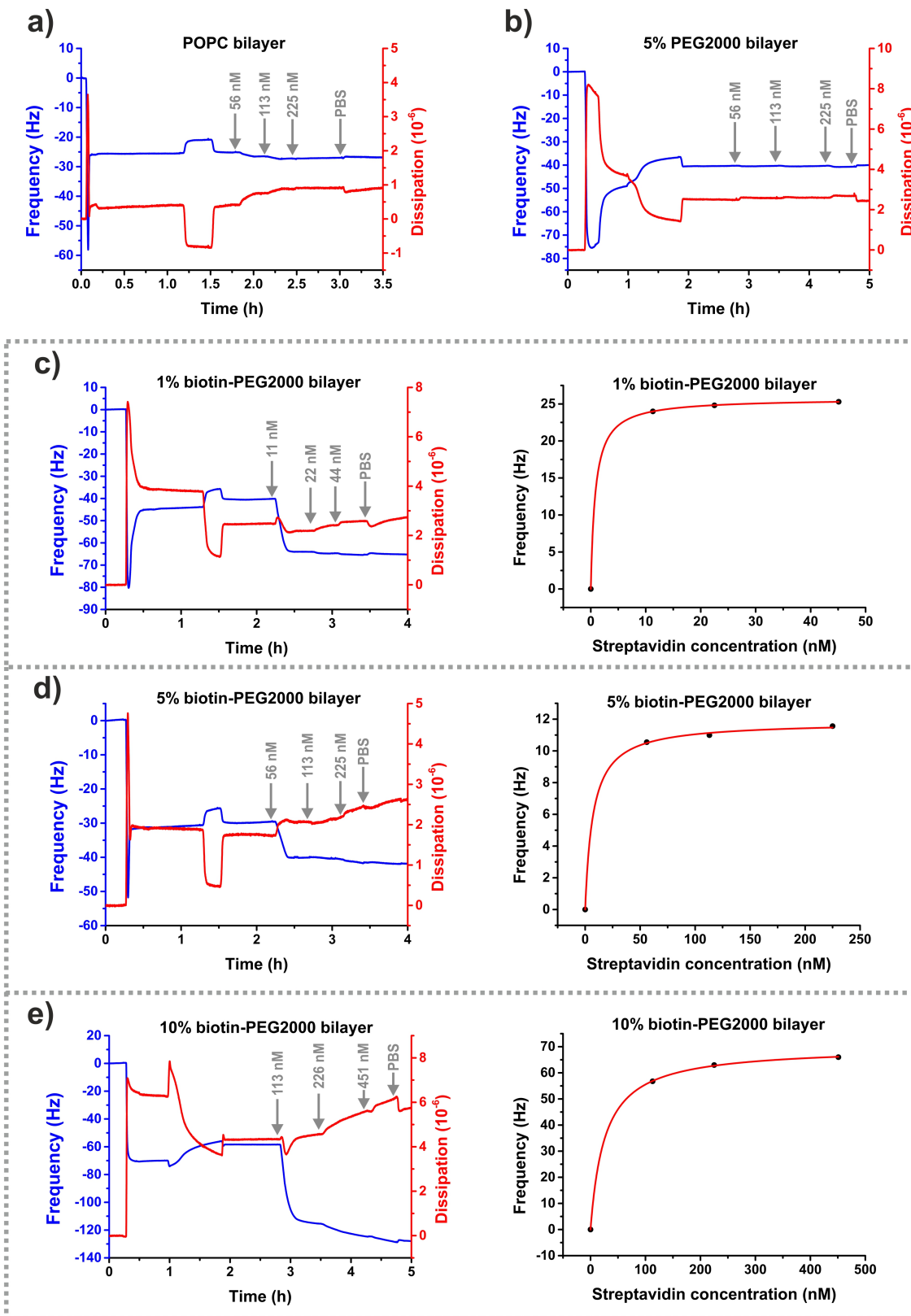


Figure 7.2: Changes in frequency and dissipation of a SiO₂-coated quartz crystal as a result of the binding of StreptAvidin to biotinylated SBLMs, as measured by QCM-D. The graphs were produced averaging overtones 5th-11th. The gray arrows indicate the times at which different concentrations of StreptAvidin solution were added to the SBLMs. Frequency changes were plotted against the concentration of StreptAvidin in cases c, d, e, and fitted to equation 7.1.

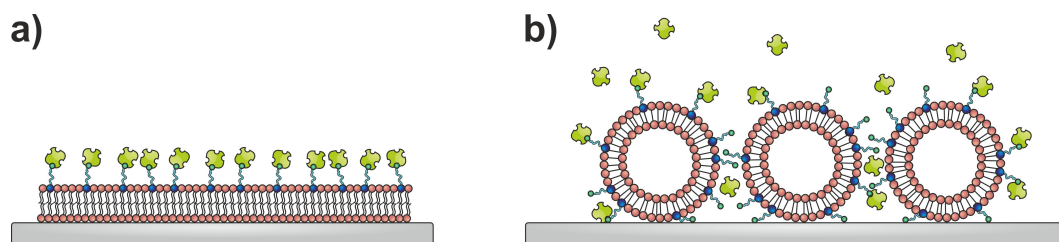


Figure 7.3: Two possible scenarios for the StreptAvidin binding to QCM-D sensors. a) SBLMs form from rupture of vesicles containing biotin-PEG in the mushroom regime ($< 5\%$), and biotin binding sites are fully accessible to the StreptAvidin. b) Vesicles with 10% biotin-PEG2000-DSPE do not rupture to form flat SBLMs, but instead they adsorb onto the surface. In this case, biotin is not restricted to a 2D surface and thus StreptAvidin binding is potentially delayed.

regions of absorbed, non-ruptured vesicles instead of a flat lipid bilayer), increasing the number of biotins available and thus changing the biotin/StreptAvidin ratio.

7.3 LONDS attachment to SBLMs

This section is concerned with the attachment of LONDS to SBLMs mimicking the MB shell. The final goal of this project was to build MB-LONDS by attaching LONDS to MBs via the high affinity interaction of biotin-NeutrAvidin. As mentioned above, the use of biotin-NeutrAvidin for the assembly of drug delivery vehicles is limited by the immunogenicity of injected proteins and thus there was an interest in exploring alternative linking chemistries. Hence the attachment of LONDS to SBLMs was studied using three different linking chemistries: biotin-NeutrAvidin, PDP-thiol and maleimide-thiol.

The following subsections use the notation ‘L’ for LONDS and ‘B’ for SBLMs. A subindex provides information about the component of interest in the system i.e. the one responsible for the interaction between LONDS and SBLMs. For example L_{MAL} refers to a LOND formed with POPC + 5% maleimide-PEG2000-DSPE, whereas B_0 denotes a SBLMs composed of POPC only (blank).

7.3.1 Three-layer systems on QCM-D

The attachment of LONDS onto SBLMs that mimic the shell of a MB is a three-step process that requires: i) the formation of a SBLM, ii) functionalisation of the SBLMs

5% BPEG bilayer + NEUTRAVIDIN + 5% BPEG vesicles

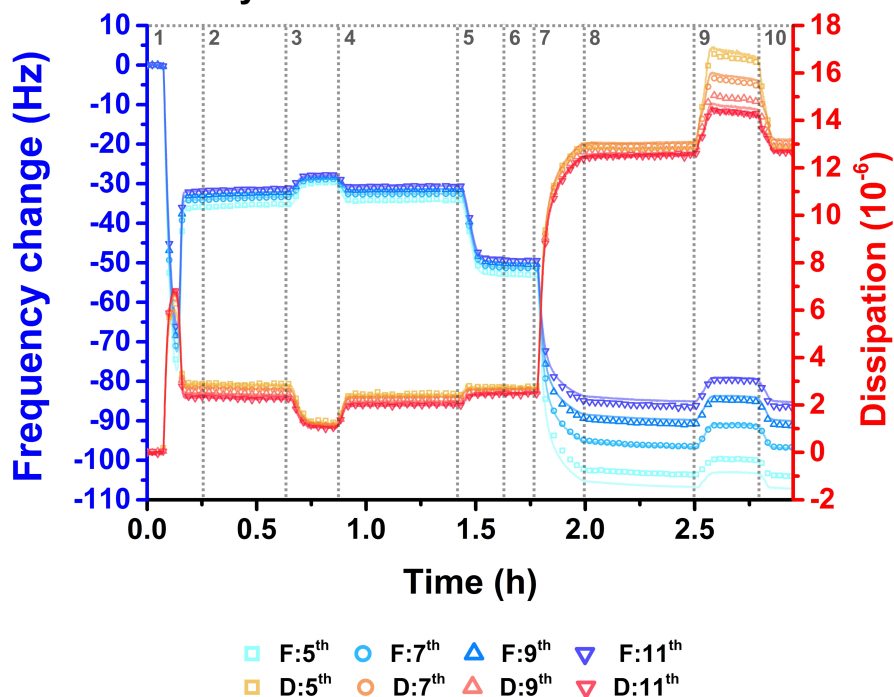


Figure 7.4: Example of a QCM-D experiment of the formation of a three-layer system. In this case biotin-PEG2000-DSPE-containing SBLM, NeutrAvidin functionalisation and attachment of biotinylated vesicles. The experimental points for each overtone (5^{th} – 11^{th}) are shown as open symbols. Fitting to the Kelvin-Voigt viscoelastic model is shown in solid lines. The different experimental stages are delimited by dotted vertical lines, and they are: 1 SBLMs formation; 2 PBS rinse; 3 MilliQ rinse; 4 PBS rinse; 5 NeutrAvidin attachment; 6 PBS rinse; 7 biotin-containing vesicles attachment; 8 PBS rinse; 9 MilliQ rinse; 10 PBS rinse.

with a bridging molecule (depending on the chemistry used, NeutrAvidin or DTT), and iii) attachment of LONs. This sequence intercalates PBS and MilliQ rinses that help removing excess material from the sensor chambers (see section 3.6.2, page 41). The subsequent attachment of layers results in a three-layer system that allows for the study of the increase of the mass and thickness of the system adhered to the sensor (SBLM-NeutrAvidin/DTT-LONs) via fitting to the Kelvin-Voigt viscoelastic model.

As an example of the type of data recorded in the LONs attachment experiments, figure 7.4 shows a typical QCM-D experiment for a three-layer system. Specifically, this figure shows the formation of a SBLM containing biotin-PEG2000-DSPE, followed by NeutrAvidin functionalisation and attachment of vesicles containing biotin-PEG2000-DSPE. The data points for frequency and dissipation for overtones 5^{th} - 11^{th} are shown as open symbols.³ The Kelvin-Voigt viscoelastic model was used to fit both the frequency and dissipation signals for each overtone (section 3.6, page 38). The different experimental

³only around 1/100 of the experimental points are shown for clarity of the figure.

Table 7.2: Mass and thickness of the adhered layer onto the SiO₂ sensor for the different experimental stages. These results correspond to the data shown in figure 7.4, and were obtained from the modeling of the experimental results (overtones 5th – 11th) using the Kelvin-Voigt viscoelastic model.

Experimental stage	Number on figure 7.4	Thickness (nm)	Mass adhered (ng/cm ²)
SBLM (in PBS)	2	9.05 ± 0.07	770 ± 7
SBLM (in MilliQ)	3	6.87 ± 0.09	580 ± 9
SBLM-NeutrAvidin (in PBS)	6	12.5 ± 0.1	1062 ± 11
SBLM-NeutrAvidin-vesicles (in PBS)	8	28.5 ± 0.2	2420 ± 124
SBLM-NeutrAvidin-vesicles (in MilliQ)	9	27.7 ± 0.3	2354 ± 25

stages are indicated on the figure as dotted vertical lines. A biotin-containing SBLM was formed first from the absorption and rupture of vesicles on the SiO₂-coated quartz crystal (1). SBLM formation was followed by PBS (2) and MilliQ rinses (3). The system was returned to PBS (4) for NeutrAvidin functionalisation (5), which was performed flowing a 3.8 μM solution of NeutrAvidin into the flow chambers. A PBS rinse (6) removed excess unattached protein. Biotin-containing vesicles attach to the NeutrAvidin previously bound to the SBLM (7). PBS (8) and MilliQ (9) rinses helped ensuring the attachment of the vesicles (or LONDS) was specific. Finally the system was returned to PBS (10). It is interesting to note that the differences between the different overtones signals are small when only a SBLMs was attached to the sensor. This holds true for SBLMs functionalisation with NeutrAvidin. However, vesicle attachment results in wide spread of the signals for the different overtones (from 6 and onwards) as compared to the previous values. This is characteristic of soft layers and it is typically associated to solvent uptake in the layer. In the context of the experiment, intact vesicles attached to a SBLMs encapsulate PBS, which is coupled to the SBLMs once the attachment takes place. Furthermore, the attached vesicles have some degree of freedom for lateral displacement, which is likely to contribute to an increase of the viscosity of the layer.

Table 7.2 contains the results from the fitting of the experimental data shown in figure 7.4. Mass and thickness of the adhered layer are provided for the different experimental stages. Note that only those values corresponding to regions where the frequency and dissipation signals reached steady values are provided. The uncertainties of the values in this table correspond to the standard deviation of the average values over the region of interest. The increase in thickness and mass of the system throughout the experiment was

consistent with the addition of additional layers (i.e. NeutrAvidin and vesicles). The *buffer effect*⁴, associated to the removal of ions from the solution when the system was changed from being in PBS to MilliQ, was noticeable for SBLMs only (difference between regions 2 and 3 on figure 7.4) and also for the system when it was SBLMs-NeutrAvidin-vesicles.

7.3.2 LOND-SBLMs attachment via biotin-NeutrAvidin

Once the binding of NeutrAvidin to SBLMs was confirmed, the attachment of LONDS to NeutrAvidin functionalised SBLMs was studied in QCM-D. These experiments aimed to provide evidence of the viability of the biotin-NeutrAvidin linkage for the attachment of LONDS to a SBLM, and also to rule out possible non-specific interactions between the LONDS and the SBLMs. All these LOND-SBLM combinations are schematically summarised in the figure 7.5. Three LOND surface functionalisations were compared: pure POPC lipid (L_0), POPC lipid + 5% PEG2000-DSPE (L_{PEG}) and POPC lipid + 5% biotin-PEG2000-DSPE (L_{BIO}). Three model MB surfaces were studied: POPC lipid (B_0), POPC + 5% PEG2000-DSPE (B_{PEG}) and POPC + 5% PEG2000-DSPE + NeutrAvidin (B_{BIO}). All nine possible LONDS-SBLMs combinations were studied, for both squalane and triacetin LONDS.

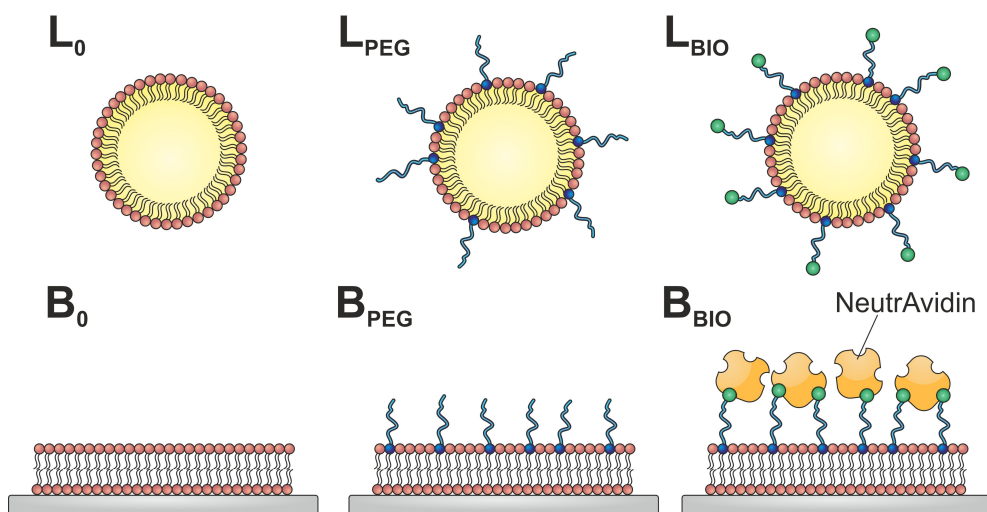


Figure 7.5: The interaction of LONDS and SBLMs was studied on model SBLMs in QCM-D. Nine different combinations of LONDS and SBLMs with different compositions were investigated. L_0 : POPC LONDS; L_{PEG} : POPC + 5% PEG2000-DSPE LONDS; L_{BIO} : POPC + 5% biotin-PEG2000-DSPE LONDS. B_0 : POPC SBLM; B_{PEG} : POPC+ 5% PEG2000-DSPE SBLM; B_{BIO} : POPC + 5% biotin-PEG2000-DSPE SBLM.

⁴increase of the frequency and reduction of the dissipation signal when the system transitions to being immersed in different solutions

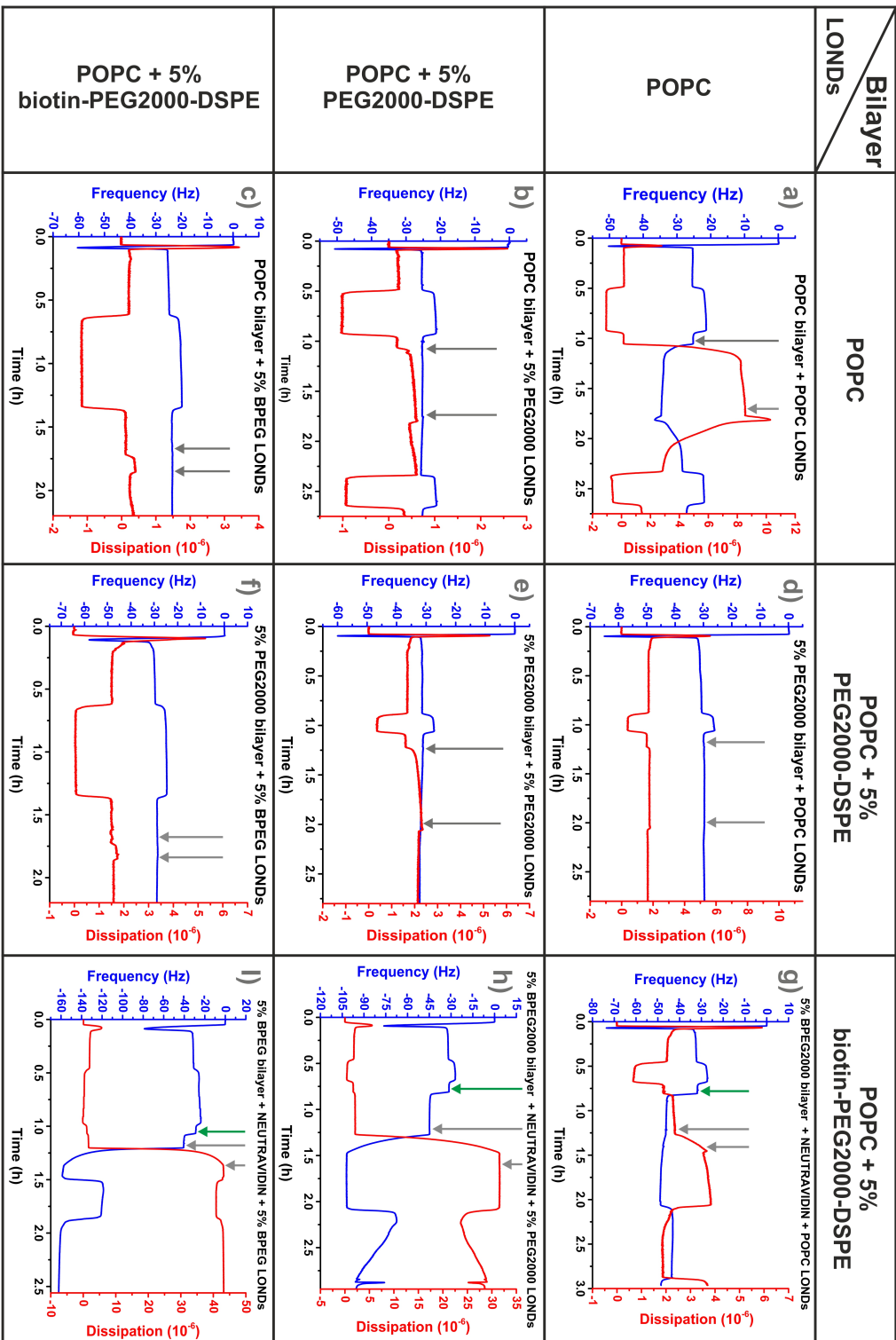
As mentioned above, QCM-D was used to monitor the interaction of LONDS and SBLMs. All of the SBLMs were formed as described in section 3.6.2. SBLM formation was always followed by PBS and MilliQ rinses, to ensure correct SBLM formation and remove excess material. For cases involving B_{BIO} SBLMs, NeutrAvidin functionalisation was done by flowing the protein into the crystal chambers at a concentration of $3.8 \mu\text{M}$. The protein solution was kept flowing until the frequency change reached a plateau, corresponding to total surface coverage with NeutrAvidin. The NeutrAvidin binding step was always followed by a PBS rinse, before the addition of LONDS, to ensure complete removal of unattached protein and avoid agglomeration problems with the LONDS. Following the rinse, LONDS were introduced to the SBLMs at 0.1 ml/min , and at 10^{12} LONDS/ml in the case of squalane LONDS, and 10^{11} LONDS/ml in the case of triacetin LONDS. When changes in the frequency and dissipation signals were observed, the flow of LONDS was kept until the signal reached a plateau. In some cases in where the frequency and dissipation did not reach a steady value (particularly for the $L_{PEG-B_{BIO}}$ and $L_{BIO-B_{BIO}}$ cases) the LOND solution flow was kept on for at least 10 min. Compared to the time that it takes for vesicles to reach the sensor, adhere and form an uniform bilayer (~ 2 min), or the times required for NeutrAvidin to fully coat a SBLM ($< 10 \text{ min}$),⁵ 10 min was considered a long enough time period for LONDS to reach the whole area of the SBLM and interact with it. The addition of the LONDS to the SBLMs was followed by an incubation period that lasted at least 30 min, during which the flow remained stopped. LOND incubation period step was followed by consecutive PBS and MilliQ rinses, to remove unbound LONDS. Within the experiment, changes in frequency and dissipation were monitored for overtones $1^{\text{th}}-13^{\text{th}}$, but only $5^{\text{th}}-11^{\text{th}}$ were used for the fitting to the Kelvin-Voigt viscoelastic model.

The results for all squalane LOND/SBLM combinations are shown in figure 7.6. In this figure, the gray arrows indicate the times at which LONDS were commenced to flow into the flow chambers, and the time at which the PBS rinse was started, respectively. A green arrow marks the time at which NeutrAvidin flow was set, in those cases involving NeutrAvidin. A few conclusions can be drawn from these results.

All cases involving pegylated LONDS and/or SBLMs showed no frequency or dissipation changes over the course of the experiments, indicating no binding of LONDS to the SBLMs. In figure 7.6, these cases are: b) L_{PEG-B_0} , c) L_{BIO-B_0} , d) L_0-B_{PEG} , e) L_{PEG} -

⁵At the same flow rate, 0.1 ml/min

Figure 7.6: Changes in frequency and dissipation of a QCM-D SiO₂-coated quartz crystal for a range of SBLM/squalane LONDS interactions. The graphs were produced averaging overtones 5th – 11th. The gray arrows indicate, in this order, the point at which LONDS were started to flow into the flow cells, and the time at which a PBS rinse was commenced. For experiments involving NeutraVidin, the point at which the protein was flowed is indicated with a green arrow.



B_{PEG} , f) $L_{BIO-B_{PEG}}$ and g) L_0-B_{BIO} . Unchanged frequency signal over time indicated no mass or thickness changes in the SBLMs on the sensor, whereas the unchanged dissipation signal showed that the viscoelastic properties of the system remained constant throughout the experiment. It is important to note that the addition of LONDS reflected as a small increase in the dissipation signal, and that it reverted to the initial value upon rinsing with PBS and MilliQ i.e. removing the LONDS from the surroundings of the SBLM. These results suggest that the presence of PEG chains on the surface of the LONDS and/or SBLMs protected the system against non-specific binding of LONDS. Indeed, PEG chains are added to lipid-based drug delivery systems such as liposomes to enhance their stability and increase their circulation time *in vivo*, as PEG undergoes steric repulsion from the surface of the lipid membrane in which it is embedded, isolating the capsules against agglomeration (see also section 5.3.3 on page 82). [10, 253, 254, 308]

The addition of LONDS stabilised with only POPC to a POPC SBLM (figure 7.6 case a, L_0-B_0), with an initial mass ~ 630 ng/cm², produced some changes in the frequency ($\Delta f = -9$ Hz) and dissipation ($\Delta D = 8.25 \times 10^{-6}$) signals. No changes were observed during the incubation period, suggesting that the interaction had reached a steady state. PBS rinsing resulted in removal of a large fraction of material, as reflected by the change in frequency at this stage, $\Delta f = +6$ Hz, which almost completely restored to initial frequency values. These results suggests that a small fraction of material from the LONDS solutions incorporated into the SBLM, hence the differences in frequency and dissipation. Data fitting to the viscoelastic model (equations 3.9, 3.10) showed that the increase in mass on the sensor, from a SBLM to a SBLM after interaction with LONDS (and subsequent PBS and MilliQ rinses) was (22.0 ± 0.6) ng/cm², whereas the change in thickness of the system was of 14 nm. This value represents the mass change on the sensor assuming homogeneous distribution of the adhered material over the area of the sensor. This would be the case if for example a number of LONDS merged or partially merged with the SBLM, potentially resulting in oil intercalation in the SBLM. [309–311] Specifically, squalane is known to incorporate in lipid bilayers and remain in its midplane. [312] This possibility is illustrated in figure 7.7 Another possible scenario for the LONDS is to remain intact on the SBLM. The recorded mass change (22 ng/cm²) is equivalent to the mass of $\sim 6 \times 10^6$ LONDS over the same area (around 6 LONDS per 100 μm^2). It is impossible to tell the configuration that LONDS adopt when they are in contact with the SBLM from the QCM-D results alone. Combination of QCM-D with another techniques, such as AFM or

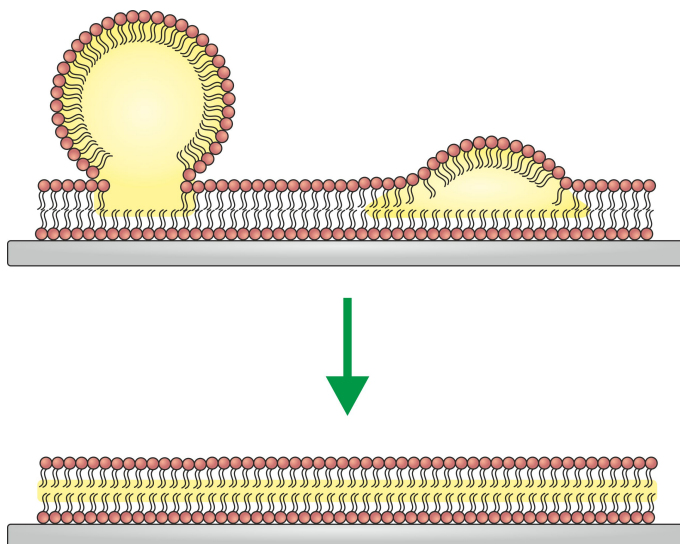


Figure 7.7: Illustration showing a possible scenario for the interaction L₀-B₀. In absence of PEG chains, LONDs could merge with the SBLM, resulting in oil intercalation in the membrane midplane.

ellipsometry [202,301,313] could provide a more complete view of the processes taking place in these systems. The differences observed between the L₀-B₀ study case and those cases that included PEG chains in the LONDs and/or the SBLM (as discussed above) reinforce the hypothesis that the PEG effectively isolates the surface of the LONDs, preventing them from interacting with other lipid barriers.

Functionalisation of B_{BIO} SBLMs with NeutrAvidin (cases g, h and i in figure 7.6) reflected as a change in frequency of around $\Delta f = -10$ Hz, which corresponds to a (2.45 ± 0.02) nm increase in the thickness of the system. This thickness change directly relates to the dimensions of the protein and the result lies close to the dimensions reported previously, $\sim 56 \times 50 \times 40$ Å. [314, 315] The differences between the value reported in the literature and the one obtained in this study is likely to be due to the experimental techniques used to size the protein (AFM and X-ray in the literature, in contrast to QCM-D in this study). NeutrAvidin facilitated the binding of L_{BIO} LONDs to the SBLM, as can be seen in case i in figure 7.6. Frequency and dissipation quickly changed after the addition of the LONDs (indicated by the first gray arrow), and PBS rinsing did not produce further changes in the signals, pointing at irreversible binding of the LONDs to the SBLM. The mass increase was $(11.67 \pm 0.02) \times 10^3$ ng/cm², which is equivalent to the mass of $\sim 3.2 \times 10^9$ LONDs/cm². The number of LONDs, N , that could accommodate on the SBLM was estimated from geometrical considerations. LONDs were assumed to be spheres of radius $R = 100$ nm, and to cover 100% of the surface of the sensor. The area

of the sensor was divided by the cross-section of the LONDS (πR^2), and then multiplied by an estimate of the LOND mass⁶. From this calculation, the number of LONDS able to bind to the SBLM was found to be $N = 3.18 \times 10^9$ LONDS/cm², the mass of which would be 11.7×10^3 ng/cm², which is in excellent agreement with the value obtained from the fitting of the data to the Kelvin-Voigt viscoelastic model. It is also interesting to note that the change in thickness of the system, 146.7 ± 0.2 nm, is very similar to the size of the LONDS used in this experiment (152 ± 1 nm).⁷

It was noted that a fraction of L_{PEG} LONDS bound to a NeutrAvidin functionalised SBLM, as shown by the frequency and dissipation changes in case h, figure 7.6. The signals reached a plateau following the cessation of the LONDS flow, and PBS rinsing did not remove any material from SBLM. At this point, the thickness of the layer attached to the SBLM was ~ 53 nm, and had a mass of ~ 3400 ng/cm². Once the MilliQ rinse commenced, the frequency was observed to increase, and the dissipation reduced. This is generally expected when transitioning from an ion-containing buffer to MilliQ. [316] This tendency can for example be observed at $t = 0.5$ h on the same graph (figure 7.6h), when the system was rinsed with MilliQ. However, 10 min later, and while MilliQ was still flowing into the flow cells, both the frequency and the dissipation changed their behaviour, and decreased and increased respectively. This is typically observed when mass adheres to the sensors, and was not expected when the system was immersed in an ion-free solution. The same behaviour was observed in a repeat of the experiment. It is, however, not clear the reason behind this unexpected observation. For example, it could be argued that the exchange of PBS to MilliQ causes LOND swelling or breakage, in a similar fashion as osmotic stress affects lipid vesicles. [317–319] However, this was not observed for L_{BIO} LONDS interacting with B_{BIO} bilayers (figure 7.6i) and therefore excludes this possibility. After resetting the PBS flow both frequency and dissipation signals reached a plateau. The mass of adhered to the SBLM was ~ 3030 ng/cm² and its thickness ~ 49 nm., which are a 10% lower than the values for the system before the MilliQ stage.

To summarise the results discussed above, and to facilitate the comparison of mass attached to the SBLMs in all the cases shown in figure 7.6, the mass change in each experiment was normalised to the mass in case i, which was considered the maximum

⁶This was done by considering the oil volume contained in the LOND core, and the mass of the lipid in the LOND shell. From this calculation, the mass of a LOND results $m = 3.7 \times 10^{-6}$ ng.

⁷Informed by this result, the number of LONDS able to bind to the SBLM can be recalculated, resulting $N = 5.7 \times 10^9$ LONDS/cm² with a mass 20×10^3 ng/cm².

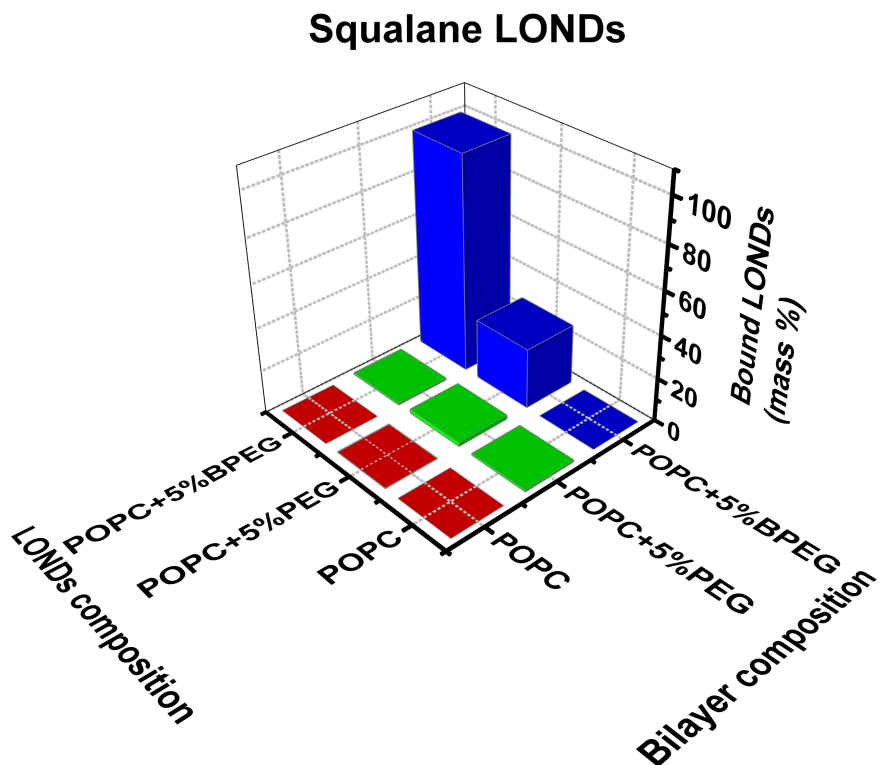


Figure 7.8: Summary of the interactions between squalane LONDS and SBLMs for different lipid coating combinations. The figure shows the mass percentage attached to a SBLM, obtained from the fitting of the frequency and dissipation signals of the overtones 5th – 11th to the Kelvin-Voigt viscoelastic model.

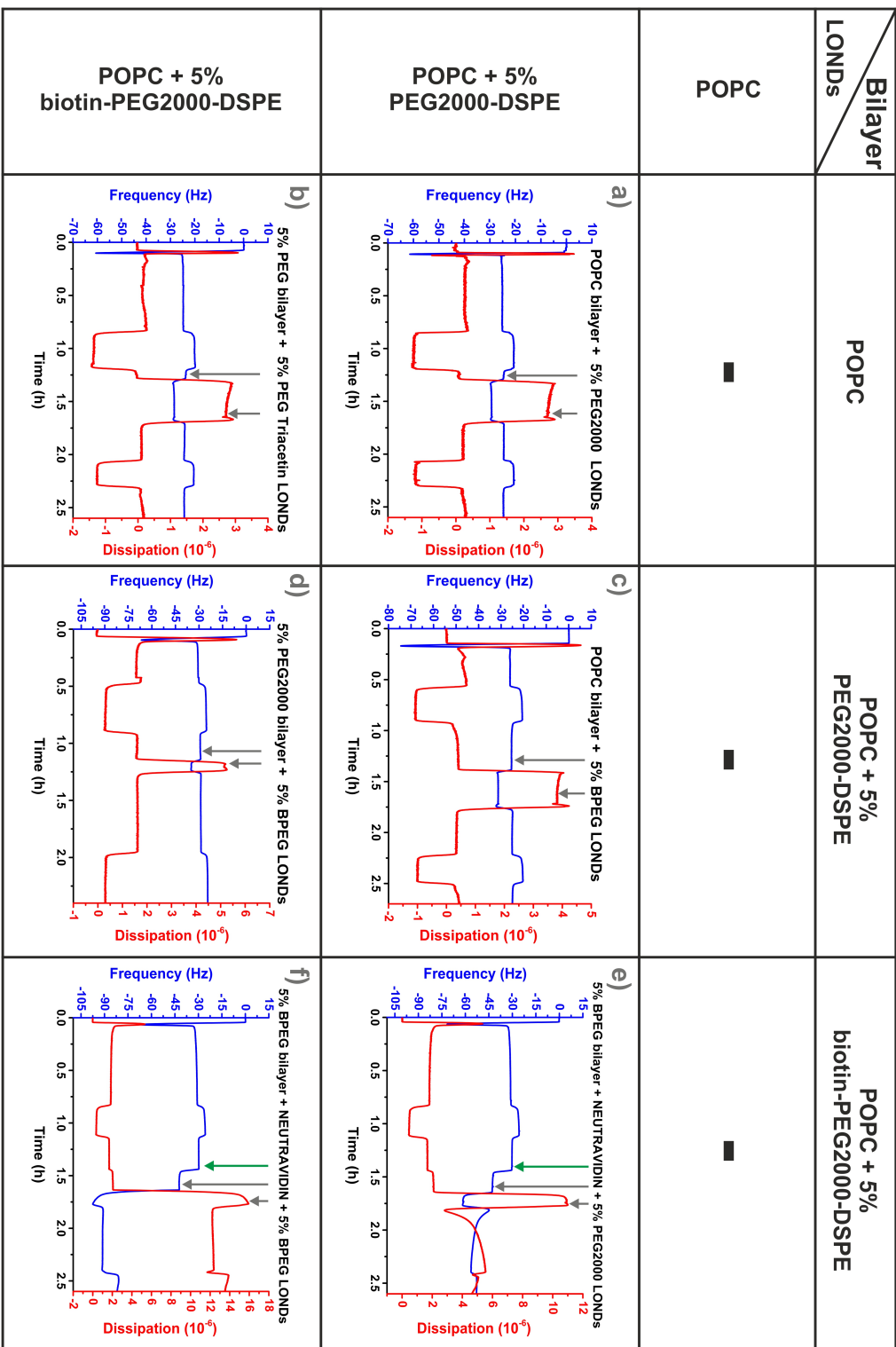
possible LOND surface coverage. The results were plotted in the form of a bar graph, as shown in figure 7.8. This figure shows the mass incorporated to the system for all LOND/SBLM combinations. Here, the mass bound to the system in case h ($L_{BIO}-B_{BIO}$) represents 100% of the mass bound to the SBLM. For the other interesting cases discussed above, the mass percentage increases are: case a (L_0-B_0), $\sim 0.2\%$; and case h ($L_{PEG}-B_{BIO}$), 26%. For all the other cases, the percentage mass increase was $< 0.03\%$.

LONDS/SBLM interaction experiments were repeated for triacetin LONDS. Figure 7.9 contains the results for all the triacetin LOND-SBLM combinations. Triacetin LONDS were found to not to form when only POPC was used (section 5.2, in page 74), and therefore no QCM-D experiments involving L_0 triacetin LONDS were performed. In this figure, the gray arrows indicate the times at which LONDS were added to the system, and the time at which a PBS rinse was set, following incubation of the SBLM with the LONDS. A green arrow in cases e and f indicates the time at which NeutrAvidin was added to the

system. In a similar fashion as for squalane LONDS, pegylation of the SBLM (cases a, b, c and d in figure 7.9) prevented any non-specific interaction of L_{PEG} and L_{BIO} LONDS. It is interesting to note the slight changes in the frequency and dissipation signal upon the addition of the LONDS, which recovered to the original values after PBS and MilliQ rinses in the four cases. These changes were not observed for the equivalent squalane LOND cases (figure 7.6a-f). One explanation for this difference could be the difference in density (805 kg/m^3 and 1160 kg/m^3) and viscosity between squalane and triacetin (11 and 23 mPa·s, respectively). See table 4.1, on page 49).

Binding of NeutrAvidin to B_{BIO} SBLMs (cases e and f) resulted in frequency and dissipation changes of $\Delta f = -11 \text{ Hz}$ and $\Delta D = 0.44 \times 10^{-6}$. Data fitting provided a value of $(2.17 \pm 0.01) \text{ nm}$ for the thickness of the protein layer, which only differs with what previously observed in B_{BIO} SBLMs for squalane LONDS experiments by 0.30 nm. In case f (L_{BIO} - B_{BIO}), NeutrAvidin allowed for triacetin LOND binding to the SBLM. PBS rinsing (second gray arrow) removed a fraction of the LONDS interacting with the sensor, as seen by the drop of the dissipation signal ($\Delta D = -3.89 \times 10^{-6}$) and frequency increase ($\Delta f = 7 \text{ Hz}$). This suggests that the number of LONDS that had reached the SBLM at this point was larger than that able to bind to it, and therefore excess material was washed off by the PBS flow. The adhered mass, at this point, and while the system remained in PBS, was $(4170 \pm 3) \text{ ng/cm}^2$ and the calculated thickness of the attached layer was $\sim 40 \text{ nm}$. It is important to note that, unlike for squalane LONDS attached to bilayers (figure 7.6i), this layer thickness does not correspond to the size of the triacetin LONDS used in this experiment ($\sim 250 \text{ nm}$ according to DLS). It has been discussed in chapter 5 that sizing data for triacetin LONDS suggested larger polydispersity of this type of LOND sample, compared to squalane LONDS. Hence, one possible explanation is that only LONDS with smaller sizes, or shrunk LONDS (see discussion in chapter 5), may be reaching and attaching to the SBLM. The sizing of the triacetin LOND samples was performed a few weeks before the day in which the this QCM-D experiment took place, and it is possible that the sample had undergone some changes in the interim. In light of the QCM-D results, it would have been desirable to resize the LOND sample immediately before carrying out the experiment. Frequency and dissipation were observed to increase and decrease, respectively, as a result of the MilliQ rinse. As discussed above, this observation was expected for the change of the solution in the flow chamber, from an ion-containing solution (i.e. the PBS) to MilliQ. As for squalane LONDS, unexpected

Figure 7.9: Changes in frequency and dissipation of a QCM-D SiO₂-coated quartz crystal for a range of SBLM/triacetin LONDS interactions. The graphs were produced averaging overtones 5th – 11th. The gray arrows indicate, in this order, the point at which LONDS were started to flow into the flow cells, and the time at which a PBS rinse was commenced. For experiments involving NeutraAvidin, the point at which the protein was flowed is indicated with a green arrow.



binding of L_{PEG} triacetin LONDS to a B_{BIO} SBLM occurred. This is shown in figure 7.9e, with recorded changes in frequency and dissipation ($\Delta f = -17$ Hz, $\Delta D = 8.81 \times 10^{-6}$). PBS rinsed resulted in partial removal of material in the surroundings of the SBLM, as indicated by the drop in the dissipation signal, and increment in the frequency. However, both signals reached a plateau with similar values to those recorded prior to the PBS rinsing. The mass attached to the system was (640 ± 2) ng/cm². The bound layer had a thickness of 15 nm, which is in the size range of micelles.

As described for squalane, the mass percentage bound to the SBLMs, normalised to the value for the attached mass in case L_{BIO} - B_{BIO} (figure 7.9f) were plotted as a bar graph, for each LOND/SBLM combination. Figure 7.10 shows the mass adhered to each SBLM as a result of LONDS addition. Here, case f represents 100% of the adhered mass, whereas case e (L_{PEG} - B_{BIO}) shows a mass binding of around 16%. For cases a-d, the mass changes were $< 0.4\%$.

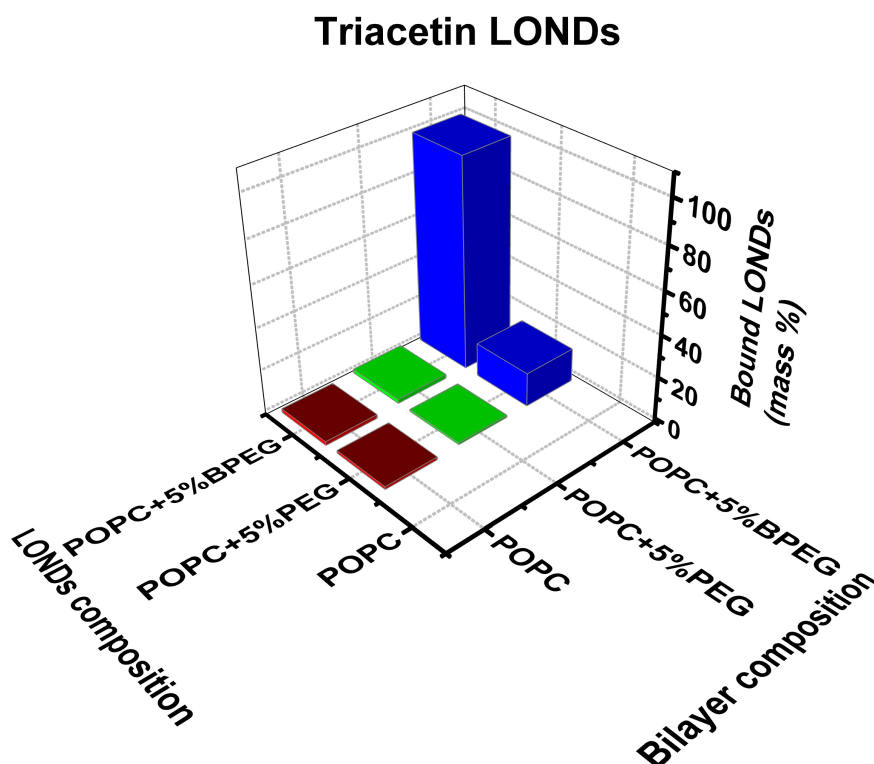


Figure 7.10: Summary of the interactions between triacetin LONDS and SBLMs for different lipid coating combinations. The figure shows the mass percentage attached to a SBLM, obtained from the fitting of the frequency and dissipation signals of the overtones 5th – 11th to the Kelvin-Voigt viscoelastic model.

7.3.3 LOND-SBLMs attachment via PDP-thiol and Maleimide-thiol

The biotin-NeutrAvidin linking chemistry has been widely used as a route for the assembly of nanomaterials, from antibodies onto the surface of liposomes [320] to vesicles onto the surface of MBs [78, 82, 133]. However, *in vivo* injection of proteins (such as Avidin/StreptAvidin/NeutrAvidin) is known to give rise to immune response. [83, 321] Proteins attached to nanomaterials, or serving as a bridge between them are no exception. Thus the use of the biotin-NeutrAvidin for *in vivo* applications is limited by its immunogenicity. Alternative linking chemistries, such as the maleimide-thiol and pyridyl disulfide (PDP)-thiol can help overcome this problem. The reaction that these molecules undergo is illustrated in figure 7.11. Thiol-containing molecules, such as DTT, react with the maleimide's double bond to form a stable carbon-sulfur bond. The same reaction can take place on the other end of the DTT molecule, which results in a bridge between two maleimide molecules. In the case of the PDP, DTT reacts to form a disulfide bond, which is practically irreversible due to the release of a very stable pyridine thione. [322] In a similar fashion as for maleimide, this reaction can occur on the other end of the DTT molecule, resulting in bridging between two PDP molecules. Provided that both PDP and maleimide are reactive to thiols, DTT could also act as link between a PDP and a maleimide molecule.

With the hope to use the alternative maleimide-thiol and PDP-thiol chemistries to bind

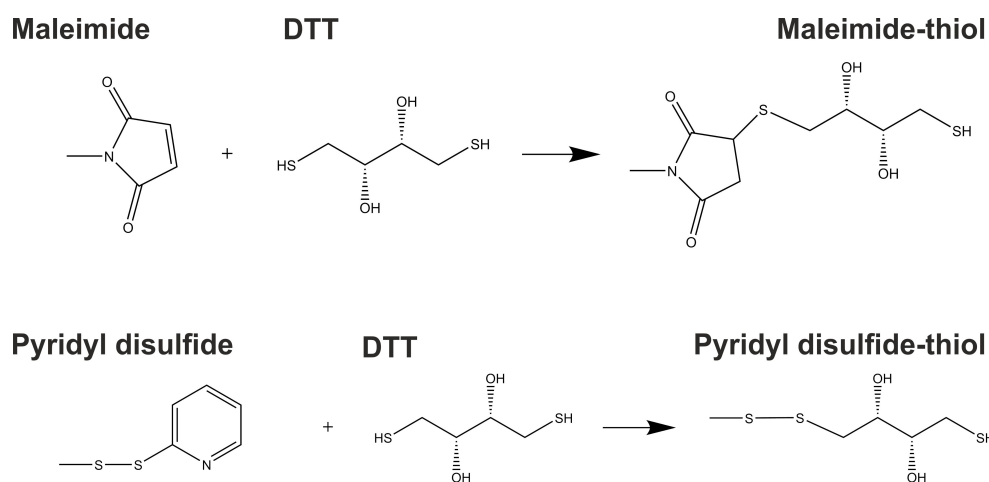


Figure 7.11: Maleimide and pyridyl disulfide (PDP) are two common thiol-reactive groups. Thiol-containing DTT reacts with the maleimide's double bond to form a stable carbon-sulfur bond. Pyridyl disulfide reacts with DTT to give a disulfide with release of a pyridine thione (not shown).

LONDS to MBs, and to understand all the possible maleimide/PDP/DTT combinations, an equivalent study to that done for the biotin-NeutrAvidin reaction was performed. Similarly to the studies previously described, the aim was to screen the interactions between LONDS and SBLMs with different lipid combinations. Although the literature on the use of the PDP and maleimide is extensive, there are no references to PDP/maleimide-PEG2000-DSPE-containing SBLMs studied in QCM-D. Hence, this study was initiated by investigating the formation of SBLMs containing different percentages of PDP-PEG2000-DSPE or maleimide-PEG2000-DSPE (SBLMs B_{PDP} and B_{MAL} , respectively). SBLMs were prepared as described earlier (section 3.6.2, page 41), from the absorption and rupture of vesicles onto a SiO_2 -coated QCM-D sensor. Figure 7.12 shows the changes in frequency of the QCM-D sensor upon formation of SBLMs containing 1%, 2% or 5% PDP-PEG2000-DSPE or 1%, 5% maleimide-PEG2000-DSPE. All the trends shown in this figure exhibit the characteristic fingerprint of the formation of a SBLM: vesicles accumulate onto the QCM-D sensor (from $t = 12$ min in this specific case), eventually breaking and forming a continuous SBLM; this breakage is characterised by an increase in the frequency (see from $t = 15$ min in figure 7.12). These results suggest successful formation of a SBLM in all the attempted lipid combinations. Note the differences in the frequency signal for the different SBLMs, once stabilised ($t = 21$ min and onwards in all the cases). The observed increase is consistent with the increase in the percentage of PDP-PEG2000-DSPE or maleimide-PEG2000-DSPE, and reflects an increase of the overall mass of the system upon incrementing the percentage of these two lipids. The characteristic frequency shift observed upon the formation of a plain POPC SBLM (as seen in sections 7.2 and 7.3.2, and previously reported [198, 201, 202, 301]), $\Delta f = -26$ Hz, coincides with the frequency shift recorded for the 1% maleimide-PEG2000-DSPE-containing SBLM. This is indicated as a dotted line in figure 7.12. 1% PDP-PEG2000-DSPE-containing bilayer produced a slightly larger frequency shift, $\Delta f = 30$ Hz. The frequency shifts recorded for the 5% PDP/MAL containing bilayers were very similar, $\Delta f = 42.5$ Hz and $\Delta f = 43$ Hz respectively. These shifts correspond to an absorbed mass of (1050 ± 100) ng/cm² in the case of the PDP-containing SBLM, and of (1082 ± 80) ng/cm² for maleimide-containing SBLM, compared to ~ 630 ng/cm² typically obtained for POPC only SBLMs (see for example 7.6). It is also interesting to note that the speed of the vesicle rupture is higher for lower percentages of PDP/maleimide-PEG2000-DSPE. This is likely due to the configuration of the PEG chains on the surface of the vesicles, in the mushroom configuration for percent-

ages $< 5\%$, and transitioning to the brush regime from percentages $\sim 5\%$. At percentages close to the boundary between the two regimes, SBLMs still form, but breakage of the vesicles onto the QCM-D sensor is slowed down due to the reduction in vesicle adsorption in presence of the PEG chains.

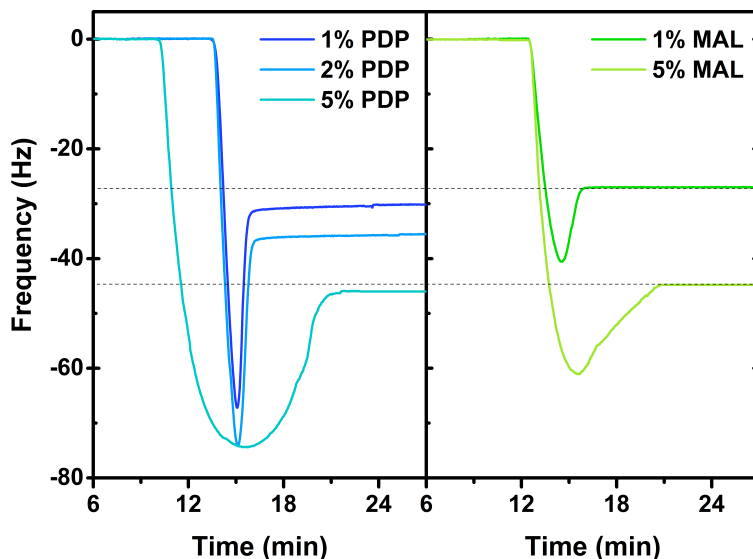


Figure 7.12: Changes in frequency of a QCM-D SiO_2 -coated quartz crystal upon formation of SBLMs containing different percentages of PDP-PEG2000-DSPE (1%, 2%, 5% PDP) or Maleimide-PEG2000-DSPE (1%, 5% PDP). The dotted lines are included as a guide to the eye, and they indicate the frequency reached by the Maleimide-PEG2000-DSPE-containing SBLMs upon formation, $f = -26$ Hz, which coincides with the frequency change recorded for a regular POPC bilayer.

Informed by the results on the formation of SBLMs containing PDP/maleimide-PEG2000-DSPE, 5% PDP/maleimide-PEG2000-DSPE-containing SBLMs were chosen to study the interaction of LONDS with different lipid coatings in QCM-D. These conditions directly relate to those used for the study of LONDS/SBLM interaction in the case of biotin-NeutrAvidin interaction, and should allow easy comparison between the two studies. To assess the specificity of the new chemistries, the attachment of LONDS to SBLMs was studied using QCM-D. As done previously, the interactions of different LOND/SBLM combinations were screened in order to determine the level of non-specific binding. All the interactions monitored are shown schematically in figures 7.13 and 7.14. Three types of squalane LONDS were used for these experiments, namely: L_{PEG} : POPC + 5% PEG2000-DSPE LONDS; L_{MAL} : POPC + 5% maleimide-PEG2000-DSPE LONDS; L_{PDP} : POPC + 5% PDP-PEG2000-DSPE LONDS. These were combined with PDP-containing SBLMs (figure 7.13) in absence (B_{PDP} , POPC + 5% PDP-PEG2000-DSPE) or presence of DTT (B^*_{PDP} , POPC + 5% PDP-PEG2000-DSPE + DTT). These were also let interact with maleimide-

containing SBLMs (figure 7.14) in absence (B_{MAL} , POPC + 5% PDP-PEG2000-DSPE) or presence of DTT (B^*_{MAL} , POPC + 5% PDP-PEG2000-DSPE + DTT). B_{PEG} (POPC + 5% PEG2000-DSPE) were used as control bilayers, as no LOND attachment was expected to occur onto these SBLMs. Control experiments with POPC only SBLMs (with and without DTT), and B_{PEG} with DTT were performed, and the results are shown in appendix B. For cases involving B^*_{PDP} and B^*_{MAL} SBLMs, DTT at 1 mM was flowed into the chamber prior to the addition of the LONDS. DTT solution was kept flowing until the frequency change reached a plateau and was followed by PBS rinsing to remove unreacted DTT and other residues (i.e. pyridine thiones). LONDS were introduced to the SBLMs at 0.1 ml/min, at 10^{12} LONDS/ml. Upon detection of changes in the frequency and dissipation signal the flow was stopped until the signal reached a plateau. This incubation period was followed by consecutive PBS and MilliQ rinses to remove unbound LONDS and those LONDS attached non-specifically to the SBLM. Within the experiment, changes in frequency and dissipation were monitored for overtones 1^{th} - 13^{th} , but only 5^{th} - 11^{th} were used for the fitting to the Kelvin-Voigt viscoelastic model.

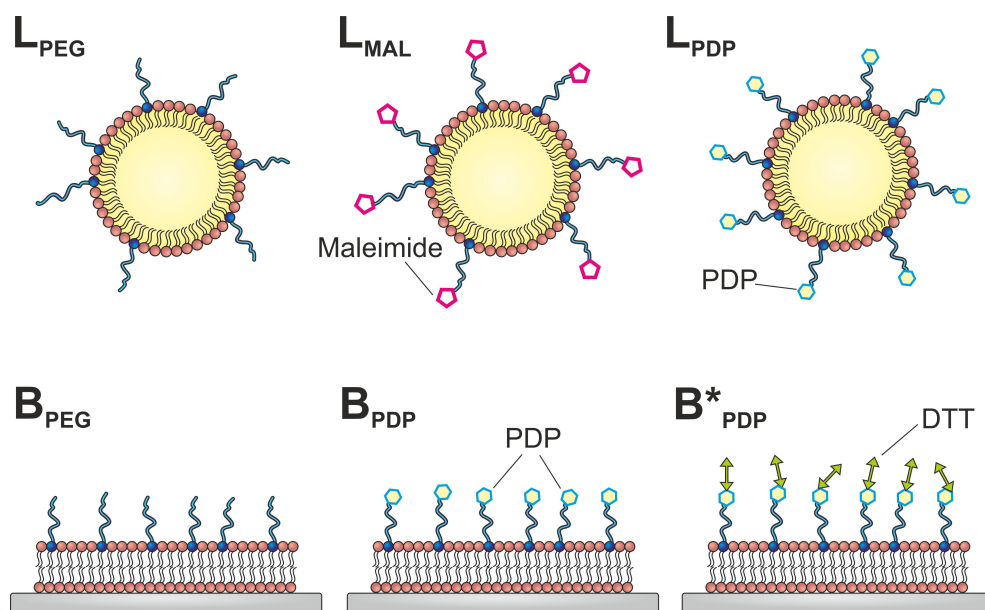


Figure 7.13: The binding of LONDS to SBLMs via the PDP-thiol chemistry was studied on model SBLMs in QCM-D. Nine different combinations of LONDS and SBLMs with different compositions were investigated. L_{PEG} : POPC + 5% PEG2000-DSPE LONDS; L_{MAL} : POPC + 5% maleimide-PEG2000-DSPE LONDS; L_{PDP} : POPC + 5% PDP-PEG2000-DSPE LONDS. B_{PEG} : POPC + 5% PEG2000-DSPE SBLM; B_{PDP} : POPC + 5% PDP-PEG2000-DSPE SBLM; B^*_{PDP} : POPC + 5% PDP-PEG2000-DSPE + DTT SBLM.

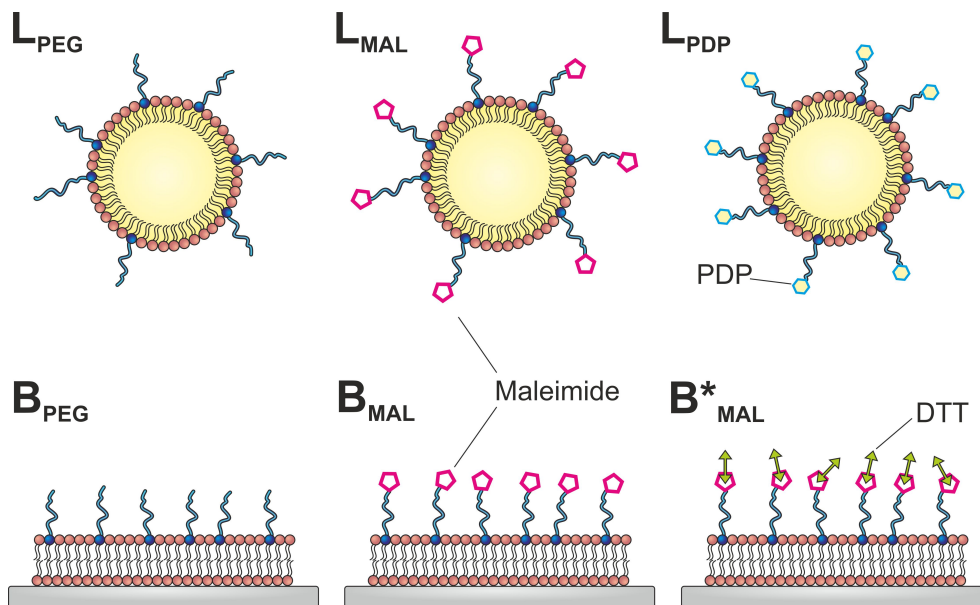


Figure 7.14: The binding of LONDS to SBLMs via the maleimide-thiol chemistry was studied on model SBLMs in QCM-D. Nine different combinations of LONDS and SBLMs with different compositions were investigated. L_{PEG} : POPC + 5% PEG2000-DSPE LONDS; L_{MAL} : POPC + 5% maleimide-PEG2000-DSPE LONDS; L_{PDP} : POPC + 5% PDP-PEG2000-DSPE LONDS. B_{PEG} : POPC + 5% PEG2000-DSPE SBLM; B_{MAL} : POPC + 5% maleimide-PEG2000-DSPE SBLM; B^*_{MAL} : POPC + 5% maleimide-PEG2000-DSPE + DTT SBLM.

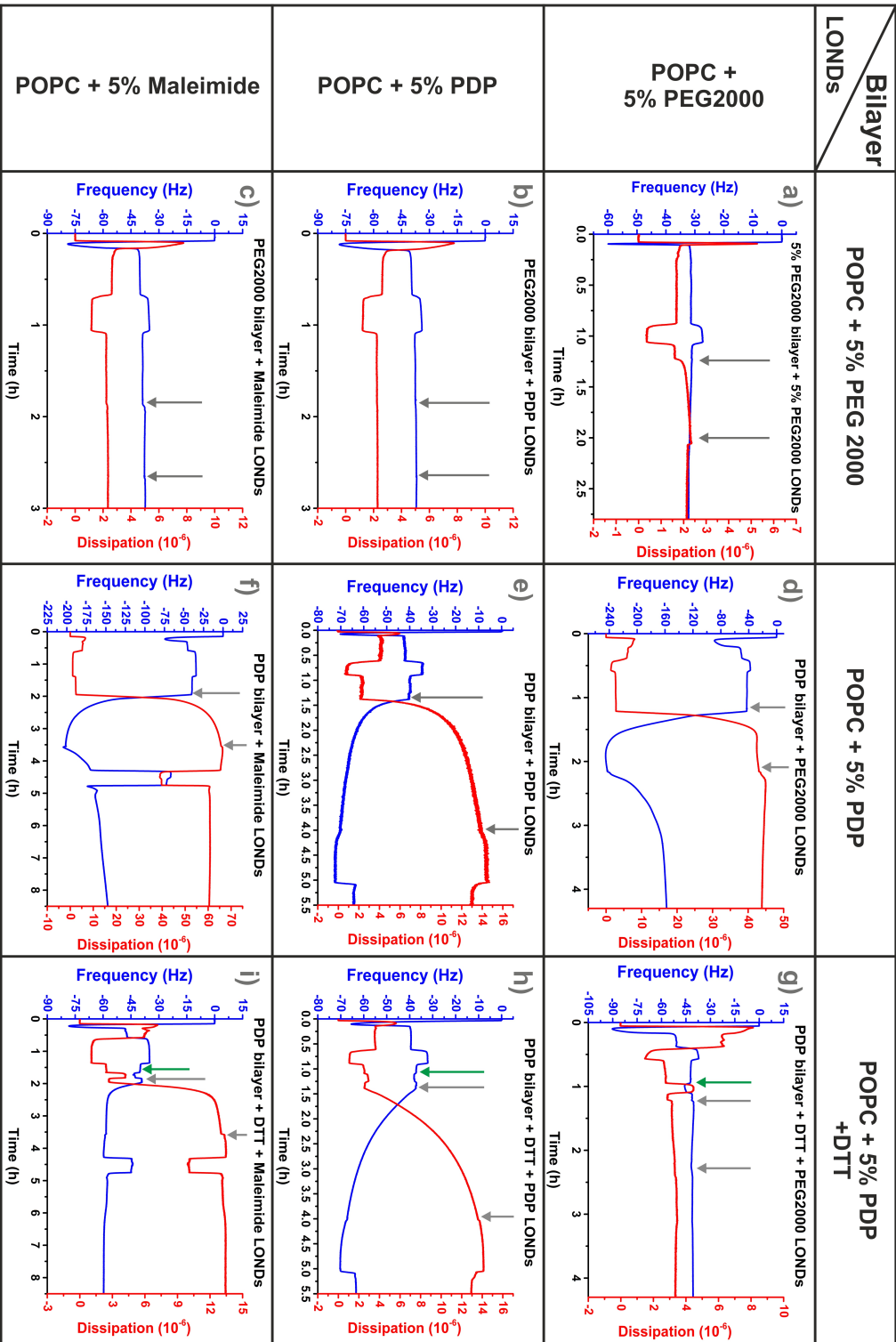
Figure 7.15 shows the results for all squalane LOND interactions with SBLMs containing 5% PDP-PEG2000-DSPE. Three control experiments involving a PEG2000-DSPE SBLM (B_{PEG}) are included in this figure. Starting from the left, the first gray arrow indicates the times at which LONDS were commenced to flow into the chambers where the QCM-D sensors were housed. The second gray arrow points at the time when the PBS rinse was started. For experiments including DTT a green arrow marks the time at which flow of DTT was set. Control experiments involving B_{PEG} (specifically, a) L_{PEG} - B_{PEG} , b) L_{PDP} - B_{PEG} , c) L_{MAL} - B_{PEG}) showed no changes in the frequency and dissipation signals upon the addition of LONDS to the flow chambers, pointing at no attachment of the LONDS to the SBLMs. These observations agree with the previous ones for the biotin-NeutrAvidin interaction (L_{PEG} - B_{PEG} and L_{BIO} - B_{BIO} cases, see figure 7.5 and results in figures 7.6 and 7.9), and are consistent with the increased stability of SBLMs as a result of the steric repulsion due to the PEG displayed on their surface. Similar behaviour was observed for case g) L_{PEG} - B^*_{PDP} . In this case, despite the addition of the DTT, L_{PEG} did not produce changes in the frequency and dissipation signals, suggesting that no attachment took place. In the other cases involving DTT (cases h and i in figure 7.15), a small frequency shift of around $\Delta f = -4$ Hz, accompanied by a increase in the dissipation

signal $\Delta D = 1.65$, was observed following the addition of DTT to the SBLMs. The PBS rinse following the DTT step reverted the system to its original state, suggesting complete removal of the reagent upon washing. Considering the small dimensions of the DTT ($Mw = 154$ g/mol), and the reduced number of PDP sites available on the sensor (5×10^{12} PDP-PEG2000-DSPE per SBLM), the expected mass change upon reaction of DTT with the PDPs on the SBLM is of around 1.3 ng/cm², which is close to the theoretical resolution limit of the QCM-D of 0.5 ng/cm² and may be undetectable.

The attachment of LONDS to SBLMs was only expected in the cases L_{MAL-B^*PDP} and L_{PDP-B^*PDP} , as the presence of the DTT was thought to be crucial for the PDP contained in the SBLM to exhibit the thiol groups necessary for the LONDS to bind. However, frequency and dissipation shifts that suggested LOND binding to SBLMs were recorded also in absence of DTT. LOND attachment was observed for all cases involving PDP/MAL SBLMs, specifically d) $L_{PEG-BPDP}$, e) $L_{PDP-BPDP}$, f) $L_{MAL-BPDP}$, h) L_{PDP-B^*PDP} and i) L_{MAL-B^*PDP} . The PBS rinse following the addition of the LONDS was observed to increase the frequency signal in cases d) $L_{PEG-BPDP}$ and f) $L_{MAL-BPDP}$, suggesting that the attachment of the LONDS in these cases was partially non-specific and that the PBS rinse was enough to remove some of these LONDS. No frequency changes upon PBS rinsing were observed for cases e) $L_{PDP-BPDP}$, h) L_{PDP-B^*PDP} and i) L_{MAL-B^*PDP} , suggesting attachment of LONDS via thiol linking. It is interesting to note that L_{PEG} LONDS appeared to bind to a B_{PDP} SBLM (case d). This was not observed when L_{PDP} were added to B_{PEG} , which was expected to be an equivalent scenario. The reasons for this are unclear. It could be argued that the differences in curvature between the LOND shell and the surface of the SBLM could affect how the PEG2000 and PGP-PEG2000 chains arrange in one or the other, and this could for example enhance entanglement of the PEG chains. However, this would not explain why addition of DTT prior to incorporating the LONDS (case g) eliminates any binding.

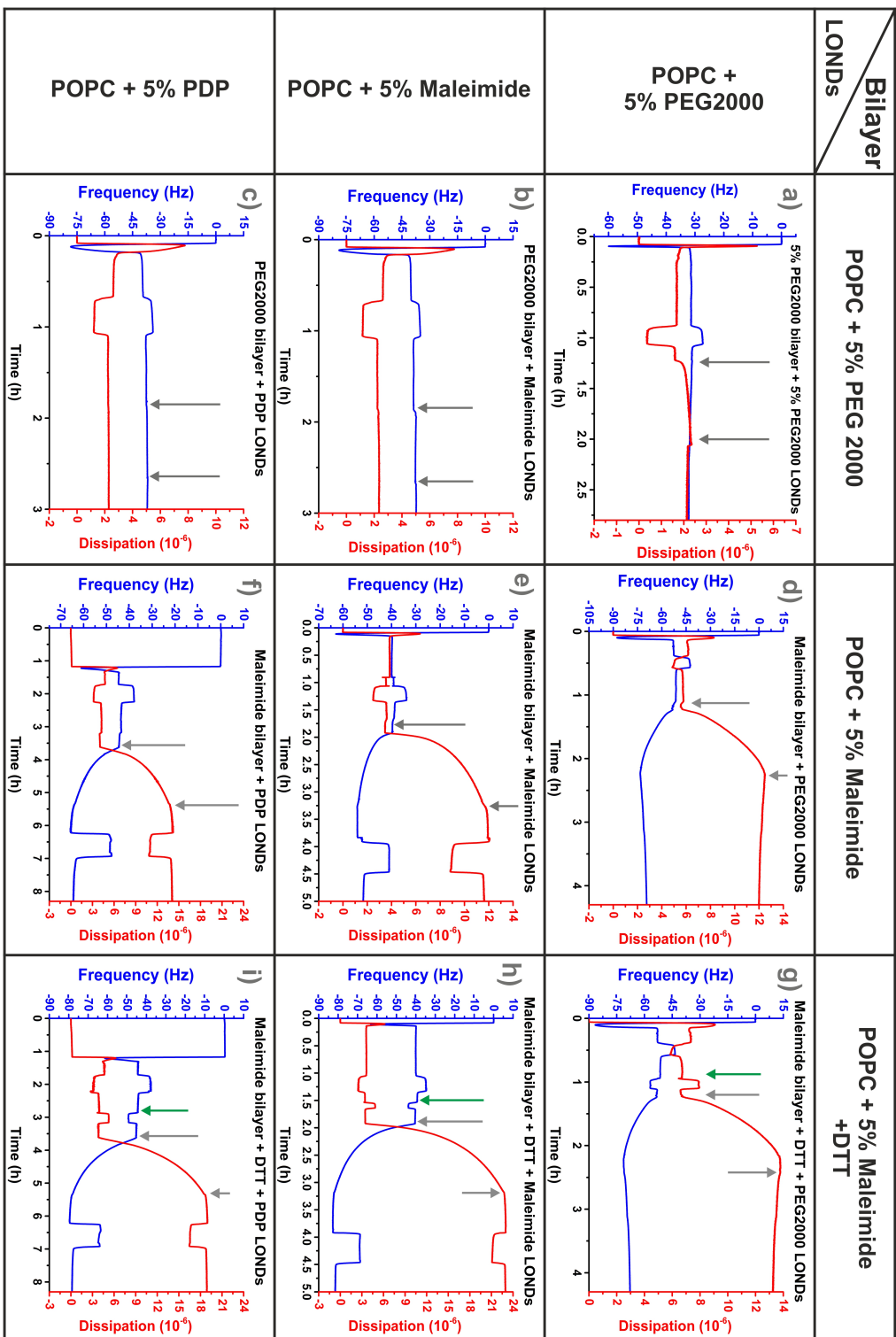
Figure 7.16 shows the results for all squalane LOND interactions with SBLMs containing 5% maleimide-PEG2000-DSPE. As for the PDP bilayers (figure 7.15) three control experiments involving a PEG2000-DSPE SBLM (B_{PEG}) are included for comparison. These control experiments have been discussed above. As before, the green arrows point at the time at which LONDS were started to flow into the sensor chambers and when the PBS rinse was set, respectively. The green arrow marks the time at which flow of DTT was set, when applicable. Upon incorporation of the LONDS into the sensor chambers,

Figure 7.15: Changes in frequency and dissipation of a QCM-D SiO_2 -coated quartz crystal for a range of PDP-containing SBLM/squalane LONDS interactions. The graphs were produced averaging overtones 5^{th} – 11^{th} . The gray arrows indicate, in this order, the point at which LONDS were started to flow into the flow cells, and the time at which a PBS rinse was commenced. For experiments involving DTT, the point at which the molecule was flowed is indicated with a green arrow.



frequency and dissipation changes were observed in all cases involving B_{MAL} and B^*_{MAL} SBLMs (d-i), which suggests LOND attachment to the SBLMs. It is important to remember that linking of the maleimide to the DTT is a result of the formation of a stable thioether bond as a result of the interaction with a thiol. The same process can occur on the other end of the DTT molecule thereby allowing another maleimide (or PDP) to bind by the same mechanism. Thus, the presence of DTT for the binding of LONDS to these SBLMs was thought to be essential. From the graphs in figure 7.16, it can be seen that frequency changes upon the addition of LONDS for B^*_{MAL} SBLMs are larger than for B_{MAL} ; addition of LONDS in cases e) L_{MAL} - B_{MAL} and h) L_{MAL} - B^*_{MAL} resulted in frequency changes $\Delta f = -15$ Hz and $\Delta f = -42$ Hz respectively, which points are larger mass attachment in presence of DTT, as expected. Similarly, comparing cases f) L_{PDP} - B_{MAL} and i) L_{PDP} - B^*_{MAL} , the recorded frequency changes of $\Delta f = -22$ Hz and $\Delta f = -33$ Hz, respectively, suggest that the attachment of LONDS to the SBLM was more efficient in presence of the DTT. Furthermore, rinses with PBS (and also MilliQ in cases e, f, h, i) did not produce changes in the frequency or dissipation signals, suggesting that the LOND binding was specific. Cases d) L_{PEG} - B_{MAL} and g) L_{PEG} - B^*_{MAL} , in which no LOND attachment was expected, are also interesting to note. Unlike for B_{PDP} SBLMs (figure 7.15), the interaction of L_{PEG} with B_{MAL} was similar in the presence and in the absence of DTT, with a frequency change of around $\Delta f = -20$ Hz in both cases. This suggests that the binding of L_{PEG} was non-specific, as it was not affected by the thiolation of the SBLM. The reason for this attachment is however not well understood, as pegylation of vesicles and other lipid carriers is known to enhance their stability and reduce non-specific interactions.

Figure 7.16: Changes in frequency and dissipation of a QCM-D SiO_2 -coated quartz crystal for a range of maleimide-containing SBLM/squalane LONDS interactions. The graphs were produced averaging overtones 5th – 11th. The gray arrows indicate, in this order, the point at which LONDS were started to flow into the flow cells, and the time at which a PBS rinse was commenced. For experiments involving DTT, the point at which the molecule was flowed is indicated with a green arrow.



All the data presented in figures 7.15 and 7.16 was analysed by fitting frequency and dissipation of the overtones 5^{th} - 11^{th} to the Kelvin-Voigt viscoelastic model. The fitting provided information about system mass and thickness changes throughout the experiment. The results are summarised in figure 7.17. Mass and thickness variation were obtained subtracting the mass of the SBLMs from the mass of the system in its final state, after the addition of LONDS and stabilisation of the frequency/dissipation. Figure 7.17 shows that the larger mass (and thickness) increase was recorded for L_{PEG} - B_{PDP} , followed by L_{MAL} - B^*_{MAL} . PEG2000-DSPE-containing LONDS and SBLMs were expected to not to exhibit attachment, as PEG2000 steric repulsion from the lipid shell, which is known to reduce non-specific interactions and enhance the stability of lipid carriers. The reasons for this strong binding are unknown and repeats of this experiment would be necessary to better understand the conditions that result in this attachment.

The binding of LONDS to the SBLM in the L_{MAL} - B^*_{MAL} case was expected, and this result confirms the viability of the maleimide-thiol chemistry to attach LONDS to SBLM. The observed thickness increase in this case (around 130 nm) is similar to the average size of the L_{MAL} LONDS used in the experiment, (168 ± 5) nm as determined with DLS. It is important to note that data modeling using the Kelvin-Voigt viscoelastic model provides values for the thickness (and mass) on the sensor assuming homogeneous distribution of the adhered material over the area of the sensor. Hence small inhomogeneities, such as size differences of the attached LONDS, would be simply averaged over the whole surface, which could then give rise to the differences between the measured thickness and the average size of the LONDS used in the experiment. It is also possible that the intrinsic buoyancy of the squalane LONDS could give rise to creaming of the LOND sample during the experiment (see 2.2.4, page 24). As the LOND solution is kept upright in a falcon tube during the duration of the experiments, larger LONDS would rise faster than the smaller ones, and thus more smaller ones, from the bottom of the solution, would be injected into the sensors chambers. It is interesting to note that PDP-containing SBLMs show, overall, more non-specific interactions than maleimide-containing SBLMs. Thiolated products remaining from the synthesis of PDP, or as a result of autoxidation of the PDP, could lead to thiol groups readily available on the surface of the SBLM/LONDS for binding. This would explain why attachment onto SBLMs containing 5% PDP-PEG2000-DSPE occurs both in absence and presence of DTT.

Binding of LONDS to B_{MAL} SBLMs resulted in thickness increases > 25 nm. As

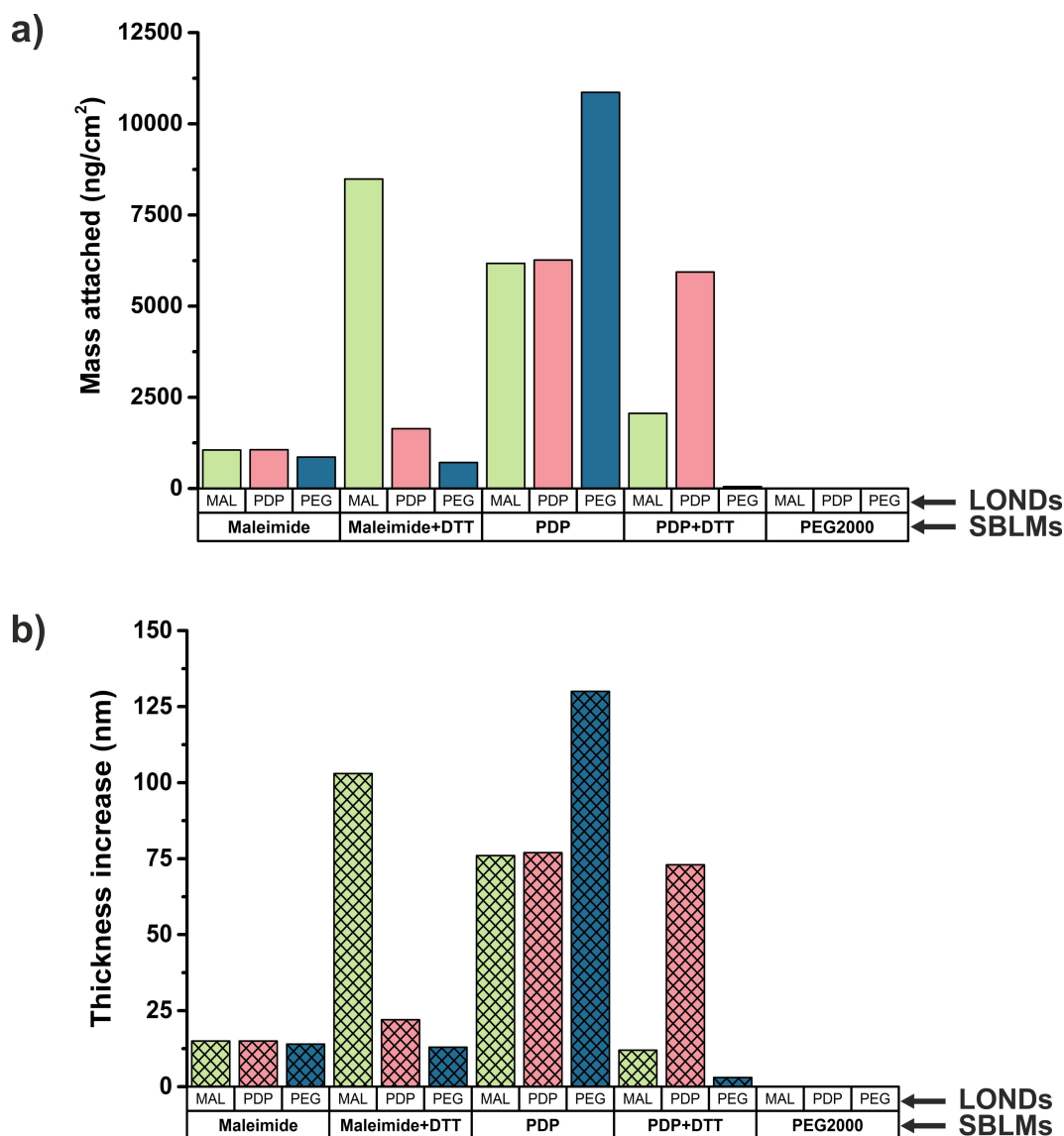


Figure 7.17: Summary of the interactions between squalane LONDS and SBLMs for different PDP/Maleimide/PEG2000 lipid coating combinations. Five different SBLMs were used in this experiment: B_{MAL} , B^*_{MAL} , B_{PDP} , B^*_{PDP} and B_{PEG} (schematically represented in figures 7.13 and 7.14). This figure shows: a) the mass attached to SBLMs and b) the thickness increase (over the SBLM), both obtained from the fitting of the frequency and dissipation signals of the overtones $5^{th} - 11^{th}$ to the Kelvin-Voigt viscoelastic model.

discussed before, this thickness increase assumes homogeneous distribution of the adhered material on the sensor. In the likely scenario that LONDS remain intact when adhered to the SBLMs, this thickness increase (and its mass, $\sim 1000 \text{ ng/cm}^2$) would be equivalent to having ~ 12 LONDS per $100 \mu\text{m}^2$. Furthermore, no significant differences across the three types of LONDS were observed, further suggesting that the attachment in this case was non-specific.

7.4 Discussion

The literature on vesicle attachment to other lipid structures such as SBLMs [323–325] or MBs [78, 85, 133, 326, 327] is extensive. In contrast, although lipid-stabilised nanoemulsions have been previously functionalised with antibodies for tumour targeting, [50, 328, 329], to date there are no references to the attachment of lipid-stabilised oil-nanodroplets to other lipid structures (such as SBLMs or MBs). The assembly of MB-LONDS architectures relies on the attachment of LONDS to the surface of the MBs. Verifying this was important for ensuring the viability of the MB-LONDS. However, monitoring this process directly on MBs is difficult, due to the size of the both the MB and the LONDS, and also the limited lifetime of the MBs. Furthermore, the kinetics of this attachment are important for the assembly of the architectures, as they would assist designing the protocols for the preparation i.e. deciding incubation times.

Solid-supported bilayers (SBLMs) were chosen as model membranes to mimic the shell of the MBs and to study the interaction of LONDS with them. SBLMs are robust systems, easy and quick to prepare, typically by vesicle adsorption and fusion on a surface. The properties of the SBLMs can be easily tuned by simply modifying the lipid composition of the vesicles used for their preparation. For example, different chemical ligands, such as biotin, can be introduced to the SBLMs by adding a percentage of phospholipids to which biotin has been covalently attached. This versatility allows for the incorporation of the ligands of interest in this project: biotin, maleimide, and PDP. Not only there was an interest in studying the successful tethering of LONDS to SBLMs via one of these linking chemistries, but also the negative controls, in where the entire experimental procedure was repeated with the omission of a key reagent for test i.e. the NeutrAvidin in the biotin-NeutrAvidin linking chemistry, or the DTT in the PDP-thiol and maleimide-thiol reactions. These experiments were to confirm the success of the *positive* result, supporting the specificity of the binding in the specific chemistries and ruling out the possibility of successful attachment due to non-specific interactions.

Specifically, this study focused on the binding of LONDS to SBLMs via: i) the biotin-NeutrAvidin link chemistry, ii) the maleimide-thiol reaction, and iii) PDP-thiol chemistry. All the case studies were monitored using QCM-D. [330] When the mass attached to the sensor has high viscosity, which is typical for organic layers, the Voigt-Kelvin viscoelastic

model is used for modeling the data, providing information about the mass attached on the sensor (ng/cm^2) and the thickness variation of the system as a result of this process (nm). SBLMs were formed on SiO_2 coated crystals by adsorption and rupture of vesicles. The formation of SBLM has a characteristic fingerprint when monitored in QCM-D (section 3.6.2, page 41), [200–202, 301, 331], which was used as a guide to assess the successful formation of a SBLM prior to the LOND attachment experiments.

The initial experiments tested the attachment of StreptAvidin to biotinylated SBLMs. These were to provide the evidence on the successful formation of SBLMs incorporating biotin-PEG2000-DSPE, as well as to provide a measurement for the K_d of the biotin-StreptAvidin reaction. Three different cases were studied, with POPC SBLMs incorporating 1% biotin-PEG2000-DSPE, 5% biotin-PEG2000-DSPE or 10% biotin-PEG2000-DSPE. Two negative controls were performed, including a POPC only SBLM, and a 5% PEG2000-DSPE SBLM, in which no attachment of the protein was expected to occur. SBLMs were formed with 1% and 5% biotin-PEG2000-DSPE (figure 7.2). Vesicles containing 10% biotin-PEG2000-DSPE adsorbed onto the surface of the sensor, as indicated by the reduction in the frequency signal, but remained intact and did not form a SBLM, as indicated by the absence of a sudden increase in the frequency signal. Previous studies have reported the formation of SBLMs from PEG-containing vesicles, and the impossibility of forming SBLMs from vesicles with PEG in the brush regime, which is in agreement with the observations made in this experiment. [305, 306, 332] StreptAvidin solutions were introduced to the SBLMs at increasing concentrations, adjusted to keep the ratio of biotin/StreptAvidin constant across the different experiments. As expected, attachment of StreptAvidin was only observed on SBLMs containing biotin-PEG2000-DSPE. The SBLMs were fully covered by the protein in about 10 min for the 1% and 5% cases, and in about 20 min for the 10%. Informed by these results, the incubation times for the formation of MB-LONDS off-chip were extended to 15 min, to ensure complete binding of the MBs with the LONDS. These results will be discussed in chapter 8 (page 155). The frequency changes for the different StreptAvidin solutions were plotted, and the Hill-Langmuir (equation 7.1) equation was used to fit the results. K_d of the biotin-StreptAvidin reaction was found to be $K_d = (8.3 \pm 0.2) \times 10^{-10}$ M, $K_d = (7.1 \pm 1.4) \times 10^{-10}$ M and $K_d = (2.6 \pm 1.0) \times 10^{-10}$ M for the 1%, 5% and 10% biotin-PEG2000-DSPE-containing SBLMs, which fall far from the expected value. [307] Reasons for this discrepancy include insufficient experimental points (particularly for concentrations of StreptAvidin in the region 0 – 10 nM) and possibly the

resolution limit of the instrument.

The experiments on the attachment of StreptAvidin to SBLMs provided the basis for the study of the attachment of LONDS to SBLMs via the biotin-NeutrAvidin link chemistry. SBLMs containing 5% biotin-PEG2000-DSPE were chosen as model SBLMs in this study because MBs are typically formed with a lipid mixture that includes 5% PEG2000-DSPE, and there was a desire to replicate the MB shell as closely as possible. [133,177,333] These attachment experiments were performed for different LONDS/SBLMs combinations, to study the attachment via the biotin-NeutrAvidin link chemistry but to also monitor possible non-specific interactions. The experiment was repeated for squalane and triacetin LONDS to ensure that the method was valid for both LOND types. The results, presented in figures 7.6 and 7.9 provide a complete view of the interactions taking place between the LONDS and the SBLMs used in each case. PEG2000-DSPE incorporated in either the LONDS or the SBLMs was found to prevent any non-specific interaction, as reflected by the stable frequency and dissipation signal in those cases. This is in agreement with the literature and the extensive use of PEG to enhance the stability of drug carriers such as liposomes. [10] When neither the LONDS or the SBLMs had PEG incorporated (case 7.6a) low levels of adsorption were observed, which could indicate the incorporation of some squalane in the middle plane of the SBLM. Attachment of LONDS to SBLMs via the biotin-NeutrAvidin link chemistry was confirmed for both LONDS types (cases 7.6i and 7.9f). Non-specific interaction appeared to occur between PEG-containing LONDS and NeutrAvidin functionalised SBLMs (as seen in figure 7.6h and 7.9f). Entanglement of the PEG chains in presence of the NeutrAvidin could be one explanation for this observation, but the nature of this interaction remains unclear.

Although the initial aim of this project was to assemble LONDS on to the MB shells via

Table 7.3: Mass attachment percentage of LONDS to maleimide-containing SBLMs, in presence and absence of DTT. The data was normalised to the L_{MAL} - B^*_{MAL} case, considered 100%.

	Maleimide SBLM B_{MAL}	DTT-Maleimide SBLM B^*_{MAL}
PEG LONDS L_{PEG}	10%	8.4%
PDP LONDS L_{PDP}	12.5%	20%
Maleimide LONDS L_{MAL}	12.5%	100%

the biotin-NeutrAvidin link chemistry, alternative chemical linkers (i.e. maleimide-thiol, PDP-thiol) were also explored, since it is known that the injection of exogenous proteins (such as StreptAvidin/NeutrAvidin) *in vivo* gives rise to a number of immune responses and represents a potential impediment for the use of Avidin-like molecules for drug delivery applications in humans. [83] Hence the interest in finding alternative linkers for LONDS to the MB shell if the MB-LOND complexes are to find a medical application. The maleimide-thiol link is present in FDA antibody-drug conjugates such as Brentuximab vedotin [334], currently undergoing Phase III clinical trials, which highlights this linking chemistry for the development of drug vehicles for medical applications. The experiments performed to study the attachment of LONDS to SBLMs via the maleimide-thiol and PDP-thiol reaction were analogous to those performed with biotin-NeutrAvidin. DTT was chosen as the molecule to act as a bridge between the thiol-reactive groups in the LONDS and the SBLMs. In the experiments, *functionalisation* of the SBLMs with DTT was done prior to the addition of the LONDS (see 7.11 for the maleimide/PDP-DTT reactions). Interactions for LONDS/SBLMs with different lipid compositions were screened, to monitor successful attachment and also detect possible non-specific binding. In this case, the negative control consisted of SBLMs containing PDP-PEG2000-DSPE or maleimide-PEG2000-DSPE to which no DTT was added. No attachment of LONDS containing either PDP or maleimide was expected, as the absence of thiol groups on the SBLM should prevent the LONDS from attaching. However, the results for this experiment showed a very different scenario (figures 7.15 and 7.16). LOND attachment was pinpointed in all cases involving maleimide or PDP-containing SBLMs (except in case 7.15g), both in presence and absence of DTT. PBS rinses following the LOND interaction stage resulted in mass removal (as seen by the increase in the frequency signal) in cases 7.15d,f and figure 7.16d,g, which suggests that this non-specific interaction between the LONDS and the SBLM was weak. The analysis of these results was summarised in figure 7.17. considering only the maleimide-containing SBLMs, the presence of DTT resulted in an enhancement of the LOND attachment. Table 7.3 contains a comparison of the mass attachment results in this case. The results were normalised to the $L_{MAL}-B^*_{MAL}$ case, which was considered 100% of the attachment. DTT allowed for a 87.5% increase of the mass attached to the system for the case L_{MAL} and B^*_{MAL} , as compared to the L_{MAL} and B_{MAL} . This suggests successful attachment of LONDS via the maleimide-thiol linking, and also points at the important role played by the DTT as a bridging molecule between the LONDS and the SBLM.

One of the most interesting aspects of the results shown in figure 7.17 is the apparent lack of symmetry in the attachment of LONDS/SBLMs with binding molecules (PDP/maleimide or control PEG2000) in either the SBLM or the LONDS. For example, L_{PDP} LONDS did not bind to B_{PEG} SBLMs, but L_{PEG} exhibited attachment onto B_{PDP} bilayers. One reason for this could be the different handling of the vesicle used for the formation of the SBLM as compared to that of the LONDS. LONDS (including L_{PDP}) were always formed first, sometimes a few days prior to the QCM-D experiments⁸. If PDP is for example susceptible to autoxidation or hydrolysis when in aqueous solution, the storage period between LOND production and the experiments could provide a sufficiently long time frame for the PDP-PEG2000-DSPE to undergo these chemical process. In contrast, vesicles for SBLM formation were always sonicated on the day of the QCM-D experiment, which therefore could have left not enough time for oxidative processes to occur. It could also be argued that the radius of curvature in the LONDS, compared to that in the SBLMS (~ 0 m), affects the arrangement of the PEG2000 (with or without DPP/maleimide) chains in such way that they are more likely to entangle. [335–337] The reasons why this would promote the non-specific attachment of LONDS only in some of the cases remain unknown and further experiments would be necessary to clarify this point.

Unlike for the biotin-NeutrAvidin binding experiments, the attachment of LONDS via PDP-thiol and maleimide-thiol chemistry was found to involve a high number of non-specific interactions between the LONDS and the SBLM. The use of maleimide-thiol and PDP-thiol has been used extensively for fluorescent labelling proteins [338,339] and linking of antibodies to drugs and delivery vehicles, [340,341] among other applications. [342] However, the literature on the use of this linking chemistry for assembling more complex structures (i.e. comparable to MB-LONDS) is limited. Geers et al. reported the formation of liposome-loaded MBs using a maleimide-thiol reaction for the attachment. [85,326] They claimed that the PDP-PEG2000-DSPE in the MBs could interact with the maleimide-PEG2000-DSPE contained in the liposomes, which resulted in spontaneous formation of liposome-loaded MBs. They did not provide details on thiol-containing molecules used to mediate this interaction, which would be required according to the reactions undergone by PDP and maleimide presented above (figure 7.11). The experiments reported in this chapter arise a concern about non-specific interaction between PDP and maleimide groups. As discussed above, many factors may contribute to this unexpected linking,

⁸as the study of the LOND stability indicated that LOND samples had no changes for at least six weeks when stored at 4 °C (figure 5.12, page 92).

such as autoxidative processes undergone by the PDP groups. Additionally, it is possible that impurities present in the lipid samples, as a result of their manufacture, could also contribute to the observed attachment.

The results presented in this chapter evidence the need for careful evaluation of the attachment between LONDS and MBs mimicking the MB shell. The results support the specificity of the biotin-NeutrAvidin binding, as well as the use of NeutrAvidin as a bridge between a SBLM and a LOND, both exhibiting biotin groups on their shells. Similarly, the results point at the successful attachment of LONDS and SBLMs via the maleimide-thiol chemistry, using the DTT molecule as a linker of maleimide groups. The results also suggest that non-specific binding of LONDS to the shell of the MBs could occur, and that care should be taken in confirming specific attachment, as non-specific interactions could result in unwanted detachment of LONDS from the MB shell.

Chapter 8

Topic: MBs and MB-LONDS

This chapter is concerned with the formation of MBs and MB-LONDS. The attachment of LONDS onto the MB shell via the biotin-NeutrAvidin link chemistry was performed off-chip, in a single-step on-chip and in two-step on-chip. The chapter also includes a study to determine the lifetime of the MB-LONDS architectures. The ultrasound response of these novel architectures was preliminary studied with help from Dr. James McLaughlan.

8.1 On-chip preparation of MBs

Compared to other production methods, such as mechanical agitation, microfluidics offer higher control over the size distribution of MBs and surface functionalisation. For these reasons, this project was concerned with the on-chip production of MB-LOND composites. Initially, the formation of MBs in the spray regime on-chip was tested. The design of the microfluidic devices used for this experiments are shown in section 3.7.1.2 (page 44). The devices were assembled as described above (section 3.7.1.1, page 43). A mixture of DPPC + 5% PEG2000-DSPE was used as the lipid shell to stabilise the MBs (section 3.1.2), and C_4F_{10} was used for their gas cores. The formation of MBs in the spray regime is characterised by a jet-like stream at the nozzle, where the gas and liquid phase meet (figure 8.1a). This is a result of the additional depth step into a flow-focusing device. [133] A video showing the formation of MBs in the spray regime is included in the supplementary (see appendix C). Figure 8.1b shows an image of a 1 : 10 dilution of the resulting MB sample. As described above (section 3.5.4, page 37), bright field images of MB populations were used to count the number of MBs in the sample and to size them.

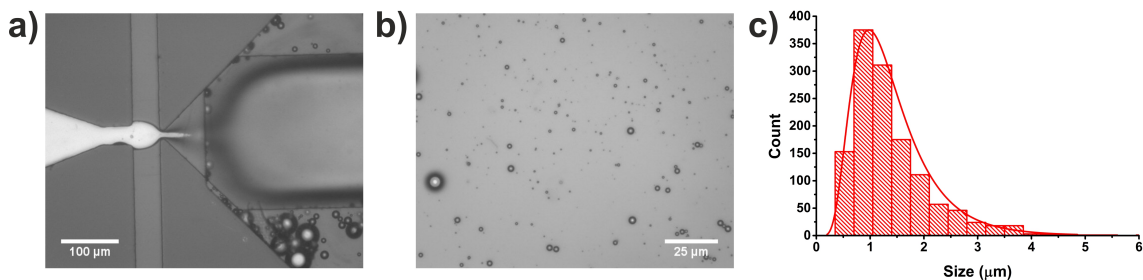


Figure 8.1: a) Image of MBs forming in the micro-spray regime. b) Bright field image of a 1:10 dilution of the resulting MB sample. The images was taken using a $40\times$ objective with $1.5\times$ internal magnification c) Histogram of the MB size distribution in the sample, with a total of 1308 MBs from 10 images sized.

Figure 8.1c shows the histogram for the size of the MBs in this sample, and shows a MB population with sizes in the range $1 - 6 \mu\text{m}$ with average size $(1.50 \pm 0.03) \mu\text{m}$ ($\sigma = 1.2 \mu\text{m}$). The concentration of this MB sample was obtained from the analysis of the bright field images, and the value was found to be 8.2×10^8 MBs/ml. Both the average size and the concentration values for these MB samples are similar to that previously reported for MBs prepared with this method. [98, 133, 178, 333]

8.2 Key considerations for preparing MB-LONDS

The number of LONDS that can theoretically bind to a MB depends on the radius of both the LONDS and the MBs (see figure 5.4, on page 76). Furthermore, the number of MBs in the solution determines the number of LONDS that can be transported. For MB samples prepared off-chip, it was possible to know the number and average size of the MBs prior to LOND incorporation. This allowed for tailoring the amount of StreptAvidin and LONDS added to the solution to match the number required in the specific samples. However, this was not possible for samples prepared on-chip, as MB production and LOND attachment occurred before sample collection. Therefore the number of LONDS required for the MB sample was estimated for a sample with a concentration of the order of 10^9 MBs/ml,¹ with an average size of $2 \mu\text{m}$. With these considerations, and knowing that the number of LONDS that can bind to a single MB is $N = 4 \frac{r_{MB}^2}{r_{LONDS}^2}$, the number of LONDS necessary to completely cover each MB in this sample was $\sim 8 \times 10^{11}$. The amount of protein required to functionalise 10^{11} LONDS was estimated from geometrical

¹This corresponds to the maximum expected MB concentration, produced by mechanical agitation. In any other case, the MB concentration was expected to be lower, and therefore LONDS should be in excess in the solution.

considerations, assuming that the StreptAvidin has a surface area of 25 nm^2 [314] and that it would cover 100% of the LOND surface. $3 \mu\text{M}$ of StreptAvidin or NeutrAvidin were added to the LOND solution, and incubated for around 15 min with gentle shaking throughout. These steps were followed for the functionalisation of all LOND samples towards MB-LONDS assembly, unless otherwise stated. After functionalisation, LONDS were added to the already prepared MB solution (for off-chip attachment), or to the MB lipid precursor, and allowed to bind for 10 min (for single-step). The choice of the incubation time was a result of the experiments on the binding of LONDS to SBLMs showed in chapter 7 (page 119).

8.2.1 The lensing effect

MBs formed with a fluorescently tagged lipid in their shell typically show as a fluorescent ring (figure 8.2a), when observed in an epifluorescence microscope. This has also been observed for MB-liposome complexes in which the liposomes were fluorescently tagged (i.e. with the incorporation of a fluorescently tagged phospholipid into their shell, or the encapsulation of a fluorophore in its core). This is generally considered as an indicator of successful attachment of liposomes onto the MB shell. [78, 133, 326, 327] MB-LONDS formed with fluorescently tagged LONDS were expected to appear alike.

Within this project, MBs with no added fluorescence either into their lipid shells or incorporated in their attachments (i.e. liposomes) were observed to have a fluorescent halo around them when other fluorophores were present in the solution. Figure 8.2b shows an

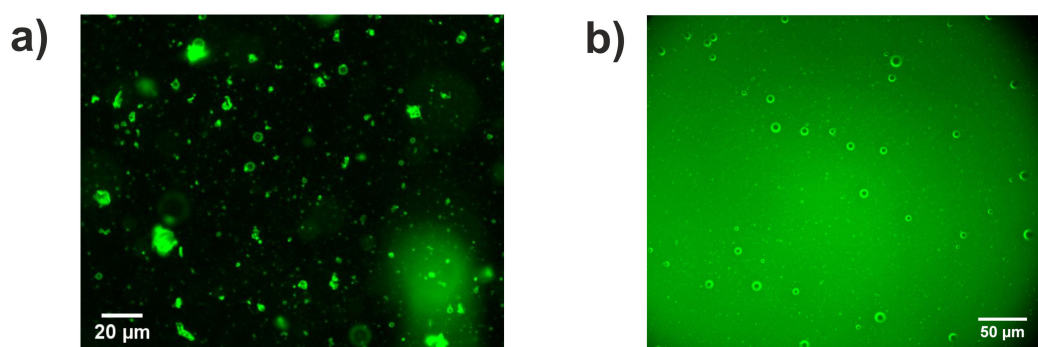


Figure 8.2: a) MBs stabilised with a lipid mixture containing fluorescently tagged phospholipids show as a fluorescent ring. In this case, Atto 488 DOPE was incorporated into the MB shell, and the sample was imaged under the FITC filter block. b) The addition of fluorescein to the MB solution causes the MBs, with no intrinsic fluorescence, to show as fluorescent rings. This sample was imaged using the FITC filter block.

example of this observation. In this case, the fluorophore fluorescein was added to the MBs solution. A fluorescent ring can be seen around the MB, characteristic of MB samples with intrinsic fluorescence, as discussed above. This phenomenon is referred to as *lensing effect* within this report. This phenomenon could be attributed to i) non-specific binding of the fluorophore to the MB shell, resulting in an increased concentration of the fluorescein around the MB shell; or ii) the refractive index mismatch between the MB gas core and the surroundings, together with the curvature of the gas-liquid interface. [343, 344] This observation suggests that fluorescent signals in the surroundings of the MBs, such as from unattached LONDS, could be easily mistaken as to be produced by the MBs themselves. This could be a problem for determining successful attachment of liposomes or LONDS onto the MB shell, unless careful washing is undertaken.

Removal of unattached fluorescent material (i.e. LONDS) from the solution could help reduce the signal produced by the MBs due to the lensing effect. Hence, within this project, extra care was put into washing MB-LOND solutions for detailed imaging of the structures. However, methods for MB sample washing often lead to a significant reduction in the concentration of MBs. For example, as described above (section 3.7.1.3, page 45), MB-LOND washing was typically done through flotation of the MB-LONDS due to the intrinsic buoyancy of the MBs through 1 ml of clean PBS. In this way, MB-LONDS were able to move towards the top of the solution, leaving behind any unattached LONDS and excess lipid. However, this method contributed to sample dilution, as only a small fraction of MB-LOND solution could be added to the PBS (1 ml) for cleaning. Furthermore, the MBs distributed over the area of the PBS container, making recovery of the whole

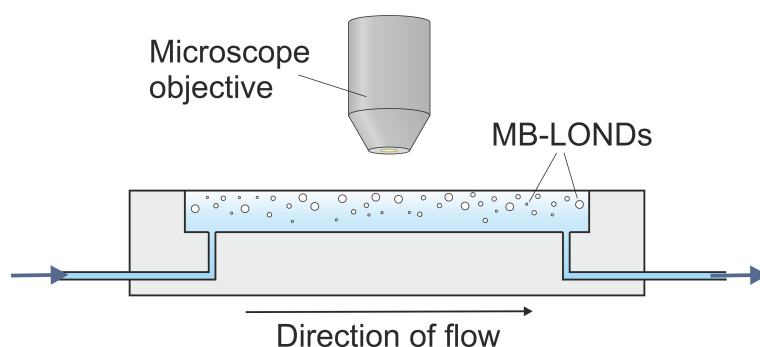


Figure 8.3: Schematic showing the cross-section of a flow cell used to wash and image MB-LOND samples. The MB-LONDS are contained in a chamber delimited by a coverslip, which allows for microscope imaging. A flow can be set simultaneously, helping removing unbound fluorescent material (such as excess LONDS) and enhancing the quality of the imaging by reducing the fluorescence background.

MB population difficult.² A flow cell was used for imaging MB-LOND samples and to confirm LOND attachment to the MB shell. This flow-cell allows for simultaneous sample washing and imaging (figure 8.3). A flow of buffer at 0.1 ml/min is set in the chamber, which removes unattached material but leaves the MB-LONDS in the chamber. This was expected to enhance the quality of the images by reducing the fluorescence background, and also assist the unambiguous identification of attachment of LONDS onto MBs.

8.3 Off-chip preparation of MB-LONDS

To assess the viability of LONDS assembly onto the surface of MBs, MB-LONDS were preliminary prepared off-chip. In this case the experimental conditions are simplified with respect to the formation of MB-LONDS on-chip. The attachment of the LONDS to the MBs occurs in a static environment, in contrast to the turbulent regimes existent in the microchips used in this project. Once added to the MB solution, the LONDS should diffuse due to Brownian motion, whereas the movement of the MBs should be dominated by their intrinsic buoyancy. Hence, in the absence of more complicated flow patterns, the MB surface should be fully accessible to the LONDS, and homogeneous coating was expected. Furthermore, MB stabilisation occurs prior to the addition of LONDS, which could help ensuring they have a suitably formed lipid shell to which LONDS can bind.

For this specific experiment, C_3F_8 was used to form the MBs by mechanical agitation (section 3.7.2, on page 46). The MBs were characterised by optical counting (section 3.5.4, page 37) prior to the addition of squalane LONDS; these results are shown in table 8.1. StreptAvidin functionalised squalane LONDS were readily added to the MB solution, and

Table 8.1: Average size and concentration of MBs prepared by mechanical agitation, before and after the addition of LONDS. A mixture of DPPC + 5% biotin-PEG2000-DSPE was used to stabilise the MBs. Squalane LONDS were stabilised with POPC + 5% biotin-PEG2000-DSPE + 0.1% Atto 488 DOPE.

Sample	Size (μm)	SD (μm)	Concentration ($\times 10^9 \text{ ml}^{-1}$)
MBs only	1.77 ± 0.07	1.1	2.6 ± 0.1
MB-LONDS (+StreptAvidin)	1.90 ± 0.07	1.3	1.9 ± 0.5
MB + LONDS (control)	1.70 ± 0.06	1.8	2.0 ± 0.5

²other cleaning methods previously reported, such as centrifugation of the MB sample, also compromise the number of MBs in the solution. [345]

incubated together for about 10 min to ensure full LONDS attachment onto the MBs, informed by the results on LOND attachment shown previously (chapter 7). The LONDS contained Atto 488 DOPE in their shell for fluorescence detection. To evidence the crucial role of the StreptAvidin in the formation of the MB-LONDS, a control sample consisted of MBs and LONDS mixed together in absence of StreptAvidin was also prepared. In this case, no binding of LONDS to the MBs was expected.

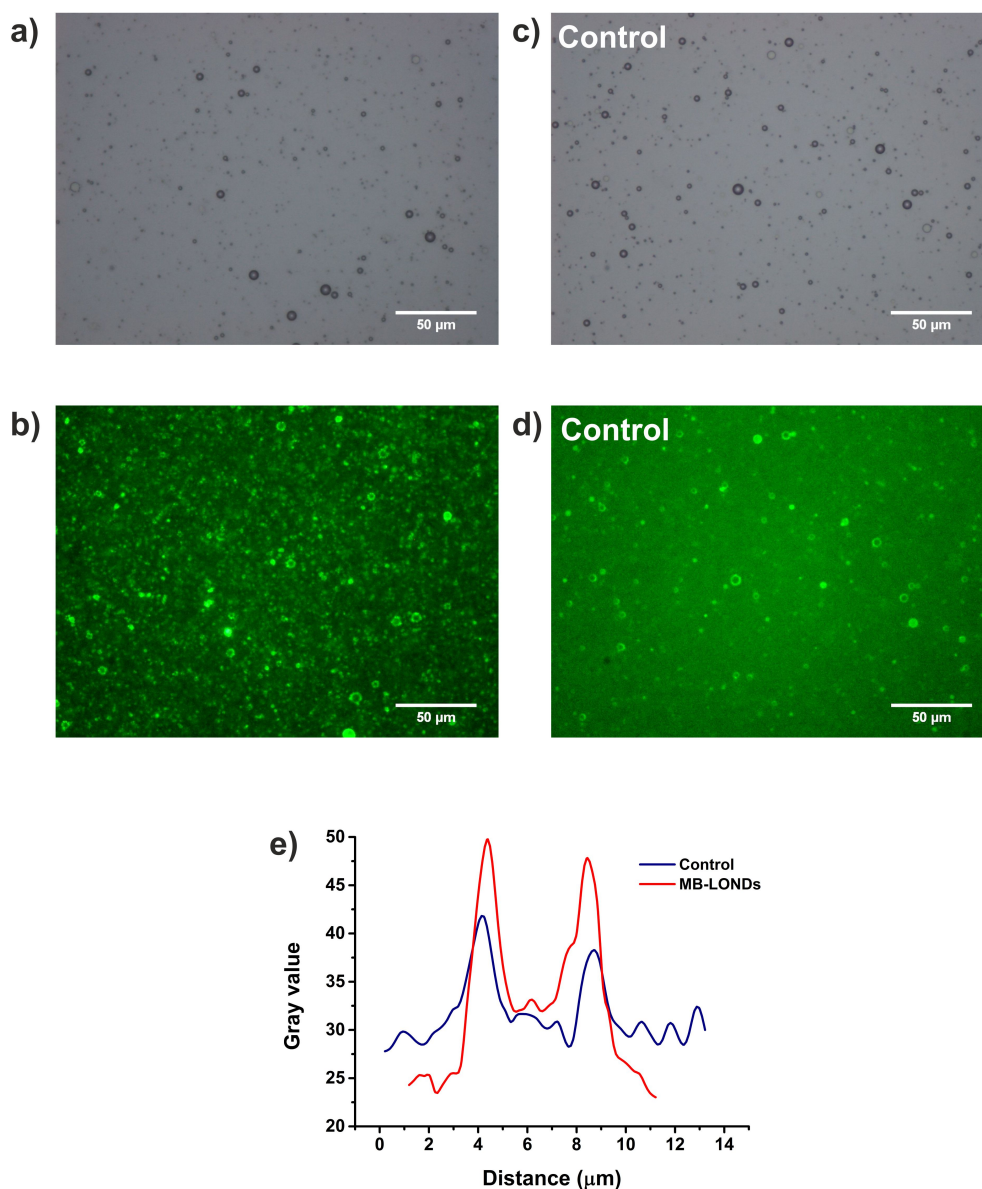


Figure 8.4: Images of MB-LONDS formed off-chip. All the images were taken using a $40\times$ objective with $1.5\times$ internal magnification and a FITC filter block. Images a) and b) show the bright field and epifluorescence images of MB-LONDS formed off-chip (in presence of StreptAvidin), respectively. c) and d) show the bright field and fluorescence images of a control experiment, where MB and LONDS were mixed together in absence of StreptAvidin. MBs show a green halo around, corresponding to the Atto 488 DOPE contained in the LONDS shell. e) Intensity profiles of MB-LONDS and MB from the control experiment. Each profile was produced averaging five different intensity profiles of the specific MB.

Figure 8.4 shows images of MB-LONDS formed off-chip, as well as of the control experiment that consisted of MB and LONDS mixed together in absence of StreptAvidin (control). The analysis of the bright field images (10 images were taken per sample) allowed for determining the average size and concentration of the MBs after the addition of LONDS; these results are summarised in table 8.1. Within experimental error the size and concentration of the MBs remained unchanged upon the addition of LONDS. This suggested good stability of the MB in presence of the LONDS, and points at the viability of the MB-LOND complexes. Figure 8.4b and c show the epifluorescence images of the MB-LOND sample and the control experiment, and in these, the fluorescence signal came from the Atto 488 DOPE contained in the LONDS shell. In the presence of StreptAvidin (figure 8.4b), MBs showed a fluorescent halo with granular appearance, which was likely due to the attachment of small agglomerates of LONDS to the MB shell. A non-homogeneous fluorescent background was observed in the image, which was attributed to the presence of excess LONDS and StreptAvidin agglomerations in the solution. The fluorescence background in the control image (figure 8.4d) appeared homogeneous, which is consistent with a reduced LOND agglomeration in absence of StreptAvidin. The MBs in the control experiment do also exhibit a fluorescence halo. As discussed above, this effect could be due to either the existence of non-specific binding between the LONDS and the MBs, or to the lensing effect (section 8.2.1). Figure 8.4e shows the intensity profiles for a MB-LONDS complex formed in presence of StreptAvidin, and for a MB of similar size from the control sample (no StreptAvidin added). The profiles were obtained averaging five different intensity profiles for each of the MBs analysed. In both cases, the fluorescence signal around the MB shell can be distinguished over the background intensity. This shows that MB lensing could make difficult the unambiguous identification of LONDS bound to the MB shell, and emphasises the need for sample washing to remove unbound material and confirm the attachment.

8.4 On-chip, single-step MB-LONDS preparation

In light of the successful attachment of LONDS to MBs off-chip, on-chip single-step attachment was attempted. This experiment aimed to replicate what was previously done for the preparation of MB-liposome complexes. [85,133] Here, the attachment of triacetin

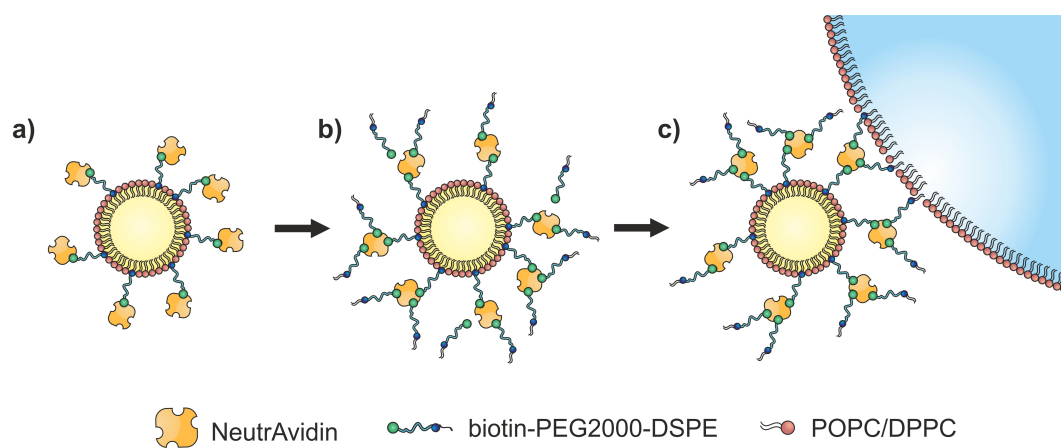


Figure 8.5: Illustration showing the formation of MB-LONDS on a single-step on-chip. a) LONDS were incubated with NeutrAvidin for 15 min for functionalisation. b) NeutrAvidin functionalised LONDS were incubated with the lipid for MB stabilisation for 15 min, to allow for biotin-PEG2000-DSPE to bind to the NeutrAvidin. c) Biotin-PEG2000-DSPE bound to NeutrAvidin-functionalised LONDS was incorporated into the MB shell upon formation.

and squalane LONDS to MBs was attempted in a single-step process, which is illustrated in figure 8.5.

The LONDS were incubated with $3 \mu\text{M}$ of NeutrAvidin during 15 min for functionalisation. Both LOND samples were fluorescently tagged with Atto 590 DOPE for imaging. After this the LONDS were added to the lipid for the MBs and incubated for around 15 min to allow for attachment of the biotin-PEG2000-DSPE to the NeutrAvidin on the LONDS surface. This lipid and LONDS mixture was introduced to a multiplex microspray chip through the liquid inlet, at $80 \mu\text{l}/\text{min}$. C_4F_{10} was used for the MB core, and it was injected into the microchip through the gas inlet at 140 kPa. The production of MB-LONDS following this protocol resulted in the formation of large oil droplets beyond the nozzle area in the microchip. A video showing this process is included in the supplementary (see appendix C). This was attributed to destabilisation of the LONDS as a result of shear forces during their transit through the nozzle and was thought to have the potential to affect the MBs i.e. hindering their formation. After collection of the MB-LONDS, the samples were imaged and the bright field images used to determine their concentration and size. The results for both MB-LOND samples, with squalane or triacetin LONDS attached, are summarised in table 8.2. The concentration of the MB-LONDS were comparable in both cases, and both were lower than what was obtained for MBs in the absence of LONDS (section 8.1). The flow conditions used for MB-LONDS formation in this experiment were identical to those used previously for the production of MBs only, thus the concentration of both samples was expected to be comparable. The larger difference observed could be

Table 8.2: Average size and concentration of MB-LONDS with attached squalane or triacetin LONDS, prepared in a single-step on-chip. A mixture of DPPC + 5% biotin-PEG2000-DSPE was used to stabilise the MBs. The LONDS were stabilised with POPC + 5% biotin-PEG2000-DSPE with 0.1% Atto 590 DOPE for fluorescence detection.

Sample	Size (μm)	SD (μm)	Concentration ($\times 10^7 \text{ ml}^{-1}$)
Triacetin MB-LONDS	3.0 ± 0.1	2.5	4.4 ± 0.2
Squalane MB-LONDS	2.10 ± 0.06	2.0	4.5 ± 0.5

arguably due to the LONDS in the solution, which might negatively affect the stability of the MBs.

The MB-LONDS were placed in a flow cell for washing and subsequent imaging (see figure 8.3). For the injection, the top layer of the MB-LONDS solution was discarded, as this layer typically contains larger MBs product of excess gas in the solution and MB coalescence. Once the sample was set in the flow cell, it was left for ~ 10 min to allow for the MBs to rise to the top of the chamber. Then a PBS flow at 0.1 ml/min was set through the chamber to remove excess lipid and unattached LONDS. Figure 8.6a and d show epifluorescence images of MB-LONDS formed using squalane or triacetin LONDS, respectively, after sample washing for 5 min. Both MB-LOND samples appeared as bright red rings. The concentration of the MB-LONDS in both samples was high,³ which resulted in overlapping of the fluorescence of the different MBs. The presence of oil droplets was also noted in the squalane LONDS samples. Roughly, these had diameters between $\sim 2 - 5 \mu\text{m}$, and could be a result of LOND destabilisation in the microfluidic device. Despite sample washing, some background fluorescence and fluorescence agglomerates could be seen in both images, particularly for the case of squalane MB-LONDS (figure 8.6d). The buoyancy of squalane in water ($\rho_{\text{squalane}} = 0.81 \text{ kg/m}^3$) could make the squalane LONDS accumulate on top of the chamber, compared to triacetin LONDS, which would have the tendency to sink ($\rho_{\text{triacetin}} = 1.16 \text{ kg/m}^3$). This could result in a more efficient washing in the case of triacetin MB-LONDS. At $t = 5$ min, larger MBs ($> 20 \mu\text{m}$) were present in the solution (figure 8.6a, d). These MBs were partially merged with the coverslip at the top on the chamber and were likely produced by coalescence of the MBs once they were set in the flow chamber. The average size of the samples at this point, $d = (7.2 \pm 0.6) \mu\text{m}$ for triacetin MB-LONDS and $d = (12.2 \pm 0.6) \mu\text{m}$ for squalane LONDS, was larger than

³the intrinsic buoyancy of the MBs caused them to accumulate on top of the chamber, concentrating the sample in this region.

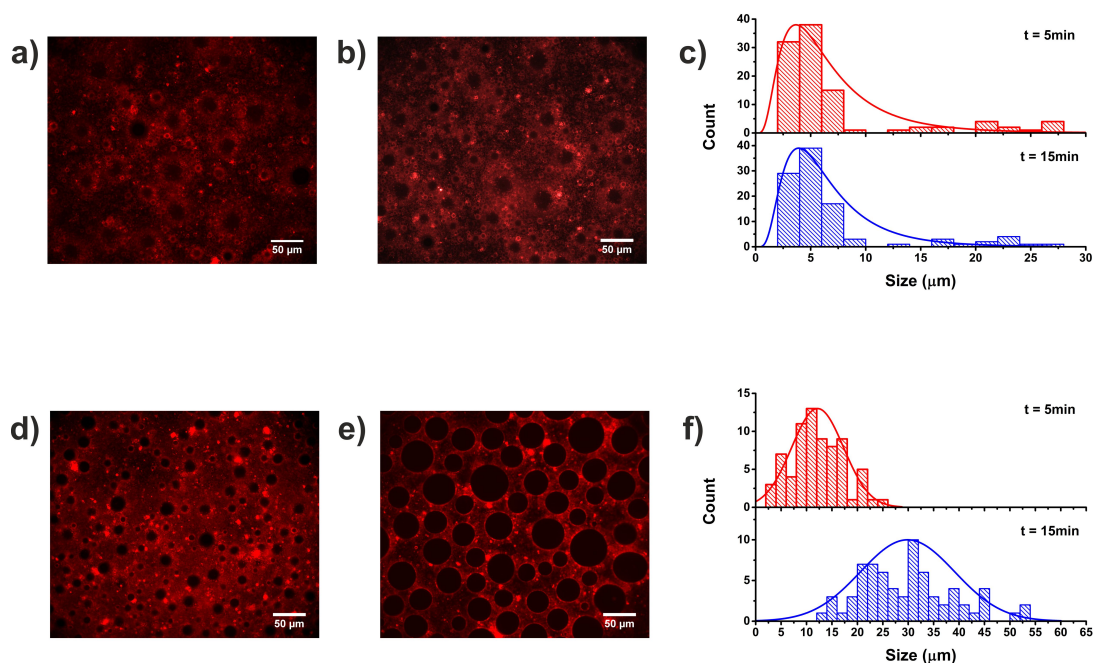


Figure 8.6: Epi-fluorescence images of MB-LONDS prepared in a single-step on chip. A flow cell was used to image the samples, with a $40\times$ objective and the TR filter block. a) Triacetin LONDS containing 5% Atto 590 DOPE were attached to the MBs, imaged after a 5 min wash. b) Triacetin LONDS containing 5% Atto 590 DOPE were attached to the MBs, imaged after a 15 min wash. c) Size histograms for triacetin MB-LONDS at $t = 5$ min and $t = 15$ min ($n = 102$ and $n = 100$, respectively). d) Squalane LONDS containing 5% Atto 590 DOPE were attached to the MBs, imaged after a 5 min wash. e) Squalane LONDS containing 5% Atto 590 DOPE were attached to the MBs, imaged after a 15 min wash. f) Size histograms for squalane MB-LONDS at $t = 5$ min and $t = 15$ min ($n = 72$ and $n = 70$, respectively)

that determined by optical counting (which results were summarised in table 8.2). The bright field images of the sample were acquired immediately after production, thus this increase in the average size of the population (around 133% for triacetin MB-LONDS, and 500% for squalane MB-LONDS) could be a result of MB-LOND instability.

The MB-LOND samples in the flow chamber were monitored for a few minutes, in order to assess changes taking place over time. Figure 8.6b and e show epifluorescence images of both the squalane and triacetin MB-LOND samples after 15 min wash. In the case of the triacetin MB-LONDS (8.6c) no significant changes in the sample were observed i.e. the number of MBs did not change noticeably. In the case of squalane MB-LONDS (figure 8.6d), large gas bubbles with sizes between $\sim 20 - 50 \mu\text{m}$ appeared within the washing time. Figure 8.6c and f show the size histograms for the triacetin and squalane MB-LONDS, at $t = 5$ min and $t = 15$ min. Triacetin MB-LONDS exhibited an average size $d = (7.2 \pm 0.6) \mu\text{m}$ ($\sigma = 6.5 \mu\text{m}$) at $t = 5$, and $d = (6.9 \pm 0.6) \mu\text{m}$ ($\sigma = 5.8 \mu\text{m}$) at $t = 15$. This indicates that, within experimental error, the size of the triacetin MB-LONDS did not change within this time. The size of the squalane MB-LONDS changed

from $d = (12.2 \pm 0.6) \mu\text{m}$ ($\sigma = 5.1 \mu\text{m}$) to $d = (30 \pm 1) \mu\text{m}$ ($\sigma = 9.3 \mu\text{m}$) at $t = 15$, which is an increase of around 150%. The formation of large gas pockets was likely a result of MB coalesce, and Ostwald ripening (equation 2.23, page 26). [130] In this specific case, the Ostwald ripening rate, ω of the C_4F_{10} was calculated⁴ to be approximately $\omega = 8.2 \times 10^{-20} \text{ m}^3/\text{s}$. This implies that a MB with an initial diameter of around $10 \mu\text{m}$ would result in a MB with a size $\sim 40 \mu\text{m}$ within 15 min. This value is comparable to the increase in the average size observed for this MB-LOND sample, thus suggesting that Ostwald ripening may have played an important role in the instability observed.

However, the reasons why coalescence and Ostwald ripening were only observed in the case of squalane LONDS are not clear. Although there are no reports on the stability of MBs in presence of oil nanodroplets, the literature on stability of foams (as compared to MBs) in presence of oil or oil emulsions is extensive in the food industry field. [346–349] Most authors have reported that the presence of hydrocarbon droplets in the solution adversely affects the foam’s stability, as a result of the interfacial activity of the hydrocarbon molecules. In the microfluidic device used to assemble the MB-LONDS architectures, oil droplets were observed to form beyond the nozzle, which was tentatively attributed to LOND instability upon passage through the nozzle. It is possible that destabilisation of a fraction of the LONDS in the solution could result in oil release into the solution, affecting the stability of the MBs.

8.5 On-chip, two-step MB-LONDS preparation

To overcome the stability problems observed in MB-LOND samples prepared in a single-step process, a microfluidic device with an added mixing serpentine was used for assembling the structures. In a mixing serpentine, the fluid velocity mismatch between the center and the periphery of the channels, at the bends, give rise to turbulent mixing (section 2.1.2.1, page 13). The design of the chip used for the experiments is shown in figure 3.9, (page 45). Figure 8.7 shows a section of the CAD design for this chip. In this device, MBs are formed first under the spray regime (inset a). LONDS are subsequently added to the MB solution further downstream (inset b); in this example, the LONDS

⁴the parameters for C_4F_{10} MBs used for these calculations were $\gamma = 45 \text{ mN/m}$, $S_b = 1.5 \times 10^{-3} \text{ kg/m}^3$, $V_m = 21 \times 10^{-3} \text{ m}^3/\text{mol}$, $D = 2 \times 10^{-9}$ taken from reference [93] and $\rho = 11.2 \text{ kg/m}^3$. T was considered 293 K and $R = 8.31 \text{ kgm}^2/\text{s}^2\text{Kmol}$.

were tripropionin LONDS containing 0.1% Atto 590 DOPE, and the area where they were incorporated to the MB solution was imaged under the TR filter block ($10\times$ magnification). In inset b the LOND solution can be seen in red, and the MB solution and gas stream appears black, in the center of the channel. MBs and LONDS are mixed together throughout the serpentine, which provides the LONDS with extra time to assemble onto the MB shells, compared to the single-step production. Insets c, d and e on figure 8.7 show the mixing stage at different points throughout the serpentine. After the first turn (inset c) the MB and LOND solutions remained unmixed, as can be seen from the separation between the central black region in the channel (the MBs and gas stream) and the fluorescent LONDS solution. This is illustrated by the intensity profile across the channel, including in the inset. After the third turn (inset d) LONDS were distributed across the section of the channel, suggesting mixing with the MB solution. Inset e shows the stage of the mixing towards the end of the serpentine. The LOND solution can be seen concentrated in the center of the channel, also observable from the intensity profile across the channel including in the inset. The liquid velocity in the center of the channel is higher, thus the pressure in this region is lower, resulting in concentration increase of the LONDS towards the center. The time during which MB and LONDS mix together throughout the serpentine can be estimated from the dimensions of the serpentine and considering the flow rates used in the device. The cross-section of the mixing serpentine is $270 \times 50 \mu\text{m}$, and has a total length of 56.6 mm. The flow rate in the channel was considered to be the sum of the flow rate used for MB production at which the LONDS are incorporated into the device, $40 \mu\text{l}/\text{min}$. With these assumptions, the time that MB and LONDS spend in the serpentine was found to be 1.14 s. It is important to note that in this device attachment takes place under a dynamic regime in which the flow turbulences mix the LONDS and the MBs throughout the serpentine. This is very different to conditions in the QCM-D experiments and off-chip preparation of MB-LONDS, where LONDS attachment occurs in a static fluid and it is limited by diffusion of the LONDS in the solution.

The preparation of MB-LONDS in a two-step process was attempted with triacetin, squalane and tripropionin LONDS. In all the cases, the LONDS were formed with POPC and 5% biotin-PEG2000-DSPE to facilitate the attachment via the NeutrAvidin-biotin binding, and 0.1% Atto 590 DOPE was included for fluorescence detection. The MB shell was composed of DPPC and 5% biotin-PEG2000-DSPE. Figure 8.8 shows images of MB-LONDS samples prepared with different types of LONDS. These images correspond

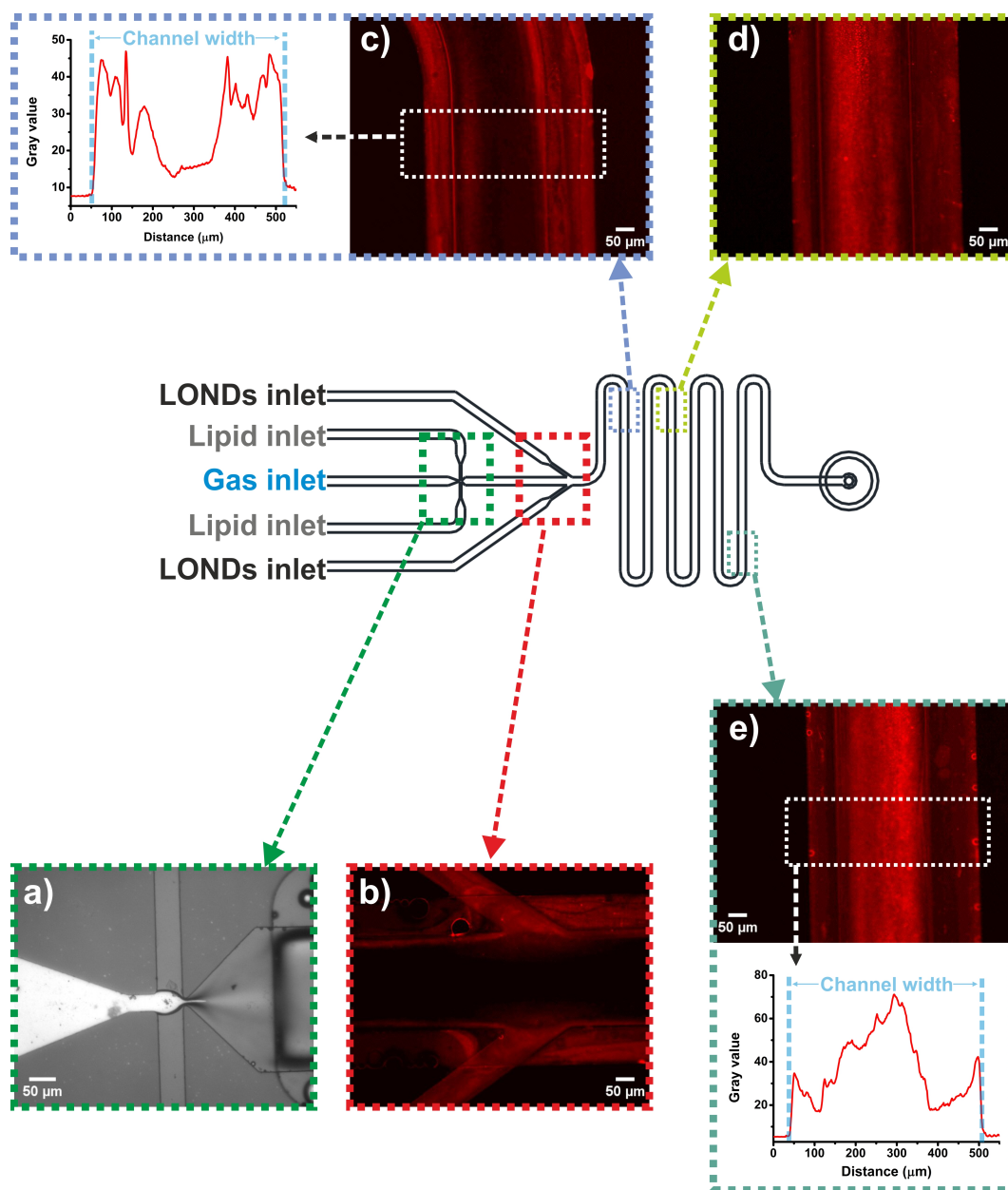


Figure 8.7: Section of the chip design used to prepare MB-LONDS in a two-step process. The whole design is shown in figure 3.9 (page 45). Insets show: a) bright field image of the formation of the MBs under the spray regime, b) fluorescence image of the region where the LONDS are added to the MB solution; in this example, tripropionin LONDS tagged with 5% Atto 590 DOPE were added at a concentration 10^{11} LONDS/ml, c-e) different stages of the LONDS and MBs mixing throughout the serpentine. The mixing allows for binding of the LONDS to the MB shell. Insets c and e include an the intensity profile across the channel.

to undiluted, unwashed samples that were imaged to assess the success of the experiment. Pictures of the region of the MB sample were taken both in the bright field and under the TR filter block for the fluorescence images. Table 8.3 contains the average size and concentration for all the MB-LOND samples, and also for MBs only prepared in the same device, under the same conditions⁵. The data for MBs only, triacetin MB-LONDS and

⁵clean PBS was incorporated through the LONDS inlet, instead of the LOND solution.

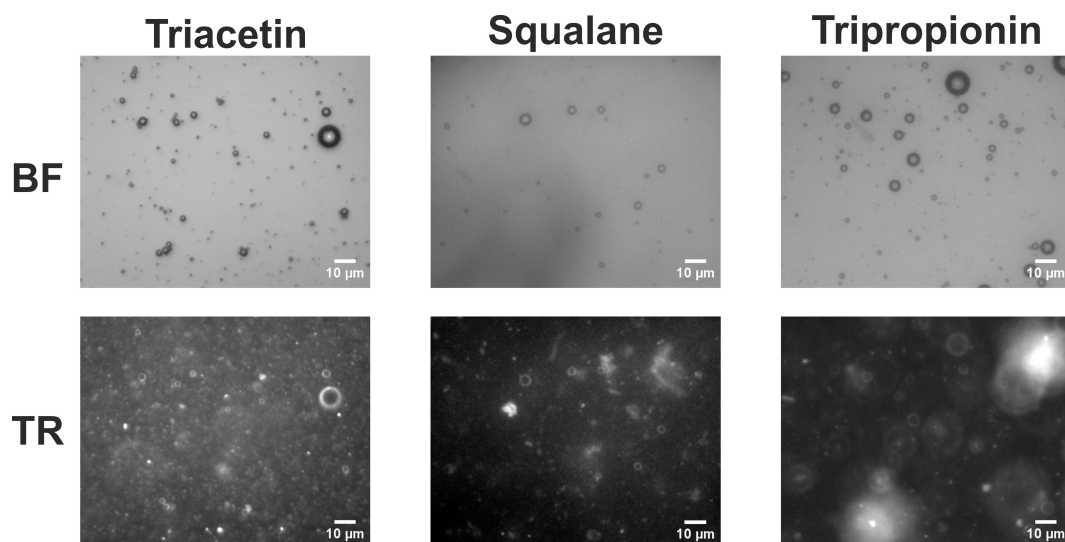


Figure 8.8: MB-LONDS formed in a two-step process on-chip. The panel contains bright field and fluorescence images (taken using the TR filter block) of the same areas, under the 40 \times objective with 1.5 \times internal magnification. Triacetin, squalane and tripropionin LONDS have been successfully attached to MBs following this protocol.

Table 8.3: Average size and concentration of MB-LONDS prepared with different LOND types. MB average size and concentration are included. A mixture of DPPC + 5% biotin-PEG2000-DSPE was used to stabilise the MBs. Squalane and triacetin LONDS were stabilised with POPC + 5% biotin-PEG2000-DSPE, whereas tripropionin LONDS were stabilised with DSPC + 20% cholesterol + 5% biotin-PEG2000-DSPE. All LONDS contained 0.1% Atto 590 DOPE for fluorescence imaging.

Sample	Size (μm)	SD (μm)	Concentration ($\times 10^7 \text{ ml}^{-1}$)
MBs only	2.33 ± 0.08	2.1	4.4 ± 0.7
Triacetin MB-LONDS	1.9 ± 0.2	1.6	3.8 ± 0.6
Squalane MB-LONDS	2.4 ± 0.1	1.8	1.5 ± 0.2
Tripropionin MB-LONDS*	2.6 ± 0.2	2.2	5.3 ± 0.4

* Data for tripropionin MB-LONDS corresponds to only one repeat of the experiment,

squalane MB-LONDS correspond to averaged results of three repeats of the experiment. Only one data set was available for tripropionin MB-LONDS, due to the late addition of tripropionin LONDS to the project. Triacetin MB-LONDS were found to have the smallest size, and to be around 26% smaller than tripropionin MB-LONDS, which exhibited the largest size. Within experimental error, the sizes of squalane and triacetin MB-LONDS were comparable, and were also comparable to the size of MBs in the absence of LONDS.

The concentration of the samples was of the order of 10^7 MBs/ml, which is lower than what is usually obtained for MBs produced in this microfluidic regime ($10^8 - 10^9$ MBs/ml, section 8.1). This was due to the incorporation of the LONDS through a second liquid inlet, which increases the total liquid volume produced by the chip and contributed to the

dilution of the final MB-LONDS structures by a factor of 2, in comparison to conventional microspray device. The concentration of MB-LONDS formed with squalane LONDS was found to be lower than the concentration of the other MB-LOND samples. Generally, this was observed observed for all squalane MB-LONDS prepared in a two-step process on-chip. It is possible that a fraction of squalane from the LONDS could incorporate into the MB shell, affecting their surface tension and enhancing MB coalescence. This could result in a reduction of the MB-LONDS concentration, as compared to MB-LONDS formed with triacetin LONDS.

MB-LONDS were washed and imaged in a flow cell. Figure 8.9 shows epifluorescence images of squalane and triacetin MB-LONDS in a flow chamber, and after sample washing for 90 min. Considering the volume of the flow cell (~ 0.5 ml) and the washing flow rate (0.1 ml/min), the liquid volume in the flow cell was replenished approximately 18 times during the 90 min washing step. This was considered enough liquid volume for any unbound LONDS to be removed from the chamber. Informed by previous results (section 8.4), these MB-LOND samples were diluted 1 : 10 prior to the injection in the flow chamber. This notably reduced the number of MBs in the chamber, improving the quality of the imaging (if comparing figures 8.6 and 8.9). As discussed above, the MB-LOND architectures appear as fluorescence rings as a result of the attachment of fluorescent LONDS (incorporating Atto 590 in this case) onto the shell of the MBs. The MB-LONDS were videoed, and these are included in the supplementary (see appendix C). Diffusion of the fluorescent material attached to the MB shells (i.e. LONDS) can be seen in these videos. These confirmed the successful assembly of the architectures.

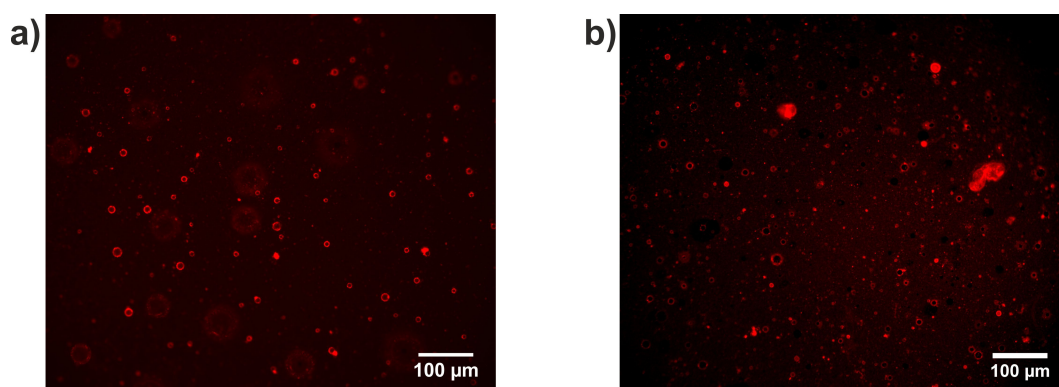


Figure 8.9: Epifluorescence images of MB-LONDS prepared in a two-step process on-chip. The samples were washed and imaged using a flow cell for 90 min. The LONDS were fluorescently tagged with 0.1% Atto 590 DOPE, and the TR filter block and a 20x objective were used to take the images. a) Triacetin MB-LONDS. b) Squalane MB-LONDS.

MB-LOND architectures formed in the two-step process were also imaged by confocal microscopy. In this case, the shell of the MBs was fluorescently tagged by adding 0.1% Atto 488 DOPE into their shell composition. The LONDS incorporated 0.1% Atto 590 DOPE in the shells. After preparation following the protocol described above, the MB-LONDS were washed via flotation (section 3.7.1.3, page 45). The aim of this experiment was to image individual MB-LOND composites, thus the reduction of the sample concentration due to the washing step was not a concern. Figure 8.10 shows fluorescence confocal images of triacetin and squalane MB-LONDS. The attachment of LONDS to the MB shell was confirmed by the presence of a fluorescent red rings around the MB shell, which corresponds to the signal from the Atto 590 DOPE contained in the LONDS shell. Composite images were produced by superimposing the fluorescence image in the FITC channel, corresponding to the Atto 488 in the MB shell, and the TR channel, corresponding to the LONDS. Spatial coincidence of both the red and the green signals can be seen in the merged imaged, which is supported by the intensity profiles across the MB-LONDS (also shown in figure 8.10). This further supports the successful attachment of the LONDS and the MBs. A Z-stack of the squalane MB-LONDS architecture was recorded using the confocal system, and it is included in appendix C.

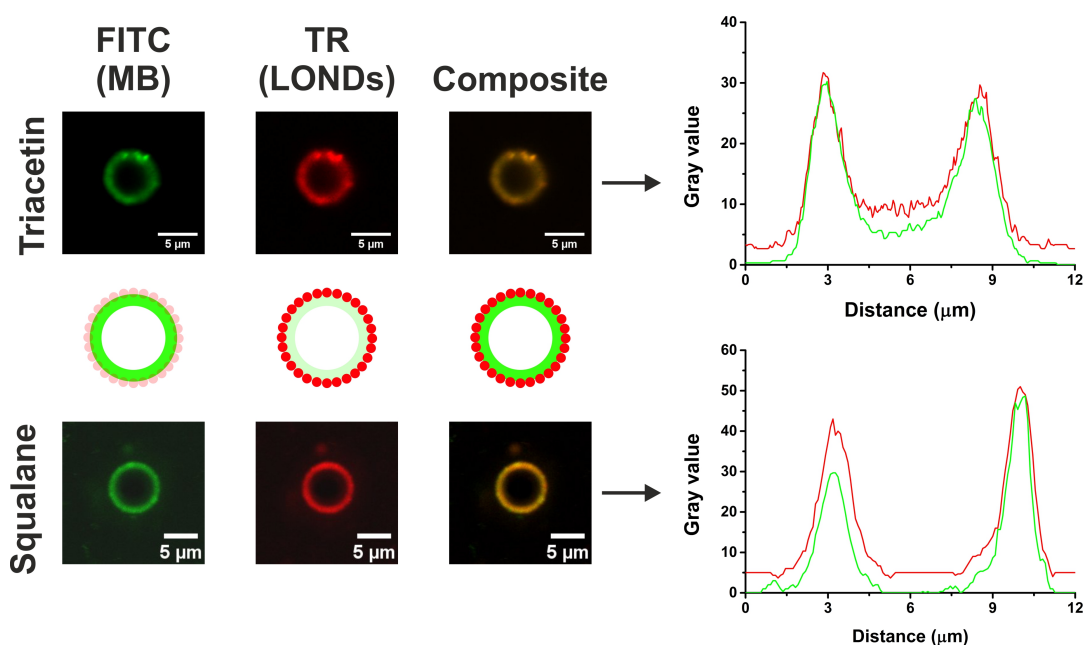


Figure 8.10: Confocal images of MB-LONDS formed in a two-step process on-chip. The images were taken using a 60x oil immersion objective. The samples were washed by flotation of the MBs prior to imaging. 0.1% Atto 488 DOPE was incorporated to the MB shell (FITC, 488 nm laser), and the shell of both the triacetin and the squalane LONDS was tagged with 0.1% Atto 590 DOPE (TR, 552 nm laser). The composite images were produced by superimposing the signals from the red and the green channels. The intensity profiles show the fluorescence counts across the MB-LONDS, for both colours.

8.5.1 MB with mixed squalane/triacetin LONDs attachment

The combination of different LOND types onto a single MB-LONDs architecture has the potential of allowing for combination treatments, in which different drugs with complementary effects are administered simultaneously. [350–352] The reason for this is that the solubility of different therapeutic agents differs across different oils, as suggested by the results with drug mimics and CA4 presented above. Thus attachment of different oil type LONDs could facilitate the incorporation of different therapeutic agents onto the MB-LOND architectures.

To serve as a proof of concept, MB-LONDs were prepared with a 50/50 combination of squalane and triacetin LONDs. The architectures were produced by following the two-step preparation method, described above, and were washed through flotation prior to imaging. Figure 8.11 shows fluorescence confocal images of MB-LONDs formed from a mixture of triacetin and squalane LONDs attached. In this case, the shell of the MBs did not include any fluorescent lipid. Triacetin LONDs were tagged with Atto 488 DOPE and imaged in the FITC channel, and squalane LONDs included Atto 590 DOPE and were seen in TR. The images show fluorescence rings (in each colour channel) around the MB, which is characteristic of the attachment of LONDs onto the MB shell. The composite image shows coincidence of the red and green fluorescence, which is supported by the intensity profile across the structure. This suggests that both the triacetin and the squalane LONDs successfully attached to the MB, and reinforces the potential of MB-LONDs to serve as vehicles for combination therapy drugs.

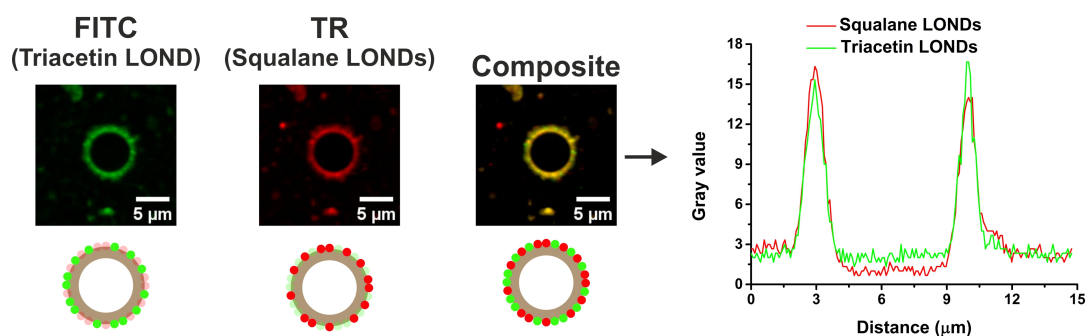


Figure 8.11: Confocal images of a MB coated with a 50/50 mixture of squalane and triacetin LONDs. The images were taken using a 60x oil immersion objective. Triacetin LONDs contained 0.1% Atto 488 DOPE in their shell (FITC, 488 nm laser), whereas the shell of the squalane LONDs was tagged with 0.1% Atto 590 DOPE (TR, 552 nm laser). The samples were washed by flotation of the MBs prior to imaging.

8.6 Stability of MBs and MB-LONDS

The lifetime of the MB-LONDS is an important parameter if the composites are to find a medical application. Upon injection of the MB-LONDS *in vivo*, the architectures should remain stable until reaching the place of interest, which would enhance the specificity of the treatments and reduce side effects associated to the transported drugs.

To study the lifetime of the MB-LONDS, their concentration was monitored over time, whilst kept at 37 °C. MB dissolution was expected to translate into a reduction in the number of structures in the solution therefore diminishing their concentration. The temperature conditions in this experiment aimed to better resemble those to which the MB-LONDS would be exposed to *in vivo*. Upon preparation of the MB-LONDS in a two-step process on-chip, as described above (section 8.5), C₆F₁₀ was added to the MB-LOND solution to enhance the stability of the MBs. [178] The samples were kept at 37 °C using a block heater, and sets of 15 bright field images were taken every 15 min. The duration of the experiment was 2 h, as there was an interest in monitoring the stability of the MB-LOND for a time period similar to the time required for the architectures to reach the target site following injection and accumulate over time in a human patient. Figure 8.12 shows the reduction on the concentration of triacetin and squalane MB-LOND samples within 2 h and at 37 °C. Populations of bare MBs were studied as a comparison. The initial concentrations were determined by optical imaging and counting, and were found to be very similar for all of the samples, with squalane MB-LONDS exhibiting the lowest value, as discussed above (section 8.5). The data points for MBs and triacetin MB-LONDS were fitted to an exponential decay, and their half-lives τ were determined from the fitting. In the case of bare MBs, $\tau = 61$ min, whereas $\tau = 17$ min for triacetin MB-LONDS. These values indicate that the dissolution rate for triacetin MB-LONDS is around 3-fold higher than for bare MBs. One reason could be oil leakage from the triacetin LONDS, which could result in oil insertion into the MB shell and thus affect the stability of the MBs. The data points for squalane MB-LONDS were fitted to a linear regression, and the reduction of the concentration in this case was of around 39%.

The results shown in figure 8.12 for MBs and MB-LONDS suggest that LONDS attachment had no negative effect in the lifetime of the MBs. The results also suggest that a coating of squalane LONDS slowed the rate of dissolution of the MBs, as seen by the

slower reduction of the MB-LONDS concentration over time, compared to bare MBs. This is similar to what has been observed for MB-liposome complexes before, and has been hypothesised to be due to the additional lipid coating around the gas core, (i.e. the liposomes) which increases the resistance to gas permeation. [133] Increased MB stability has been observed for MBs stabilised with nanoparticles, known as *armoured* MBs [353,354]. Given that the ability of the gas to escape from the MB core depends on the interfacial area available for the gas molecules to cross the MB shell (equation 2.2, page 11), the incorporation of solid nanoparticles into the MB shell results in enhanced MB lifetime, as they reduce the interfacial area. [355,356] It is possible that the attachment of LONDS onto the MB shell could have a similar effect in reducing the area available for the gas to solubilise. However, more experiments would be necessary to prove this hypothesis.

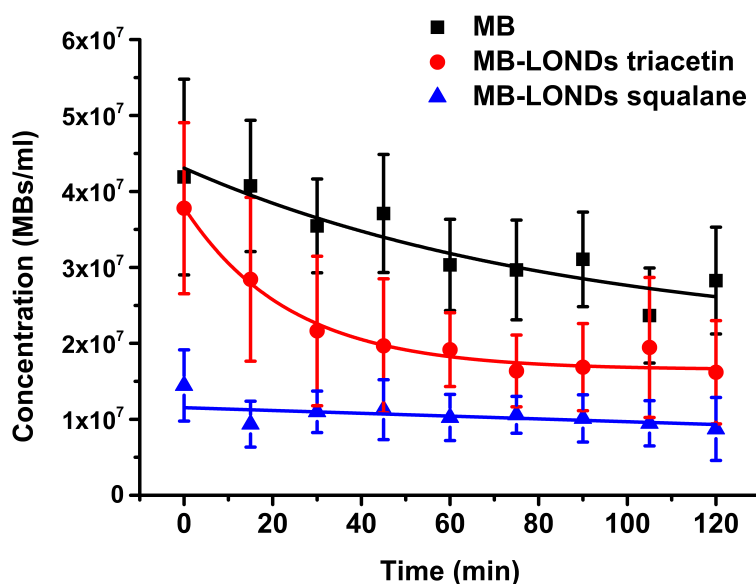


Figure 8.12: Lifetime of MBs and MB-LONDS at 37 °C, studied as the changes in their concentration over time. Data is the result of averaging the results for three different MB or MB-LONDS preparations, and the error bars represent the standard deviation between the repeats. C_6F_{10} was added to the solution to improve MB lifetime. MBs and triacetin MB-LONDS lifetime were fitted to an exponential decay, with $\tau = 61$ min and $\tau = 17$ min, respectively. Concentration decay of squalane MB-LONDS was fitted to a linear regression.

8.7 Ultrasound response

The US response of the MB-LONDS was tested with help from Dr James McLaughlan. This was important to ensure that the MB-LOND composites retained the echogenicity of the MBs, and hence that they could be used for theranostic purposes. Sample preparation

was performed by the author and data collection was done jointly with Dr McLaughlan. Data analysis was performed by Dr McLaughlan. All the MB-LOND samples used for these experiments were produced on-chip in a two-step process as described above (section 8.5).

The acoustic attenuation of US pulses propagating through a test chamber containing MBs at a concentration⁶ $\sim 10^6$ MBs/ml was measured. [357] A broadband (1 – 20 MHz) transducer was used to generate the US signal, and a needle hydrophone was used as a receiver. A pre-distorted chirp signal [358] was used to transmit a 20 ms, 25 kPa broadband (214 MHz) US pulse. The MB chamber, the transducer and the hydrophone were submerged in a large water tank containing degassed and filtered water. The US attenuation was calculated by subtracting the signal in presence of MBs and the reference value obtained for the chamber filled with filtered water. This process was repeated ($n = 3$) for each sample tested. Figure 8.13 shows the frequency dependent acoustic attenuation for bare MBs and squalane or triacetin MB-LONDS. To serve as a control experiment, the acoustic attenuation of squalane and triacetin LONDS was also studied. In this case, the similar acoustic impedance of the oils and the surrounding water was expected to translate into negligible attenuation of the ultrasound signal by the LONDS. As anticipated, the results in figure 8.13 show that the LONDS did not attenuate the ultrasound signal, which is consistent with a negligible interaction with the ultrasound waves. All of the MB and MB-LOND samples showed a peak attenuation value between 3.5 – 4.5 MHz, which marks a resonance frequency for the different populations. The resonance peak shifted to higher frequencies for both MB-LOND samples, suggesting that these MB types had an increased shell stiffness when compared with the equivalent MB without attached LONDS. Similar behaviour has been reported before for MB-liposome complexes, in which the addition of liposomes resulted in an increase in the shell viscosity. [359] Both MB-LONDS samples were found to have a lower level of attenuation than the MB population, and the reasons for this differences are unclear. Comparable attenuation levels have been reported for bare MBs and MB-liposomes; similarly, liposome loading has been seen to have negligible effect in the ultrasound response of MBs. [98, 360] One reason to explain the differences in attenuation between bare MBs and MB-LONDS could be concentration differences of the samples. The concentration of the samples was determined immediately after production, and these values were used to prepare the dilution used in the US experiment (10^6 MBs/ml). It is possible that some MBs dissolved prior to the US experiment, which took place around 30

⁶sample dilution was based on the concentration values obtained for each sample immediately after production.

min after the production, thus reducing the MB-LOND concentration and resulting in a lower attenuation signal. This would be particularly noticeable for MB-LONDS triacetin (see figure 8.12).

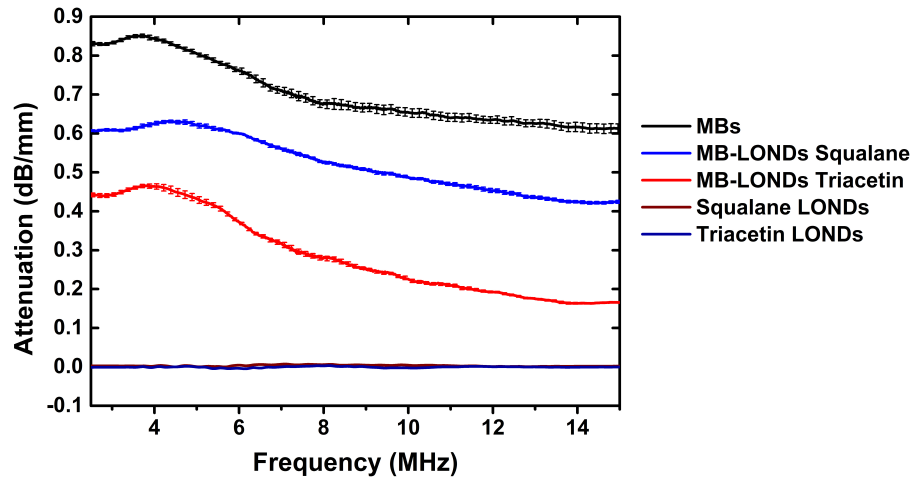


Figure 8.13: Attenuation of different MB and MB-LOND populations as a function of the ultrasound excitation frequency (2 – 14 MHz). All samples had an equivalent concentration of 10^6 MB/m, and the concentration of the two LOND samples was 10^9 LONDS/ml. The error bars represent the standard deviation of three repeat measurements of each population.

To investigate the echogenicity of the MB-LONDS, samples were imaged in a tissue-mimicking agar-based gel flow phantom. In these, the *in vivo* blood microcirculation can be replicated for the assessment of the MB perfusion; compared to an animal model, wall-less flow phantoms provide a better control over the experiment, as the size of the vessels and the dimensions of the system are well-defined. [361,362] A schematic of the experimental set-up is shown in figure 8.14a. A syringe driver was used to generate a MB flow through the mimicking vessel, from a reservoir containing a MB population at a concentration $\sim 10^8$ MBs/ml. An in-house build diagnostic US imaging system was used for image recording. A transmitted pulse with a frequency of 7.6 MHz was selected and focused at 40 mm from the transducer surface. This coincided with the location of the vessel in the tissue-mimicking gel, through which the MBs circulated. Data was recorded and post processed to generate B-mode images. Imaging was performed on MB and MB-LOND populations, and water alone was used as a control, as water is known not to scatter US. Figure 8.14b shows the B-mode images for all of the samples. Lack of US scattering shows in black (i.e. -50 dB loss), and signal received from echoes shows in a grey-to-white scale (0 to ~ -35 dB loss). As expected, water showed no US scattering. Scattering of the US signal was detected for all the samples containing MBs, as seen from

the increased brightness inside the vessel (shown in yellow on figure 8.14b). These results confirm the US properties of the MB-LOND architectures, and suggest that they could be used as theranostic agents. Furthermore, the US could be used to control spatially and temporarily the release of the LONs from the MB shells, hence improving treatment specificity and potentially reducing adverse side effects in patients. Further experiments are required in order to fully explore the US properties of the complexes, as well as to better understand the release of the LONs from them, in a similar fashion to what has been previously done for MB-liposome complexes. [98, 359, 360, 363, 364]

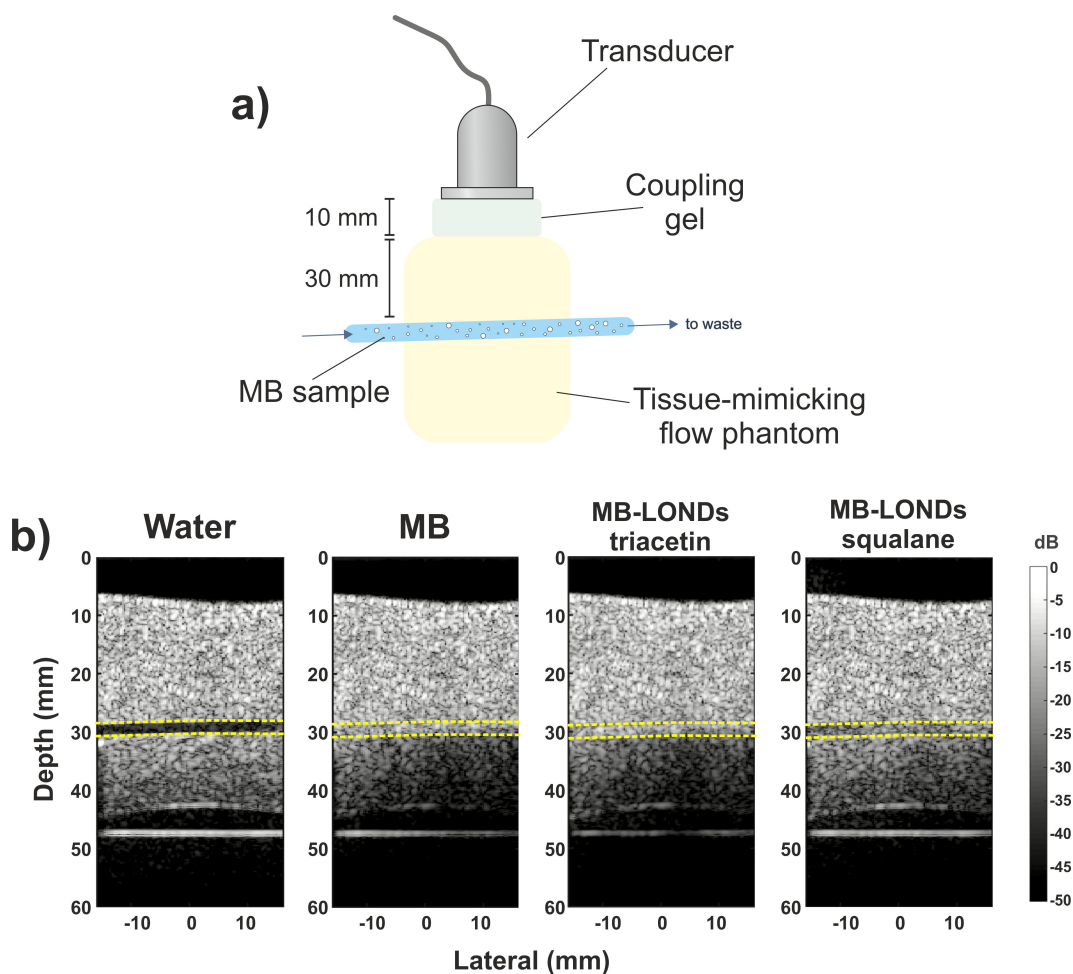


Figure 8.14: Echogenicity of MB-LONs was tested in a wall-less flow phantom. a) Schematic showing the set-up for the experiment. MBs flow through a vessel in a tissue-mimicking material. A transducer was used to produce a 7.6 MHz ultrasound pulse focused on the vessel. b) B-mode images showing the US response of water (control), MBs, triacetin and squalane MB-LONs. These images are representative frames extracted from the videos included in the supplementary (see appendix C). The samples were flown through a wall-less vessel, marked in yellow. The B-mode images were generated by computer processing the received radio frequency signal.

8.8 Discussion

The aim of this project was to fabricate a novel MB architecture for the enhanced delivery of hydrophobic drugs. LONds assembly onto the shell of the MBs would allow for the transport of poorly water soluble therapeutic agents encapsulated in their oil core. Particularly, this work was concerned with the on-chip fabrication of MB-LONds, provided that microfluidics are a robust technique for the production of MB, which offers reproducible size distribution of the samples and also allows for controlled MB surface functionalisation. This chapter has shown the production of MB-LONds following three different routes: i) off-chip, in where LONds are added to the MBs once these are formed, ii) on-chip, in a single-step process in where the LONds are combined with the lipid for the MB shell, and introduced jointly into the microfluidic device, and iii) on-chip, in a two-step-process in which MBs are formed first and LONds are incorporated to the MB solution further down stream.

The production of MB-LONds off-chip was attempted first in order to assess the formation of the architectures in a simpler experimental set-up, as compared to the on-chip production. MBs were prepared by mechanical agitation, and NeutrAvidin functionalised LONds were added to the solution afterwards. Sample sizing revealed comparable sizes for MB-LONds and bare MBs produced using the same method, suggesting that LONds had no negative effect in the stability of the MBs. Similarly, the concentration of the MB-LONds did not change compared to the concentration of MBs in samples with no LONds. Fluorescence images of the sample revealed the assembly of the LONds onto the MB-shell. The negative control exhibited differences with respect to the positive result, such as homogeneous background appearance. However, MBs from both samples exhibited a bright ring around their shell, which is characteristic of MBs with intrinsic fluorescence (i.e. with fluorescently tagged lipid in their shells) or fluorescent attachment. This phenomenon was observed throughout the project, and has been referred as *lensing* in this report. The effect can potentially lead to incorrect interpretation of the results, as for example to interpret fluorescence rings product of lensing as attached LONds to the MBs. Although light mirroring by water-air interfaces is a widely studied phenomenon, [343,344,365,366], there are no references to this in relation to echogenic MBs. During this project, sample washing prior to imaging was done thoroughly to ensure maximum removal of excess lipid

and unbound LONDS from the solution, as their presence contributed to the lensing effect and induced an incorrect interpretation of the results. It is important to note that sample washing procedures generally led to a reduction in the concentration of the MBs, thus bright field images for sample quantitation were always recorded preceding sample washing.

The assembly of MB-LONDS was also performed on a single-step on-chip (design in figure 3.8, page 44). This approach was used first and it aimed to replicate what was previously done to produce MB-liposome complexes. [133] Here, MBs are formed in the spray regime, and LOND attachment occurs simultaneously. The results shown in section 8.4 suggest that although formation of MB-LONDS following this protocol is possible, their stability is adversely affected by the addition of the LONDS prior to MB stabilisation⁷. This is suggested by the quick size increase of the MB-LONDS, particularly for squalane LONDS (figure 8.6c and f). One possibility is that the passage through the nozzle in the microfluidic device may promote LONDS coalescence, resulting in larger oil droplets or release of oil into the solution. The stability of air-in-water foams has been widely studied in the context of the oil and food industry, [346–349,367,368] and it is reported to decrease in presence of oil. In a similar way, it is possible that MB formation are affected by the presence of oil in the solution at the time of MB formation. The differences observed between triacetin and squalane MB-LONDS could be due to the different buoyancy of the oils, which could enhance the accumulation of squalane LONDS at the top of the chamber in the flow cell, whereas the washing of triacetin LONDS could be more efficient in this set-up (see figure 8.3 for the schematic of the flow cell).

The stability problems observed for MB-LONDS prepared in a single-step on-chip were overcome by incorporating a mixing serpentine in the microspray devices (design in figure 3.9, page 45). In this device MBs are formed first, and the incorporation of the LONDS occurs further down stream once the MBs are stabilised. The addition of the serpentine allows for on-chip mixing of the MB-LONDS for ~ 1.14 s. MB-LONDS using triacetin, squalane and tripropionin LONDS were formed in these devices, and all of them exhibited sizes around $\sim 2 \mu\text{m}$. The incorporation of the LOND solution through a different inlet results in additional liquid volume in the final sample, reducing the final concentration of the MB-LONDS by a factor of 2. The attachment of LONDS to the MB shell was confirmed by epifluorescence microscopy, after thoroughly washing the sample to remove

⁷as no evident stability issues were observed when LONDS were added to MB samples prepared off-chip.

unbound LONDS. Images obtained by confocal microscopy (figure 8.10) revealed spatial coincidence of the fluorescence signal from the MB shell and the LONDS, which pointed at successful assembly of the architectures. Unlike for the single-step protocol, MB-LONDS formed in a two-step on-chip did not show stability problems, as reflected by the study of their lifetime shown in section 8.6. It is interesting to note how the addition of the LONDS after MB formation (in both off-chip and two-step on-chip MB-LOND production) contributed to the stability of the MB-LONDS and prevented premature MB coalescence. Indeed, the results from the experiments suggest increased lifetime of the squalane MB-LONDS with respect to bare MBs prepared with the same method, with C_6F_{10} in the solution and upon incubation at 37 °C. This was thought to relate to the reduction in the gas permeation from the MB gas core upon the addition of a layer of LONDS onto the MB shell. These results suggest viability of the MB-LOND architectures for the *in vivo* applications.

MB-LONDS prepared in a two-step process on-chip retained the US properties of the MBs, as shown by the results in section 8.7. These results are similar to what has been previously observed for MB-liposome complexes. [78,359] These complexes are echogenic, and only small differences in their US properties are reported, such as lowered subharmonic threshold. [98] The preliminary experiments on the US response of MB-LONDS showed attenuation of the US signal in presence of the MB-LONDS (figure 8.13). The echogenicity of the architectures was tested using a flow phantom through a tissue-mimicking material. The B-mode images (figure 8.14) show US scattering by the MB-LONDS. These results suggest that MB-LONDS could be used as theranostic agents for simultaneous US imaging and delivery of hydrophobic drugs. Exploring the US capabilities of the MB-LONDS architectures will be an endeavour for future studies, particularly their resonant frequency and US response *in vivo*. Particularly, studying sonoporative effects in presence of MB-LONDS will be of great interest, as it has the potential to notably enhance treatments with drugs transported in the architectures.

Chapter 9

Conclusion and future challenges

The aim of this project was to develop a novel architecture for enhancing the delivery of hydrophobic drugs, the MB-LONDS. This composite consists of an echogenic MB with LONDS attached to its surface. The MB acts as a vehicle for the LONDS, which may encapsulate hydrophobic drug molecules. The work towards the construction of this architecture included the following: i) a study of a range of biocompatible oils, their luminescent properties and ability to dissolve hydrophobic drugs and drug mimics; ii) a study on the production of LONDS, with different oils and under different conditions; iii) a series of tests to assess the ability of LONDS to encapsulate hydrophobic drugs and drug mimics; iv) a study on the attachment of LONDS to model membranes mimicking the MB shell; and v) the production of MB-LONDS.

This chapter summarises the points covered in this thesis and discusses the challenges that remain after this work.

9.1 Current perspectives

This work has addressed the following questions:

Is LOND formation with biocompatible oils possible?

The literature on oil-in-water emulsion formation is extensive, particularly in the context of the food industry. Although the use of nanoemulsions for the delivery of hydrophobic drugs is not new, references that combine optimisation studies and application

of the nanoemulsions are limited. Chapters 4 (page 48) and 5 (page 71) addressed the selection, characterisation and implementation of a number of biocompatible oils for the formation of LONDS. The candidate oils were characterised in terms of their optical absorption and emission, and their ability to dissolve drugs and drug mimics was tested. In this project, LONDS were formed in a two-step process that included high pressure homogenisation of oil-in water mixtures. Preparation of LONDS following this protocol resulted in samples with average size ranging 80–300 nm, for the different LOND samples. Squalane, triacetin and tripropionin were profiled as the best candidates for the formation of LONDS. The formation of LONDS was studied in terms of the production pressure, lipid coating and encapsulated oil. The size of the LONDS was found to decrease upon increasing pressures, and the presence of pegylated lipids in the LONDS shell had the effect of reducing the size of the LONDS. LOND samples typically showed concentrations of the order of $10^{10} - 10^{14} \text{ ml}^{-1}$, with triacetin LONDS exhibiting the lowest and tripropionin LONDS the largest concentration. All LOND types had good stability over time, with measurements showing no size changes for at least six weeks. Furthermore, LONDS remained stable when incubated at 37 °C for > 2 h. Overall, the results obtained in this project suggest that LONDS are versatile, suitable capsules for the delivery of hydrophobic drugs.

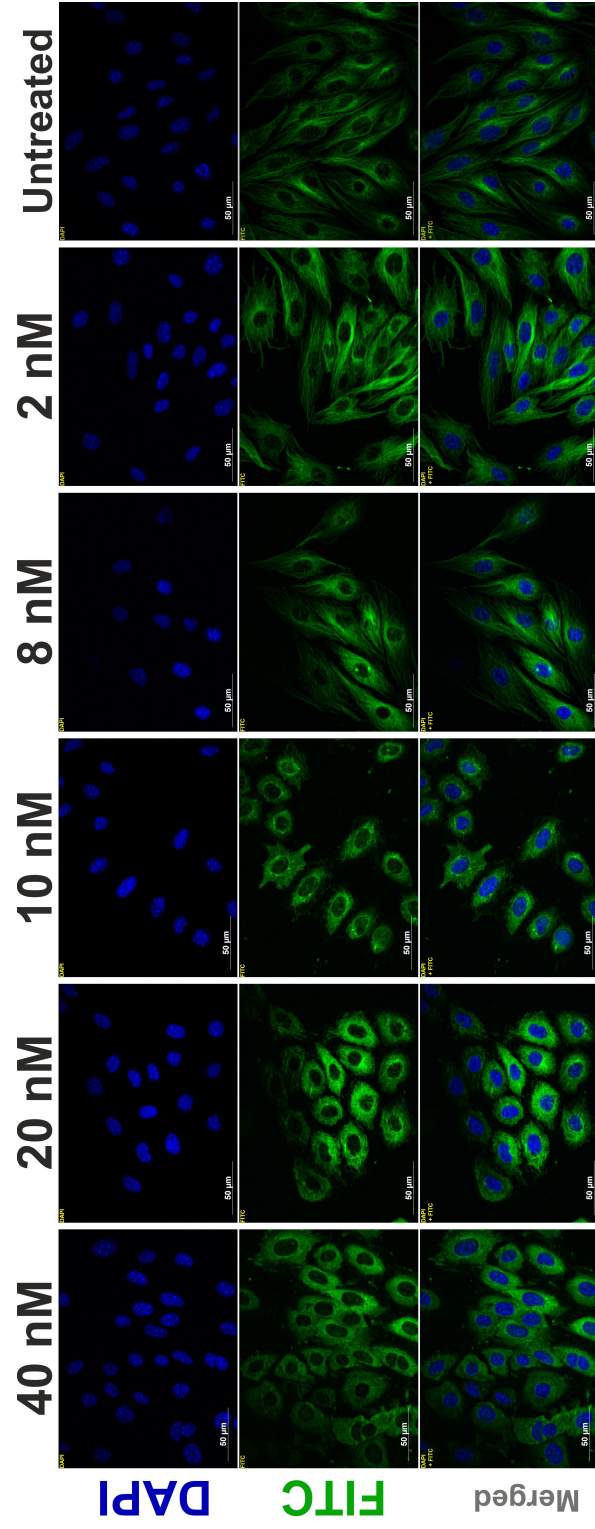
Do LONDS encapsulate and facilitate the delivery of hydrophobic compounds?

One of the most challenging aspects encountered by this work was the solubilisation of hydrophobic drugs and drug mimics in the candidate oils. The polarity of the molecules of any given compound plays a crucial role in determining the solubility of that compound in a liquid. Generally speaking, polar molecules are dissolved better by solvents with high levels of polarity. Chapters 4 (page 48) and 6 (page 104) discussed the solubility of model hydrophobic compounds (including the hydrophobic drug CA4) in the candidate oils, and the production of LONDS encapsulating them. Out of the range of hydrophobic drugs and drug mimics used within this project, only QDots with a dodecanethiol coating were largely non-polar. Squalane, which is a hydrocarbon and is therefore non-polar, showed poor solubilisation of the target compounds in this project, CA4 among them. Hence, and despite the good physical characteristics of LONDS produced with squalane,

no drug encapsulation was possible in them. In contrast, triacetin molecules are polar and solubility of CA4 was possible in this oil. Triacetin was used to form LONDS encapsulating CA4. However, the results from the experiments suggested that retention of CA4 in triacetin LONDS was poor. This could relate to both the high solubility of triacetin in water and the lipid shell used to stabilise these LONDS (POPC + 5% biotin-PEG2000-DSPE). In an effort to alleviate this problem, tripropionin was incorporated as a candidate oil due to its reduced water solubility and ability to solubilise CA4. LONDS formed with tripropionin were stabilised with a DSPC + 20% cholesterol + 5% biotin-PEG2000-DSPE, as this lipid shell composition enhanced the stability. Encapsulation tests showed promising encapsulation efficiency of CA4 in tripropionin LONDS of around $\sim 76\%$, which was retained through sample cross-filtration therefore suggesting improved retention of the therapeutic compound in this type of LONDS.

To assess the capabilities of tripropionin LONDS for the delivery of CA4, SVR mouse endothelial cells were treated with escalating doses of CA4 tripropionin LONDS from 2 – 100 nM. This experiment was performed by Miss Antonia Charalambous using a sample prepared by the author. The cells were incubated with the LONDS for 2 h at 37 °C, and washed with PBS after the treatment. Indirect immunostaining of the cells allowed for visualisation of the β -tubulin (in green). Prolong Gold with DAPI was used to mount the slides and fluorescently stain the cells nuclei (in blue). Figure 9.1 shows the results from the experiment on the delivery of CA4 in tripropionin LONDS to SVR cells. The cells showed disruption of the microtubules, an action characteristic of the CA4. The drug caused complete microtubule disruption in all SVR cells treated with 40 – 100 nM, with microtubules appearing as uniform fluorescence surrounding the cells nuclei. At concentrations lower than 2 – 20 nM, some short microtubules could be seen. In the control experiment, untreated SVR cells showed normal microtubule structures, which confirmed the specific action of the drug and suggested non-inherent toxicity of the LONDS. These preliminary results suggest that the CA4 was released from the LONDS, and point at LONDS as a promising route for the delivery of CA4 *in vivo*.

Figure 9.1: CA4 tripropionin LONDs disrupt microtubules *in vitro*. SVR mouse endothelial cells were treated with CA4 tripropionin LONDs at a dose escalation range between 2 nM to 100 nM for 2h at 37 °C followed by washing and fixing with 4% paraformaldehyde. Immunofluorescence staining of β -tubulin was carried out. Prolong Gold with DAPI was used to mount and visualise the nuclei. The results show at higher doses of 100 nM to 40 nM CA4 released from the LONDs causes complete microtubule disruption leading to a uniform fluorescence around the nuclei. Lower doses of 20 nM to 2 nM show a varying lengths of microtubule filaments. Untreated cells were used as control where normal microtubules can be seen. Scale bar 50 μ m. The pictures in this panel were kindly provided by Miss Antonia Charalambous.



Is the attachment of LONDS to model membranes via the biotin-NeutrAvidin specific?

The goal of this project was to assemble LONDS onto the shell of MBs to form a hybrid MB-LONDS architecture. Thus, the binding of the LONDS to the lipid shell was a crucial step in the development of the composites. Chapter 7 (page 119) presented a detailed study on the attachment of LONDS to model, solid supported lipid membranes in QCM-D. This study included a range of different LOND/SBLM combinations, in which the lipid shell composition of both was varied. Preliminary experiments on the attachment of StreptAvidin to biotinylated SBLMs showed the specificity of the binding, and allowed for studying the kinetics of this reaction. These experiments provided the basis for the attachment of LONDS to NeutrAvidin functionalised SBLMs. LONDS containing biotinylated lipids in their shells were found to successfully attach to NeutrAvidin functionalised SBLMs. A number of non-specific interaction between the LONDS and the SBLMs were also detected. These could arise from entanglement of PEG chains in the LONDS and the SBLMs, or from the presence of impurities in the lipid as a result of the manufacturing process. The positive results obtained in this study provided the basis for the assembly of MB-LOND composites via the biotin-NeutrAvidin link chemistry.

Are there alternative chemistries to biotin-NeutrAvidin for the attachment of LONDS to model membranes?

The use of exogenous proteins in therapeutic treatments is known to give rise to immune response, which compromise the efficacy of said treatments. NeutrAvidin linking the LONDS to the MB shell would be no exception. The maleimide-thiol and PPD-thiol linking chemistries were explored as an alternative to the biotin-NeutrAvidin. Chapter 7 (page 119) included a detailed study on the attachment of LONDS to SBLMs using these linkers. This study, analogous to that performed for biotin-NeutrAvidin, screened a number of LOND/SBLMs interactions to evidence the viability of the attachment and to also detect possible non-specific interactions. Overall, the results showed that the attachment of LONDS to SBLMs via the maleimide-thiol chemistry was possible when using the thiol-containing DTT molecule as a bridge between the maleimides in a LOND and the maleimide contained in the SBLM. This suggests that MB-LONDS assembly could be

performed following this route. The experiments showed that LONDS containing PDP are subjected to a number of non-specific interactions, which could be a result of autoxidative processes undergone by the PDP molecule or impurities present in the lipid from manufacturing. This study, as the one carried on for biotin-NeutrAvidin, highlighted the existence of non-specific binding when using these chemistries in this model system. The same phenomenon could take place between the LONDS and the MBs, which, depending on the strength of the non-specific interaction, could lead to unwanted LOND detachment from the MB shell. This study thus reinforced the need for MB washing in order to unambiguously identify LOND attachment over lensing effects. The successful binding of LONDS to model membranes via the maleimide-thiol chemistry suggests that this linkage could be used for the assembly of MB-LONDS. With this, no protein (i.e. NeutrAvidin) would be required for the construction of the architectures, which could enhance the performance of the architectures *in vivo* by reducing the immune response upon injection of the MB-LONDS.

Is it possible to assemble LONDS onto the MB shells to form MB-LOND architectures?

Chapter 8 showed that the assembly of LONDS onto the MB shell via the biotin-NeutrAvidin link chemistry is possible. The results presented in this chapter suggest that the formation of MB-LONDS is benefited by the later addition of LONDS to the MB solution. In this way LONDS bind the the shell of already stabilised MBs, and do not interfere with the coating of the water-gas interface by the phospholipids. Particularly, this project explored a two-step process on-chip for the formation of MB-LONDS. As discussed above, on-chip formation was preferred over off-chip preparation of MBs because the control over the size of the MBs produced by microfluidic means is higher than in those produced by mechanical agitation. This production method resulted in MB-LOND samples with average sizes around $2 \mu\text{m}$, with slight differences between preparations with different LOND types. Overall, this method resulted in concentrations of MB-LONDS (and MBs only) of the order of 10^7 ml^{-1} , which are lower than those typically achieved in the spray regime. This is due to the additional liquid inlet through which the LONDS are introduced to the device, as it contributes to sample dilution by a factor of 2. MB-LONDS produced in a two-step process were found to have longer lifetimes compared to bare MBs,

which was attributed to increased shell resistance to gas permeation by the addition of the LOND layer. This chapter also showed that the combination of different types of LONDS in MB-LONDS was possible. This widens the spectra of applications that the architectures could find. Particularly, combination treatments with synergic drugs that exhibit low water solubility could be greatly enhanced by optimising the use of MB-LONDS for their administration. Preliminary results on the US properties of the MB-LONDS showed that the complex is responsive to US, suggesting that they retain the echogenic properties of the MBs.

9.2 Alternative applications of MB-LONDS

This project was concerned with the development of MB-LONDS for clinical application, with particular interest in anticancer treatments. Nonetheless, MB-LONDS could potentially find applications beyond the therapeutics.

One example of a novel application for MB-LONDS could be to aid treatments against bacterial biofilms. Nowadays there is no anti-bacterial biofilm treatments in clinical use [369] and thus there is a growing interest in finding new treatments against them. Some references have shown promising results when treating bacterial biofilms with US responsive MBs, [370–372] and also MBs used in combination with antimicrobial agents such as vancomycin. [373,374] Anti-biofilm treatments with MB-LONDS could benefit not only from the US properties of the MBs, but also the drug delivery capabilities of the LONDS. Hence, LONDS could transport a suitable, hydrophobic antimicrobial agent, facilitating its delivery *in vivo* and also preventing undesired side effects. Furthermore, the encapsulation of an antibiotic and its localised release at the biofilm, upon application of a US destruction pulse, could help reducing newly developed cases of bacterial antibiotic resistance. [375]

Biofilms are of particular concern in medical devices such as urinary catheters, as they are relatively common, often result in chronic infections and thus complicate patient care. [376] One possible approach for early treatment of forming biofilms could be an US responsive coating on the inner walls of the catheter. This coating could be for example hydrogel-based, with embedded MB-LONDS. This idea is illustrated in figure 9.2. Upon bacterial colonization, the US properties of the MBs could be used to treat the growing

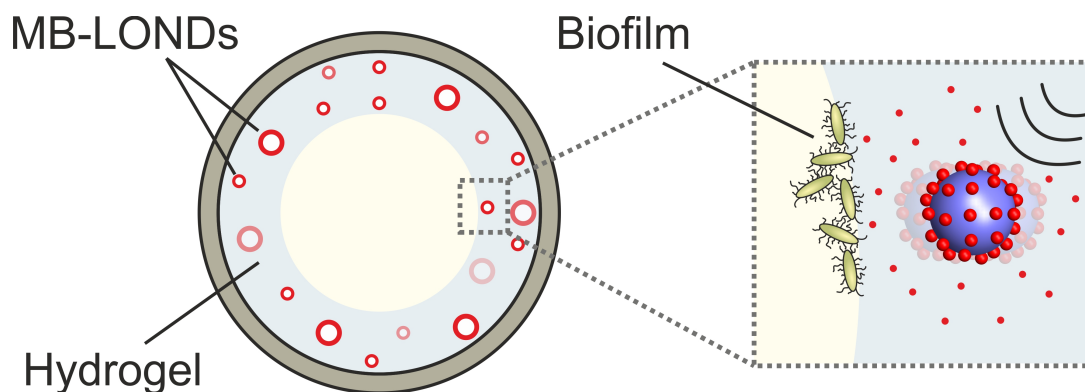


Figure 9.2: Schematic showing the cross-section of a hydrogel/MB catheter. MB-LONDs are embedded in the hydrogel coating, which sheathes the inner catheter walls. Upon bacterial biofilm growth, the MB-LONDs could be externally triggered with US, as pictured in the inset. The cavitation of the MBs would potentially affect the stability of the biofilm, and enhance intake of antimicrobial compounds encapsulated in the LONDs.

colonies, and also trigger the release of antimicrobial agents encapsulated in the LONDs. This application would require a redesign of the MB-LONDs as stability over time would be imperative, and it should be longer than the the MB-LONDs lifetimes reported in this thesis. This could be done by stabilising the MBs with alternative surfactants such as polymers, [74] or bovine serum albumin, which has been shown to yield MBs stable for up to 8 months. [377]

MB-LONDs may also find an application in the food industry. For example, air pockets are crucial for the production of ice cream, and their presence also increases the ice cream melt-down resistance. [378] The incorporation of stabilised MBs could assist the formation of ice cream, and also benefit other aspects such as its texture and fluffiness. Moreover the presence of the MBs could help reducing the calorie content of the mixtures, which may be desirable for certain markets. Specific flavouring molecules could be encapsulated in the LONDs, and used to design foods with controlled flavour release. The resistance of the LOND shell could be tuned, so that the different LONDs would release their contents at different times. This could be used to subsequently release of different flavouring agents and hence enhance the consumer's experience. [379]

MB-LONDs could be used to simultaneously deliver gases and nutrients. There are a few references in the literature to the use of MBs and nanobubbles to promote the growth of plants and certain animal species. [380,381] In the case of plant growth in presence of MBs, it is hypothesised that the small surface area of the MBs enhances their adhesion to the roots thus increasing oxygen supply and possibly assisting nutrient absorption. The

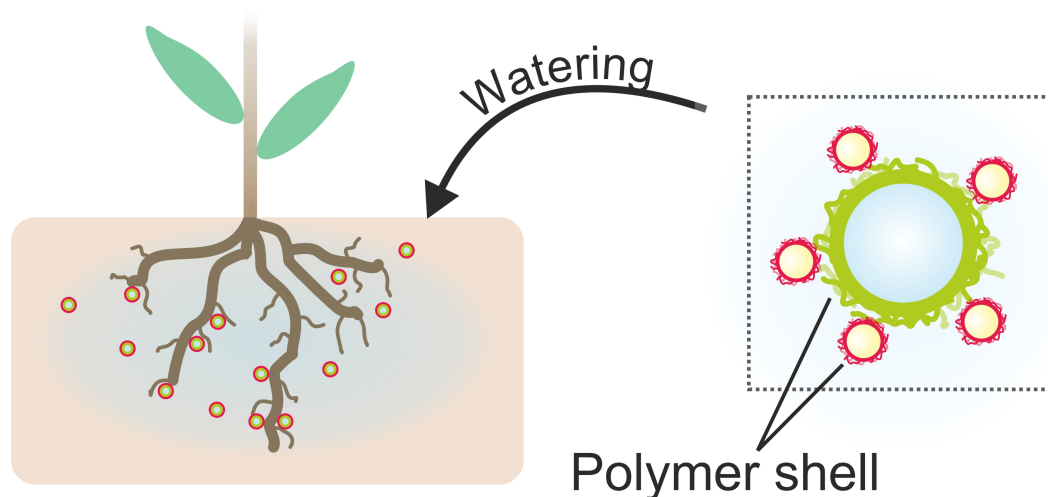


Figure 9.3: Schematic showing MB-LONDS with a hardened shell to be used as vehicles for gas, in the MB shell, and nutrients/fertiliser, encapsulated in the LONDS, to the roots of growing plants.

use of MB-LONDS would not only allow for the delivery of gases encapsulated in the MB core, but would also facilitate the delivery of salts or fertilisers encapsulated in the LONDS. [382] This is illustrated in figure 9.3. The MB-LONDS would be kept in solution, and dosed to the plants via watering. For certain applications, such as for plants in soil, a redesign of the MB shell would be required, in order to increase the lifetime of the MB-LONDS and prevent gas leakage prior to reaching the place of interest.

9.3 MB-LONDS: conclusions and the future

This thesis has shown that:

- the formation of LONDS with biocompatible oils, such as squalane, triacetin and tripropionin is possible via a two-step homogenisation process.
- the LONDS have great stability overtime, with negligible changes over size months when stored at 4 °C.
- tripropionin LONDS stabilised with DSPC + 20% cholesterol + 5% biotin-PEG2000-DSPE are suitable carriers for CA4.
- the LONDS can attach to model membranes via the biotin-NeutrAvidin chemistry, and also via alternative linking chemistries such as the maleimide-thiol and the PDP-thiol.

- MB-LONDS can be assembled in a two-step process on chip.
- the MB-LONDS have echogenic properties and lifetimes relevant for clinical applications.

Interesting tasks remain for future studies after the work presented in this thesis.

In this project, the development of LONDS to encapsulate and retain the hydrophobic drug CA4 led to the use of tripropionin encapsulated with a lipid shell composed of DSPC, cholesterol and biotin-PEG2000-DSPE. Tripropionin LONDS have shown promising results in drug encapsulation efficiency and also in preliminary experiments that delivered CA4 to cells *in vitro* using this type of LONDS. The dynamics of the CA4 release from the LONDS is a crucial experiment for better understanding treatments using them. Due to its high polarity but reduced water solubility, tripropionin holds the potential for being a suitable oil for the delivery of other highly polar, poorly water soluble compounds. Identifying new agents could expand the field of application of tripropionin LONDS, for example to the treatment of other diseases.

Significant improvements could be made in the production of MB-LONDS. These could include a concentration increase of the MB-LONDS produced in a two-step on-chip. This could be done by reducing the amount of liquid incorporated to the device through the LONDS inlet, which would require chip-redesign to avoid back-pressure problems. Another route for a concentration increase could be to concentrate the MBs after production, and before LOND mixing. This could be done with US, pushing the MBs towards one region of the channel, or a hydrodynamic flow. An increase in the concentration would benefit the use of the architectures as vehicles for hydrophobic drugs, and also their application for US imaging. A detailed study on the US capabilities of the architectures will be vital to understand their echogenic properties, and also to profile the release of LONDS from their surface. It will be interesting to study any sonoporation that these new architectures may cause to cells, and how this affects the cellular intake of LONDS and *in vitro* treatments with poorly water soluble drugs.

The production cost of the MB-LONDS is an important factor if the architectures are to find a clinical applications. Moreover, the manufacture time will be crucial for producing MB-LONDS samples adequate for patient treatment. At the present, the production of a 1 ml MB-LONDS samples requires about 30 min, and has a cost of around £3, without considering the costs associated to the operator nor the microfluidic device. Improving

the production process could be crucial for large scale usability of the architectures. For example, the microfluidic device could be multiplexed to reduce the production time of the samples. Automation of the production could help reducing production costs by reducing the steps in which an operator is required.

The attachment of LONDS to MBs using maleimide/PDP-thiol is an area that remains unexplored. The use of these chemistries for the assembly of the composites has the potential to enhance *in vivo* treatments, as immunological responses as a result of foreign protein injection would be avoided. The work presented in this thesis has highlighted the existence of multiple, unexpected non-specific interactions between the LONDS and model membranes. Thus studies to implement the maleimide/PDP chemistries into MBs may focus first in better understanding of the non-specific interactions between these molecules.

Exploring the therapeutic capabilities of the architectures in a *in vivo* setting will also be of major importance in future studies. These may study the potential enhancement of the delivery of hydrophobic drugs using MB-LONDS, which could also benefit from sonoporative effects as a result of the interaction of MBs with the US. The use of US to spatially and temporarily control the release of the LONDS from the MB shell, as a result a US destruction pulse, could help reducing the required drug doses. It will be also interesting to assess the possible reduction in adverse side effects as a result of these advances.

Future studies may also be concerned with the optimisation of the MB-LOND architecture for use in combination treatments. The attachment of different types of LONDS to MBs could provide the basis for the delivery of synergistic drugs to enhance anticancer treatments.

Appendix A

List of chemicals and instruments

Chemicals

This section provides a list of all chemicals used in this project. All buffers were prepared in 18 M Ω UltraPure water.

Name	Supplier
A	
Atto 488 DOPE	Atto-TEC, Germany
Atto 590 DOPE	Atto-TEC Germany
B	
Biotin-PEG2000-DSPE	Atto-TEC, Germany
C	
Calcein AM	AnaSpec, USA
Combretastatin A4	Sigma-Aldrich, UK
Copper iodide	Sigma-Aldrich, UK
D	

Decon90	Sigma-Aldrich, UK
DMEM, Dulbecco's Modified Eagle Medium	ThermoFisher Scientific, UK
DMSO, dimethyl sulfoxide	Sigma-Aldrich, UK
1-dodecanethiol	Sigma-Aldrich, UK
DPPC	Avanti Lipids, USA
DPBS, Dulbecco's Phosphate-Buffered Saline	
DTT, dithiothreitol	Sigma-Aldrich, UK
E	
EggPC	Avanti Lipids, USA
Eicosapentaenoic acid	Sigma-Aldrich, UK
Ethanol	Sigma-Aldrich, UK
G	
GlutaMAX, L-alanyl-L-glutamine	ThermoFisher Scientific, UK
L-Glutamine	ThermoFisher Scientific, UK
Glycerol	Sigma-Aldrich, UK
I	
Indium acetate	Sigma-Aldrich, UK
Isoamyl acetate	Sigma-Aldrich, UK
Isopropanol	Sigma-Aldrich, UK
L	
LB Broth agar	Sigma-Aldrich, UK

N

NeutrAvidin ThermoFisher Scientific, UK

Nile Red Sigma-Aldrich, UK

O

ODE, 1-octadecene Sigma-Aldrich, UK

Olive oil Sigma-Aldrich, UK

P

PBS tablets (0.14 M NaCl, 0.003 M KCl, 0.01 M PO₄) ThermoFisher Scientific, UK

PEG2000-DSPE Avanti Lipids, USA

Perfluorobutane C₄F₁₀ Air Liquide, UK

Perfluorohexane C₆F₁₄ Sigma-Aldrich, UK

POPC Avanti Lipids, USA

S

Serum (fetal bovine) Sigma-Aldrich, UK

SDS, sodium dodecyl sulfate Sigma-Aldrich, UK

Sodium Chloride, NaCl Sigma-Aldrich, UK

Squalane Sigma-Aldrich, UK

Squalene Sigma-Aldrich, UK

StreptAvidin ThermoFisher Scientific, UK

T

Triacetin Sigma-Aldrich, UK

Tripropionin

Sigma-Aldrich, UK

Instruments and consumables

This section contains the details of the instruments and consumables used within this project.

Name	Supplier
B	
Block heater Grant QBD1	Grant Instruments, UK
C	
Calibration carboxylated polystyrene particles	Izon Science, UK
Camera Hamamatsu Orca-ER	Hamamatsu Photonics, UK
Camera Nikon Digital Sight DS-U3	Nikon Systems, USA
CapMix 3M ESPE	3M ESPE, UK
Confocal Laser Scanning Leica TCS SP8	Leica Microsystems, UK
D	
Dialysis tubes, 8 kDa cut-off	GE Healthcare, UK
E	
Emulsiflex C5	Avestin Europe, Germany
Epi-fluorescent Nikon E600	Nikon Systems, USA
Epi-fluorescent Nikon Eclipse Ti-U	Nikon Systems, USA
F	

Flasks, cell culture	Greiner Bio-One, UK
Fluorescence Spectrometer LS 55	Perkin Elmer, USA
G	
Gas and temperature controlled chamber	Ibidi Germany
Gas flow controller	Alicat Scientific
H	
Needle hydrophone	Precision Acoustics, UK
K	
KrosFlow Research Ili Tangential Flow Filtration System	SpectrumLABs, The Netherlands
M	
μ -Slide VI Ibidi chips	Ibidi, Germany
Microscope VisiScope IT404	VWR, UK
Mini-Discover 12, 60 kDa filtration column	WaterSep, USA
MiniSartorius 200 nm syringe filter	VWR, UK
Multichannel dispenser	Ismatec, Germany
N	
NanoSight	Malvern Instruments, UK
P	
Polytron PT1300 D	Kinematic AG, Switzerland
P-Pump Mitos	Dolomite Ltd, UK

Q

QCM-D Q-Sense E4 Biolin Scientific, Sweden

QCM-D silica-coated quartz crystals Biolin Scientific, Sweden

qNano Izon Science, UK

S

Spacers, polyethylene terephthalate GoodFellow, UK

Syringe Pump Aladdin World Precision Instruments,
USA

T

Transducer H107, broadband (1 – 20 MHz) Sonic Concepts, USA

Transmission Electron Microscope JEM1400 JEOL, USA

Tubes for microfluidics, PTFE Supelco Analytical, USA

U

Ultrasound system Vevo770 Fujifilm Visualsonics, UK

UV/VIC Spectrophotometer Lambda 35 Perkin Elmer, USA

W

Well plates Greiner Bio-One, UK

Z

ZetaSizer Nano ZSP Malvern Instruments, UK

Appendix B

Supplementary information for chapter 7

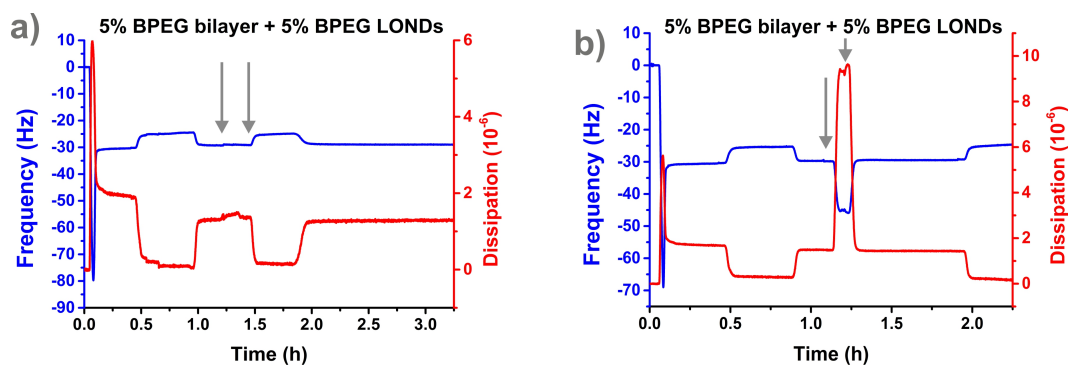


Figure B.1: Changes in frequency and dissipation of an oscillating SiO₂-coated quartz crystal during a LOND interaction experiments with the biotin-NeutrAvidin link chemistry. These experiments were performed as part of the study described in section 7.3.2 (page 128). a) 5% biotin-PEG2000-DSPE SBLM and 5% biotin-PEG2000-DSPE squalane LONDS, in absence of NeutrAvidin b) 5% biotin-PEG2000-DSPE SBLM and 5% biotin-PEG2000-DSPE triacetin LONDS, in absence of NeutrAvidin. The gray arrows indicate the addition of the LONDS and subsequent PBS rinse to remove unbound material, respectively.

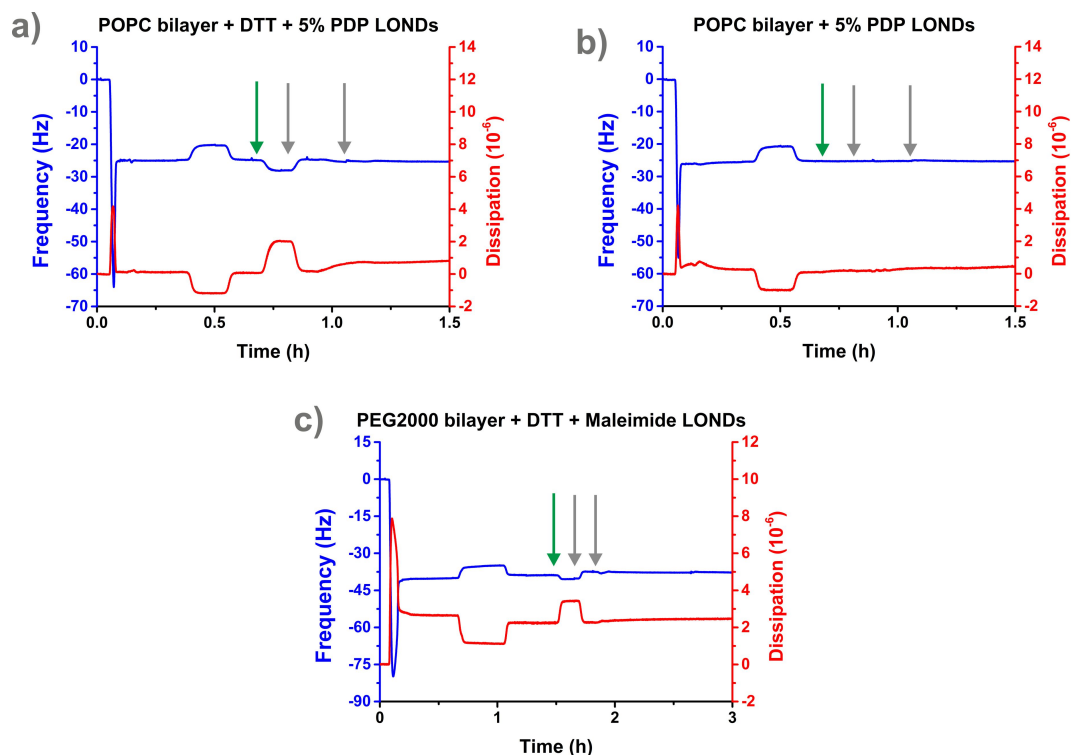


Figure B.2: Changes in frequency and dissipation of an oscillating SiO_2 -coated quartz crystal during a LOND interaction experiments. These experiments were performed as part of the study described in section 7.3.3 (page 138). These negative controls looked at the possible interaction between a) POPC SBLM, DTT and L_{PDP} LONDS, b) POPC SBLM and L_{PDP} LONDS (in absence of DTT), c) B_{PEG} SBLM, DTT and L_{MAL} LONDS. The green arrow indicates the time at which DTT was added incorporated to the crystals chambers. The gray arrows indicate the addition of the LONDS and subsequent PBS rinse to remove unbound material, respectively.

Appendix C

Supplementary information for chapter 8

1. **Video 1:** Functioning of a microspray microfluidic device. This video shows the nozzle region, where the gas and liquid phase meet; MBs are formed as a result of the gas pinch-off at the nozzle. A jet-like stream can be seen in the recording, which is characteristic of the microspray devices with an added step depth.
2. **Video 2:** Microspray device used for MB-LOND formation. In this case, NeutrAvidin functionalised triacetin LONDS were added to the lipid mix prior to its incorporation into the device. The video shows what appear to be oil droplets coalescing beyond the nozzle. This was attributed to LOND destabilisation as a result of their pass through the nozzle.
3. **Video 3:** Squalane MB-LONDS imaged in a flow cell, after a 90 min wash. The architectures appear as fluorescence rings as a result of the attachment of squalane LONDS fluorescently tagged with Atto 590. The MB-LONDS had sizes around 8 μm . The video were recorded using the TR filter block and under a 40x objective. The video is on real time.
4. **Video 4:** Triacetin MB-LONDS imaged in a flow cell, after a 90 min wash. The architectures appear as fluorescence rings as a result of the attachment of triacetin LONDS fluorescently tagged with Atto 590. The MB-LONDS had sizes between 2–20 μm . The video were recorded using the TR filter block and under a 20x objective. The video is on real time.

5. **Video 5:** Triacetin MB-LONDS imaged in a flow cell, after a 90 min wash. The architectures appear as fluorescence rings as a result of the attachment of triacetin LONDS fluorescently tagged with Atto 590. The MB-LONDS in this video have sizes around 20 μm . The video was recorded using the TR filter block and under a 40x objective. The video is on real time.
6. **Video 6:** Confocal Z-stack of a squalane MB-LONDS architecture. The shell of the MB was labelled with Atto 488 DOPE and shows green, whereas the LONDS contained Atto 590 DOPE in their shells and show red.
7. **Videos 7-10:** B-mode videos of water, bare MBs, triacetin MB-LONDS and squalane MB-LONDS in a flow phantom. The brightness of the image shows the magnitude of the US scattering by the specific substance. No scattering reflects as a colour closer to black, as in the case of water flow.

References

- [1] V. Mico, A. Charalambous, S. A. Peyman, R. H. Abou-Saleh, A. F. Markham, P. L. Coletta, and S. D. Evans. Evaluation of lipid-stabilised tripropionin nanodroplets as a delivery route for combretastatin A4. *International Journal of Pharmaceutics*, 526(1-2):547–555, 2017.
- [2] K. D. Miller, R. L. Siegel, C. C. Lin, A. B. Mariotto, J. L. Kramer, J. H. Rowland, K. D. Stein, R. Alteri, and A. Jemal. Cancer treatment and survivorship statistics, 2016. *CA: A Cancer Journal for Clinicians*, 66(4):271–289, 2016.
- [3] M. Slingerland, H. J. Guchelaar, and H. Gelderblom. Liposomal drug formulations in cancer therapy: 15 years along the road. *Drug Discovery Today*, 17(3-4):160–166, 2012.
- [4] T. M. Allen and P. R. Cullis. Drug delivery systems: entering the mainstream. *Science*, 303(5665):1818–1822, 3 2004.
- [5] S. Mitragotri, P. A. Burke, and R. Langer. Overcoming the challenges in administering biopharmaceuticals: formulation and delivery strategies. *Nature reviews. Drug discovery*, 13(9):655–72, 2014.
- [6] T. M. Allen and P. R. Cullis. Liposomal drug delivery systems: From concept to clinical applications. *Advanced Drug Delivery Reviews*, 65(1):36–48, 2013.
- [7] J. Kopeček. Polymer-drug conjugates: Origins, progress to date and future directions. *Advanced Drug Delivery Reviews*, 65(1):49–59, 2013.
- [8] W. H. De Jong and P. J. A. Borm. Drug delivery and nanoparticles: applications and hazards. *International journal of nanomedicine*, 3(2):133–149, 2008.
- [9] K. Cho, X. Wang, S. Nie, Z. Chen, and D. M. Shin. Therapeutic nanoparticles for drug delivery in cancer. *Clinical Cancer Research*, 14(5):1310–1316, 2008.

- [10] M. L. Immordino and L. Cattel. Stealth Liposomes: Review of the Basic Science , Rationale , and Clinical Applications , Existing and Potential. *International Journal of Nanomedicine*, 1(3):297–315, 2006.
- [11] A. L. Klivanov, K. Maruyama, V. P. Torchilin, and L. Huang. Amphipathic polyethyleneglycols effectively prolong the circulation time of liposomes. *FEBS Letters*, 268(1):235–237, 1990.
- [12] T. M. Allen, C. Hansen, F. Martin, C. Redemann, and A. Yau-Young. Liposomes containing synthetic lipid derivatives of poly(ethylene glycol) show prolonged circulation half-lives in vivo. *BBA - Biomembranes*, 1066(1):29–36, 1991.
- [13] A. Gabizon, R. Catane, B. Uziely, B. Kaufman, T. Safra, R. Cohen, F. Martin, and A. Huang. Prolonged circulating time and enhanced accumulation in malignant exudates of doxorubicin encapsulated in polyethylene- glycol coated liposomes. *Cancer Research*, 54:987–992, 1994.
- [14] V. D. Awasthi, D. Garcia, B. A. Goins, and W. T. Phillips. Circulation and biodistribution profiles of long-circulating PEG-liposomes of various sizes in rabbits. *International Journal of Pharmaceutics*, 253(1-2):121–132, 2003.
- [15] J. Y. Kim, J. K. Kim, J. S. Park, Y. Byun, and C. K. Kim. The use of PEGylated liposomes to prolong circulation lifetimes of tissue plasminogen activator. *Biomaterials*, 30(29):5751–5756, 2009.
- [16] J. A. Sparano, A. N. Makhson, V. F. Semiglazov, S. A. Tjulandin, O. I. Balashova, V. a. Chatikhine, S. H. Zhuang, L. Xiu, Z. Yuan, and W. R. Rackoff. Pegylated Liposomal Doxorubicin Plus Docetaxel Significantly Improves Time to Progression Without Additive Cardiotoxicity Compared With Docetaxel Monotherapy in Patients With Advanced Breast Cancer Previously Treated With N. *Journal of Clinical Oncology*, 27(27):1–9, 2009.
- [17] E. Alba, M. Ruiz-Borrego, M. Margelí, A. Rodríguez-Lescure, P. Sánchez-Rovira, A. Ruiz, J. R. Mel-Lorenzo, M. Ramos-Vázquez, N. Ribelles, E. Calvo, A. Casado, A. Márquez, D. Vicente, J. A. García-Sáenz, and M. Martín. Maintenance treatment with pegylated liposomal doxorubicin versus observation following induction chemotherapy for metastatic breast cancer: GEICAM 2001-01 study. *Breast cancer research and treatment*, 122(1):169–76, 2010.

- [18] C. H. Smorenburg, S. M. de Groot, A. E. van Leeuwen-Stok, M. E. Hamaker, A. N. Wymenga, H. de Graaf, F. E. de Jongh, J. J. Braun, M. Los, E. Maartense, H. van Tinteren, J. W. R. Nortier, and C. Seynaeve. A randomized phase III study comparing pegylated liposomal doxorubicin with capecitabine as first-line chemotherapy in elderly patients with metastatic breast cancer: results of the OMEGA study of the Dutch Breast Cancer Research Group BOOG. *Ann. Oncol.*, 25(3):599–605, 2014.
- [19] E. Pujade-Lauraine, U. Wagner, E. Aavall-Lundqvist, V. Gebiski, M. Heywood, P. A. Vasey, B. Volgger, I. Vergote, S. Pignata, A. Ferrero, J. Sehouli, A. Lortholary, G. Kristensen, C. Jackisch, F. Joly, C. Brown, N. Le Fur, and A. Du Bois. Pegylated liposomal doxorubicin and carboplatin compared with paclitaxel and carboplatin for patients with platinum-sensitive ovarian cancer in late relapse. *Journal of Clinical Oncology*, 28(20):3323–3329, 2010.
- [20] M. Markman, J. Moon, S. Wilczynski, A. M. Lopez, K. M. Rowland, D. P. Michelin, V. J. Lanzotti, G. L. Anderson, and D. S. Alberts. Single agent carboplatin versus carboplatin plus pegylated liposomal doxorubicin in recurrent ovarian cancer: Final survival results of a SWOG (S0200) phase 3 randomized trial. *Gynecologic Oncology*, 116(3):323–325, 2010.
- [21] R. Z. Orlowski, A. Nagler, P. Sonneveld, J. Blade, R. Hajek, A. Spencer, J. San Miguel, T. Robak, A. Dmoszynska, N. Horvath, I. Spicka, H. J. Sutherland, A. N. Suvorov, S. H. Zhuang, T. Parekh, L. Xiu, Z. Yuan, W. Rackoff, and J. L. Harousseau. Randomized phase III study of pegylated liposomal doxorubicin plus bortezomib compared with bortezomib alone in relapsed or refractory multiple myeloma: Combination therapy improves time to progression. *Journal of Clinical Oncology*, 25(25):3892–3901, 2007.
- [22] M. Lindenberg, S. Kopp, and J. B. Dressman. Classification of orally administered drugs on the World Health Organization Model list of Essential Medicines according to the biopharmaceutics classification system. *European Journal of Pharmaceutics and Biopharmaceutics*, 58(2):265–278, 2004.
- [23] N. T. Southall, K. A. Dill, and A. D. J. Haymet. A View of the Hydrophobic Effect. *J. Phys. Chem.*, 106(3):521–533, 2002.

- [24] C. W. Pouton. Formulation of poorly water-soluble drugs for oral administration: Physicochemical and physiological issues and the lipid formulation classification system. *European Journal of Pharmaceutical Sciences*, 29:278–287, 2006.
- [25] Y. Kawabata, K. Wada, M. Nakatani, S. Yamada, and S. Onoue. Formulation design for poorly water-soluble drugs based on biopharmaceutics classification system: Basic approaches and practical applications. *International Journal of Pharmaceutics*, 420(1):1–10, 2011.
- [26] C. A. Lipinski, F. Lombardo, B. W. Dominy, and P. J. Feeney. Experimental and computational approaches to estimate solubility and permeability in drug discovery and development settings. *Advanced Drug Delivery Reviews*, 23:3–25, 1997.
- [27] C. A. Lipinski. Lead- and drug-like compounds: The rule-of-five revolution. *Drug Discovery Today: Technologies*, 1(4):337–341, 2004.
- [28] A. K. Ghose, V. N. Viswanadhan, and J. J. Wendoloski. A Knowledge-Based Approach in Designing Combinatorial or Medicinal Chemistry Libraries for Drug Discovery. 1. A Qualitative and Quantitative Characterization of Known Drug Databases. *Journal of Combinatorial Chemistry*, 1:55–68, 1999.
- [29] M. A. Walker. Improving Solubility via Structural Modification. In N. A. Meanwell, editor, *Tactics in Contemporary Drug Design*, pages 69–106. Springer Berlin Heidelberg, Berlin, Heidelberg, 2015.
- [30] J. Rautio, H. Kumpulainen, T. Heimbach, R. Oliyai, D. Oh, T. Järvinen, and J. Savolainen. Prodrugs: design and clinical applications. *Nature reviews. Drug discovery*, 7(3):255–70, 2008.
- [31] V. J. Stella. Prodrugs: Some thoughts and current issues. *Journal of Pharmaceutical Sciences*, 99(12):4755–4765, 2010.
- [32] K. M. Huttunen, H. Raunio, and J. Rautio. Prodrugs - from serendipity to rational design. *Pharmacological Reviews*, 63(3):750–71, 2011.
- [33] N. I. Marupudi, J. E. Han, K. W. Li, V. M. Renard, B. M. Tyler, and H. Brem. Pacilitaxel: a review of adverse toxicities and novel delivery strategies. *Expert Opinion on Drug Safety*, 6(5):609–621, 2007.

- [34] H. Gelderblom, J. Verweij, K. Nooter, and A. Sparreboom. Cremophor EL: The drawbacks and advantages of vehicle selection for drug formulation. *European Journal of Cancer*, 37(13):1590–1598, 2001.
- [35] C. D. O. Rangel-Yagui, A. Pessoa, and L. C. Tavares. Micellar solubilization of drugs. *Journal of Pharmacy and Pharmaceutical Sciences*, 8(2):147–163, 2005.
- [36] H. M. Aliabadi, S. Elhasi, A. Mahmud, R. Gulamhusein, P. Mahdipoor, and A. Lavasanifar. Encapsulation of hydrophobic drugs in polymeric micelles through co-solvent evaporation: The effect of solvent composition on micellar properties and drug loading. *International Journal of Pharmaceutics*, 329(1-2):158–165, 2 2007.
- [37] R. Basak and R. Bandyopadhyay. Encapsulation of Hydrophobic Drugs in Pluronic F127 Micelles : Effects of Drug Hydrophobicity, Solution Temperature and pH. *Langmuir*, (29):4350–4356, 2013.
- [38] A. Bohr, J. Kristensen, E. Stride, M. Dyas, and M. Edirisinghe. Preparation of microspheres containing low solubility drug compound by electrohydrodynamic spraying. *International Journal of Pharmaceutics*, 412(1-2):59–67, 2011.
- [39] C. Wischke and S. P. Schwendeman. Principles of encapsulating hydrophobic drugs in PLA/PLGA microparticles. *International Journal of Pharmaceutics*, 364(2):298–327, 2008.
- [40] K. Hörmann and A. Zimmer. Drug delivery and drug targeting with parenteral lipid nanoemulsions - A review. *Journal of Controlled Release*, 223:85–98, 2016.
- [41] E. Dickinson. Hydrocolloids as emulsifiers and emulsion stabilizers. *Food Hydrocolloids*, 23(6):1473–1482, 2009.
- [42] K. K. Singh and S. K. Vingkar. Formulation, antimalarial activity and biodistribution of oral lipid nanoemulsion of primaquine. *International journal of pharmaceutics*, 347(1-2):136–43, 1 2008.
- [43] A. Gianella, P. A. Jarzyna, V. Mani, S. Ramachandran, C. Calcagno, J. Tang, B. Kann, W. J. R. Dijk, V. L. Thijssen, A. W. Griffioen, G. Storm, Z. A. Fayad, and W. J. M. Mulder. Multifunctional nanoemulsion platform for imaging guided therapy evaluated in experimental cancer. *ACS Nano*, 5(6):4422–4433, 2011.

- [44] D. Deshpande, D. R. Janero, and M. Amiji. Engineering of an Ω -3 polyunsaturated fatty acid-containing nanoemulsion system for combination C6-ceramide and 17 β -estradiol delivery and bioactivity in human vascular endothelial and smooth muscle cells. *Nanomedicine: Nanotechnology, Biology, and Medicine*, 9(7):885–894, 2013.
- [45] S. Hak, Z. Garaiova, L. T. Olsen, A. M. Nilsen, and C. de Lange Davies. The effects of oil-in-water nanoemulsion polyethylene glycol surface density on intracellular stability, pharmacokinetics, and biodistribution in tumor bearing mice. *Pharmaceutical research*, 32(4):1475–85, 2014.
- [46] T. C. Contente, I. F. Kretzer, F. B. Filippin-Monteiro, D. A. Maria, and R. C. Maranhão. Association of daunorubicin to a lipid nanoemulsion that binds to low-density lipoprotein receptors enhances the antitumour action and decreases the toxicity of the drug in melanoma-bearing mice. *The Journal of pharmacy and pharmacology*, pages 1–12, 8 2014.
- [47] A. Alayoubi, S. Alqahtani, A. Kaddoumi, and S. Nazzal. Effect of PEG surface conformation on anticancer activity and blood circulation of nanoemulsions loaded with tocotrienol-rich fraction of palm oil. *The AAPS journal*, 15(4):1168–79, 2013.
- [48] S. Ganta, P. Sharma, J. W. Paxton, B. C. Baguley, and S. Garg. Pharmacokinetics and pharmacodynamics of chlorambucil delivered in long-circulating nanoemulsion. *Journal of Drug Targeting*, 18(2):125–133, 2010.
- [49] F. Liu and D. Liu. Long-Circulating Emulsions (Oil-in-Water) as Carriers for Lipophilic Drugs. *Pharmaceutical Research*, 12(7):1060–1064, 1995.
- [50] S. Hak, E. Helgesen, H. H. Hektoen, E. M. Huuse, P. A. Jarzyna, W. J. M. Mulder, O. Haraldseth, and C. D. L. Davies. The effect of nanoparticle polyethylene glycol surface density on ligand-directed tumor targeting studied in vivo by dual modality imaging. *ACS Nano*, 6(6):5648–5658, 2012.
- [51] S. Ganta and M. Amiji. Coadministration of paclitaxel and curcumin in nanoemulsion formulations to overcome multidrug resistance in tumor cells. *Molecular Pharmaceutics*, 6(3):928–939, 2009.
- [52] X. Jing, L. Deng, B. Gao, L. Xiao, Y. Zhang, X. Ke, J. Lian, Q. Zhao, L. Ma, J. Yao, and J. Chen. A novel polyethylene glycol mediated lipid nanoemulsion as

- drug delivery carrier for paclitaxel. *Nanomedicine : nanotechnology, biology, and medicine*, 10(2):371–380, 2 2014.
- [53] J. B. Tagne, S. Kakumanu, and R. J. Nicolosi. Nanoemulsion preparations of the anticancer drug dacarbazine significantly increase its efficacy in a xenograft mouse melanoma model. *Molecular Pharmaceutics*, 5(6):1055–1063, 2008.
- [54] N. J. Schork. Personalized medicine: Time for one-person trials. *Nature*, 520(7549):609–611, 2015.
- [55] S. S. Kelkar and T. M. Reineke. Theranostics: Combining imaging and therapy. *Bioconjugate Chemistry*, 22(10):1879–1903, 2011.
- [56] E. K. Lim, T. Kim, S. Paik, S. Haam, Y. M. Huh, and K. Lee. Nanomaterials for Theranostics: Recent Advances and Future Challenges. *Chemical Reviews*, 115(1):327–394, 2015.
- [57] Y. P. Ho, H. H. Chen, K. W. Leong, and T. H. Wang. Evaluating the intracellular stability and unpacking of DNA nanocomplexes by quantum dots-FRET. *Journal of Controlled Release*, 116(1):83–89, 2006.
- [58] H. Ke, J. Wang, Z. Dai, Y. Jin, E. Qu, Z. Xing, C. Guo, X. Yue, and J. Liu. Gold-nanoshelled microcapsules: A theranostic agent for ultrasound contrast imaging and photothermal therapy. *Angewandte Chemie - International Edition*, 50(13):3017–3021, 2011.
- [59] J. Chen, S. Ratnayaka, A. Alford, V. Kozlovskaya, F. Liu, B. Xue, K. Hoyt, and E. Kharlampieva. Theranostic Multilayer Capsules for Ultrasound Imaging and Guided Drug Delivery. *ACS Nano*, DOI: 10.10, 2017.
- [60] D. Cosgrove. Ultrasound contrast agents: An overview. *European Journal of Radiology*, 60(3):324–330, 2006.
- [61] E. G. Schutt, D. H. Klein, R. M. Mattrey, and J. G. Riess. Injectable microbubbles as contrast agents for diagnostic ultrasound imaging: The key role of perfluorochemicals. *Angewandte Chemie - International Edition*, 42(28):3218–3235, 7 2003.
- [62] J. R. Lindner. Microbubbles in medical imaging: current applications and future directions. *Nature reviews. Drug discovery*, 3(6):527–32, 2004.

- [63] F. Forsberg, N. M. Rawool, D. A. Merton, J. B. Liu, W. Wang, P. Kankate, J. Alessandro, B. B. Goldberg, and M. A. Wheatley. Comparison of air and perfluorocarbon filled microbubbles for ultrasound contrast studies. *Proceedings of the IEEE Ultrasonics Symposium*, 2:1337–1340, 1996.
- [64] K. Ferrara, R. Pollard, and M. Borden. Ultrasound microbubble contrast agents: fundamentals and application to gene and drug delivery. *Annual review of biomedical engineering*, 9:415–447, 2007.
- [65] I. Rosenthal, J. Z. Sostaric, and P. Riesz. Sonodynamic therapy: a review of the synergistic effects of drugs and ultrasound. *Ultrasonics Sonochemistry*, 11(6):349–363, 2004.
- [66] S. Bao, B. D. Thrall, and D. L. Miller. Transfection of a reporter plasmid into cultured cells by sonoporation in vitro. *Ultrasound in Medicine and Biology*, 23(6):953–959, 1997.
- [67] M. Ward, J. Wu, and J. F. Chiu. Ultrasound-induced cell lysis and sonoporation enhanced by contrast agents. *The Journal of the Acoustical Society of America*, 105(5):2951–2957, 1999.
- [68] P. Marmottant and S. Hilgenfeldt. Controlled vesicle deformation and lysis by single oscillating bubbles. *Nature*, 423(6936):153–156, 2003.
- [69] P. Prentice, A. Cuschieri, K. Dholakia, M. Prausnitz, and P. Campbell. Membrane disruption by optically controlled microbubble cavitation. *Nature Physics*, 1(11):107–110, 2005.
- [70] C. D. Ohl, M. Arora, R. Ikink, N. de Jong, M. Versluis, M. Delius, and D. Lohse. Sonoporation from jetting cavitation bubbles. *Biophysical journal*, 91(11):4285–95, 2006.
- [71] A. van Wamel, K. Kooiman, M. Hartevelde, M. Emmer, F. J. ten Cate, M. Versluis, and N. de Jong. Vibrating microbubbles poking individual cells: Drug transfer into cells via sonoporation. *Journal of Controlled Release*, 112(2):149–155, 5 2006.
- [72] K. Kooiman, M. Foppen-Hartevelde, A. F. W. V. Der Steen, and N. De Jong. Sonoporation of endothelial cells by vibrating targeted microbubbles. *Journal of Controlled Release*, 154(1):35–41, 2011.

- [73] I. Lentacker, I. De Cock, R. Deckers, S. C. De Smedt, and C. T. W. Moonen. Understanding ultrasound induced sonoporation: Definitions and underlying mechanisms. *Advanced Drug Delivery Reviews*, 72:49–64, 6 2014.
- [74] I. Lentacker, B. G. De Geest, R. E. Vandenbroucke, L. Peeters, J. Demeester, S. C. De Smedt, and N. N. Sanders. Ultrasound-responsive polymer-coated microbubbles that bind and protect DNA. *Langmuir*, 22(17):7273–7278, 2006.
- [75] E. C. Unger, T. McCreery, R. Sweitzer, G. Vielhauer, G. Wu, D. Shen, and D. Yellowhair. MRX 501: A Novel Ultrasound Contrast Agent with Therapeutic properties. *Academic Radiology*, 5:247–249, 1998.
- [76] S. Ibsen, M. Benchimol, D. Simberg, C. Schutt, J. Steiner, and S. Esener. A novel nested liposome drug delivery vehicle capable of ultrasound triggered release of its payload. *Journal of Controlled Release*, 155(3):358–366, 2011.
- [77] E. C. Unger, T. McCreery, R. Sweitzer, H. Robert, V. E. Caldwell, and Y. Wu. Acoustically Active Lipospheres Containing Paclitaxel: A New Therapeutic Ultrasound Contrast Agent. *Investigative Radiology*, 33(12):886–892, 1998.
- [78] A. Kheirrolomoom, P. A. Dayton, A. F. H. Lum, E. Little, E. E. Paoli, H. Zheng, and K. W. Ferrara. Acoustically-active microbubbles conjugated to liposomes: Characterization of a proposed drug delivery vehicle. *Journal of Controlled Release*, 118(3):275–284, 4 2007.
- [79] R. Suzuki and A. L. Klivanov. Co-administration of Microbubbles and Drugs in Ultrasound-Assisted Drug Delivery: Comparison with Drug-Carrying Particles. In J.-M. Escoffre and A. Bouakaz, editors, *Therapeutic Ultrasound*, pages 205–220. Springer International Publishing, 2016.
- [80] S. Ibsen, C. E. Schutt, and S. Esener. Microbubble-mediated ultrasound therapy : a review of its potential in cancer treatment. *Drug Design, Development and Therapy*, pages 375–388, 2013.
- [81] I. Lentacker, B. Geers, J. Demeester, S. C. De Smedt, and N. N. Sanders. Design and evaluation of doxorubicin-containing microbubbles for ultrasound-triggered doxorubicin delivery: cytotoxicity and mechanisms involved. *Molecular therapy : the journal of the American Society of Gene Therapy*, 18(1):101–8, 2010.

- [82] I. Lentacker, S. C. De Smedt, J. Demeester, V. Van Marck, M. Bracke, and N. N. Sanders. Lipoplex-loaded microbubbles for gene delivery: A trojan horse controlled by ultrasound. *Advanced Functional Materials*, 17(12):1910–1916, 2007.
- [83] D. D. Chaplin. Overview of the immune response. *Journal of Allergy and Clinical Immunology*, 125:S3–S23, 2010.
- [84] M. M. Lozano, C. D. Starkel, and M. L. Longo. Vesicles tethered to microbubbles by hybridized DNA oligonucleotides: flow cytometry analysis of this new drug delivery vehicle design. *Langmuir : the ACS journal of surfaces and colloids*, 26(11):8517–24, 2010.
- [85] B. Geers, I. Lentacker, N. N. Sanders, J. Demeester, S. Meairs, and S. C. De Smedt. Self-assembled liposome-loaded microbubbles: The missing link for safe and efficient ultrasound triggered drug-delivery. *Journal of Controlled Release*, 152(2):249–256, 2011.
- [86] P. Somasundaran. *Encyclopedia of Surface and Colloid Science, Volume 5*. CRC Press, 2006.
- [87] T. H. Chou and C. H. Chang. Thermodynamic behavior and relaxation processes of mixed DPPC/cholesterol monolayers at the air/water interface. *Colloids and Surfaces B: Biointerfaces*, 17:71–79, 2000.
- [88] M. A. Borden, G. Pu, G. J. Runner, and M. L. Longo. Surface phase behavior and microstructure of lipid/PEG-emulsifier monolayer-coated microbubbles. *Colloids and Surfaces B: Biointerfaces*, 35(3-4):209–223, 2004.
- [89] P. B. Duncan and D. Needham. Test of the Epstein-Plesset model for gas micro-particle dissolution in aqueous media: Effect of surface tension and gas undersaturation in solution. *Langmuir*, 20(7):2567–2578, 2004.
- [90] T. I. M. Segers, M. Versluis, and D. Lohse. Microbubbles for Medical Applications. In A. van den Berg and L. Segerik, editors, *Microfluidics for Medical Applications*, chapter 5, pages 81–101. Royal Society of Chemistry, 2015.
- [91] P. Epstein and M. Plesset. On the Stability of Gas Bubbles in Liquid-Gas Solutions. *Journal of Chemical physics*, 18(11):1505–1509, 1950.

- [92] M. Parhizkar, M. Edirisinghe, and E. Stride. Effect of operating conditions and liquid physical properties on the size of monodisperse microbubbles produced in a capillary embedded T-junction device. *Microfluidics and Nanofluidics*, 14(5):797–808, 2013.
- [93] M. A. Borden and M. L. Longo. Dissolution behavior of lipid monolayer-coated, air-filled microbubbles: Effect of lipid hydrophobic chain length. *Langmuir*, 18(24):9225–9233, 2002.
- [94] K. Sarkar, A. Katiyar, and P. Jain. Growth and Dissolution of an Encapsulated Contrast Microbubble: Effects of Encapsulation Permeability. *Ultrasound in Medicine and Biology*, 35(8):1385–1396, 2009.
- [95] M. S. Plesset. The Dynamics of Cavitation Bubbles. *Journal of Applied Mechanics*, 16:277–282, 1949.
- [96] R. Gorder. Dynamics of the Rayleigh–Plesset equation modelling a gas-filled bubble immersed in an incompressible fluid. *Journal of Fluid Mechanics*, 807(2016):478–508, 2016.
- [97] K. E. Morgan, J. S. Allen, P. A. Dayton, J. E. Chomas, A. L. Klibanov, and K. W. Ferrara. Experimental and theoretical evaluation of microbubble behavior: effect of transmitted phase and bubble size. *IEEE Transactions on Ultrasonics, Ferroelectrics, and Frequency Control*, 47(6):1494–1509, 2000.
- [98] J. R. McLaughlan, S. Harput, R. H. Abou-Saleh, S. a. Peyman, S. Evans, and S. Freear. Characterisation of Liposome-Loaded Microbubble Populations for Subharmonic Imaging. *Ultrasound in Medicine & Biology*, pages 1–11, 2016.
- [99] E. Stride and M. Edirisinghe. Novel microbubble preparation technologies. *Soft Matter*, 4:2350–2359, 2008.
- [100] E. Stride and M. Edirisinghe. Novel preparation techniques for controlling microbubble uniformity: A comparison. *Medical and Biological Engineering and Computing*, 47(8):883–892, 2009.
- [101] A. Manz, H. M. Widmers, and N. Graber. Miniaturized total chemical analysis systems: A novel concept for chemical sensing. *Sensors and Actuators B: Chemical*, 1(1-6):244–248, 1990.

- [102] M. J. Davies, M. P. C. Marques, and A. N. P. Radhakrishnan. Chapter 2 Microfluidics Theory in Practice. In *Microfluidics in Detection Science: Lab-on-a-chip Technologies*. The Royal Society of Chemistry, 2015.
- [103] I. Shestopalov, J. D. Tice, and R. F. Ismagilov. Multi-step synthesis of nanoparticles performed on millisecond time scale in a microfluidic droplet-based system. *Lab on a chip*, 4(4):316–321, 2004.
- [104] L. H. Hung, K. M. Choi, W. Y. Tseng, Y. C. Tan, K. J. Shea, and A. P. Lee. Alternating droplet generation and controlled dynamic droplet fusion in microfluidic device for CdS nanoparticle synthesis. *Lab on a chip*, 6(2):174–178, 2006.
- [105] K. Liu, H. J. Ding, J. Liu, Y. Chen, and X. Z. Zhao. Shape-controlled production of biodegradable calcium alginate gel microparticles using a novel microfluidic device. *Langmuir*, 22(22):9453–9457, 2006.
- [106] J. Wan, A. Bick, M. Sullivan, and H. A. Stone. Controllable Microfluidic Production of Microbubbles in Water-in-Oil Emulsions and the Formation of Porous Microparticles. *Advanced Materials*, 20:3314–3318, 2008.
- [107] Q. Xu, M. Hashimoto, T. T. Dang, T. Hoare, D. S. Kohane, G. M. Whitesides, R. Langer, D. G. Anderson, and H. David. Preparation of monodisperse biodegradable polymer microparticles using a microfluidic flow-focusing device for controlled drug delivery. *Small*, 5(13):1575–1581, 2009.
- [108] L. Zhang, Q. Feng, J. Wang, S. Zhang, B. Ding, Y. Wei, M. Dong, J. Y. Ryu, T. Y. Yoon, X. Shi, J. Sun, and X. Jiang. Microfluidic Synthesis of Hybrid Nanoparticles with Controlled Lipid Layers : Understanding Flexibility-Regulated Cell-Nanoparticle Interaction. *ACS nano*, (10):9912–9921, 2015.
- [109] P. M. Valencia, O. C. Farokhzad, R. Karnik, and R. Langer. Microfluidic technologies for accelerating the clinical translation of nanoparticles. *Nature Nanotechnology*, 7(10):623–629, 2012.
- [110] H. A. Stone, A. D. Stroock, and A. Ajdari. Engineering flows in small devices . Microfluidics Toward a Lab-on-a-Chip. *Annual Review of Fluid Mechanics*, 36(1):381–411, 2004.

- [111] K. E. Herold and A. Rasooly. *Lab on a Chip Technology: Fabrication and microfluidics*. Lab on a Chip Technology. Caister Academic Press, 2009.
- [112] N. Schwesinger, T. Frank, and H. Wurmus. A modular microfluid system with an integrated micromixer. *Journal of Micromechanics and Microengineering*, 6(1):99–102, 1996.
- [113] A. D. Stroock, S. K. W. Dertinger, A. Ajdari, I. Mezic, H. A. Stone, and G. M. Whitesides. Chaotic mixer for microchannels. *Science (New York, N.Y.)*, 295(5555):647–651, 2002.
- [114] S. Jeon, V. Malyarchuk, J. O. White, and J. A. Rogere. Optically Fabricated Three Dimensional Nanofluidic Mixers for Microfluidic Devices. *Nano Letters*, 5(7):1351–1356, 2005.
- [115] P. Garstecki, M. J Fuerstman, M. A. Fischbach, S. K. Sia, and G. M. Whitesides. Mixing with bubbles: a practical technology for use with portable microfluidic devices. *Lab on a chip*, 6(2):207–212, 2006.
- [116] T. G. Kang, M. A. Hulsen, P. D. Anderson, J. M. J. den Toonder, and H. E. H. Meijer. Chaotic advection using passive and externally actuated particles in a serpentine channel flow. *Chemical Engineering Science*, 62(23):6677–6686, 2007.
- [117] C. Y. Lee, C. L. Chang, Y. N. Wang, and L. M. Fu. Microfluidic mixing: A review. *International Journal of Molecular Sciences*, 12(5):3263–3287, 2011.
- [118] K. J. Cook. Mixing Evaluation of a Passive Scaled-Up Serpentine Micromixer With Slanted Grooves. *Journal of Fluids Engineering*, 135(8), 2013.
- [119] R. H. Liu, M. A. Stremmer, K. V. Sharp, M. G. Olsen, J. G. Santiago, R. J. Adrian, H. Aref, and D. J. Beebe. Passive Mixing in a Three-Dimensional Serpentine Microchannel Passive Mixing in a Three-Dimensional Serpentine Microchannel. *Journal of Microelectromechanical systems*, 9(2):190–197, 2000.
- [120] F. Schönfeld and S. Hardt. Simulation of Helical Flows in Microchannels. *AIChE Journal*, 50(4):771–778, 2004.
- [121] S. A. Berger, L. Talbot, and L. S. Yao. Flow in Curved Pipes. *Annual Review of Fluid Mechanics*, 15:461–512, 1983.

- [122] D. Di Carlo. Inertial microfluidics. *Lab on a chip*, 9(21):3038–3046, 2009.
- [123] P. Garstecki, M. J. Fuerstman, H. A. Stone, and G. M. Whitesides. Formation of droplets and bubbles in a microfluidic T-junction—scaling and mechanism of break-up. *Lab on a chip*, 6(3):437–46, 2006.
- [124] A. M. Gañán-Calvo. Generation of Steady Liquid Microthreads and Micron-Sized Monodisperse Sprays in Gas Streams. *Physical Review Letters*, 80(2):285–288, 1998.
- [125] L. Martín-Banderas, M. Flores-Mosquera, P. Riesco-Chueca, A. Rodríguez-Gil, A. Cebolla, S. Chávez, and A. M. Gañán-Calvo. Flow Focusing : A Versatile Technology to Produce Size- Controlled and Specific-Morphology Microparticles. *Small*, 1(7):2–6, 2005.
- [126] B. Dollet, W. Van Hoeve, J. P. Raven, P. Marmottant, and M. Versluis. Role of the channel geometry on the bubble pinch-off in flow-focusing devices. *Physical Review Letters*, 100(3):1–4, 2008.
- [127] P. Garstecki, A. M. Gañán-Calvo, and G. M. Whitesides. Formation of bubbles and droplets in microfluidic systems. *Bulletin of the Polish Academy of Sciences*, 53(4):361–372, 2005.
- [128] K. Hettiarachchi, E. Talu, M. L. Longo, P. A. Dayton, and A. P. Lee. On-chip generation of microbubbles as a practical technology for manufacturing contrast agents for ultrasonic imaging. *Lab on a chip*, 7(4):463–468, 2007.
- [129] M. Hashimoto, P. Garstecki, and G. M. Whitesides. Synthesis of composite emulsions and complex foams with the use of microfluidic flow-focusing devices. *Small (Weinheim an der Bergstrasse, Germany)*, 3(10):1792–1802, 2007.
- [130] E. Talu, K. Hettiarachchi, S. Zhao, R. L. Powell, A. P. Lee, M. L. Longo, and P. A. Dayton. Tailoring the Size Distribution of Ultrasound Contrast Agents: Possible Method for Improving Sensitivity in Molecular Imaging. *Molecular Imaging*, 6(6):384–392, 2008.
- [131] E. Talu, K. Hettiarachchi, R. L. Powell, A. P. Lee, P. A. Dayton, and M. L. Longo. Maintaining Monodispersity in a Microbubble Population Formed by Flow-Focusing. *Langmuir*, 24(5):1745–1749, 2009.

- [132] P. D. Hede, P. Bach, and A. D. Jensen. Two-fluid spray atomisation and pneumatic nozzles for fluid bed coating/agglomeration purposes: A review. *Chemical Engineering Science*, 63(14):3821–3842, 2008.
- [133] S. A. Peyman, R. H. Abou-Saleh, J. R. McLaughlan, N. Ingram, B. R. G. Johnson, K. Critchley, S. Freear, J. A. Evans, A. F. Markham, P. L. Coletta, and S. D. Evans. Expanding 3D geometry for enhanced on-chip microbubble production and single step formation of liposome modified microbubbles. *Lab on a Chip*, 12(21):4544–4552, 2012.
- [134] E. Dickinson. Emulsions and droplet size control. In D. J. Wedlock, editor, *Controlled Particle, Droplet and Bubble formation*, pages 191–216. Butterworth Heinemann, 2004.
- [135] P. Walstra. Principles of emulsion formation. *Chemical Engineering Science*, 48(2):333–349, 1993.
- [136] T. F. Tadros. *Emulsion Formation, Stability, and Rheology*. WILEY-VCH, 2013.
- [137] D. J. McClements. Nanoemulsions versus microemulsions: terminology, differences, and similarities. *Soft Matter*, 8(6):1719, 2012.
- [138] P. Calvo, J. L. Vila-Jato, and M. J. Alonso. Comparative in vitro evaluation of several colloidal systems, nanoparticles, nanocapsules, and nanoemulsions, as ocular drug carriers. *Journal of Pharmaceutical Sciences*, 85(5):530–536, 1996.
- [139] H. Wennerström, O. Söderman, U. Olsson, and B. Lindman. Macroemulsions versus microemulsions. *Colloids and Surfaces A: Physicochemical and Engineering Aspects*, 123-124:13–26, 1997.
- [140] P. L. Tang, E. D. Sudol, C. A. Silebi, and M. S. El-Asser. Miniemulsion Polymerization-A Comparative Study of Preparative Variables. *Journal of Applied Polymer Science*, 43:1059–1066, 1991.
- [141] T. G. Mason, J. N. Wilking, K. Meleson, C. B. Chang, and S. M. Graves. Nanoemulsions: formation, structure, and physical properties. *Journal of Physics: Condensed Matter*, 18(41):R635–R666, 2006.

- [142] N. Anton, J. P. Benoit, and P. Saulnier. Design and production of nanoparticles formulated from nano-emulsion templates-A review. *Journal of Controlled Release*, 128(3):185–199, 2008.
- [143] H. Yu and Q. Huang. Bioavailability and Delivery of Nutraceuticals and Functional Foods Using Nanotechnology. *Journal of Food Science*, 75(1):593–604, 2013.
- [144] J. Rao and D. J. McClements. Food-grade microemulsions, nanoemulsions and emulsions: Fabrication from sucrose monopalmitate & lemon oil. *Food Hydrocolloids*, 25(6):1413–1423, 2011.
- [145] T. Okazawa and J. Bron. On thermodynamically stable emulsions. I. Thermodynamic Background. *Journal of Colloid And Interface Science*, 69(1):86–96, 1979.
- [146] D. Myers. *Surfaces, interfaces, and colloids*. John Wiley & Sons, Ltd, 2nd edition, 1999.
- [147] D. J. McClements. *Food Emulsions. Principles, Practices and Techniques*. CRC Press, 3rd edition, 2016.
- [148] M. J. Rosen. Surfactants and interfacial phenomena. In *Colloids and Surfaces*, chapter Reduction. John Wiley & Sons, Ltd, 3rd edition, 2004.
- [149] A. Grumezescu. *Emulsions, Volume 3*. Academic Press, 2016.
- [150] J. P. Canselier, H. Delmas, A. M. Wilhelm, and B. Abismail. Ultrasound Emulsification—An Overview. *Journal of Dispersion Science and Technology*, 23(1-3):333–349, 2002.
- [151] T. S. H. Leong, T. J. Wooster, S. E. Kentish, and M. Ashokkumar. Minimising oil droplet size using ultrasonic emulsification. *Ultrasonics sonochemistry*, 16(6):721–7, 2009.
- [152] D. J. McClements. Advances in fabrication of emulsions with enhanced functionality using structural design principles. *Current Opinion in Colloid and Interface Science*, 17(5):235–245, 2012.
- [153] T. Varzakas and C. Tzia. *Food Engineering Handbook: Food Processing Engineering*. 2014.

- [154] Y. F. Maa and C. Hsu. Liquid-liquid emulsification by rotor/stator homogenization. *Journal of Controlled Release*, 38(2-3):219–228, 1996.
- [155] M. Stang, H. Schuchmann, and H. Schubert. Emulsification in High-Pressure Homogenizers. *Engineering in Life Sciences*, 1(4):151–157, 2001.
- [156] S. Pinnamaneni, N. G. Das, and S. K. Das. Comparison of oil-in-water emulsions manufactured by microfluidization and homogenization. *Pharmazie*, 58(8):554–558, 2003.
- [157] S. Schultz, G. Wagner, K. Urban, and J. Ulrich. High-pressure homogenization as a process for emulsion formation. *Chemical Engineering and Technology*, 27(4):361–368, 2004.
- [158] K. Urban, G. Wagner, D. Schaffner, D. Röglin, and J. Ulrich. Rotor-stator and disc systems for emulsification processes. *Chemical Engineering and Technology*, 29(1):24–31, 2006.
- [159] S. M. Jafari, E. Assadpoor, Y. He, and B. Bhandari. Re-coalescence of emulsion droplets during high-energy emulsification. *Food Hydrocolloids*, 22(7):1191–1202, 2008.
- [160] A. M. J. Diels and C. W. Michiels. High-Pressure Homogenization as a Non-Thermal Technique for the Inactivation of Microorganisms. *Critical Reviews in Microbiology*, 32(4):201–216, 2006.
- [161] F. Patrignani and R. Lanciotti. Applications of high and ultra high pressure homogenization for food safety. *Frontiers in Microbiology*, 7:1–13, 2016.
- [162] A. Zamora and B. Guamis. Opportunities for Ultra-High-Pressure Homogenisation (UHPH) for the Food Industry. *Food Engineering Reviews*, 7(2):130–142, 2014.
- [163] E. Dumay, D. Chevalier-Lucia, L. Picart-Palmade, A. Benzaria, A. Gràcia-Julià, and C. Blayo. Technological aspects and potential applications of (ultra) high-pressure homogenisation. *Trends in Food Science and Technology*, 31(1):13–26, 2013.
- [164] M. Thiebaud, E. Dumay, L. Picart, J. P. Guiraud, and J. C. Cheftel. High-pressure homogenisation of raw bovine milk. Effects on fat globule size distribution and microbial inactivation. *International Dairy Journal*, 13(6):427–439, 2003.

- [165] M. Cortés-Muñoz, D. Chevalier-Lucia, and E. Dumay. Characteristics of submicron emulsions prepared by ultra-high pressure homogenisation: Effect of chilled or frozen storage. *Food Hydrocolloids*, 23(3):640–654, 2009.
- [166] J. Flourey, A. Desrumaux, M. A. V. Axelos, and J. Legrand. Effect of high pressure homogenisation on methylcellulose as food emulsifier. *Journal of Food Engineering*, 58(3):227–238, 2003.
- [167] H. Karbstein and H. Schubert. Developments in the continuous mechanical production of oil-in-water macro-emulsions. *Chemical Engineering and Processing: Process Intensification*, 34(3):205–211, 1995.
- [168] J. Flourey, A. Desrumaux, and D. Legrand. Effect of Ultra-high-pressure Homogenization on Structure and on Rheological Properties of Soy Protein-stabilized Emulsions. *Journal of Food Engineering and Physical Properties*, 67(9):3388–3395, 2002.
- [169] S. Tesch, C. Gerhards, and H. Schubert. Stabilization of emulsions by OSA starches. *Journal of Food Engineering*, 54(2):167–174, 2002.
- [170] G. Kolb, K. Viardot, G. Wagner, and J. Ulrich. Evaluation of a new high-pressure dispersion unit (HPN) for emulsification. *Chemical Engineering and Technology*, 24(3):293–296, 2001.
- [171] P. Walstra and P. E. A. Smulders. Emulsion Formation. In B. Blinks, editor, *Modern aspects of emulsion science*, chapter 2. Royal Society of Chemistry, 1998.
- [172] I. N. Seekkuarachchi, K. Tanaka, and H. Kumazawa. Formation and characterization of submicrometer oil-in-water (O/W) emulsions, using high-energy emulsification. *Industrial & engineering chemistry research*, 45(1):372–390, 2006.
- [173] C. Solans, P. Izquierdo, J. Nolla, N. Azemar, and M. J. Garcia-Celma. Nano-emulsions. *Current Opinion in Colloid and Interface Science*, 10(3-4):102–110, 2005.
- [174] D. F. Evans and H. Wennerstrom. *The Colloidal Domain: Where Physics, Chemistry, Biology and Technology Meet*. WILEY-VCH, 2nd edition, 1999.
- [175] P. Taylor. Ostwald ripening in emulsions: Estimation of solution thermodynamics of the disperse phase. *Advances in Colloid and Interface Science*, 106(1-3):261–285, 2003.

- [176] T. Tadros, P. Izquierdo, J. Esquena, and C. Solans. Formation and stability of nano-emulsions. *Advances in Colloid and Interface Science*, 108-109:303–318, 2004.
- [177] R. H. Abou-Saleh, M. Swain, S. D. Evans, and N. H. Thomson. Poly(ethylene glycol) lipid-shelled microbubbles: abundance, stability, and mechanical properties. *Langmuir*, 30(19):5557–5563, 2014.
- [178] R. H. Abou-Saleh, S. A. Peyman, B. R. G. Johnson, G. Marston, N. Ingram, R. J. Bushby, P. L. Coletta, A. F. Markham, and S. D. Evans. Influence of intercalating perfluorohexane into the lipid shell on nano and microbubbles stability. *Soft Matter*, page DOI: 10.1039/C6SM00956E, 2016.
- [179] L. Li, A. Pandey, D. J. Werder, B. P. Khanal, J. M. Pietryga, and V. I. Klimov. Efficient synthesis of highly luminescent copper indium sulfide-based core/shell nanocrystals with surprisingly long-lived emission. *Journal of the American Chemical Society*, 133(5):1176–1179, 2011.
- [180] M. Booth, A. P. Brown, S. D. Evans, and K. Critchley. Determining the Concentration of CuInS₂ Quantum Dots from the Size Dependent Molar Extinction Coefficient. *Chem. Mater.*, 24:2064–2070, 2012.
- [181] C. A. Leatherdale, W. K. Woo, F. V. Mikulec, and M. G. Bawendi. On the Absorption Cross Section of CdSe Nanocrystal Quantum Dots. *The Journal of Physical Chemistry B*, 106:7619–7622, 2002.
- [182] W. W. Yu, L. Qu, W. Guo, and X. Peng. Experimental Determination of the Extinction Coefficient of CdTe, CdSe, and CdS Nanocrystals. *Chemistry of Materials*, 15(14):2854–2860, 2003.
- [183] C. Wayne and R. P. Wayne. *Photochemistry*. Oxford University Press, 1996.
- [184] J. R. Lakowicz. *Principles of fluorescence spectroscopy*. Kluwer Academic / Plenum Publishers, 2nd edition, 1999.
- [185] N. Vij, T. Min, R. Marasigan, C. N. Belcher, S. Mazur, H. Ding, K.-T. Yong, and I. Roy. Development of PEGylated PLGA nanoparticle for controlled and sustained drug delivery in cystic fibrosis. *Journal of Nanobiotechnology*, 8(22), 2010.

- [186] B. C. Baumann, G. D. Kao, A. Mahmud, T. Harada, J. Swift, C. Chapman, X. Xu, D. E. Discher, and J. F. Dorsey. Enhancing the efficacy of drug-loaded nanocarriers against brain tumors by targeted radiation therapy. *Oncotarget*, 4(1):64–79, 2013.
- [187] F. Varenne, A. Makky, M. Gaucher-Delmas, F. Violleau, and C. Vauthier. Multimodal Dispersion of Nanoparticles: A Comprehensive Evaluation of Size Distribution with 9 Size Measurement Methods. *Pharmaceutical Research*, 33(5):1220–1234, 2016.
- [188] B. J. Frisken. Revisiting the Method of Cumulants for the Analysis of Dynamic Light-Scattering Data. *Applied Optics*, 40(24):4087, 2001.
- [189] V. Filipe, A. Hawe, and W. Jiskoot. Critical evaluation of nanoparticle tracking analysis (NTA) by NanoSight for the measurement of nanoparticles and protein aggregates. *Pharmaceutical Research*, 27(5):796–810, 2010.
- [190] E. Weatherall. Applications of tunable resistive pulse sensing. *The Analyst*, 140(10):3318, 2015.
- [191] S. A. Peyman, J. R. McLaughlan, R. H. Abou-Saleh, G. Marston, B. R. G. Johnson, S. Freear, P. L. Coletta, A. F. Markham, and S. D. Evans. On-chip preparation of nanoscale contrast agents towards high-resolution ultrasound imaging. *Lab Chip*, 2016.
- [192] G. Sauerbrey. Verwendung von Schwingquarzen zur Wagungdiinner Schichten und zur Mikrowagung. *Zeitschrift fur Physik*, 155:206–222, 1959.
- [193] S. X. Liu and J. T. Kim. Application of Kevin-Voigt Model in Quantifying Whey Protein Adsorption on Polyethersulfone Using QCM-D. *Journal of the Association for Laboratory Automation*, 14(4):213–220, 2009.
- [194] N. J. Cho, K. K. Kanazawa, J. S. Glenn, and C. W. Frank. Employing two different quartz crystal microbalance models to study changes in viscoelastic behavior upon transformation of lipid vesicles to a bilayer on a gold surface. *Analytical Chemistry*, 79(18):7027–7035, 2007.
- [195] M. V. Voinova, M. Rodahl, M. Jonson, and B. Kasemo. Viscoelastic Acoustic Response of Layered Polymer Films at Fluid-Solid Interfaces: Continuum Mechanics Approach. *Physica Scripta*, 59(5):391–396, 1999.

- [196] K. Kastl, M. Ross, V. Gerke, and C. Steinem. Kinetics and thermodynamics of annexin A1 binding to solid-supported membranes: A QCM study. *Biochemistry*, 41(31):10087–10094, 2002.
- [197] T. Muramoto, R. Shimoya, K. Yoshida, and Y. Watanabe. Evaluation of the specific adsorption of biotinylated microbubbles using a quartz crystal microbalance. *Ultrasound in medicine & biology*, 40(5):1027–1033, 2014.
- [198] C. Larsson, M. Rodahl, and F. Höök. Characterization of DNA immobilization and subsequent hybridization on a 2D arrangement of streptavidin on a biotin-modified lipid bilayer supported on SiO₂. *Analytical Chemistry*, 75(19):5080–5087, 2003.
- [199] N. K. Nadermann, E. P. Chan, and C. M. Stafford. Bilayer Mass Transport Model for Determining Swelling and Diffusion in Coated, Ultrathin Membranes. *ACS Applied Materials & Interfaces*, 3502(1):3492–3502, 2015.
- [200] C. A. Keller and B. Kasemo. Surface specific kinetics of lipid vesicle adsorption measured with a quartz crystal microbalance. *Biophysical Journal*, 75(September):1397–1402, 1998.
- [201] C. A. Keller, K. Glasmästar, V. P. Zhdanov, and B. Kasemo. Formation of supported membranes from vesicles. *Physical review letters*, 84(23):5443–6, 2000.
- [202] R. Richter, A. Mukhopadhyay, and A. Brisson. Pathways of lipid vesicle deposition on solid surfaces: a combined QCM-D and AFM study. *Biophysical journal*, 85(5):3035–47, 2003.
- [203] B. Gandul-Rojas and M. I. Minguez-Mosquera. Chlorophyll and Carotenoid Composition in Virgin Olive Oils from Various Spanish Olive Varieties. *Journal of the Science of Food and Agriculture*, 72(1):31–39, 1996.
- [204] V. Domenici, D. Ancora, M. Cifelli, C. A. Veracini, M. Zandomenighi, C. A. Veracini, M. Zandomenighi, and U. Pisa. Extraction of Pigments Information from near-UV Vis Absorption Spectra of Extra Virgin Olive Oils Extraction of Pigments Information from near-UV Vis Absorption Spectra of Extra Virgin Olive Oils. *Journal of Agricultural and Food Chemistry*, 62:9317–9325, 2014.

- [205] A. Giuliani, L. Cerretani, and A. Cichelli. Chlorophylls in olive and in olive oil: chemistry and occurrences. *Critical reviews in food science and nutrition*, 51(7):678–690, 2011.
- [206] H. L. Newmark. Squalene, Olive Oil, and and Cancer Risk: A Review and Hypothesis. *Annals of the New York Academy of Sciences*, 6(December):1101–1103, 1999.
- [207] M. Spanova and G. Daum. Squalene - biochemistry, molecular biology, process biotechnology, and applications. *European Journal of Lipid Science and Technology*, 113(11):1299–1320, 2011.
- [208] A. K. T. Wann, J. Mistry, E. J. Blain, A. T. Michael-Titus, and M. M. Knight. Eicosapentaenoic acid and docosahexaenoic acid reduce interleukin-1 β -mediated cartilage degradation. *Arthritis research & therapy*, 12(6), 2010.
- [209] A. J. Cockbain, M. Volpato, A. D. Race, A. Munarini, C. Fazio, A. Belluzzi, P. M. Loadman, G. J. Toogood, and M. a. Hull. Anticorectal cancer activity of the omega-3 polyunsaturated fatty acid eicosapentaenoic acid. *Gut*, 2014.
- [210] M. J. Moyano, F. J. Heredia, and A. J. Meléndez-Martínez. The color of olive oils: The pigments and their likely health benefits and visual and instrumental methods of analysis. *Comprehensive Reviews in Food Science and Food Safety*, 9(3):278–291, 2010.
- [211] S. Passaloglou-Emmanouilidou. A comparative study of UV spectrophotometric methods for detection of olive oil adulteration by refined oils. *Lebensmittel-Untersuchung und -Forschung*, 191(2):132–134, 1990.
- [212] T. Albi, A. Lanzón, A. Guinda, M. León, and M. C. Pérez-Camino. Microwave and Conventional Heating Effects on thermoxidative degradation of edible fats. *Journal of Agricultural and Food Chemistry*, 45:3795–3798, 1997.
- [213] F. Shahidi and Y. Zhong. Lipid oxidation: measurement methods. In *Bailey's industrial oil and fat products*, chapter 8, pages 357–385. Wiley Online Library, 2005.
- [214] M. Sauer, J. Hofkens, and J. Enderlein. *Handbook of Fluorescence spectroscopy*. WILEY-VCH Verlag, 2011.

- [215] C. Turek and F. C. Stintzing. Stability of essential oils: A review. *Comprehensive Reviews in Food Science and Food Safety*, 12(1):40–53, 2013.
- [216] S. Kim, Y. T. Lim, E. G. Soltesz, A. M. De Grand, J. Lee, A. Nakayama, J. A. Parker, T. Mihaljevic, R. G. Laurence, D. M. Dor, L. H. Cohn, M. G. Bawendi, and J. V. Frangioni. Near-infrared fluorescent type II quantum dots for sentinel lymph node mapping. *Nat.Biotechnol.*, 22(1):93–97, 2004.
- [217] W. Jiang, A. Singhal, B. Kim, J. Zheng, J. Rutka, C. Wang, and W. Chan. Assessing Near-Infrared Quantum Dots for Deep Tissue, Organ, and Animal Imaging Applications. *Journal of the Association for Laboratory Automation*, 13(1):6–12, 2008.
- [218] R. Tang, J. Xue, B. Xu, D. Shen, G. P. Sudlow, and S. Achilefu. Tunable Ultrasmall Visible-to- Extended Near-Infrared Emitting Silver Sulfide Quantum Dots for Integrin-Targeted Cancer Imaging. *ACS nano*, 9(1):220–230, 2015.
- [219] M. Green, S. J. Haigh, E. A. Lewis, L. Sandiford, M. Burkitt-Gray, R. Fleck, G. Vizcay-Barrena, L. Jensen, H. Mirzai, R. J. Curry, and L. Dailey. The biosynthesis of infrared-emitting quantum dots in *Allium fistulosum*. *Scientific Reports*, 6:20480, 2016.
- [220] P. H. Chuang, C. C. Lin, and R. S. Liu. Emission-Tunable CuInS₂/ZnS Quantum Dots: Structure, Optical Properties, and Application in White Light-Emitting Diodes with High Color Rendering Index. *ACS Applied Materials & Interfaces*, 6(17):15379–15387, 2014.
- [221] D. I. Reingold. *Organic Chemistry, Or "The Happy Carbon": An Introductory Text Emphasizing Biological Connections*. Indo American Books, 2007.
- [222] P. Greenspan, E. P. Mayer, and S. D. Fowler. Nile red: a selective fluorescent stain for intracellular lipid droplets. *The Journal of Cell Biology*, 100(3):965–973, 1985.
- [223] M. T. Ta, T. S. Kapterian, W. Fei, X. Du, A. J. Brown, I. W. Dawes, and H. Yang. Accumulation of squalene is associated with the clustering of lipid droplets. *FEBS Journal*, 279(22):4231–4244, 2012.

- [224] F. Gao, Z. Zhang, H. Bu, Y. Huang, Z. Gao, J. Shen, C. Zhao, and Y. Li. Nanoemulsion improves the oral absorption of candesartan cilexetil in rats: Performance and mechanism. *Journal of controlled release*, 149(2):168–174, 2011.
- [225] P. Greenspan and S. D. Fowler. Spectrofluorometric studies of the lipid probe, Nile red. *Journal of Lipid Research*, 26(7):781–789, 1985.
- [226] R. Lichtenfels, W. E. Biddison, H. Schulz, A. B. Vogt, and R. Martin. CARE-LASS (calcein-release-assay), an improved fluorescence-based test system to measure cytotoxic T lymphocyte activity. *Journal of Immunological Methods*, 172(2):227–239, 1994.
- [227] S. Neri, E. Mariani, A. Meneghetti, L. Cattini, and A. Facchini. Calcein-acetyoxymethyl cytotoxicity assay: standardization of a method allowing additional analyses on recovered effector cells and supernatants. *Clinical and diagnostic laboratory immunology*, 8(6):1131–1135, 2001.
- [228] G. R. Pettit, B. S. Sheo, M. R. Boyd, E. Hamel, R. K. Pettit, J. M. Schmidt, and F. Hogan. Antineoplastic agents. 291. Isolation and synthesis of combretastatins A-4, A-5, and A-6. *Journal of Medicinal Chemistry*, 38(15):1666–1672, 1995.
- [229] G. M. Tozer, C. Kanthou, and B. C. Baguley. Disrupting tumour blood vessels. *Nature reviews. Cancer*, 5(6):423–435, 2005.
- [230] R. T. Dorr, K. Dvorakova, K. Snead, D. S. Alberts, S. E. Salmon, and G. R. Pettit. Antitumor activity of combretastatin-A4 phosphate, a natural product tubulin inhibitor. *Investigational new drugs*, 14:131–137, 1996.
- [231] G. J. S. Rustin, S. M. Galbraith, H. Anderson, M. Stratford, L. K. Folkes, L. Sena, L. Gumbrell, and P. M. Price. Phase I clinical trial of weekly combretastatin A4 phosphate: Clinical and pharmacokinetic results. *Journal of Clinical Oncology*, 21(15):2815–2822, 2003.
- [232] C. Kanthou, O. Greco, A. Stratford, I. Cook, R. Knight, O. Benzakour, and G. Tozer. The tubulin-binding agent combretastatin A-4-phosphate arrests endothelial cells in mitosis and induces mitotic cell death. *The American journal of pathology*, 165(4):1401–1411, 2004.

- [233] M. Zhang, R. Guo, Y. Wang, X. Cao, M. Shen, and X. Shi. Multifunctional dendrimer/combretastatin A4 inclusion complexes enable in vitro targeted cancer therapy. *International journal of nanomedicine*, 6:2337–2349, 2011.
- [234] Y. Oki, E. Aoki, and J. P. J. Issa. Decitabine-Bedside to bench. *Critical Reviews in Oncology/Hematology*, 61(2):140–152, 2007.
- [235] J. Nie, L. Liu, X. Li, and W. Han. Decitabine, a new star in epigenetic therapy: the clinical application and biological mechanism in solid tumors. *Cancer letters*, 354(1):12–20, 2014.
- [236] D. K. Rogstad, J. L. Herring, J. A. Theruvathu, A. Burdzy, C. C. Perry, J. W. Neidigh, and L. C. Sowers. Chemical Decomposition of 5-Aza-2'-deoxycytidine (Decitabine): Kinetic Analyses and Identification of Products by NMR , HPLC , and Mass Spectrometry. *Chemical Research in Toxicology*, 22:1194–1204, 2009.
- [237] M. Karahoca and R. L. Momparler. Pharmacokinetic and pharmacodynamic analysis of 5-aza-2'-deoxycytidine (decitabine) in the design of its dose-schedule for cancer therapy. *Clinical Epigenetics*, 5(3), 2013.
- [238] S. P. Lim, R. Kumar, Y. Akkamsetty, W. Wang, K. Ho, P. M. Neilsen, D. J. Walther, R. J. Suetani, C. Prestidge, and D. F. Callen. Development of a novel cell-based assay system EPISSAY for screening epigenetic drugs and liposome formulated decitabine. *BMC cancer*, 13(1):113, 2013.
- [239] S. Y. Li, R. Sun, H. X. Wang, S. Shen, Y. Liu, X. J. Du, Y. H. Zhu, and W. Jun. Combination therapy with epigenetic-targeted and chemotherapeutic drugs delivered by nanoparticles to enhance the chemotherapy response and overcome resistance by breast cancer stem cells. *Journal of controlled release : official journal of the Controlled Release Society*, 2014.
- [240] D. A. Skoog, D. M. West, F. J. Holler, and S. R. Crouch. *Fundamentals of Analytical Chemistry*. Brooks/Cole, 9th edition, 2014.
- [241] K. Grosios, S. E. Holwell, A. T. McGown, G. R. Pettit, and M. C. Bibby. In vivo and in vitro evaluation of combretastatin A-4 and its sodium phosphate prodrug. *British journal of cancer*, 81(8):1318–27, 1999.

- [242] K. Wormuth, O. Brüggemann, and R. Strey. Emulsions which appear brightly colored upon illumination with white light. *Langmuir*, 18(16):5989–5994, 2002.
- [243] E. Naziri, R. Consonni, and M. Z. Tsimidou. Squalene oxidation products: Monitoring the formation, characterisation and pro-oxidant activity. *European Journal of Lipid Science and Technology*, 116:1400–1411, 2014.
- [244] B. B. Lundberg. A submicron lipid emulsion coated with amphipathic polyethylene glycol for parenteral administration of paclitaxel (Taxol). *The Journal of Pharmacy and Pharmacology*, 49(1):16–21, 1997.
- [245] G. Bozzuto and A. Molinari. Liposomes as nanomedical devices. *International Journal of Nanomedicine*, 10:975–999, 2015.
- [246] E. Blanco, H. Shen, and M. Ferrari. Principles of nanoparticle design for overcoming biological barriers to drug delivery. *Nature biotechnology*, 33(9):941–951, 2015.
- [247] W. Anderson, D. Kozak, V. A. Coleman, A. K. Jämting, and M. Trau. A comparative study of submicron particle sizing platforms: Accuracy, precision and resolution analysis of polydisperse particle size distributions. *Journal of Colloid and Interface Science*, 405:322–330, 2013.
- [248] J. Flourey, A. Desrumaux, and J. Lardières. Effect of high-pressure homogenization on droplet size distributions and rheological properties of model oil-in-water emulsions. *Innovative Food Science & Emerging Technologies*, 1(2):127–134, 2000.
- [249] P. J. Wilde. Interfaces: Their role in foam and emulsion behaviour. *Current Opinion in Colloid and Interface Science*, 5(3-4):176–181, 2000.
- [250] S. S. Feng and G. Huang. Effects of emulsifiers on the controlled release of paclitaxel (Taxol®) from nanospheres of biodegradable polymers. *Journal of Controlled Release*, 71(1):53–69, 2001.
- [251] J. P. Hsu and A. Nacu. Behavior of soybean oil-in-water emulsion stabilized by nonionic surfactant. *Journal of Colloid and Interface Science*, 259(2):374–381, 2003.
- [252] B. Ashok, L. Arleth, R. P. Hjelm, I. Rubinstein, and H. Onyüksel. In vitro characterization of PEGylated phospholipid micelles for improved drug solubilization: effects of PEG chain length and PC incorporation. *Journal of pharmaceutical sciences*, 93(10):2476–87, 2004.

- [253] O. Tirosh, Y. Barenholz, J. Katzhendler, and A. Priev. Hydration of Polyethylene Glycol-Grafted Liposomes. *Biophysical Journal*, 74(3):1371–1379, 1998.
- [254] O. Garbuzenko, Y. Barenholz, and A. Priev. Effect of grafted PEG on liposome size and on compressibility and packing of lipid bilayer. *Chemistry and Physics of Lipids*, 135(2):117–129, 2005.
- [255] H. Yoshioka. Surface modification of haemoglobin-containing liposomes with polyethylene glycol prevents liposome aggregation in blood plasma. *Biomaterials*, 12(9):861–864, 1991.
- [256] D. Needham, T. J. McIntosh, and D. D. Lasic. Repulsive interactions and mechanical stability of polymer-grafted lipid membranes. *BBA - Biomembranes*, 1108(1):40–48, 1992.
- [257] C. Allen, N. Dos Santos, R. Gallagher, G. N. C. Chiu, Y. Shu, W. M. Li, S. A. Johnstone, A. S. Janoff, L. D. Mayer, M. S. Webb, and M. B. Bally. Controlling the Physical Behavior and Biological Performance of Liposome Formulations through Use of Surface Grafted Poly(ethylene Glycol). *Bioscience Reports*, 22(2):225–250, 2002.
- [258] T. J. Wooster, M. Golding, and P. Sanguansri. Impact of Oil Type on Nanoemulsion Formation and Ostwald Ripening Stability. *Langmuir*, 24(10):12758–12765, 2008.
- [259] J. Wacker, V. K. Parashar, and M. A. M. Gijs. Influence of Oil Type and Viscosity on Droplet Size in a Flow Focusing Microfluidic Device. *Procedia Chemistry*, 1(1):1083–1086, 2009.
- [260] C. Qian and D. J. McClements. Formation of nanoemulsions stabilized by model food-grade emulsifiers using high-pressure homogenization: Factors affecting particle size. *Food Hydrocolloids*, 25(5):1000–1008, 2011.
- [261] T. Dapčević Hadnadev, P. Dokić, V. Krstonošić, and M. Hadnadev. Influence of oil phase concentration on droplet size distribution and stability of oil-in-water emulsions. *European Journal of Lipid Science and Technology*, 115(3):313–321, 2013.
- [262] A. Gupta, H. B. Eral, T. A. Hatton, and P. S. Doyle. Controlling and predicting droplet size of nanoemulsions: scaling relations with experimental validation. *Soft matter*, 12(5):1452–1458, 2016.

- [263] W. D. Pandolfe. Effect of Dispersed and Continuous Phase Viscosity on Droplet Size of Emulsions Generated By Homogenization. *Journal of Dispersion Science and Technology*, 2(4):459–474, 1981.
- [264] K. A. G. Schmidt, D. Pagnutti, M. D. Curran, A. Singh, J. P. M. Trusler, C. Maitland, and M. McBride-wright. New Experimental Data and Reference Models for the Viscosity and Density of Squalane. *Journal of Chemical & Engineering Data*, 60(1):137–150, 2015.
- [265] A. J. Fillery-Travis, L. H. Foster, and M. M. Robins. Stability of emulsions stabilised by two physiological surfactants: L- α -phosphatidylcholine and sodium taurocholate. *Biophysical Chemistry*, 54(3):253–260, 1995.
- [266] S. Uluata, E. A. Decker, and D. J. McClements. Optimization of Nanoemulsion Fabrication Using Microfluidization: Role of Surfactant Concentration on Formation and Stability. *Food Biophysics*, 11(1):52–59, 2016.
- [267] S. Sugiura, M. Nakajima, K. Yamamoto, S. Iwamoto, T. Oda, M. Satake, and M. Seki. Preparation characteristics of water-in-oil-in-water multiple emulsions using microchannel emulsification. *Journal of Colloid and Interface Science*, 270(1):221–228, 2004.
- [268] C. K. Weiss, M. R. Lorenz, K. Landfester, and V. Mailänder. Cellular uptake behavior of unfunctionalized and functionalized PBCA particles prepared in a miniemulsion. *Macromolecular bioscience*, 7(7):883–896, 2007.
- [269] S. Matsuoka and M. Murata. Membrane permeabilizing activity of amphotericin B is affected by chain length of phosphatidylcholine added as minor constituent. *Biochimica et Biophysica Acta - Biomembranes*, 1617:109–115, 2003.
- [270] L. Redondo-Morata, M. I. Giannotti, and F. Sanz. Influence of cholesterol on the phase transition of lipid bilayers: A temperature-controlled force spectroscopy study. *Langmuir*, 28(35):12851–12860, 2012.
- [271] F. Ostertag, J. Weiss, and D. J. McClements. Low-energy formation of edible nanoemulsions: Factors influencing droplet size produced by emulsion phase inversion. *Journal of Colloid and Interface Science*, 388(1):95–102, 2012.

- [272] C. B. Chang, C. M. Knobler, W. M. Gelbart, and T. G. Mason. Curvature dependence of viral protein structures on encapsidated nanoemulsion droplets. *ACS Nano*, 2(2):281–286, 2008.
- [273] H. Z. An, E. R. Safai, H. Burak Eral, and P. S. Doyle. Synthesis of biomimetic oxygen-carrying compartmentalized microparticles using flow lithography. *Lab on a chip*, 13(24):4765–74, 2013.
- [274] A. Gupta, H. B. Eral, T. A. Hatton, and P. S. Doyle. Nanoemulsions: formation, properties and applications. *Soft Matter*, 12(11):2826–2841, 2016.
- [275] S. M. Dordević, T. S. Radulović, N. D. Cekić, D. V. Randelović, M. M. Savić, D. R. Krajišnik, J. R. Milić, and S. D. Savić. Experimental design in formulation of diazepam nanoemulsions: Physicochemical and pharmacokinetic performances. *Journal of Pharmaceutical Sciences*, 102(11):4159–4172, 2013.
- [276] T. Lian and R. J. Ho. Trends and developments in liposome drug delivery systems. *Journal of pharmaceutical sciences*, 90(6):667–680, 2001.
- [277] K. J. Harrington, G. Rowlinson-Busza, K. N. Syrigos, P. S. Uster, R. M. Abra, and J. S. Stewart. Biodistribution and pharmacokinetics of ¹¹¹In-DTPA-labelled pegylated liposomes in a human tumour xenograft model: implications for novel targeting strategies. *British journal of cancer*, 83:232–238, 2000.
- [278] M. L. Immordino, P. Brusa, S. Arpicco, B. Stella, F. Dosio, and L. Cattel. Preparation, characterization, cytotoxicity and pharmacokinetics of liposomes containing docetaxel. *Journal of Controlled Release*, 91(3):417–429, 2003.
- [279] W. C. Zamboni, A. C. Gervais, M. J. Egorin, J. H. M. Schellens, E. G. Zuhowski, D. Pluim, E. Joseph, D. R. Hamburger, P. K. Working, G. Colbern, M. E. Tonda, D. M. Potter, and J. L. Eiseman. Systemic and tumor disposition of platinum after administration of cisplatin or STEALTH liposomal-cisplatin formulations (SPI-077 and SPI-077 B103) in a preclinical tumor model of melanoma. *Cancer Chemotherapy and Pharmacology*, 53(4):329–336, 2004.
- [280] T. Ishida, M. Harada, Y. W. Xin, M. Ichihara, K. Irimura, and H. Kiwada. Accelerated blood clearance of PEGylated liposomes following preceding liposome injection: Effects of lipid dose and PEG surface-density and chain length of the first-dose liposomes. *Journal of Controlled Release*, 105(3):305–317, 2005.

- [281] S. N. Jayasinghe and M. J. Edirisinghe. Effect of viscosity on the size of relics produced by electrostatic atomization. *Journal of Aerosol Science*, 33(10):1379–1388, 2002.
- [282] H. T. Osborn and C. C. Akoh. Effect of emulsifier type, droplet size, and oil concentration on lipid oxidation in structured lipid-based oil-in-water emulsions. *Food Chemistry*, 84(3):451–456, 2004.
- [283] J. V. L. Henry, P. J. Fryer, W. J. Frith, and I. T. Norton. The influence of phospholipids and food proteins on the size and stability of model sub-micron emulsions. *Food Hydrocolloids*, 24(1):66–71, 2010.
- [284] S. Ganta, J. W. Paxton, B. C. Baguley, and S. Garg. Pharmacokinetics and pharmacodynamics of chlorambucil delivered in parenteral emulsion. *International Journal of Pharmaceutics*, 360(1-2):115–121, 2008.
- [285] D. Bratosin, L. Mitrofan, C. Paliu, J. Estaquier, and J. Montreuil. Novel fluorescence assay using calcein-AM for the determination of human erythrocyte viability and aging. *Cytometry Part A*, 66(1):78–84, 2005.
- [286] T. Shimanouchi, H. Ishii, N. Yoshimoto, H. Umakoshi, and R. Kuboi. Calcein permeation across phosphatidylcholine bilayer membrane: Effects of membrane fluidity, liposome size, and immobilization. *Colloids and Surfaces B: Biointerfaces*, 73(1):156–160, 2009.
- [287] B. Maherani, E. Arab-Tehrany, A. Kheiriloom, D. Geny, and M. Linder. Calcein release behavior from liposomal bilayer; Influence of physicochemical/mechanical/structural properties of lipids. *Biochimie*, 95(11):2018–2033, 2013.
- [288] R. Notman, M. Noro, B. O’Malley, and J. Anwar. Molecular basis for dimethylsulfoxide (DMSO) action on lipid membranes. *Journal of the American Chemical Society*, 128(43):13982–13983, 2006.
- [289] C. Y. Cheng, J. Song, J. Pas, L. H. H. Meijer, and S. Han. DMSO Induces Dehydration near Lipid Membrane Surfaces. *Biophysical journal*, 109(2):330–339, 2015.
- [290] J. W. Meisel and G. W. Gokel. A Simplified Direct Lipid Mixing Lipoplex Preparation: Comparison of Liposomal-, Dimethylsulfoxide-, and Ethanol-Based Methods. *Scientific Reports*, 6(January), 2016.

- [291] X. Xu, M. A. Khan, and D. J. Burgess. A two-stage reverse dialysis in vitro dissolution testing method for passive targeted liposomes. *International Journal of Pharmaceutics*, 426(1-2):211–218, 2012.
- [292] M. Anderson and A. Omri. The effect of different lipid components on the in vitro stability and release kinetics of liposome formulations. *Drug delivery*, 11:33–39, 2004.
- [293] M. Rossignol, T. Uso, and P. Thomas. Relationship between fluidity and ionic permeability of bilayers from natural mixtures of phospholipids. *The Journal of Membrane Biology*, 87(3):269–275, 1985.
- [294] S. Fowler and P. Greenspan. Application of Nile Red, a Fluorescent Hydrophobic Probe, for the Detection of Neutral Lipid Deposits in Tissue Sections. *The Journal of Histochemistry and Cytochemistry*, 33(8):833–836, 1985.
- [295] H. Jung, H. Ishii, T. Shimanouchi, H. Umakoshi, and R. Kuboi. Immobilized-Liposome Sensor System for Detection of Proteins under Stress Conditions. *Membrane*, 32(5):294–301, 2007.
- [296] N. Bao, J. Wang, and C. Lu. Microfluidic electroporation for selective release of intracellular molecules at the single-cell level. *Electrophoresis*, 29(14):2939–2944, 2008.
- [297] E. Kang, D. H. Lee, C. B. Kim, S. J. Yoo, and S. H. Lee. A hemispherical microfluidic channel for the trapping and passive dissipation of microbubbles. *Journal of Micromechanics and Microengineering*, 20(4):045009, 2010.
- [298] G. G. Giobbe, F. Michielin, C. Luni, S. Giulitti, S. Martewicz, S. Dupont, A. Floreani, and N. Elvassore. Functional differentiation of human pluripotent stem cells on a chip. *Nature methods*, 12(7), 2015.
- [299] S. L. Veatch and S. L. Keller. Organization in lipid membranes containing cholesterol. *Physical review letters*, 89(26):268101, 2002.
- [300] M. Tanaka, H. Saito, I. Arimoto, M. Nakano, and T. Handa. Evidence for interpenetration of core triglycerides into surface phospholipid monolayers in lipid emulsions. *Langmuir*, 19(13):5192–5196, 2003.

- [301] R. P. Richter and A. R. Brisson. Following the formation of supported lipid bilayers on mica: a study combining AFM, QCM-D, and ellipsometry. *Biophysical journal*, 88(5):3422–33, 2005.
- [302] S. M. Rigby-Singleton, M. C. Davies, H. Harris, P. O. Shea, and S. Allen. Visualizing the Solubilization of Supported Lipid Bilayers by an Amphiphilic Peptide. *Langmuir*, (15):6273–6279, 2006.
- [303] T. D. Pollard. A guide to simple and informative binding assays. *Molecular biology of the cell*, 21(23):4061–4067, 2010.
- [304] P. Drücker, M. Pejic, D. Grill, H. J. Galla, and V. Gerke. Cooperative binding of annexin A2 to cholesterol- and phosphatidylinositol-4,5-bisphosphate-containing bilayers. *Biophysical Journal*, 107(9):2070–2081, 2014.
- [305] F. Albertorio, A. J. Diaz, T. Yang, V. A. Chapa, S. Kataoka, E. T. Castellana, and P. S. Cremer. Fluid and air-stable lipopolymer membranes for biosensor applications. *Langmuir*, 21(16):7476–7482, 2005.
- [306] S. Kaufmann, G. Papastavrou, K. Kumar, M. Textor, and E. Reimhult. A detailed investigation of the formation kinetics and layer structure of poly(ethylene glycol) tether supported lipid bilayers. *Soft Matter*, 5(14):2804, 2009.
- [307] N. M. Green. Avidin and streptavidin. *Methods in Enzymology*, 184:51–67, 1990.
- [308] H. Ishihara. Current status and prospects of polyethyleneglycol-modified medicines. *Biological & pharmaceutical bulletin*, 36(6):883–8, 2012.
- [309] M. Spanova, D. Zweytick, K. Lohner, L. Klug, E. Leitner, A. Hermetter, and G. Daum. Influence of squalene on lipid particle/droplet and membrane organization in the yeast *Saccharomyces cerevisiae*. *Biochimica et Biophysica Acta - Molecular and Cell Biology of Lipids*, 1821(4):647–653, 2012.
- [310] S. F. Gilmore, A. I. Yao, Z. Tietel, T. Kind, M. T. Facciotti, and A. N. Parikh. Role of squalene in the organization of monolayers derived from lipid extracts of halobacterium salinarum. *Langmuir*, 29(25):7922–7930, 2013.
- [311] J. L. Richens, J. S. Lane, M. L. Mather, and P. O’Shea. The interactions of squalene, alkanes and other mineral oils with model membranes; effects on membrane heterogeneity and function. *Journal of Colloid and Interface Science*, 457:225–231, 2015.

- [312] T. Hauß, S. Dante, N. A. Dencher, and T. H. Haines. Squalane is in the midplane of the lipid bilayer: Implications for its function as a proton permeability barrier. *Biochimica et Biophysica Acta - Bioenergetics*, 1556(2-3):149–154, 2002.
- [313] H. Jung, J. Y. Kim, Y. Kim, G. Tae, Y. H. Kim, and D. Johannsmann. QCM and AFM analysis of anticoagulant activities of sulfonated polymers against fibrin formation. *Langmuir*, 25(12):7032–7041, 2009.
- [314] C. S. Neish, I. L. Martin, R. M. Henderson, and J. M. Edwardson. Direct visualization of ligand-protein interactions using atomic force microscopy. *British journal of pharmacology*, 135(8):1943–50, 2002.
- [315] C. Rosano, P. Arosio, and M. Bolognesi. The X-ray three-dimensional structure of avidin. *Biomolecular Engineering*, 16(1-4):5–12, 1999.
- [316] M. F. Delcroix, S. Demoustier-Champagne, and C. C. Dupont-Gillain. Quartz crystal microbalance study of ionic strength and pH-dependent polymer conformation and protein adsorption/desorption on PAA, PEO, and mixed PEO/PAA brushes. *Langmuir*, 30(1):268–277, 2013.
- [317] E. Boroske, M. Elwenspoek, and W. Helfrich. Osmotic shrinkage of giant egg-lecithin vesicles. *Biophysical Journal*, 34(1):95–109, 1981.
- [318] A. Finkelstein, J. Zimmerberg, and F. S. Cohen. Osmotic swelling of vesicles: its role in the fusion of vesicles with planar phospholipid bilayer membranes and its possible role in exocytosis. *Annual review of Physiology*, 48:163–174, 1986.
- [319] T. Zhu, Z. Jiang, E. M. R. Nurlybaeva, J. Sheng, and Y. Ma. Effect of osmotic stress on membrane fusion on solid substrate. *Langmuir*, 29(21):6377–85, 2013.
- [320] J. Lehtinen, M. Raki, K. A. Bergström, P. Uutela, K. Lehtinen, A. Hiltunen, J. Pikkarainen, H. Liang, S. Pitkänen, A. M. Määttä, R. A. Ketola, M. Yliperttula, T. Wirth, and A. Urtti. Pre-targeting and direct immunotargeting of liposomal drug carriers to ovarian carcinoma. *PLoS ONE*, 7(7):1–10, 2012.
- [321] E. A. Bayer and M. Wilchek. The Use of the Avidin-Biotin Complex as a Tool in Molecular Biology. In *Methods of Biochemical Analysis*. John Wiley & Sons, Inc., 2006.

- [322] A. J. Van Der Vlies, C. P. Oneil, U. Hasegawa, N. Hammond, and J. A. Hubbell. Synthesis of pyridyl disulfide-functionalized nanoparticles for conjugating thiol-containing small molecules, peptides, and proteins. *Bioconjugate Chemistry*, 21(4):653–662, 2010.
- [323] C. Yoshina-Ishii, Y. H. M. Chan, J. M. Johnson, L. A. Kung, P. Lenz, and S. G. Boxer. Diffusive dynamics of vesicles tethered to a fluid supported bilayer by single-particle tracking. *Langmuir*, 22(13):5682–5689, 2006.
- [324] F. Höök, G. Stengel, A. B. Dahlin, A. Gunnarsson, M. P. Jonsson, P. Jönsson, E. Reimhult, L. Simonsson, and S. Svedhem. Supported lipid bilayers, tethered lipid vesicles, and vesicle fusion investigated using gravimetric, plasmonic, and microscopy techniques. *Biointerphases*, 3(2):108–116, 2008.
- [325] B. Van Lengerich, R. J. Rawle, and S. G. Boxer. Covalent attachment of lipid vesicles to a fluid-supported bilayer allows observation of DNA-mediated vesicle interactions. *Langmuir*, 26(11):8666–8672, 2010.
- [326] B. Geers, O. De Wever, J. Demeester, M. Bracke, S. C. De Smedt, and I. Lentacker. Targeted liposome-loaded microbubbles for cell-specific ultrasound-triggered drug delivery. *Small (Weinheim an der Bergstrasse, Germany)*, 9(23):4027–35, 12 2013.
- [327] S. K. Cool, B. Geers, S. Roels, S. Stremersch, K. Vanderperren, J. H. Saunders, S. C. De Smedt, J. Demeester, and N. N. Sanders. Coupling of drug containing liposomes to microbubbles improves ultrasound triggered drug delivery in mice. *Journal of controlled release*, 172(3):885–93, 2013.
- [328] A. Béduneau, P. Saulnier, F. Hindré, A. Clavreul, J. C. Leroux, and J. P. Benoit. Design of targeted lipid nanocapsules by conjugation of whole antibodies and antibody Fab’ fragments. *Biomaterials*, 28(33):4978–4990, 2007.
- [329] Y. Ohguchi, K. Kawano, Y. Hattori, and Y. Maitani. Selective delivery of folate-PEG-linked, nanoemulsion-loaded aclacinomycin A to KB nasopharyngeal cells and xenograft: effect of chain length and amount of folate-PEG linker. *Journal of drug targeting*, 16(9):660–667, 2008.
- [330] M. C. Dixon. Quartz Crystal Microbalance with Dissipation Monitoring : Enabling Real-Time Characterization of Biological Materials and Their Interactions. *Journal of Biomolecular Techniques*, 19:151–158, 2008.

- [331] C. E. Dodd, B. R. G. Johnson, L. J. C. Jeuken, T. D. H. Bugg, R. J. Bushby, and S. D. Evans. Native E. coli inner membrane incorporation in solid-supported lipid bilayer membranes. *Biointerphases*, 3(2), 2008.
- [332] A. J. Diaz, F. Albertorio, S. Daniel, and P. S. Cremer. Double cushions preserve transmembrane protein mobility in supported bilayer systems. *Langmuir*, 24(13):6820–6826, 2008.
- [333] R. H. Abou-Saleh, S. A. Peyman, K. Critchley, S. D. Evans, and N. H. Thomson. Nanomechanics of lipid encapsulated microbubbles with functional coatings. *Langmuir*, 29(12):4096–4103, 2013.
- [334] S. D. Fontaine, R. Reid, L. Robinson, G. W. Ashley, and D. V. Santi. Long-term stabilization of maleimide-thiol conjugates. *Bioconjugate Chemistry*, 26(1):145–152, 2015.
- [335] M. Daoud and J. Cotton. Star shaped polymers : a model for the conformation and its concentration dependence. *Journal de Physique*, 43:531–538, 1982.
- [336] E. M. Sevick. Shear swelling of polymer brushes grafted onto convex and concave surfaces. *Macromolecules*, 29(21):6952–6958, 1996.
- [337] K. Binder and A. Milchev. Polymer brushes on flat and curved surfaces: How computer simulations can help to test theories and to interpret experiments. *Journal of Polymer Science: Polymer Physics*, 50(22):1515–1555, 2012.
- [338] J. E. T. Corrie. Thiol-reactive fluorescent probes for protein labelling. *Journal of the Chemical Society, Perkin Transactions 1*, (20):2975, 1994.
- [339] M. Brinkley. A brief survey of methods for preparing protein conjugates with dyes, haptens, and cross-linking reagents. *Bioconjugate chemistry*, 3(1):2–13, 1991.
- [340] R. P. Lyon, J. R. Setter, T. D. Bovee, S. O. Doronina, J. H. Hunter, M. E. Anderson, C. L. Balasubramanian, S. M. Duniho, C. I. Leiske, F. Li, and P. D. Senter. Self-hydrolyzing maleimides improve the stability and pharmacological properties of antibody-drug conjugates. *Nature Biotechnology*, 32(10):1059–1062, 2014.
- [341] T. M. Allen, E. Brandeis, C. B. Hansen, G. Y. Kao, and S. Zalipsky. A new strategy for attachment of antibodies to sterically stabilized liposomes resulting in efficient targeting to cancer cells. *BBA - Biomembranes*, 1237(2):99–108, 1995.

- [342] A. S. M. Kamruzzahan, A. Ebner, L. Wildling, F. Kienberger, C. K. Riener, C. D. Hahn, P. D. Pollheimer, P. Winklehner, M. Hölzl, B. Lackner, D. M. Schörkl, P. Hinterdorfer, and H. J. Gruber. Antibody Linking to AFM Tips via Disulfide Bond Formation. *Bioconjugate chemistry*, 17(6):1473–81, 2006.
- [343] G. E. Davis. Scattering of Light by an Air Bubble in Water. *Journal of the Optical Society of America*, 45(7):572, 1955.
- [344] D. Sinton, D. Erickson, and D. Li. Microbubble lensing-induced photobleaching (μ -BLIP) with application to microflow visualization. *Experiments in Fluids*, 35(2):178–187, 2003.
- [345] C. M. Panje, D. S. Wang, and J. K. Willmann. Ultrasound and microbubble-mediated gene delivery in cancer: progress and perspectives. *Investigative radiology*, 48(11):755–69, 2013.
- [346] R. Aveyard, B. P. Binks, P. D. I. Fletcher, T. G. Peck, and C. E. Rutherford. Aspects of aqueous foam stability in the presence of hydrocarbon oils and solid particles. *Advances in Colloid and Interface Science*, 48(C):93–120, 1994.
- [347] B. S. Murray, E. Dickinson, and Y. Wang. Bubble stability in the presence of oil-in-water emulsion droplets: Influence of surface shear versus dilatational rheology. *Food Hydrocolloids*, 23(4):1198–1208, 2009.
- [348] J. Lee, A. Nikolov, and D. Wasan. Stability of aqueous foams in the presence of oil: On the importance of dispersed vs solubilized oil. *Industrial and Engineering Chemistry Research*, 52(1):66–72, 2013.
- [349] K. Osei-Bonsu, N. Shokri, and P. Grassia. Foam stability in the presence and absence of hydrocarbons: From bubble- to bulk-scale. *Colloids and Surfaces A: Physicochemical and Engineering Aspects*, 481:514–526, 2015.
- [350] R. K. Jain. Normalizing tumor vasculature with anti-angiogenic therapy: a new paradigm for combination therapy. *Nature medicine*, 7(9):987–989, 2001.
- [351] M. L. Toews. Pharmacologic Principles for Combination Therapy. *Proceedings of the American Thoracic Society*, 2(4):282–289, 2005.
- [352] T. C. Chou. Drug combination studies and their synergy quantification using the chou-talalay method. *Cancer Research*, 70(2):440–446, 2010.

- [353] A. B. Subramaniam, M. Abkarian, and H. A. Stone. Controlled assembly of jammed colloidal shells on fluid droplets. *Nature materials*, 4(7):553–556, 2005.
- [354] M. Abkarian, A. B. Subramaniam, S. H. Kim, R. J. Larsen, S. M. Yang, and H. A. Stone. Dissolution arrest and stability of particle-covered bubbles. *Physical Review Letters*, 99(18):1–4, 2007.
- [355] M. Azmin, G. Mohamedi, M. Edirisinghe, and E. P. Stride. Dissolution of coated microbubbles: The effect of nanoparticles and surfactant concentration. *Materials Science and Engineering C*, 32(8):2654–2658, 2012.
- [356] G. Mohamedi, M. Azmin, I. Pastoriza-Santos, V. Huang, J. Pe, L. M. Liz-Marza, M. Edirisinghe, and E. Stride. Effects of Gold Nanoparticles on the Stability of Microbubbles. *Langmuir*, (28):13808–13812, 2012.
- [357] J. L. Raymond, K. J. Haworth, K. B. Bader, K. Radhakrishnan, J. K. Griffin, S. L. Huang, D. D. McPherson, and C. K. Holland. Broadband attenuation measurements of phospholipid-shelled ultrasound contrast agents. *Ultrasound in Medicine and Biology*, 40(2):410–421, 2014.
- [358] J. R. McLaughlan, N. Ingram, P. R. Smith, S. Harput, P. L. Coletta, S. D. Evans, and S. Freear. Increasing the sonoporation efficiency of targeted polydisperse microbubble populations using chirp excitation. *IEEE Transactions on Ultrasonics, Ferroelectrics, and Frequency Control*, 60(12):2511–2520, 2013.
- [359] Y. Luan, T. Faez, E. Gelderblom, I. Skachkov, B. Geers, I. Lentacker, T. van der Steen, M. Versluis, and N. de Jong. Acoustical Properties of Individual Liposome-Loaded Microbubbles. *Ultrasound in Medicine and Biology*, 38(12):2174–2185, 2012.
- [360] J. R. McLaughlan, N. Ingram, R. Abou-Saleh, S. Harput, A. T. Evans, S. D. Evans, P. L. Coletta, and S. Freear. High-frequency subharmonic imaging of liposome-loaded microbubbles. *IEEE International Ultrasonics Symposium, IUS*, pages 1501–1504, 2013.
- [361] D. W. Rickey, P. A. Picot, D. A. Christopher, and F. A. A Wall-Less Vessel Phantom for Doppler Ultrasound Studies. *Ultrasound in Medicine and Biology*, 21(9):1163–1176, 1995.

- [362] C. Veltmann, S. Lohmaier, T. Schlosser, S. Shai, A. Ehlgen, C. Pohl, H. Becher, and K. Tiemann. On the design of a capillary flow phantom for the evaluation of ultrasound contrast agents at very low flow velocities. *Ultrasound in Medicine and Biology*, 28(5):625–634, 2002.
- [363] I. De Cock, E. Zagato, K. Braeckmans, Y. Luan, N. de Jong, S. C. De Smedt, and I. Lentacker. Ultrasound and microbubble mediated drug delivery: acoustic pressure as determinant for uptake via membrane pores or endocytosis. *Journal of controlled release : official journal of the Controlled Release Society*, 197:20–8, 1 2015.
- [364] I. De Cock, G. Lajoinie, M. Versluis, S. C. De Smedt, and I. Lentacker. Sonoprinting and the importance of microbubble loading for the ultrasound mediated cellular delivery of nanoparticles. *Biomaterials*, 83:294–307, 2016.
- [365] A. van der Net, L. Blondel, A. Saugey, and W. Drenckhan. Simulating and interpreting images of foams with computational ray-tracing techniques. *Colloids and Surfaces A: Physicochemical and Engineering Aspects*, 309(1-3):159–176, 2007.
- [366] T. Gaillard, C. Honorez, M. Jumeau, F. Elias, and W. Drenckhan. A simple technique for the automation of bubble size measurements. *Colloids and Surfaces A: Physicochemical and Engineering Aspects*, 473:68–74, 2015.
- [367] A. D. Nikolov, D. Wasan, D. Huang, and D. A. Edwards. The Effect of Oil on Foam Stability: Mechanisms and Implications for Oil Displacement by Foam in Porous Media. *Proceedings of SPE Annual Technical Conference and Exhibition*, 1, 1986.
- [368] K. Koczó, L. A. Lobo, and D. T. Wasan. Effect of oil on foam stability: Aqueous foams stabilized by emulsions. *Journal of Colloid And Interface Science*, 150(2):492–506, 1992.
- [369] U. Römling and C. Balsalobre. Biofilm infections, their resilience to therapy and innovative treatment strategies. *Journal of Internal Medicine*, 272(6):541–561, 2012.
- [370] P. K. Sharma, M. J. Gibcus, H. C. V. Der, H. J. Busscher, and H. C. V. D. Mei. Influence of Fluid Shear and Microbubbles on Bacterial Detachment from a Surface Influence of Fluid Shear and Microbubbles on Bacterial Detachment from a Surface. *American Society for Microbiology*, 71(7):3668–3673, 2005.

- [371] C. Zhu, N. He, T. Cheng, H. Tan, Y. Guo, D. Chen, M. Cheng, Z. Yang, and X. Zhang. Ultrasound-targeted microbubble destruction enhances human β -defensin 3 activity against antibiotic-resistant staphylococcus biofilms. *Inflammation*, 36(5):983–996, 2013.
- [372] B. H. T. Goh, M. Conneely, H. Kneuper, T. Palmer, E. Klaseboer, B. C. Khoo, and P. Campbell. High-Speed Imaging of Ultrasound-Mediated Bacterial Biofilm Disruption. In I. Lacković and D. Vasic, editors, *6th European Conference of the International Federation for Medical and Biological Engineering: MBEC 2014, 7-11 September 2014, Dubrovnik, Croatia*, pages 533–536, Cham, 2015. Springer International Publishing.
- [373] N. He, J. Hu, H. Liu, T. Zhu, B. Huang, X. Wang, Y. Wu, W. Wang, and D. Qu. Enhancement of vancomycin activity against biofilms by using ultrasound-targeted microbubble destruction. *Antimicrobial Agents and Chemotherapy*, 55(11):5331–5337, 2011.
- [374] Y. Dong, S. Chen, Z. Wang, N. Peng, and J. Yu. Synergy of ultrasound microbubbles and vancomycin against *Staphylococcus epidermidis* biofilm. *Journal of Antimicrobial Chemotherapy*, 68(4):816–826, 2013.
- [375] C. L. Ventola. The antibiotic resistance crisis: part 1: causes and threats. *P & T : A peer-reviewed journal for formulary management*, 40(4):277–83, 2015.
- [376] D. J. Stickler. Bacterial biofilms in patients with indwelling urinary catheters. *Nature Clinical Practice Urology*, 5(11):598–608, 2008.
- [377] A. Upadhyay and S. V. Dalvi. Synthesis, characterization and stability of BSA-encapsulated microbubbles. *RSC Adv.*, 6(18):15016–15026, 2016.
- [378] X. E., Z. Pei, and K. Schmidt. Ice Cream: Foam Formation and Stabilization—A Review. *Food Reviews International*, 26(2):122–137, 2010.
- [379] A. Madene, M. Jacquot, J. Scher, and S. Desobry. Flavour encapsulation and controlled release - A review. *International Journal of Food Science and Technology*, 41(1):1–21, 2006.
- [380] J. S. Park and K. Kurata. Application of Microbubbles to Hydroponics Solution Promotes Lettuce Growth. *HortThecnology*, 19(1):212–215, 2009.

- [381] K. Ebina, K. Shi, M. Hirao, J. Hashimoto, Y. Kawato, S. Kaneshiro, T. Morimoto, K. Koizumi, and H. Yoshikawa. Oxygen and Air Nanobubble Water Solution Promote the Growth of Plants, Fishes, and Mice. *PLoS ONE*, 8(6):2–8, 2013.
- [382] B. Singh Sekhon. Nanotechnology in agri-food production: An overview. *Nanotechnology, Science and Applications*, 7(2):31–53, 2014.